INNOVATION LAB

FORUM ORGANIC ELECTRONICS

Sami Hamwi

Transition Metal Oxides in Organic Light Emitting Diodes

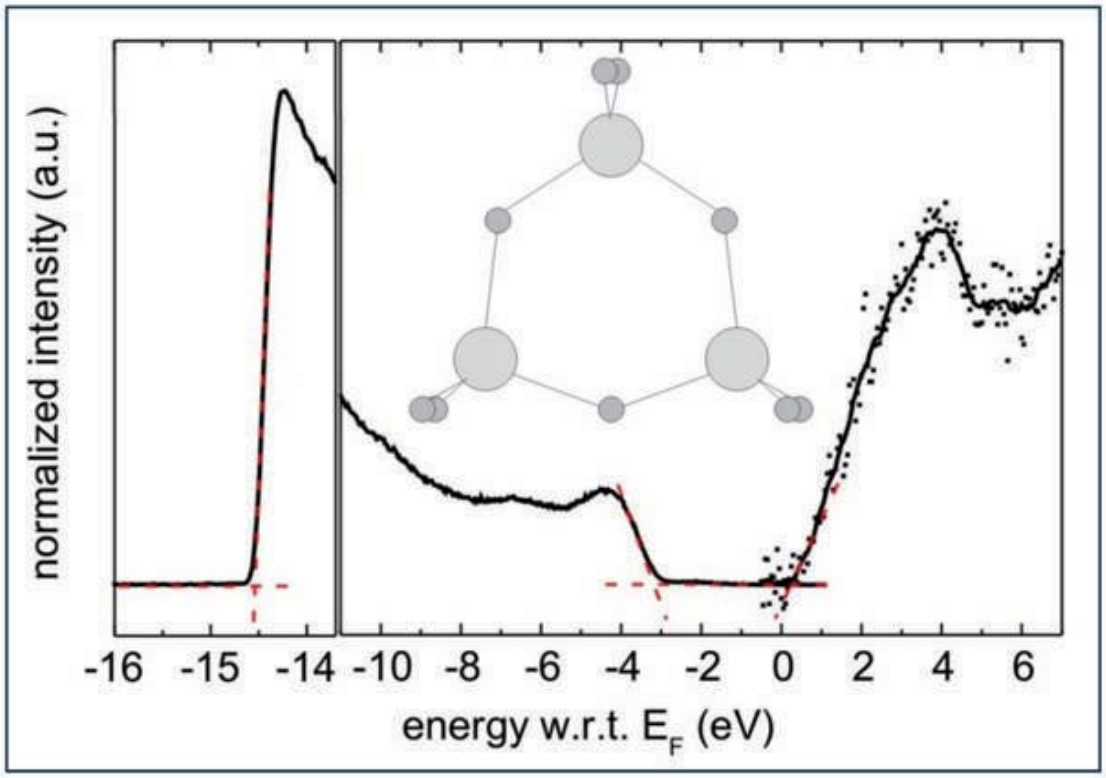

Volume 1 | Forum Organic Electronics Science Series
Edited by Wolfgang Kowalsky and Bernhard Schweizer

Cuvillier Verlag Göttingen
Internationaler wissenschaftlicher Fachverlag

Transition Metal Oxides in Organic Light Emitting Diodes

Von der Fakultät für Elektrotechnik, Informationstechnik, Physik
der Technischen Universität Carolo-Wilhelmina zu Braunschweig

zur Erlangung der Würde eines
Doktor-Ingenieurs (Dr.-Ing.)
genehmigte

Dissertation

von
Dipl.-Wirtsch.-Ing. Sami Hamwi
aus Lüdenscheid

Eingereicht am:	07. Juni 2010
Mündliche Prüfung am:	09. Juli 2010
Referenten:	Prof. Dr.-Ing. W. Kowalsky
	Prof. Dr. rer. nat. A. Waag

2010

Bibliografische Information der Deutschen Nationalbibliothek
Die Deutsche Nationalbibliothek verzeichnet diese Publikation in der Deutschen Nationalbibliographie; detaillierte bibliographische Daten sind im Internet über http://dnb.d-nb.de abrufbar.
1. Aufl. - Göttingen: Cuvillier, 2010
Zugl.: (TU) Braunschweig, Univ., Diss., 2010

ISBN 978-3-86955-484-6

Nonnenstieg 8, 37075 Göttingen
Telefon: 0551-54724-0
Telefax: 0551-54724-21
www.cuvillier.de

1. Auflage 2010
Gedruckt auf säurefreiem Papier.

ISBN 978-3-86955-484-6
ISSN 2191-1428

Editor's preface

This book is the first in the Forum Organic Electronics Science Series, which is intended to highlight and promote selected scientific achievements within the field of organic and printed electronics.

Forum Organic Electronics is a distinguished leading-edge cluster centered in the Rhine-Neckar Metropolitan Region and combines the scientific excellence and economic strength of its academic and corporate partners to grow the seeds of a new technology into a prosperous plastic semiconductors industry in the German southwest. The partners' network includes 3 DAX-noted and 7 internationally involved enterprises, 6 middle-sized businesses and 9 universities respectively research institutions. These partners operate at complementary positions along the value chain which ranges from the design and synthesis of novel materials, the research on next-generation devices, the development of inexpensive processing technology and production systems -especially printing technology- and finally the marketing of breakthrough applications and services.

As the vital strategy tool of the cluster, the leading partners have jointly founded InnovationLab GmbH (iL), an application-oriented research and transfer platform of business and science with the common goal of driving innovation.

We have selected the dissertation thesis of Dr.-Ing. Sami Hamwi for publication as the first edition of the Forum Organic Electronics Science Series, as it is a representative piece of science generated within the cluster network. Further, we identified Dr. Hamwi as a talented researcher at an early career stage whose research work is inspired by genuine curiosity, fueled by strong dedication and carried by his intellectual power and personal integrity. These values are reflected in the excellence of his research and serve as key values to be pursued by other young researchers, which will follow.

In this book, Dr. Hamwi presents a conclusive study on the various effects of transition metal oxides when applied to organic electronic devices. He starts with describing the physical properties of the studied metal oxides and the interaction with or in organic thin films. Finally, he succeeded in transferring ideas generated from fundamental research to new device concepts, such as stacked organic light emitting diodes which can be used in next-generation lighting applications.

We would like to thank the author for his important contribution and we are confident that this work will spur new and interesting ideas for the future.

Heidelberg, September 2010

Prof. Dr. Wolfgang Kowalsky

Bernhard Schweizer

Managing Directors, InnovationLab GmbH

Danksagung

Die vorliegende Arbeit entstand während meiner Tätigkeit als wissenschaftlicher Mitarbeiter am Institut für Hochfrequenztechnik an der Technischen Universität Braunschweig. Das von Prof. Dr.-Ing. Wolfgang Kowalsky geleitete Institut beschäftigt sich seit mehr als fünfzehn Jahren höchst erfolgreich im Bereich der organischen Optoelektronik. Ein besonderer Forschungsschwerpunkt liegt hierbei im Bereich der organischen Leuchtdioden, die vielversprechende Eigenschaften für Display- und Beleuchtungsanwendungen aufweisen.

Daher gilt zuerst mein Dank Prof. Dr.-Ing. Wolfgang Kowalsky, der es mir ermöglichte, in diesem dynamischen und spannenden Forschungsumfeld eigenverantwortlich und gemeinsam mit universitären und industriellen Kooperationspartnern zu arbeiten und von der interdisziplinären Zusammenarbeit mit Kollegen unterschiedlicher Fachrichtung sowie der ausgezeichneten Ausstattung des Instituts zu profitieren.

Mein Dank gilt auch der Prüfungskommission, in der Prof. Dr. rer. nat. Andreas Waag, Leiter des Instituts für Halbleitertechnik, das Koreferat und Prof. Dr. rer. nat. Andreas Hangleiter, Leiter des Instituts für Angewandte Physik, den Prüfungsvorsitz übernahmen.

Weiterhin möchte ich mich besonders bei meinem damaligen Arbeitsgruppenleiter und jetzigen Leiter des Lehrstuhls für Elektronische Bauelemente an der Bergischen Universität Wuppertal - Prof. Dr. rer. nat. Thomas Riedl - für die wissenschaftliche Unterstützung bedanken. Die fachlichen Diskussionen und strategischen Besprechungen mit ihm aber auch die gemeinsamen Ausflüge zum Braunschweiger Weihnachtsmarkt bleiben in allerbester Erinnerung.

Prof. Antoine Kahn vom Department of Electrical Engineering und seiner gesamten Gruppe möchte ich herzlich danken für die freundliche Aufnahme im Rahmen meiner wissenschaftlichen Aufenthalte an der Princeton University und für die überaus fruchtbare Zusammenarbeit. Viele der von mir präsentierten Ergebnisse wären ohne die präzisen Arbeiten an deren Vakuumsystem zur Photoelektronenspektroskopie nicht möglich gewesen.

Zu ganz besonderem Dank bin ich zwei meiner ehemaligen Kollegen verpflichtet: Dr.-Ing. Michael Kröger und Dr.-Ing. Jens Meyer. Beide haben mich bei meiner vorangegangenen Diplomarbeit hervorragend betreut. Und beide haben mich während meiner Promotionszeit wissenschaftlich begleitet. Sowohl die Zielstrebigkeit und das hohe Engagement von Michael

als auch die ansteckende Begeisterung von Jens sowie seine pragmatische Art und Weise, offen an die wissenschaftlichen Problemstellungen heranzugehen, haben mich geprägt und bleiben genauso wie ihr Beitrag zu den spektroskopischen Arbeiten in Princeton unvergessen.

Desweiteren möchte ich meinen Bürokollegen Dipl.-Ing. Stephan Schmale und Dipl.-Ing. Thomas Winkler dafür danken, dass sie immer zu einer angenehmen Atmosphäre im Büro beigetragen haben unabhängig von der Höhe der jeweiligen Arbeitsbelastung oder des terminlichen Zeitdrucks. Die enge Zusammenarbeit mit Thomas im Rahmen eines Forschungsprojekts möchte ich hierbei besonders hervorheben - sei es aufgrund der exzellenten Teamarbeit im Labor oder der erkenntnisreichen Diskussionen im Büro - für beides möchte ich mich bei Thomas bedanken. Die überaus unterhaltsamen Skat-Abende zusammen mit Dr.-Ing. Torsten Rabe und Dr.-Ing. Patrick Görrn im Aufenthaltsraum des Instituts bleiben genauso in bester Erinnerung wie die tägliche Kaffeerunde mit Ursula Heydecke, die seit ihrem altersbedingten Ausscheiden dem Institut als tatkräftige Unterstützung im Labor schmerzlich fehlt. Allen hier nicht weiter genannten Kollegen möchte ich an dieser Stelle ebenfalls ganz herzlich danken für den kollegialen Umgang und die sehr gute Stimmung im Institut sowie für die gemeinsamen Institutsaktionen, die immer eine willkommene Abwechslung darstellten.

Ebenso geht mein Dank an die Studenten, die mich durch ihr hohes Engagement im Rahmen von Diplom- und Projektarbeiten wissenschaftlich vorangebracht haben. Hierfür möchte ich mich namentlich bei Johannes Reinker, Marco Witte, Markus Krückemeier, Tobias Göhring, Walerij Wehage sowie Abdel-Rassidou Ayeva bedanken.

Für die zügige Durchsicht meiner Arbeit möchte ich mich nochmals bei Prof. Dr. rer. nat. Thomas Riedl und für die englische Rechtschreib- und Grammatiküberprüfung bei Frau Rebecca Schulz bedanken.

Meine Eltern haben mich von Anfang an unterstützt und gefördert, bei allem was ich in den bisherigen dreißig Jahren meines Lebens angepackt habe. Ohne das Vertrauen, das sie in mich gesetzt haben, und ohne die Sicherheit, die sie mir entgegengebracht haben, wäre ich nicht so schnell und so weit bis hierher gekommen. Dafür danke ich meiner Familie bis in alle Ewigkeit.

Mein höchster Dank gilt meiner Frau Daniela, die nicht nur viel gemeinsame Zeit während der Promotion geopfert hat, sondern auch eine riesige moralische Unterstützung gewesen ist. Mir ihrer liebevollen Zuwendung und Geduld, ihrem Verständnis und ihrem starken Willen ist uns alles möglich. Dafür danke ich Dir und dafür liebe ich Dich!

Braunschweig, im August 2010

Sami Hamwi

Kurzfassung

Organische Leuchtdioden (engl. organic light emitting diode, OLED) besitzen spezielle Eigenschaften, die sie für den Einsatz in Displayanwendungen und Raumbeleuchtung prädestinieren. Sie können in extrem flacher Bauweise ausgeführt werden und besitzen eine weite Abstrahlcharakteristik. Vor allem die Perspektive auf eine kostengünstige Massenproduktion für großflächige Anwendungen treibt die Entwicklung der OLEDs massiv an. Entsprechend konnten in den letzten Jahren erhebliche Fortschritte bezüglich Effizienz und Lebensdauer der organischen Leuchtdioden erzielt werden. Eine Aussicht auf eine positive Weiterentwicklung stellt der Einsatz von inorganischen Schichten aus Übergangsmetalloxiden (engl. transition metal oxide, TMO) dar wegen ihrer hohen thermischen Stabilität und technologischen Kompatibilität zu organischen Schichten. Erste Resultate deuten auf einen vielseitigen Einsatz der TMOs als funktionelle Schichten wie auch elektrochemische Dotanden von organischen Halbleitern hin. Gleichzeitig fehlen jedoch Kenntnisse über deren elektronische Eigenschaften sowie die genaue Wirkungsweise innerhalb organischer Leuchtdioden. Im Zusammenhang damit wird deutlich, dass trotz der technologischen Fortschritte bei OLEDs, grundlegende Fragestellungen wie der Mechanismus der elektrochemischen Dotierung organischer Halbleiter oder der Mechanismus von ladungserzeugenden Zwischenschichten (engl. charge generation layer, CGL) in gestapelten OLEDs bisher nicht vollständig geklärt worden sind.

Deshalb werden in dieser Arbeit die physikalischen und technologischen Zusammenhänge beim Einsatz von Übergangsmetalloxiden in OLEDs im Fokus stehen. Mittels Photoelektronenspektroskopie und Kelvinsondenmessungen wird zunächst die elektronische Struktur ausgewählter TMOs wie Molybdänoxid (MoO_3) und Wolframoxid (WO_3) näher analysiert. Es zeigt sich, dass es sich hierbei um intrinsisch n-dotierte Halbleiter handelt, die im Vergleich zu organischen Halbleitern sehr tief liegende Energieniveaus für Löcher- und Elektronentransport besitzen. Basierend auf der Betrachtung der Grenzflächen zwischen TMOs und benachbarter Schichten wird ein neuartiges Modell zur Erklärung der effizienten Löcherinjektion durch den Einsatz dünner TMO Schichten aufgestellt.

Die elektrochemische Dotierung stellt einen wichtigen Ansatz zur Erhöhung der Effizienzen von OLEDs dar. Deshalb wird die Eignung von MoO_3 und Cs_2CO_3 (Cäsiumcarbonat) als p- und n-Dotanden von organischen Halbleitern mit großer Bandlücke untersucht. Vor allem

die Bestimmung der dotierkonzentrationsabhängigen Ladungsträgerdichte steht im Vordergrund. Hierzu werden Methoden eingesetzt, wie sie aus der Welt der anorganischen Halbleiter bekannt sind, und miteinander verglichen. Neben Kapazitäts-Spannungs-Messungen an Metall-Isolator-Halbleiter Strukturen wird die direkte Ermittlung der Raumladungszone in dotierten Schichten bei Angrenzung an metallischen Elektroden untersucht. Ein annähernd linearer Anstieg der Ladungsträgerdichte mit der Dotierkonzentration wird als generelles Resultat nachgewiesen. Gleichzeitig ergeben sich unerwartet niedrige Dotiereffizienzen von durchschnittlich weniger als fünf Prozent für MoO_3.

Das vertikale Stapeln organischer Leuchtdioden übereinander kann zur Erhöhung der Lebensdauer der Bauteile beitragen. Hierfür wird das physikalische Verständnis der ladungserzeugenden Zwischenschichten erarbeitet. Neben der Angrenzung zweier komplementär dotierter Bereiche ein- und desselben ambipolaren organischen Halbleiters aneinander, wird vor allem der Einsatz von TMOs in diesen CGLs untersucht. Der Mechanismus der Ladungsträgerseparation wird mit der Ausbildung einer Raumladungszone in Verbindung gebracht. Außerdem zeigt sich, dass jeweils zwischen dem TMO und der angrenzenden lochtransportierenden Schicht die Ladungsträgergeneration stattfindet.

Aus den gewonnenen Erkenntnissen im Laufe der Arbeit wird schließlich die erste organische p-i-n Homodiode verwirklicht, die als violette Leuchtdiode und ultraviolette Photodiode betrieben werden kann.

Abstract

Organic light emitting diodes (OLEDs) exhibit several specific properties such as an extremely thin design and a wide viewing angle, making them favorable for the application in display technology and general lighting. The development of OLEDs is strongly driven by the prospect of low-cost production of large-area applications in the future. Accordingly, their performance was considerably enhanced in terms of efficiency and lifetime over the past years. The introduction of transition metal oxides (TMOs) in OLEDs is regarded as a promising concept for further improving their properties due to their technological compatibility with organic layers and their high thermal stability. The first results from the insertion of TMOs in OLEDs indicate their versatile application as neat functional layers and electrochemical dopants of organic semiconductors. On the other hand, the knowledge of their electronic properties and the mode of operation in OLEDs is very limited so far. In this context, it becomes apparent that fundamental mechanisms such as the electrochemical doping of organic semiconductors or the charge generation in interconnecting units of stacked OLEDs are not yet completely clarified.

Thus, this work focuses on the physical and technological correlations arising from the application of transition metal oxides in organic light emitting diodes. First, the electronic structure of molybdenum oxide (MoO_3) and tungsten oxide (WO_3) is analyzed by photoelectron spectroscopy and Kelvin probe. It is demonstrated that both TMOs exhibit comparably deep-lying energy levels. Moreover, their electronic structure indicates them as intrinsically n-doped semiconductors. The functional principle of the efficient hole injection by neat layers of TMO is then studied by the examination of the interfaces between the TMO and its adjacent layers. As a result, a new model of hole injection by thin TMO layers is developed.

The concept of electrochemical doping in OLEDs represents a very important technique to improve their overall efficiency. For that reason, the suitability of MoO_3 as p-type dopant and Cs_2CO_3 (cesium carbonate) as n-type dopant of organic wide band gap semiconductors is studied, respectively. First, the impact of electrochemical doping on the electrical, optical and morphological properties is analyzed. The focus, however, is on the determination of the doping concentration dependent charge carrier densities. Measurement techniques, known from the world of inorganic semiconductors, such as capacitance-voltage measurements on metal-insulator-semiconductor structures or the direct analysis of the space charge region

in doped semiconductors at the metallic electrode are applied for the determination of the densities and compared with each other. The study reveals an approximately linear increase of the charge carrier density with higher doping concentrations as a general result. At the same time, the doping efficiency of MoO_3 is unexpectedly low and under five percent on average.

The stacking of several light emitting units on top of each other is known to increase the lifetime of organic devices. Therefore, it is important to reveal the functional principle of the charge generation layers (CGL) as the interconnecting units of the stacked OLEDs. Besides the analysis of a complementarily doped homojunction-CGL, the role of neat layers of TMO in CGLs is investigated. The mechanism of charge generation between doped layers is explained by the formation of a space charge region. On the other hand, it is demonstrated that the actual charge generation in interconnecting units using transition metal oxides occurs at the interface between the TMO and the adjacent hole transporting layer.

Finally, the investigations of the physical aspects in this work allowed for the realization of the first organic p-i-n homojunction device which operates both as violet light emitting diode and visible blind photodiode.

Contents

List of Abbreviations

ALD	atomic layer deposition
AFM	atomic force microscopy
CB	conduction band
CGL	charge generation layer
CIE	Commision internationale de l'*é*clairage
CMA	cylindrical mirror analyzer
CNL	charge neutrality level
DOS	density of states
EA	electron affinity
EBL	electron blocking layer
EIL	electron injection layer
EL	electroluminescence
EML	emission layer
ETL	electron transport layer
FN	Fowler-Nordheim
HBL	hole blocking layer
HIL	hole injection layer
HOMO	highest occupied molecular orbital
HTL	hole transport layer
IE	ionization energy
IPES	inverse photoelectron spectroscopy
ITO	indium tin oxide
KP	Kelvin probe
KPFM	Kelvin probe force microscope
LUMO	lowest unoccupied molecular orbital
MBE	molecular beam epitaxy
MIS	metal-insulator-semiconductor
OLED	organic light emitting diode
OSC	organic solar cell

PL	photoluminescence
RS	Richardson-Schottky
SCLC	space charge limited current
SMU	source measure unit
STM	scanning tunneling microscopy
TCO	transparent conductive oxide
TFL	trap filled limit
TMO	transition metal oxide
UHV	ultra high vacuum
UPS	ultraviolet photoelectron spectroscopy
VB	valence band
VL	vacuum level
WF	work function

1 Introduction

Organic light emitting diodes (OLEDs) have attracted much interest in research and development in the last two decades because of their potential use in displays as self-emitting pixels or backlight solution. They are very thin and therefore lightweight, exhibit low power consumption and can be deposited on different substrates and backplanes allowing for the use in mobile applications. They permit completely new areas of application, not only for displays but also for the field of general lighting, if they are combined with transparent electronics or flexible substrates. This opens up a variety of new design possibilities particularly in ambient lighting. That is why, OLEDs are considered to be the next generation of solid-state lighting, displacing current technologies and shaping the world and its future appearance.

1.1 Organic Light Emitting Diodes

The research on light emitting organic semiconductors goes back to Pope *et al.* who first demonstrated the light emission of anthracene crystals [1]. However, high operating voltages were needed for sufficiently high luminance values so that low efficiencies were the consequence. After the development of a novel concept of OLEDs by Tang and VanSlyke a quarter of century later, efficiencies around 1 % were obtained, arousing the interest on the part of display and lighting companies [2]. The revolutionary breakthrough was realized by the introduction of an organic heterostructure allowing for separate transport of holes and electrons into the device. To this day, conventional OLEDs are based on this basic concept comprising at least an organic hole transport layer (HTL) deposited on indium tin oxide (ITO) as the transparent bottom anode, an organic electron transport layer (ETL) and an opaque metallic cathode on top. An additional organic emission layer (EML) is usually sandwiched between the charge transport materials containing dye molecules which allow for light emission in the visible region. In operation, holes and electrons are injected into the device, recombine within the EML and form excitons whose radiative decay leads to the light generation and emission through the ITO coated transparent substrate as schematically shown in Figure 1.1a. In the mean time, further concepts have been established such as the insertion of additional organic layers as exciton and charge carrier blockers localizing the

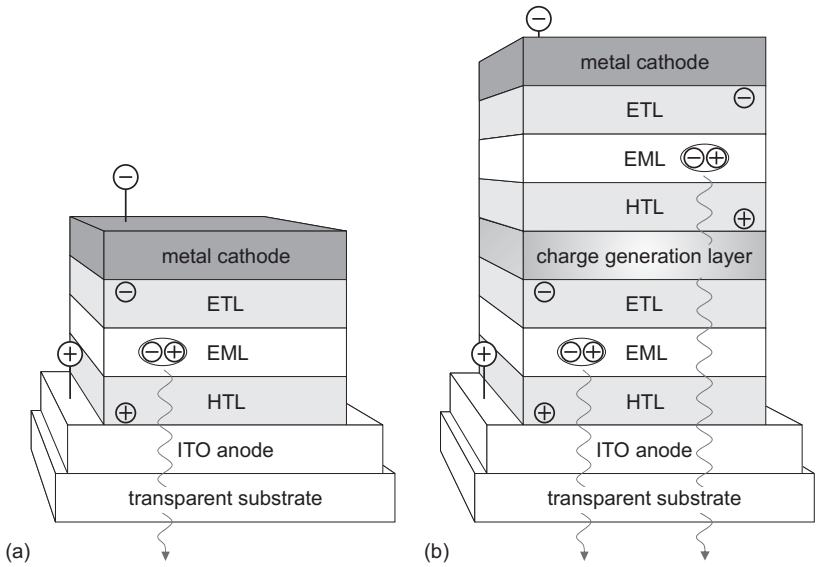

Figure 1.1: Scheme and working principle of a conventional bottom-emitting (a) single OLED structure and (b) twofold stacked OLED structure with charge generation layer.

emission zone and preventing exciton quenching effects as well as charge carrier imbalance. Particularly, the introduction of phosphorescent emitters led to highly efficient OLEDs with low operating voltages and efficiencies up to 130 lm/W [3, 4], underlining their potential use in future display and lighting applications.

However, OLEDs are still lacking long operating lifetimes. One possibility to increase their lifetime, using present organic materials and devices, is to stack a number of OLEDs on top of each other, in order to reduce the current through the light emitting units, while still achieving a given luminance level. This approach is supported by the fact that organic semiconductors provide a large Stokes shift and therefore cause only low intrinsic absorption losses. Moreover, considerations in respect to epitaxial lattice matching as known for inorganic semiconductors do not exist for organic devices. This reduces the cost and complexity of stacking several light emitting units. One has to distinguish between two concepts of stacking. On the one hand, the sub-OLEDs can be separated by a combination of thin transparent electrodes and insulators in order to drive the light emitting units individually. This concept not only allows for longer lifetimes but also for a tunable color emission [5]. On the other hand, the whole stacked device can be driven by only one voltage source when specific charge generation layers are inserted between the light emitting units [6]. Figure 1.1b exemplarily shows the schematic and working principle for a twofold stacked OLED according to the second concept.

1.2 Transition Metal Oxides

Transition metal oxides (TMOs) are well known for their fascinating magnetic and electronic properties. For instance, Manganites are found to possess extremely large magnetoresistance and the discovery of high temperature superconductivity in Cuprates in 1986 aroused new scientific interest in TMOs [7,8]. Though the most important transition metals according to these properties are the eight elements with the atomic numbers from 22 to 29, all elements with an incomplete d shell in the periodic table are considered as transition elements. The outer d electrons are thereby responsible for their influence on the metal-oxygen bonding varying from nearly ionic to metallic [7]. In particular, the multitude of preparation techniques and possibilities for the combination of transition metals with other elements of the periodic table leads to a very large quantity of chemical compounds which is comparable to the diversity of organic materials.

Binary transition metal oxides like MoO_3 and WO_3 gained additional attention due to their specific optical properties. Their light absorbing properties change by irradiation or application of an electric field which is known as photochromism and electrochromism, respectively [9, 10]. That is why intensive research onto these materials aroused in the early nineteen-sixties which led to the first thin film deposition experiments of TMOs in ultra high vacuum (UHV) systems. Similar to organic small molecules they can be thermally evaporated and can form smooth amorphous films. Moreover, they exhibit high transparencies despite their photochromism. For this reason, TMOs show a high level of technological compatibility with organic materials which led to several combinations in organic devices such as light emitting diodes and solar cells. For example, they are used as buffer layers on top of organic materials, protecting them against the highly energetic particles emerging during the sputter deposition process of transparent conductive oxides [11, 12]. Additionally, they form semitransparent electrodes in multilayer oxide structures [13, 14] and can be used for efficient hole injection either as neat layers or as p-type dopants of organic charge transport materials [15–18]. Finally, thin layers of TMOs have been used as interconnecting units in stacked OLEDs [19, 20]. In any case, they appear to match the electronic properties of organic materials. However, the origin of these properties particularly after their thermal evaporation in UHV is unclear and needs further investigation.

1.3 Goals and Outline

This work deals with the introduction of TMOs in OLEDs as promising inorganic materials, allowing for the effective implementation of device concepts such as hole injection, p-type

doping and electric field-assisted charge generation between stacked OLEDs. The focus of the study is on the physical understanding of the TMOs and their impact on the OLED.

Therefore, Chapter 2 starts with the description of the fundamental physics of organic semiconductors and the basics of OLEDs. In Chapter 3, the most important device preparation techniques and analytical methods used in this work are summarized.

Since the electronic properties of the TMOs are the center and pivotal point of this study, Chapter 4 starts with the results of photoelectron spectroscopy and Kelvin probe analysis on thin films of MoO_3 and WO_3, providing their energy levels and electronic structure. That enables the set up of a new model for hole injection by TMOs, supported by the electronic investigation of the interface dipoles between the participating layers. Additional properties of neat TMO films such as electron blocking and luminescence quenching are discussed at the end of this chapter.

Chapter 5 demonstrates the electrochemical doping of organic semiconductors by MoO_3 and Cs_2CO_3. First, the impact of p- and n-type doping on the organic ambipolar material CBP is studied by several analytical methods, referring to its electronic, electrical, morphological and optical properties. Then, the determination of the doping-induced charge carrier densities is demonstrated mainly by two measuring techniques, including the Kelvin probe analysis of the thickness-dependent work function characteristics of doped organic semiconductors deposited on ITO, and capacitance-voltage measurements on metal-insulator-semiconductor structures. It is shown that a linear increase of charge carrier densities occurs with higher doping concentrations and that a low doping efficiency of MoO_3 as p-type dopant is existent. The chapter closes with a discussion of the doping efficiency, giving specific and general reasons for this result.

Chapter 6 is dedicated to the charge generation mechanism in interconnecting units between stacked OLEDs. A physical model of the charge generation at doped p-n homojunctions based on CBP is derived by the measurement of thickness-dependent onset voltages of charge injection and charge separation in a specific device structure. In the second part of this chapter, the role of neat TMO films in the interconnecting units is clarified by the measurement of angular-resolved emission characteristics of stacked OLEDs and the analysis of the interfaces between the TMO and its adjacent organic layers. As a result, the actual charge generation is attributed to the interface between the TMO and its neighboring hole transport layer.

Considering the results of Chapter 5 and 6 in respect to the p- and n-type doping of the ambipolar semiconductor CBP, a novel p-i-n homojunction device is presented in Chapter 7 which can be operated both as a light emitting device and a photodiode. Electro-optical

characteristics are demonstrated such as the superlinear increase of the photocurrent with higher optical power densities and the violet light emission. Despite the low external quantum efficiency as a light emitting device, the p-i-n homojunction diode is considered to offer new insights into the physical mechanisms of organic semiconductors.

2 Fundamentals of Organic Devices

Organic materials based on conjugated carbon rings can comprise both electrical conductivity and the ability to emit light after optical or electrical excitation. These properties come from their electronic structure which can be explained by considering the organic molecules in aggregated solid-state phase. In the following, the physical fundamentals of organic semiconductors and their implications for the functionality of organic light emitting diodes will be reviewed.

2.1 Small Molecules with Conjugated π-Systems

Organic semiconductors are based on aromatic compounds of carbon atoms. Normally, a carbon atom exhibits four valence electrons in such an electronic configuration that two of them are in the 2s state and the other two are in the energetically higher-lying 2p states as indicated by Figure 2.1a. Since these valence orbitals are energetically close to each other, bond hybridization can easily occur in order to minimize carbon bond energies. An sp^2 hybridization takes place in aromatic compounds with hexagonal carbon systems as schematically shown in Figure 2.1b. Three valence electrons occupy the sp^2 orbitals taking an angle of 120° to each other and lying in-plane. The remaining fourth valence electron of the carbon atom occupies the p_z orbital which is orthogonal to the plane of the sp^2 hybrid orbital. Consequently, the carbon atoms are covalently linked in hexagonal rings by the exchange of sp^2 hybrid electrons leading to strong and highly localized σ bonds, while the electrons in the p_z state only overlap with the other p_z orbital and form additional conjugated π-bonds. Due to their low binding energy, the π-electrons are delocalized within the hexagonal carbon system and form the extended π-electron system which is responsible for the intramolecular electrical conductivity. The hexagonal carbon system is illustrated in Figure 2.1c. The superposition of the p_z orbitals results in the splitting of p_z states into binding π-states and anti-binding π*-states. The highest occupied π-state of a molecule is denoted as highest occupied molecular orbital (HOMO) and the lowest π*-state is specified as the lowest unoccupied molecular orbital (LUMO).

While these considerations apply for single isolated organic molecules, the situation changes by condensation to aggregated solid-state phase. Thereby, one has to distinguish between

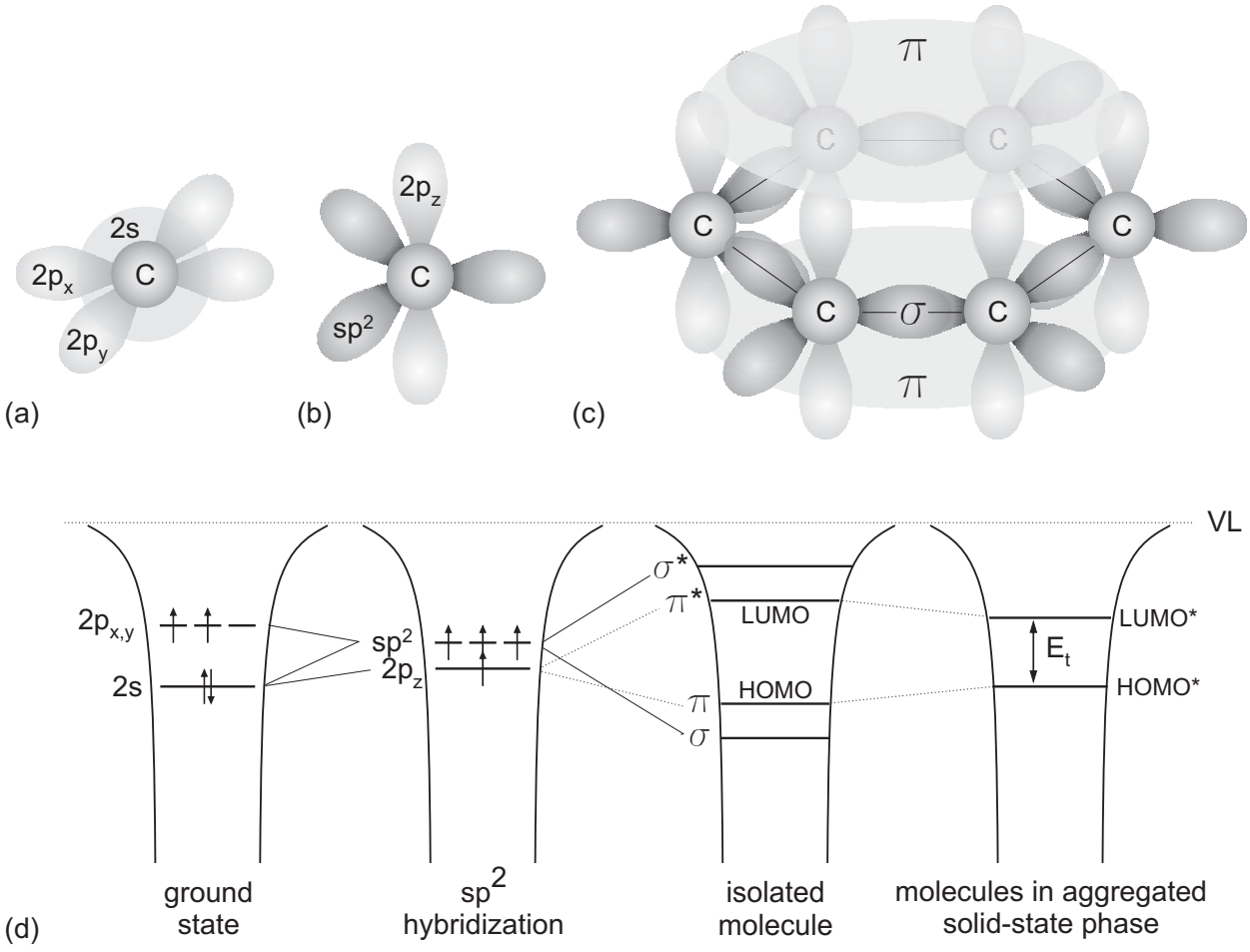

Figure 2.1: Schematic orbital model of (a) an unhybridized carbon atom, (b) a carbon atom hybridized into the sp^2 configuration, (c) a hexagonal carbon system. (d) Schematic electronic structures of the corresponding orbital models.

small low molecular weight molecules which can be thermally evaporated and long-chain polymers usually deposited by spin coating or ink-jet printing techniques. The main focus of this work is the examination of small molecules, though most of the basic principles also apply for polymers. Due to their closed shell, the organic molecules are only weakly bound to each other by van-der-Waals forces. As a consequence, interactions between π-electrons of neighboring molecules are rather low due to the small overlap of their electronic wave functions. Accordingly, the intermolecular electrical conductivity is low and directly associated with a physical transfer of charge carriers from one molecule to the next, leading to ionization effects and resulting in a strong electronic polarization of the neighboring molecules. Depending on the time scale regarding the lifetime of the excited molecule,

intramolecular and lattice relaxation add on, leading to geometrical reorganization of directly neighboring and further surrounding molecules in respect to the ionized one. All these effects have an influence on the potential energy of the charge carriers. The electronic polarization, thereby, amounts to 1-1.5 eV, contributing by far the most to the shift of HOMO and LUMO levels towards and against the vacuum level (VL, E_{vac}), respectively [21]. Therefore charge carrier transport can be described in terms of polaron transport on HOMO* and LUMO* with a transport gap E_t which is smaller than the energetic gap between HOMO and LUMO of an isolated molecule. Still, according to the common use in literature, theses transport levels will be denoted as HOMO and LUMO levels, since no further reference to organic molecules in the gas phase will be done in the following. Figure 2.1d summarizes the derivation of the transport levels discussed in this section.

2.2 Organic Semiconductors

In the following, the fundamental properties of semiconduction and light emission of organic materials will be explained, including the discription of the charge transport, charge injection, and formation of excitons and the characterization of the energetics at their interfaces. Additionally, the method of electrochemical doping of organic semiconductors will be presented.

2.2.1 Charge Transport

As seen in the former section the charge carriers are strongly localized on single organic molecules due to only weak van-der-Waals forces and a small overlap of the electronic wave functions between the molecular orbitals. Accordingly, their transport levels are narrowed to some 10 meV unlike inorganic semiconductors in which their crystalline structure leads to delocalized charge carriers and energetically broadened conduction and valence bands. The charge carrier transport in organic materials is regarded as a sequence of reduction and oxidation processes between adjacent molecules and can be described by the hopping model [22] which is illustrated in Figure 2.2. The redox process is associated with the formation of cations and anions accompanied by strong polarization and lattice relaxation effects. However, local disorder in amorphous organic materials induces energetic disorder due to a variation of polarization intensities within the bulk material. This effect leads to energetically broadened transport states which are usually modeled as Gaussian distributions [22]. The tail states of the HOMO and LUMO levels are considered to extend into the band gap of the semiconductor and influence the charge carrier mobilities. Charge carriers

occupying these trapping sites exhibit a lower hopping probability to overcome the potential barrier to the adjacent molecule. Corresponding to the energetic height of the potential barrier, they need an activation energy ΔW which may be provided by the thermal energy kT. The dependence of the mobility on the temperature T and activation energy is given by

$$\mu(T, \Delta W) = \mu_0 \exp\left(-\frac{\Delta W}{kT}\right). \tag{2.1}$$

The hopping of charge carriers between adjacent transport sites occurs randomly and without a preferential direction for charge transfer unless an external electric field F is applied. According to the Frenkel effect the presence of a strong electric field causes the effective depth of a trap to be reduced in one preferential direction [23], which is also illustrated in Figure 2.2. Thus, the charge carrier mobility is field-dependent and has been found to obey

$$\mu(E) = \mu_0 \exp\left(\frac{\beta\sqrt{F}}{kT}\right), \tag{2.2}$$

with β as the field activation coefficient.

For the description of the general current density versus voltage characteristics *(I-V)* within

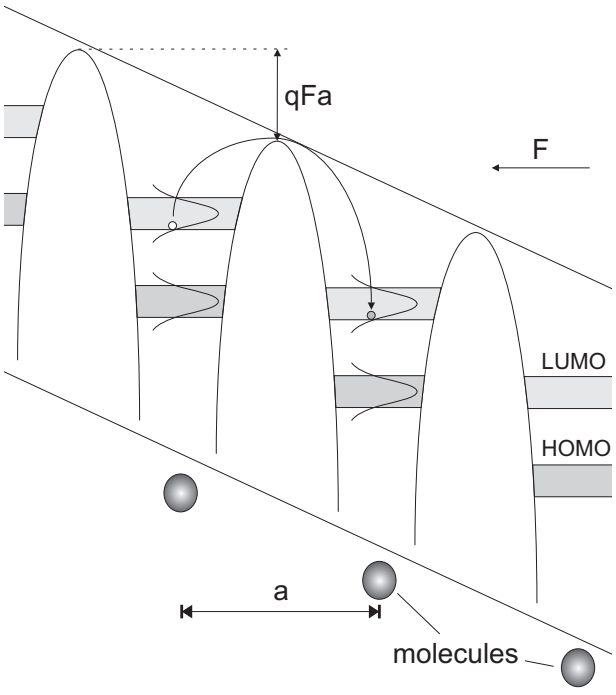

Figure 2.2: Schematic showing thermally activated hopping transport of an electron between Gaussian distributed states of adjacent molecules (with a distance a) assisted by the application of an electric field F.

unipolar organic devices, three different regions have to be distinguished, depending on the intensity of the external field and the intrinsic properties of the organic semiconductor in respect to the trap state distribution. At low electric fields the intrinsic charge carrier density dominates compared to the small amount of injected charge carriers. In this case, an Ohmic conduction takes place, which can be expressed by

$$J = q\mu n_0 \frac{V}{d}, \tag{2.3}$$

where q is the elementary charge, n_0 the intrinsic charge carrier density, V the applied voltage and d the layer thickness. Note that the applied voltage is reduced by the built-in voltage V_{bi} within real devices which arises from the use of electrodes with different work functions. Here, it is assumed that V_{bi} is negligible due to the use of contacts with the same work function. Since organic semiconductors usually exhibit a wide band gap in the range of 2-3 eV, the thermally generated and therefore intrinsic charge density is usually negligible. Thus, at an already low transition voltage V_Ω the injected charge carrier density prevails irrespective of injection limitations due to the contact which would only shift the whole current density characteristics to higher voltages. In this regime, the current flow increases rapidly since the quasi-Fermi level moves upwards and indicates the filling of the deep-lying trap states. A higher hopping probability is the result which, together with a higher charge carrier density, leads to the superlinear increase of the current with higher voltages as expressed by the power-law $J \propto V^{m+1}$. The parameter m contains information about the energetic trap distribution and is inversely proportional to the operating temperature [24].

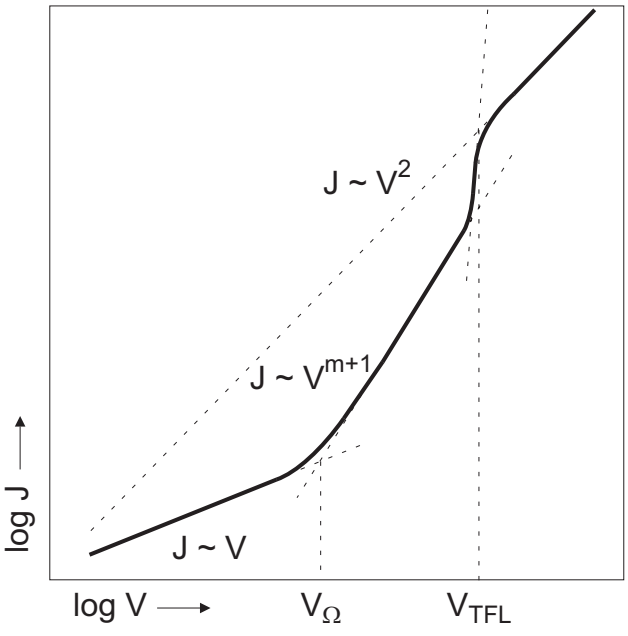

Figure 2.3: Schematic plot of current density versus voltage characteristics exhibiting the Ohmic, trap charge limited and space charge limited region for a single carrier transport.

Therefore, this part of the current versus voltage characteristics is denoted as trap charge limited region, ending at the transition voltage V_{TFL} where all traps are filled (trap filled limit, TFL). Since the charge mobility of organic materials is low and usually on the order of 10^{-3} - 10^{-7} cm^2/Vs, the injected charge carriers can not drift away sufficiently fast from the injecting contact and form a space charge region screening the electric field at the contact. Accordingly, a space charge limited current (SCLC) appears at high voltages according to the Mott-Gurney law

$$J = \frac{9}{8}\epsilon_0\epsilon_r\mu\frac{V^2}{d^3}, \tag{2.4}$$

assuming ideal contacts, no further trap limitation and neglecting any contributions of diffusion current by solving the Poisson-equation. The parameters ϵ_0 and ϵ_r denote the dielectric constant and the permittivity of the organic semiconductor, respectively. Figure 2.3 shows the typical characteristics of the current density versus voltage exhibiting the three different regions of current flow and indicating the transition voltages. These characteristics have been roughly demonstrated in several organic materials like Alq_3 (see Appendix for constitutional formula) [25]. However, special attention should be paid to the SCL current, since the quadratic field dependence of the current density is superimposed by the field dependence of the mobility as derived by the Frenkel effect. Accordingly, a more precise description of the SCLC is given by the modified Mott-Gurney law

$$J = \frac{9}{8}\epsilon_0\epsilon_r{\mu_0}^*\frac{V^2}{d^3}\exp\left(0.89\beta\sqrt{\frac{V}{d}}\right), \tag{2.5}$$

where ${\mu_0}^*$ denotes the zero-field mobility [23].

2.2.2 Energetics of Interfaces and Charge Injection

The process of charge injection from metallic electrodes into organic semiconductors plays an important role, if ideal contacts no longer exist, as assumed in the previous section for reasons of simplicity. The current density becomes injection-limited and depends on the potential barrier for charge carriers. According to the Schottky-Mott limit, the vacuum level of the organic semiconductor would align with that of the metal at the interface [26], leading to a simple calculation of the electron barrier $\phi_{B,e}$ and hole barrier $\phi_{B,h}$ given by

$$\phi_{B,e} = \phi_M - E_A, \;\; \phi_{B,h} = I_E - \phi_M, \tag{2.6}$$

where ϕ_M is the metal work function. The electron affinity E_A and ionization energy I_E represent the potential energies of the LUMO and HOMO levels of the organic semiconductor, respectively. However, deviations from the Schottky-Mott limit are often observed at the metal-organic interfaces, causing an interface dipole Δ which modifies the charge injection barriers, depending on its orientation and energetic magnitude. For instance, the reduction of the electron barrier by the dipole would concomitantly mean the increase of the hole barrier according to

$$\phi_{B,e} = \phi_M - E_A - \Delta, \;\; \phi_{B,h} = I_E - \phi_M + \Delta. \tag{2.7}$$

Several factors can lead to an interface dipole. The formation of novel chemical bonds or organometallic complexes at the interface is known as chemisorption [27]. The resulting direction of the dipole depends on the case of the specific chemical interaction at the interface [28]. The "pillow" or "cushion" effect describes the Coulomb repulsion between the electron density of the deposited molecule and the surface metal electrons, leading to a suppression of the tail of electron wave function into the vacuum. Accordingly, the push back of the electrons into the metal reduces its work function [29–31]. Similarly, the tailing of the metal electron wave function into the organic semiconductor induces a density of interface states in the organic semiconductor to which a charge neutrality level (E_{CNL}, CNL) is attributed [32, 33]. Only if the Fermi level of the metal E_F is above or below the E_{CNL}, a net charge transfer in the interface states occurs, causing again an interface dipole. Therefore, the electron injection barrier $\phi_{B,e}$ as an example is more generally given by

$$\phi_{B,e} = S(\phi_M - E_A) + (1 - S)E_{CNL}, \tag{2.8}$$

where S represents the slope parameter, depending on the density of interface states, the effective metal-semiconductor distance, and the permittivity of the semiconductor. The slope parameter ranges from $S = 0$, by which the injection barrier does not dependent on the metal work function, to $S = 1$ as the Schottky-Mott limit. Note, however, that even in the latter case a charge transfer at the interface occurs when the metal work function is smaller than EA or larger than IE. Finally, the orientation of the dipole moment of polar organic materials on the metal surface can lead to a large interface dipole [28, 31, 32]. Figure 2.4 schematically shows the electronic structure of a typical metal-semiconductor interface. Due to their closed shell only weak interactions between the molecules occur at organic-organic heterointerfaces, causing comparably small, up to negligible interface dipoles [33].

The height of the injection barrier ϕ_B at the metal-semiconductor interface and the magnitude of the applied electric field F determine the nature of charge injection. There are

mainly two injection mechanisms distinguished from each other. The thermionic injection based on the Richardson-Schottky (RS) relation is derived from the emission of electrons from a glowing cathode into the vacuum and is extended by the consideration of the image-force lowering of the energy barrier. Due to the attraction between the injected electron and the induced positive charge on the metal surface, the potential energy of the charge carrier is lowered, leading to a smaller effective energy barrier. Accordingly, the injection current is given by

$$J_{RS} = A^* T^2 \exp\left[-\frac{\phi_B - \sqrt{q^3 F/4\pi\epsilon_0\epsilon_r}}{kT}\right], \tag{2.9}$$

where A^* denotes the Richardson constant $A^* = 4\pi q m^* k^2/h^3$, m^* represents the effective mass of electrons, and k and h are the Boltzmann constant and the Planck constant, respectively [34]. The model of thermionic injection usually applies for small injection barriers and low electric fields and has to be further modified in the case of charge carrier diffusion back to the electrode due to low mobilities in the semiconductor.

In the case of higher injection barriers and comparably low temperatures, tunneling of charge carriers as a temperature-independent process is considered as the main injection mechanism which is described by the Fowler-Nordheim (FN) equation. Based on the assumption of a triangular injection barrier, the current injection is given by [34]

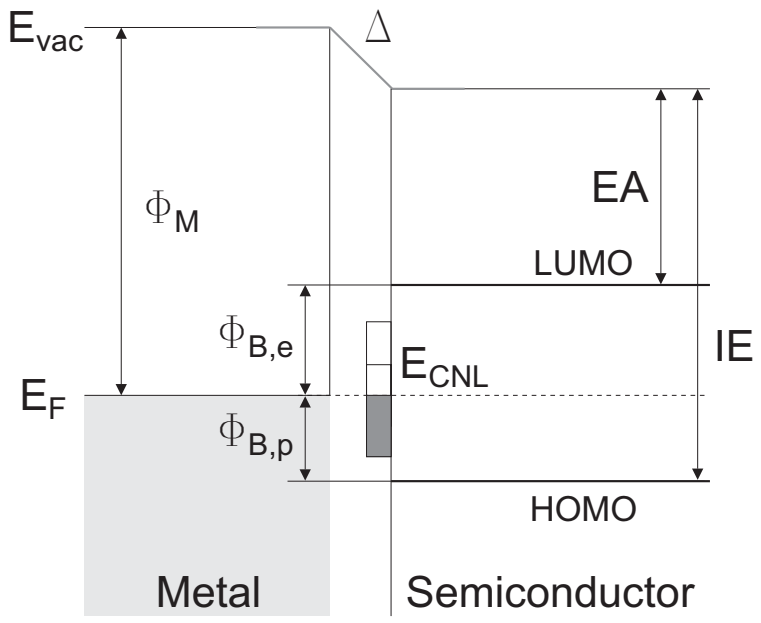

Figure 2.4: Schematic of the electronic structure of a typical metal-organic semiconductor interface [29].

$$J_{FN} = \frac{q^2 F^2}{8\pi h \phi_B} \exp\left[-\frac{8\pi\sqrt{2m^*}\phi_B^{3/2}}{3hqF}\right]. \tag{2.10}$$

It becomes clear that both RS-emission and FN-tunneling are derived from the world of inorganic semiconductors and only partially applies for organic semiconductors due to their energetically and locally disordered structure. Additional models, considering the injection into the Gaussian-distributed states and the hopping transport, are developed for a more precise description of the process at a microscopic level [35].

2.2.3 Doping Approach

The establishment of controllable doping of inorganic semiconductors led to the breakthrough of modern electronics. The doping mechanism is based on the insertion of dopant atoms considered as impurities into the semiconductor. They exhibit a differing number of valence electrons than the crystalline matrix. By partially substituting the crystal atoms, excessive electrons are generated in the case of negative doping (n-type) by donors. Excessive holes, corresponding to defect states of the periodic bonding structure, are induced by positive doping (p-type) with acceptors. Accordingly, a small binding energy refers to these charge carriers leading to comparably high free carrier densities already at room temperature. The field of organic electronic devices also benefited considerably from the discovery in 1977 that the conductivity of polyacetylene can be enhanced over many orders of magnitude by p-type doping [36]. This is all the more important for organic semiconductors due to their low charge carrier mobilities and densities. The doping-induced charge carrier densities cause higher conductivities and modify the electronic interfaces of electrodes. Accordingly, a space charge formation occurs due to the Fermi level alignment between the doped layer and electrode and is considered to enhance charge carrier injection via tunneling through the thin depletion layer [37, 38]. As will be demonstrated in the following sections, not only the charge carrier density but also the mobility increases upon doping, mainly provided by the Fermi level shift toward the transport level where higher concentrations of free states reside according to the Gaussian distribution of their density.

The principle of doping completely differs from that of inorganic semiconductors due to the lack of crystalline structures in organic materials. The insertion of dopants occurs interstitially into the amorphous layers rather than a substitution of host molecules. Referring to the p-type doping, an electron from the HOMO level of the host molecule is transferred to the LUMO level or conduction band of the organic or inorganic acceptor, respectively, leaving a hole in the organic semiconductor. This mechanism can be considered as redox

reaction and is therefore often denoted as electrochemical doping. Due to Coulomb attraction between the generated ions, charge transfer complexes are formed in the first step which may dissociate leading to a free hole, hopping through the bulk material. The effectiveness of the formation of charge transfer complexes depends on the energy level situation between host and acceptor and is supposed to be high for a HOMO level lying energetically above the electron transport level of the dopant in case of p-type doping [39].

Besides the electronic structure of the materials, technological aspects have to be taken into account. Depending on the nature of the organic host molecule and the deposition technique, various concepts for p-type doping were developed such as the exposure to oxidizing gases like iodine and bromine [40, 41] and the employment of Lewis acids like $FeCl_3$ [42, 43]. Due to the small dimensions of these molecules, they tend to diffuse within the doped layers leading to instabilities of organic devices [44]. Thus, aromatic molecules like DDQ, TCNQ and F_4-TCNQ were increasingly employed for p-type doping [45–47]. However, even the strong oxidizing acceptor molecule F_4-TCNQ has been demonstrated to diffuse at room temperature [38]. Additionally, its low glass-transition temperature along with its evaporation temperature around 90°C in-vacuo are detrimental for device preparation and operation [17, 48]. Therefore, transition metal oxides such as MoO_3 and WO_3 will be studied in this work as novel p-type dopants of organic semiconductors.

In the case of n-type doping via organic donors, the HOMO level of the dopant should be energetically above the LUMO level of the organic host material for efficient doping. Organometallic complexes such as $CoCp_2$ or $CoCp_2^*$ with an IE of 4 and 3.3 eV, respectively, as well as low work function reduced metal complexes like $[Ru(terpy)_2]^0$ have been employed for n-type doping [49–51]. However, only organic semiconductors with a comparably deep-lying LUMO level around 3 eV such as ZnPc and Pentacen could be successfully doped by these organic donors [50, 52]. On the other hand, the n-type doping of organic materials by alkali metals seems to be independent on the LUMO level due to their rather low work function. For instance, common organic electron transport layers such as Alq_3 or BPhen have been successfully n-type doped by Li, despite their low EA around 2-2.4 eV [49, 53, 54]. Accordingly, improved *I-V* characteristics along with higher conductivities and a Fermi level shift toward the electron transport level have been demonstrated upon n-type doping of ETLs [55, 56]. Thereby, the formation of charge transfer complexes has been suggested rather than a chemical reaction in terms of the modification of molecular configurations [53]. However, similar to most of the p-type dopants listed above, Li tends to strongly diffuse within organic layers leading to device degradation and lower lifetimes [56, 57].

The substitution of Li by Cs has been proposed and proven for n-type doping [58, 59]. Due to its atomic dimensions, Cs should have a lower diffusivity [60]. At the same time, it exhibits

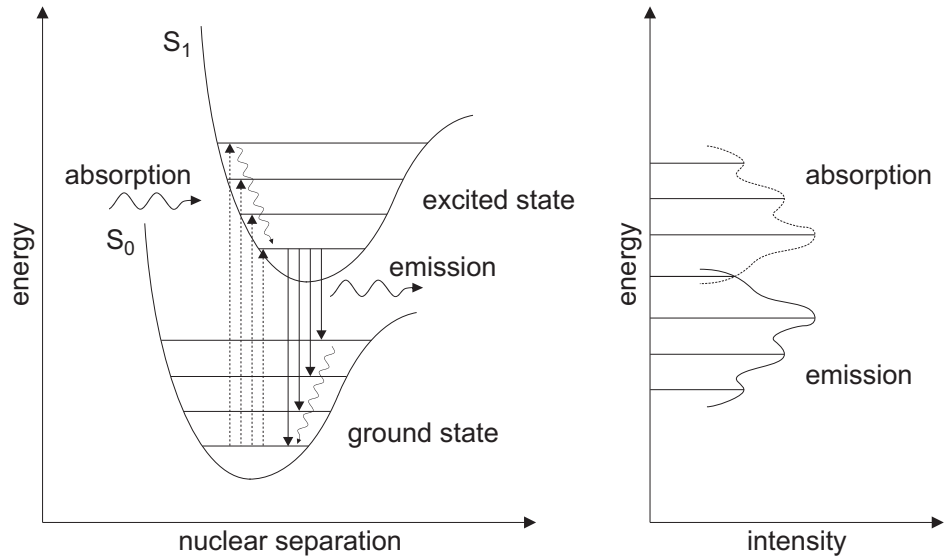

Figure 2.5: Franck-condon principle for a bi-nuclear molecule.

a higher reactivity than Li so that technological aspects have to be considered for stable deposition conditions like a very low background pressure in the UHV system. Therefore, a Cs salt, namely Cs_2CO_3 will be used in this work due to its chemical stability in air and comparable properties of n-type doping to alkali metals leading to high efficient p-i-n OLEDs [61, 62].

2.2.4 Formation and Transfer of Excitons

The absorption of light and the recombination of charge carriers on organic molecules lead to the formation of electrically neutral and bound electron-hole pairs. They are denoted as Frenkel excitons due to the low distance between the two complementary charges, both usually located on one molecule. Consequently, the large Coulomb attraction between these charges causes high exciton binding energies in the range of 0.4 to 1.4 eV [63], leading to an optical band gap which is usually smaller than the transport band gap of the organic semiconductors. In the ground state, the HOMO level of the organic molecule is filled with two electrons forming a singlet state according to the Pauli principle. After excitation and transition of an electron into the LUMO, the spins of the electrons no longer have to be paired. Therefore, triplet states with a total spin of 1 have to be distinguished from singlet states having a total spin of 0 due to the anti-parallel spin orientation. Particularly, charge carrier recombination initially leads to the formation of both singlet and triplet excitons.

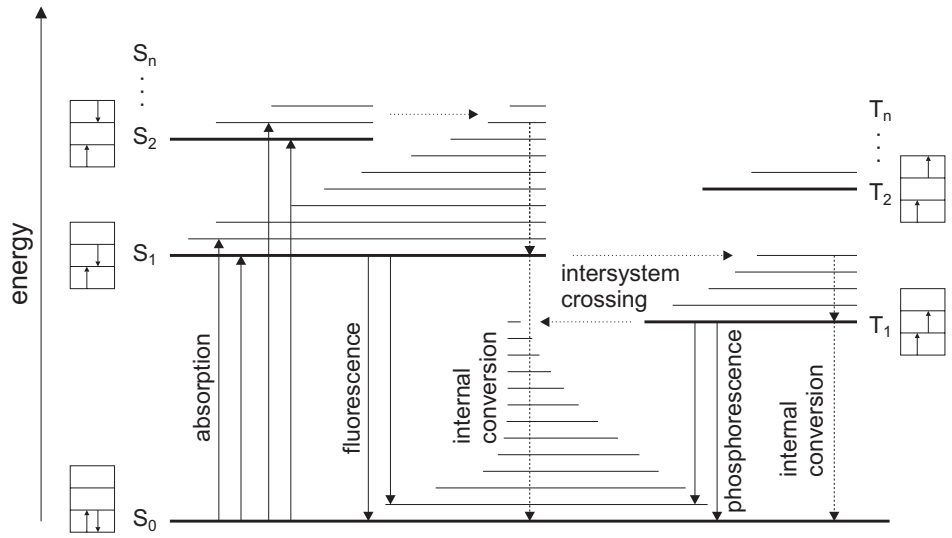

Figure 2.6: Jablonski diagram.

The singlet to triplet ratio yields 1 : 3 according to the spin multiplicity of the two states.

In contrast, the optical excitation from the ground state S_0 into an excited triplet state T is generally forbidden, due to the conservation of the total spin for electronic transitions. Figure 2.5 shows the situation for the ground and the excited singlet state S_1 after the absorption of a photon. The energy diagram indicates the potential energy of a bi-nuclear molecule depending on the nuclear separation and excitation state. Additionally, horizontal lines represent vibrational sublevels for each state, mainly induced by the σ-bonds between the atoms. Due to the reorganization of the molecular orbital and change in the bond lengths, the nuclear distance increases for higher excited states. Since the time for electronic transitions, however, is smaller by two orders of magnitude compared to the time period of nuclear motion, only vertical transitions are allowed between initial and final states having the same nuclear configuration, as stated by the Franck-Condon principle [64,65]. Additionally, it has to be considered that the transition between two states is preferred for a high overlap of the vibrational wave functions (not shown in Figure 2.5). After the absorption of a photon and transition into one sublevel of the excited state, the molecule relaxes to the vibrational ground level of S_1 via non-radiative intrastate transitions. An emission of a photon by the electronic transition back to the ground level S_0 then occurs by the same considerations in respect to the Franck-Condon principle. As a result, the emission spectrum is red-shifted to the absorption which is also known as Stokes shift.

Besides radiative transitions, non-radiative transitions and even an intersystem crossing between singlet and triplet states are possible under certain conditions. The latter is due to an

increasing spin-orbit coupling for electrons near elements with higher atomic numbers, which raises the probability of the spin-flip. This also allows for the radiative decay of the triplet state to the ground state, which is normally forbidden due to the condition of total spin conservation at electronic transitions. The Jablonski diagram, shown in Figure 2.6, summarizes most of these processes, including the transitions between vibrational sublevels. It demonstrates the possible transitions in one molecule and also describes the situation after electrical excitation by charge carrier recombination. The following processes are distinguished from each other:

Absorption means the optical excitation from the ground state S_0 to an energetically higher singlet state.

Internal conversion denotes the non-radiative decay caused by vibrational relaxation including intrastate and interstate transitions. In molecules with negligible spin-orbit coupling, this process prevails at the decay of triplet states to the ground state.

Fluorescence means the spin-conservative radiative decay of singlet states S_1 to the ground state S_0. Note that the optical excitation into higher singlet states S_n normally leads to a non-radiative decay to the S_1 level first.

Intersystem crossing comprises the non-radiative transfer from singlet to triplet states of the same energy and vice versa, implying a change in the total spin of the states.

Phosphorescence, as a another form of intersystem crossing, means the non-spin-conserving radiative decay of the triplet state T_1 to the ground state S_0. This process prevails in phosphorescent organic emitters based on heavy metal complexes due to the strong spin-orbit coupling, allowing for very high energy conversion efficiencies into light [3, 66].

These processes apply for the consideration of only one molecule and have to be extended by additional energy transfer mechanisms between an excited (*) donor molecule D and an acceptor molecule A. In the following, the two main energy transfer processes are briefly presented:

Förster Transfer

The Förster transfer is based on the dipole-dipole interaction between the excited donor and an acceptor molecule corresponding to coupled oscillators. The energy is transferred by an oscillating electric field of the donor molecule, inducing a resonant oscillation at the acceptor molecule. The transfer rate k_F mainly depends on the distance R_{DA} between the donor and acceptor molecules and is given by

$$k_F = \frac{1}{\tau_D}\left(\frac{R_0}{R_{DA}}\right)^6, \tag{2.11}$$

where τ_D denotes the intrinsic fluorescence lifetime of the donor and R_0 represents the Förster radius. R_0 comprises additional dependencies of the transfer rate based on the combination of the specific molecules, involved in the energy transfer process. Particularly, a high spectral overlap between the emission spectrum of the donor molecule and the absorption spectrum of the acceptor molecule permits an increased effectiveness of the Förster transfer. Due to the condition of individual spin-conversion for donor and acceptor molecule, the energy transfer only applies for singlet excitons as given by

$$\mathrm{D^{S*}} + \mathrm{A^S} \rightarrow \mathrm{D^S} + \mathrm{A^{S*}}. \tag{2.12}$$

The Förster transfer mechanism is also characterized by its comparably long range of influence which is usually between 4-10 nm.

Dexter Transfer

In contrast, the Dexter transfer is a short-range energy transfer mechanism due to the condition of orbital overlap between donor and acceptor molecule for an effective electron exchange. Since the tail of the electron wave function diminishes exponentially by extending into the vacuum, the transfer range is limited to only several Å, indicated by the small van-der-Waals radius L which is between 1 and 2 Å. Accordingly, the transfer rate k_D is given by

$$k_D \propto \xi \exp\left(-\frac{2R_{DA}}{L}\right), \tag{2.13}$$

where ξ represents the spectral overlap between donor and acceptor molecule. In the case of Dexter transfer, spin-conversion is only referred to the total system of donor and acceptor. Therefore, not only singlet but also triplet states can be transferred according to

$$\mathrm{D^{S*}} + \mathrm{A^S} \rightarrow \mathrm{D^S} + \mathrm{A^{S*}}, \tag{2.14}$$

$$\mathrm{D^{T*}} + \mathrm{A^S} \rightarrow \mathrm{D^S} + \mathrm{A^{T*}}. \tag{2.15}$$

Note that an energy transfer can also occur between two initially excited states, corresponding to $\mathrm{D^*}$ and $\mathrm{A^*}$. The result is a form of exciton quenching, since one of the two molecules becomes de-excited and the other reaches a higher excitation state. The most prominent exciton quenching mechanism is known as triplet-triplet annihilation, determining the efficiency loss of phosphorescent organic light emitting diodes at high exciton densities [67].

2.3 Functional Principle of Organic Light Emitting Diodes

In the following, the general functional principle of OLEDs will be explained in respect to the resulting internal and external quantum efficiency.

2.3.1 Internal Quantum Efficiency

OLEDs are usually based on multi-layer devices due to various internal processes, which have to be coordinated in order to achieve high internal quantum efficiency η_{int}. This is composed by the charge balancing factor γ, the fraction of potentially photon radiating excitons χ formed after charge recombination according to spin statistics, and the actual probability of the radiative decay of these excitons ϑ:

$$\eta_{int} = \gamma\chi\vartheta. \tag{2.16}$$

In order to explain the functional principle of OLEDs by concomitantly referring to the separate factors of η_{int}, Figure 2.7 schematically shows the energy diagram of a typical OLED structure in operation, comprising several functional layers. They are responsible for the efficient charge injection, transport, recombination, and the radiative decay of the excitons after their potential diffusion, which are explained in the following.

First, charge carriers have to be efficiently injected into the device. Holes are injected from the anode and electrons are injected from the cathode. In order to guarantee a high efficiency of charge injection, low potential barriers have to be realized at the electrodes by specific hole and electron injection layers (HIL and EIL). This can be achieved by doped organic semiconductors, forming small depletion layers at the electrodes which are easily tunneled by charge carriers, or other materials enabling an energy level alignment between their respective transport level and the work function of the electrode, taking the potential formation of interface dipoles into account.

Specific hole and electron transport layers (HTL and ETL) are then needed to remove the charge carriers from the electrodes and transfer them into the emission layer (EML). In order to confine the charge carriers within the EML, the HTL and ETL should additionally act as electron and hole blocking layer (EBL and HBL), respectively. This is usually given for hole transport layers with high-lying LUMO levels and electron transport layers with deep-lying HOMO levels. In this manner, the efficiency of injection and the transport of holes and electrons influences the charge balancing factor γ, describing the proportion of holes and electrons in the EML compared to the proportion of the charge carriers within the whole

device. It equals 1, if all holes and electrons are efficiently directed and confined into the EML. Leakage current through the device and the recombination of charge carriers outside the EML lower the factor.

After the transport to the EML, holes and electrons recombine and form excitons according to the usual spin statistics. The nature of the EML determines whether the triplet excitons contribute to the light emission or not, corresponding to the actual fraction of emissive excitons χ of 0.25 or 1. A fluorescent organic emitter converts only the singlet states into light. Therefore, phosphorescent dyes are increasingly used as dopant within the EML, leading to high internal quantum efficiencies. One decisive factor for the high efficiency is the exciton transfer rate from the host to the guest molecules. A pure electro-phosphorescence can be reached only when singlet and triplet excitons, initially formed at the host molecules, are completely transferred to the phosphorescent dye, and when the subsequent intersystem crossing process on the guest molecules converts all singlet states to triplet excitons prior to the radiative decay [3]. Therefore, the combination of host and guest molecules in the EML should always consider a high spectral overlap between the emission spectrum of the host and the absorption spectrum of the dye for high transfer rates. Note that a formation of excitons by direct charge carrier recombination on the dopant is also possible to some extent [68, 69].

On the other hand, the probability ϑ of the radiative decay of the excitons depends on the ratio of the light conversion rate to the rate of energy transfer to other competing non-radiative decay mechanisms such as exciton quenching or internal conversion processes by vibrational relaxation. Additionally, the internal quantum efficiency could be influenced by

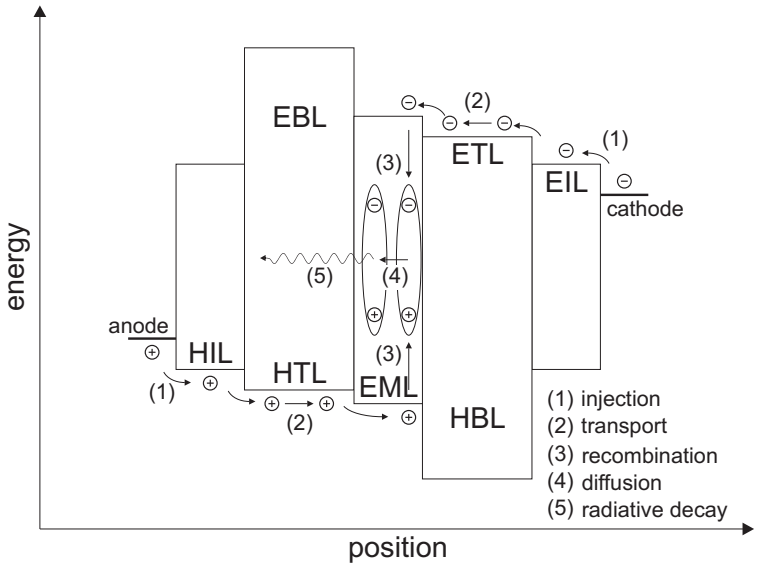

Figure 2.7: Schematic energy diagram of a multi-layer OLED and the internal processes assuming a charge carrier recombination at the EML/ETL interface.

the exciton diffusion to non-excited molecules. The exciton diffusion length depends on the lifetime of the singlet and triplet states usually lying in the order of ns, and from μs to ms, respectively [70]. Exciton diffusion can also lead to a local shift and a higher width of the emission zone against the region of charge carrier recombination within the EML. In order to at least avoid exciton diffusion out of the EML, the charge transport layers usually exhibit a large band gap and consequently, no spectral overlap with the emission spectrum of the emission layer, precluding a Förster and Dexter transfer on these layers. At the same time, they have to be sufficiently thick due to the long range of the Förster transfer.

Finally, the excitons undergo a radiative energy transfer, leading to the emission of light. Apart from a small energy loss by the light absorption in the device, particularly the outcoupling efficiency determines the overall performance of the OLED. This will be discussed in the following section.

2.3.2 External Quantum Efficiency

The external quantum efficiency η_{ext} is defined as the ratio of the number of photons outcoupled from the OLED to the number of injected electrons. It can be approximately determined with the help of the measurement of the optical power P_{opt}, of the operating current I, and of the maximum wavelength of emission λ_{max} according to

$$\eta_{ext} = \frac{P_{opt}}{hc}\frac{q}{I}\lambda_{max}, \tag{2.17}$$

where c is the velocity of light. At the same time, η_{ext} is given by the multiplication of the internal quantum efficiency η_{int} with the outcoupling efficiency η_c. Thereby, the light outcoupling plays a very important role in the OLED design due to the multi-layer stack of organic and inorganic materials having different refractive indices.

Referring to a conventional bottom-light emitting device capped by a metallic top contact, the structure comprises organic layers with a refractive index n_{org} of approximately 1.7 at the wavelengths of the visible light spectrum, a transparent bottom electrode like indium tin oxide (ITO) with $n_{ITO} \approx 1.9$, and a glass substrate with $n_{glass} \approx 1.5$. According to classical ray optics based on the light propagation by Snell's law and total reflection at angles higher than the critical angle Θ, based on the transition from high refractive to lower refractive layers, the outcoupling efficiency can be estimated by $\eta_c = 1/2n^2$ as often made for their inorganic counterparts [66]. Consequently, only a small fraction of 20 % of the internally generated light is extracted out of the device.

However, the thickness of the multi-layer stack of OLEDs is in the order of the emission wavelength, leading to interference effects which are not considered by the classical ray optics. Therefore, different models were developed to describe the behavior of the radiating molecules. They can be mainly divided into two groups, corresponding to the two different approaches of modeling the optical microcavity. One group is based on classical electrodynamics, in which the emission of a photon due to an electronic transition is assumed to be equivalent to the radiation of an electrical dipole antenna [71]. The model completely describes the radiation in the OLED microcavity and predicts the splitting of the internally generated light into different modes such as externally emitted, substrate waveguided and ITO/organic waveguided. Additionally, heat generation in electrodes and coupling into surface plasmons at the metal/organic interface particularly by transverse magnetic field polarization of the light is well predicted. The other group of models is based on a quantum mechanical approach, in which the electromagnetic field is represented by the sum of eigenmodes of the cavity and the transition probability into each mode is given by Fermi's golden rule [66]. Since it does not include the energy transfer to the electrode, a combined classical and quantum mechanical approach has been developed, allowing for the separate computation of the different modes [72], in which the light propagation in the glass substrate is still treated by ray optics, while the propagation in the OLED layers is described by wave optics.

With the help of these models, the dependence of the outcoupling efficiency and angular-dependent spectral emission characteristics on the dipole orientation, the polarization of the light and the distance of the emitter to the mirror(s) can be well described in bottom- and top-emitting structures, allowing for the appropriate optical design for efficient OLEDs. Thus, the knowledge about the shape and the positon of the actual emission zone after charge generation and exciton diffusion is of high importance. In contrast to the treatment by classical ray optics, outcoupling efficiencies of more than 50 % have been predicted by an appropriate choice of the layer thicknesses [73]. Additional concepts to improve the outcoupling efficiency by the conversion of the waveguide modes or even the decay channels to external emission were demonstrated e.g. by the introduction of periodic microstructures [74], scattering layers [75], capping layers [71], microlense arrays [76], and by the exploitation of microcavity effects via highly reflective mirrors [77].

3 Preparation and Characterization

In the following, the deposition technology used in this work and the preparation of the devices are presented. Subsequently, the main analytical methods for their characterization will be introduced.

3.1 Deposition Technology

3.1.1 Organic Molecular Beam Deposition

The preparation of organic thin films based on vaporable small molecules is conducted on an organic molecular beam deposition (OMBD) system which uses resistively heated effusion cells, allowing for the evaporation/ sublimation of organic and selective inorganic materials from thermally stable crucibles. In contrast to the deposition of inorganic semiconductors by molecular beam epitaxy (MBE), no considerations regarding epitaxial growth have to be made, due to the mostly amorphous structure of the organic layers. The system exhibits an ultra high vacuum (UHV) which is important in order to avoid chemical reactions with residual gases and particles in the coated substrates.

Figure 3.1 schematically shows the current system configuration of the OMBD-cluster tool, which was mainly used for the preparation of the organic thin films and organic devices in this study. Five OMBD chambers, one test vessel, a metallization chamber and a sputter tool are connected with each other via a UHV transfer system which is accessible from a load lock connected to a N_2-box or via a fast entry flange. Additionally, a Kelvin probe tool is integrated in the transfer system for the measurement of the surface potential in-vacuo. Separate chambers are used for p- and n-type doping to avoid cross-contamination. The OMBD system is evacuated by a combination of oil-free scroll pumps and turbomolecular pumps, leading to an average background pressure of 1 x 10^{-8} mbar in the OMBD chambers, 1 x 10^{-7} mbar in the sputter tool and in the transfer system including the Kelvin probe, and 1 x 10^{-6} mbar in the metallization chamber. The latter is equipped with three resistively heated molybdenum boats, allowing for the direct evaporation of metals, or in case of Al for the evaporation from an inserted ceramic crucible. The evaporation of the organic materials is provided by custom-built temperature-controlled effusion cells, whereas the evaporation

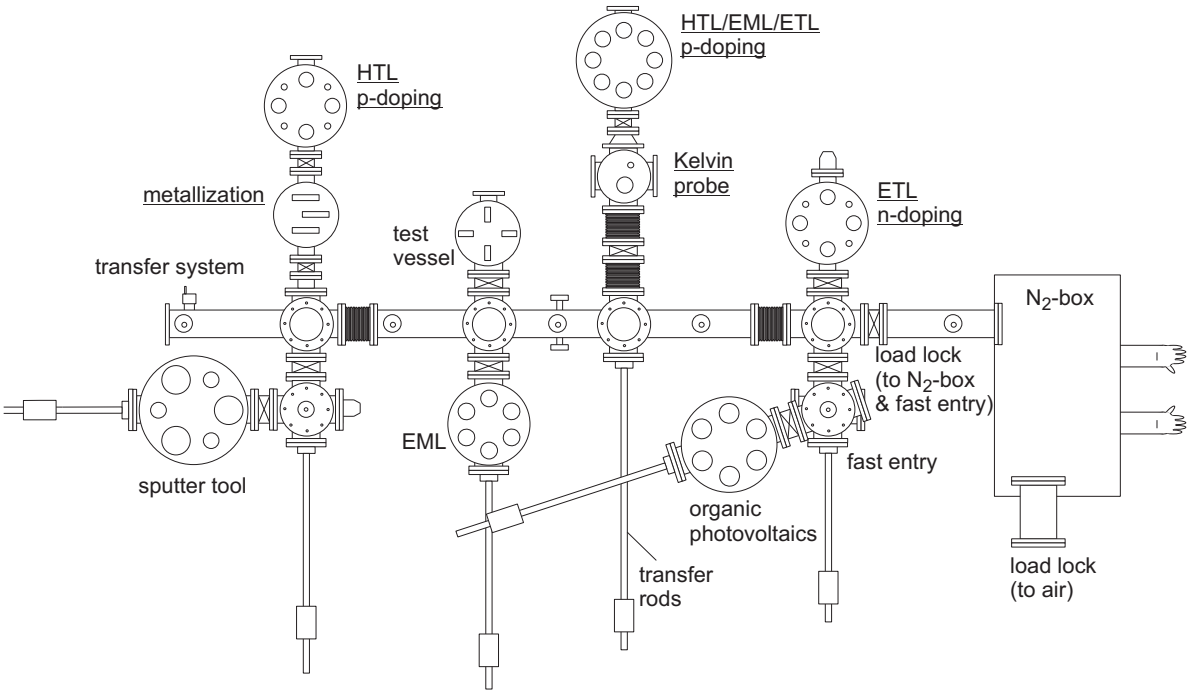

Figure 3.1: Schematic of the OMBD cluster tool. The chambers and tools mainly used in this work are indicated by their underlined label.

of the transition metal oxides and cesium carbonate is enabled by commercial MBE effusion cells, equipped with a water cooling shroud which allows high heating temperatures up to 1400°C. The evaporation rate of the materials is controlled by calibrated quartz crystal oscillator monitors. Each chamber is equipped with at least four effusion cells which exhibit a mechanical shutter, reducing the process time due to parallel heating and evaporation of materials. The distance between the effusion cells and the substrate is held sufficiently high, allowing for its homogenous coating. The possibility of rotating the substrate holder further assists the homogenous growth of the layers. The chambers and tools used in this work are highlighted in Figure 3.1. A more detailed description of the OMBD system is given in [78].

3.1.2 Atomic Layer Deposition

Atomic layer deposition (ALD) is a special form of the chemical vapor deposition process, in which the chemical reactants are alternately entrained by a chemical inert carrier gas and introduced into the reactor. The ALD is characterized by its self-limiting nature of the single process steps, allowing for the preparation of highly dense inorganic layers which can

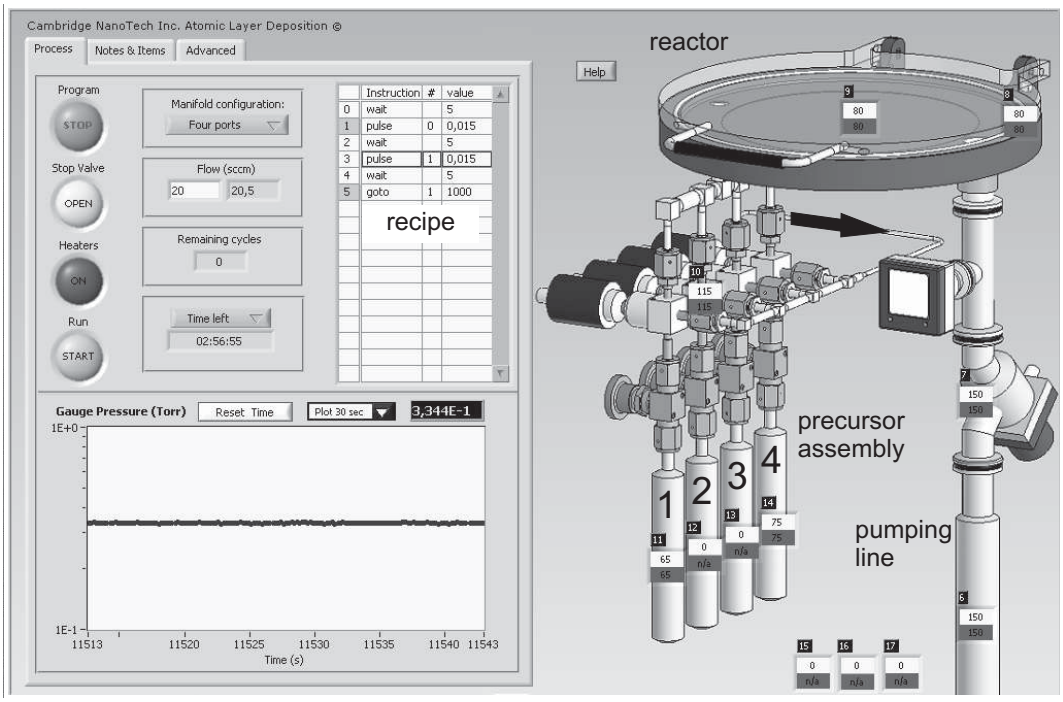

Figure 3.2: Screen shot of the graphic user interface of the ALD.

even be used for the encapsulation of OLEDs [79, 80]. The resulting conformal deposition permits the homogeneous coating of each substrate which enables the chemisorption of the first precursor on its surface.

In this work, the ALD was successfully used for the preparation of 120 nm thick Al_2O_3 layers on ITO coated glass. This oxide acts as an electrical insulator and is a well-behaved ALD system which can be created by a variety of precursors [81]. In the following, the ALD process is exemplified for the deposition of Al_2O_3 by using water (H_2O) and TMA ($Al(CH_3)_3$) as precursors, as also done in this work. After a short pulse of TMA molecules into the carrier gas leading to the reactor, chemisorption of the precursor occurs at the hydroxyl (OH) groups on the surface, leading to methane as a by-product. The constantly flowing inert carrier gas purges the reactor from the methane and the excessive TMA precursor molecules which have not found further free hydroxyl groups on the surface. In the next step, a short water pulse enriches the carrier gas and reaches the substrate. The water reacts with the remaining methyl groups of the TMA intermediate, again producing methane which is purged out together with excessive water. This reaction not only leads to the integration of oxygen between the Al atoms but also creates novel hydroxyl groups on the first monolayer. In this manner, the reaction cycle restarts with the first step of feeding TMA into the reactor.

Ideally, a stoichiometric Al_2O_3 film results in the end. The two alternating reactions can be summarized as follows [81]

$$Al{-}OH^* \ + \ Al(CH_3)_3 \ \rightarrow \ Al{-}O{-}Al(CH_3)_2^* \ + \ CH_4, \tag{3.1}$$

$$Al{-}CH_3^* \ + \ H_2O \ \rightarrow \ Al{-}OH^* \ + \ CH_4, \tag{3.2}$$

where the asterisks denote the surface species.

Figure 3.2 shows a screen shot of the graphic user interface of the ALD system "Savannah 200" from Cambridge NanoTech Inc., used in this work. The 8-inch reactor and all connections to it from the precursor assembly and the pumping line are schematically shown on the right side. The system comprises four stainless steel cylinders, containing the precursors including water. Molecular nitrogen (N_2) is used as carrier gas and is fed into the four cylinder heads through a mass flow controller, as indicated by the arrow in the schematic of the ALD setup. The gas flows into the reactor on one side and is pumped out of it on the other side through the pumping line. The vapor pressure, monitored on the pressure plot shown on the left side of Figure 3.2 at the bottom, usually ranges between 3 x 10^{-1} mbar and 5 x 10^0 mbar and is recorded by a vacuum gauge. The cylinder heads, the precursor containing cylinders, and the reactor are separately heated in order to enable a proper gas flow of the precursors without the formation of residuals in the separate parts of the system. Moreover, the temperature in the reactor influences the quality of the chemical reactions during the process. In this work, Al_2O_3 was deposited at a temperature of 120°C in the reactor, using the recipe shown on the left side of the graphic user interface. Accordingly, a first pulse of 15 ms, corresponding to the time period of opening the high-speed valve to the water-containing cylinder, leads to the enrichment of the carrier gas with water vapor, flowing into the reactor. After 5 seconds of purging, a second pulse of 15 ms follows, corresponding to the time of opening the valve to the TMA cylinder. After a further 5 seconds of purging, the deposition cycle restarts with the water pulse. One thousand cycles generated a 120 nm thick Al_2O_3 layer. The thickness was checked by profilometer measurements.

3.2 Device Preparation

In the following, the preparation of organic devices comprising doped layers is presented in the case of their deposition in the OMBD cluster tool, described in Section 3.1.1. Depending on the aimed characterization by specific electro-optical measurements, different substrates were used such as 1 mm thick borofloat glass, or 0.4 mm thick n^+-doped Si, or 0.7 mm thick

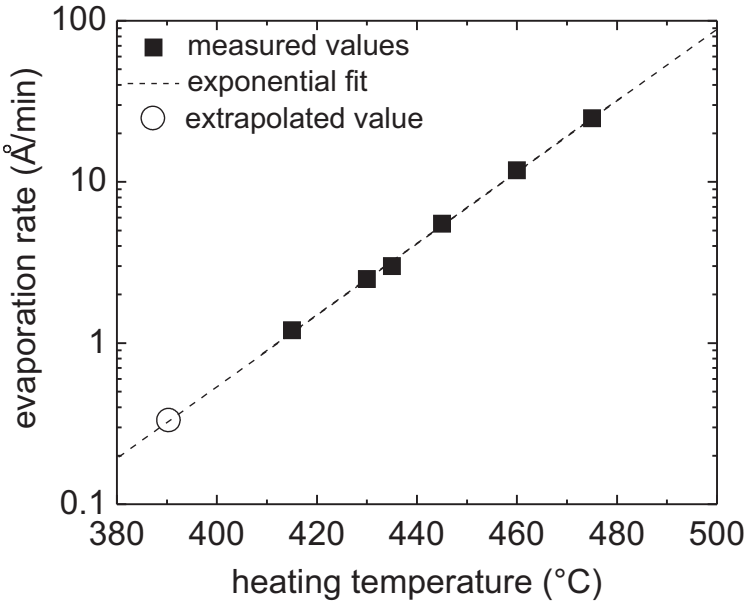

Figure 3.3: Evaporation rate versus heating temperature characteristics of the evaporation of MoO_3.

ITO coated glass which were cut into 17 x 17 mm^2 sample substrates after their preparation, respectively. Although the supplier of the ITO coated glass changed during this study from Merck to Optrex, its properties remained largely the same, exhibiting an ITO thickness around 130-140 nm, a sheet resistance of 13-14 Ω/sq and a work function between 4.5 and 4.9 eV. Furthermore, a thin SiO_2 film was placed between the ITO layer and the substrate as an additional diffusion barrier for the impurities of the glass. The substrates were ultrasonically cleaned sequentially with heated acetone and 2-propanol and dried with N_2. The preparation of the substrates and layers analyzed by photoelectron spectroscopy or capacitance-voltage measurements will be briefly outlined in the respective sections.

Focusing on the preparation of organic devices for electro-optical characterization, the ITO coated substrates were lithographically patterned using AZ 5214 photoresist, defining one ITO contact pad and three circular active layers on each substrate which were 2 mm in diameter. In this way, it was possible to subsequently deposit the organic layers and the metallic top contact without a vacuum break. For this purpose, the samples were mounted on a substrate holder, which can carry up to four substrates at the same time. They were kept in position by a metallic shadow mask which also defined the top contact pads after the completion of the device structure by metallization. The holder was transferred into the OMBD system either via the N_2-box or directly from air via the fast entry flange as shown in Figure 3.1. Since each chamber and its effusion cells exhibit a mechanical shutter, it was possible to lock in and out the substrate holder without loss of process time. A second shutter with a specific layout allowed the deposition of different layer thicknesses on the four substrates in a combinatorial way.

The heating of the custom-built effusion cells exhibiting a quartz glass crucible was carried out by a maximum ramp of 10°C/min, which was threefold higher for the MBE effusion cells, equipped by ceramic crucibles. The doped layers were prepared by co-evaporation and the evaporation rates were separately controlled by the quartz oscillator monitors. These were calibrated by profilometer measurements on test layers. Their parameters depend on the geometrical position of the quartz crystal to the molecular beam and the substrate holder. Typical deposition rates were 0.2-1 Å/s for the host material and 2-6 Å/s for the metallic top contact, whereas that of the dopant was tuned according to the targeted doping concentration. However, in the case of very low doping concentrations the quartz oscillation method failed to detect the evaporation rate. Therefore, higher evaporation rates of the dopant were first recorded prior to the preparation of the doped layer. Figure 3.3 shows the typical characteristics of the evaporation rate versus heating temperature for the deposition of MoO_3. The exponential fit of the measured values represents the typical vapor pressure curve observed for these dopants, which then allowed the extrapolation of the evaporation rates toward lower heating temperatures, where the quartz oscillation method failed.

3.3 Analytical Methods

3.3.1 Ultraviolet and Inverse Photoelectron Spectroscopy

The methods of ultraviolet and inverse photoelectron spectroscopy are used to characterize the electronic structure of materials at their surface by determining their filled and unoccupied density of states, respectively. In this work, these measurements were conducted on a three-chamber ultrahigh vacuum system from the group of Prof. Antoine Kahn at Princeton University.[1] Neat films and doped layers were evaporated in the preparation chamber, exhibiting a background pressure of $< 7 \times 10^{-9}$ mbar, and were transferred without vacuum break into the analysis chamber with a background pressure of $< 7 \times 10^{-10}$ mbar. The substrates used were Au coated n^+-doped Si wafers cleaned by sonication in acetone and methanol and ITO coated glass treated by oxygen-plasma for the removal of residual organic contaminants. The main properties of the photoelectron spectroscopy tools are briefly explained within the following description of their basics, while a detailed description of the whole three-chamber UHV system is given in [82].

[1] The measurements were mainly performed by Dr. Michael Kröger and Dr. Jens Meyer.

Ultraviolet Photoelectron Spectroscopy

The principle of (direct) photoelectron spectroscopy is based on the fundamental quantum hypothesis of Einstein. Electromagnetic radiation with a frequency ν impinging on a metal surface extracts electrons out of the material if the energy of each photon is higher than the lowest binding energy of the electrons. This mechanism is also known as photoelectric effect, in which the maximum kinetic energy of the photogenerated electrons $E_{kin}^{max}(metal)$ is given by

$$E_{kin}^{max}(metal) = h\nu - \phi_M, \tag{3.3}$$

where ϕ_M is the metal work function. Due to the process of photoemission, this method is also called photoemission spectroscopy instead of photoelectron spectroscopy. Figure 3.4a illustrates this situation for a reference metal. Depending on the energy of radiation $h\nu$, not only the electrons at the Fermi level but also energetically deeper-lying electrons are excited and extracted into the vacuum, leading to a characteristic intensity spectrum of the kinetic energy. For the investigation of valence levels, ultraviolet radiation in the range of $h\nu$ = 15-50 eV is used for ultraviolet photoelectron spectroscopy (UPS). In this work, a He plasma discharge lamp was employed, exhibiting two main photon lines He I and He II with an energy of 21.22 eV and 40.81 eV, respectively. The switch between both photon lines was achieved by varying the gas pressure [82]. Note that at the excitation of the He I line at a comparably high plasma pressure a small fraction of radiation also stems from the He Iα line with an energy of $h\nu$ = 23.09 eV, which should be considered for the interpretation of the resulting photoelectron spectra where necessary, since no monochromator was used for the light source.

The resulting photoelectron spectrum comprises the Fermi edge feature of the reference metal at the maximum kinetic energy, a sharp attenuation at the low kinetic energy side, and material-specific local maxima of intensity in between. The UPS spectrum approximately represents the electronic valence band structure of the respective material in respect to the binding energy-dependent density of filled states, referring to the measurement of free primary photogenerated electrons which are not inelastically scattered on the way to the detector [83]. However, the free mean path in the solid is low for the electrons with energies between 10-40 eV. General characteristics of their kinetic energy-dependent escape depth were deduced for different materials [83], showing that the value only amounts to approximately 5-15 Å for the energies employed in the UPS. Photoelectron spectroscopy is therefore known as a surface-sensitive method, representing the electronic structure of the materials at their surfaces. Accordingly, the UPS spectrum is increasingly superimposed to

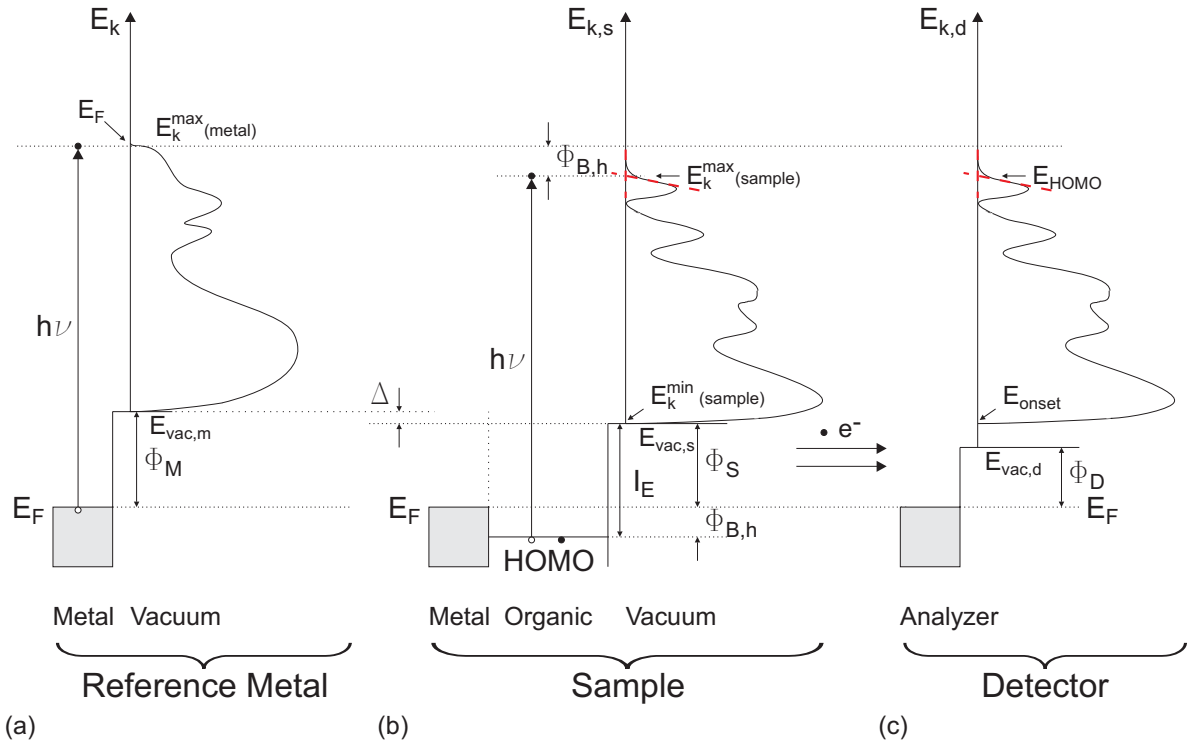

Figure 3.4: Principle of the UPS study of a metal/organic interface according to [28]. (a) Photoemission from the reference metal. (b) Photoemission from the organic layer deposited on the metal substrate and referenced to the detector system (c). The dashed lines indicate the determination of the HOMO (edge) level.

lower kinetic energies by secondary electrons resulting from inelastic electron-phonon and particularly electron-electron scattering of the primary electrons in the solid on the way to the surface [84]. The determination of the kinetic energy-dependent secondary electron spectrum is complex, but can be approximated to an exponential-like function for electron energies $E_{kin} < 100$ eV [82].

The sharp attenuation of the secondary electron spectrum at the low kinetic energy side of the UPS spectrum, also known as secondary electron cutoff and photoemission onset, clearly defines the vacuum level of the investigated metal $E_{vac,m}$. Referring to the primary electrons near this region, their kinetic energy tends to be zero due to their binding energies, precisely resembling the radiation energy which only suffices to extract them into the vacuum. Figure 3.4b schematically shows the relationship between the electronic structure and the UPS features of an organic semiconductor deposited on the metal. The possible formation of an interface dipole Δ between the metal and semiconductor does not influence the energetic

relations described in the following. The maximum kinetic energy of the photogenerated electrons E_{kin}^{max}*(sample)* is lower than that of the underlying metal, since the photoelectron emission starts for organic and inorganic semiconductors at the HOMO level or valence band egde [85]. Accordingly, the hole injection barrier $\phi_{B,h}$ is given by the energy difference of the maximum kinetic energies according to

$$\phi_{B,h} = E_{kin}^{max}(metal) - E_{kin}^{max}(sample). \tag{3.4}$$

This is only true for the situation of Fermi level alignment between the metal and the organic semiconductor. Although the sample system is earthed to avoid charge accumulation by positive charges left on the surface, this could be foiled in cases of very weakly conductive materials and very thick layers. The ionization energy I_E is obtained as

$$I_E = h\nu - (E_{kin}^{max}(sample) - E_{kin}^{min}(sample)), \tag{3.5}$$

where E_{kin}^{min}*(sample)* yields 0 eV and denotes the minimum kinetic energy of the electrons at the vacuum level of the sample $E_{vac,s}$. Since E_{kin}^{max}*(metal)* is associated with the Fermi level E_F of the system, the work function of the sample ϕ_S as the difference between I_E and $\phi_{B,h}$ is given by

$$\phi_S = I_E - \phi_{B,h} = h\nu - (E_F - E_{kin}^{min}(sample)), \tag{3.6}$$

as can be followed in Figure 3.4b.

In order to measure the kinetic energy of the photogenerated electrons, they are collected by a cylindrical mirror analyzer (CMA) consisting of a series of electron optics and an electron multiplier [82]. The main functional principle of the CMA is based on the application of a bias potential between an outer and an inner cylinder, permitting the transmission of only those electrons to the detector which have a corresponding kinetic energy [83]. Varying the bias potential, it is possible to analyze the whole kinetic energy spectrum. Since the detector is electrically connected with the sample, Fermi level alignment occurs between both parts of the system. Thus, the kinetic energy spectrum of the electrons referring to the vacuum level of the detector $E_{vac,d}$ is shifted compared to the spectrum referring to the vacuum level of the sample $E_{vac,s}$ due to the different work functions of detector (ϕ_D) and sample (ϕ_S) (Figure 3.4c). Moreover, the possible application of an additional negative bias qV on the sample ensures the measurement of a finite positive kinetic energy of the photoemission onset E_{onset} (secondary electron cutoff) given by

$$E_{onset} = \phi_S - \phi_D + qV. \tag{3.7}$$

In analogy to the equations 3.5 and 3.6, the IE and work function of the outermost layer on the sample are determined by the specific features of its UPS spectrum at the respective kinetic energies according to

$$I_E = h\nu - (E_{HOMO} - E_{onset}), \tag{3.8}$$

$$\phi_S = h\nu - (E_F - E_{onset}), \tag{3.9}$$

where E_{HOMO} denotes the energy at the HOMO level (Figure 3.4b).

Figure 3.5 focuses on the main parts of Figure 3.4, clarifying the measurement routine and the interpretation of the UPS spectra. First, the Fermi level E_F of the detector system has to be checked by the measurement of the Fermi edge characteristics of a reference metal. This was periodically done by a freshly evaporated Au substrate, made in the growth chamber of the UHV system. The width of the measured Fermi step also indicates the total resolution of the UPS system which was estimated to approximately 0.1 eV, or ± 0.05 eV [82]. Then, the organic semiconductor layer of interest is deposited on a substrate coated with a conductive layer. Compared with the UPS spectrum of this conductive layer as the actual reference of the measurement, the energetic value of a possible dipole or space charge region at the interface

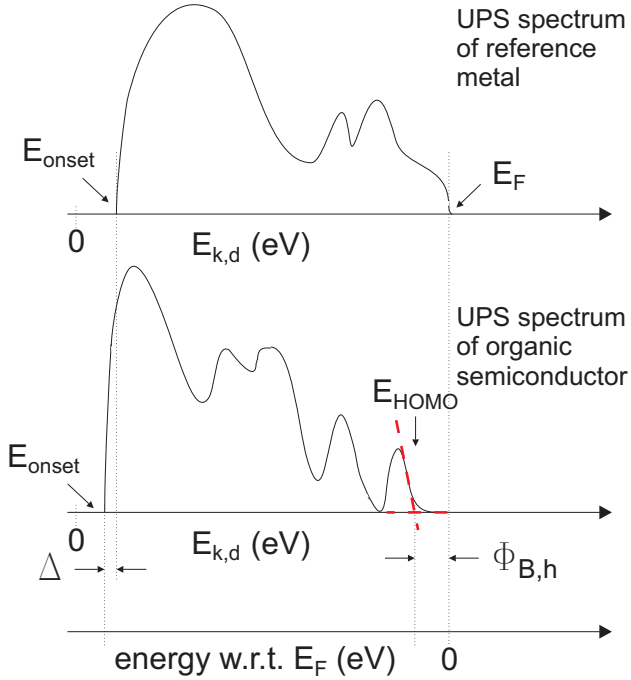

Figure 3.5: Presentation of the UPS spectra and their most important energy features of the reference metal and an organic layer deposited on it. The relationship between the energy scale $E_{k,d}$, referring to the kinetic energy in respect to the detector system, and the energy scale with respect to the Fermi level E_F is exemplarily shown at the bottom. The dashed lines indicate the determination of E_{HOMO}.

can simply be extracted out of the shift of the photoemission onset upon the deposition of the semiconductor. This is indicated by Figure 3.5 on the low kinetic energy scale of both UPS spectra. On the high kinetic energy side, the hole injection barrier between the metal and the semiconductor, or alternatively the position of the Fermi level to the hole transport level in a doped semiconductor is also easily found, particularly when the energy axis is scaled with respect to (w.r.t.) the Fermi level E_F.

The process of photoemission induces holes on the sample and generates electrons traveling through the solid into the vacuum. The time scale of the photoemission determines whether the electronic polarization and the molecular and lattice relaxation, as discussed in Section 2.1, are reflected in the photoelectron spectrum [29]. There is a broad consensus that the strong electronic polarization effects are included in the spectra due to their fast response to the photoionization (10^{-16} s) compared to the traveling time of the photogenerated electrons to the surface of the solid (10^{-15}-10^{-14} s) [29, 63, 82, 85]. Since the energy of the electronic polarization (1-1.5 eV) is one order of magnitude higher than that of the molecular relaxation and two orders of magnitude higher than that of the lattice relaxation, the latter processes would not further change the photoelectron spectrum significantly if they were in the time scale of photoemission. Thus, the UPS spectrum of the HOMO level is considered to represent the nearly fully relaxed hole transport level as the final state of the generated cation instead of the energy level of the neutral molecule system [29]. This underlines the high importance of the photoelectron spectroscopy for the examination of charge transport and charge injection phenomena.

On the other hand, it should be noted that the polarization energy in the bulk is higher than at the surface, where the ionized molecules are not completely surrounded by neutral molecules due to the proximity to the vacuum side. The difference between the binding energy of the transport level in the bulk and at the surface was estimated to 0.3 eV for anthracene [63]. In order to approximate the energy situation in the bulk, the HOMO level was determined at its high kinetic energy cutoff by extrapolating from a tangent to the steepest segment of the HOMO peak [82, 85]. The intersection between the tangent and the extrapolated background signal was then taken as the beginning of the Gaussian-distributed hole transport level, also denoted as the HOMO edge or valence band minimum for organic and inorganic semiconductors, respectively. The determination of the HOMO level is also indicated in Figure 3.4 and 3.5 by the dashed lines at the high kinetic energy side of the corresponding UPS spectra.

Inverse Photoelectron Spectroscopy

Inverse photoelectron spectroscopy (IPES) is the complementary technique to direct photoelectron spectroscopy like UPS. It probes the unoccupied density of states and is based

on the emission of photons due to the deceleration of electrons impinging onto the sample. The resulting electromagnetic radiation is also known as Bremsstrahlung. Depending on the energetic position and the density of the unoccupied states in the LUMO level or conduction band of the sample, different transition probabilities apply for the electrons with a specific kinetic energy decaying into these final states. Thus, the resulting photon spectrum represents the density of unoccupied states in a first order approximation. The electrons are provided by a low energy electron gun using thermionic emission from a low work function barium oxide coated tantalum filament [82]. The kinetic energy of the electrons can be controlled in the range of 5-25 eV in such a manner that a low energetic width of the respective electron flux is ensured. Note that IPES, like UPS, is also a surface-sensitive method due to the low free mean path of the electrons penetrating the solid and partially generating a "secondary" photon background [82].

Although it is possible to measure the entire photon spectrum with an UV monochromator, using a fixed incident electron energy source, the low quantum efficiency of the Bremsstrahlung in the ultraviolet regime of typically 10^{-8} photons per electron affords a very sensitive measurement setup and high electron intensities [86]. However, organic layers could be easily damaged by high electron currents. Therefore, the electron beam was defocused and the currents and data recording times were reduced [29]. Additionally, the data

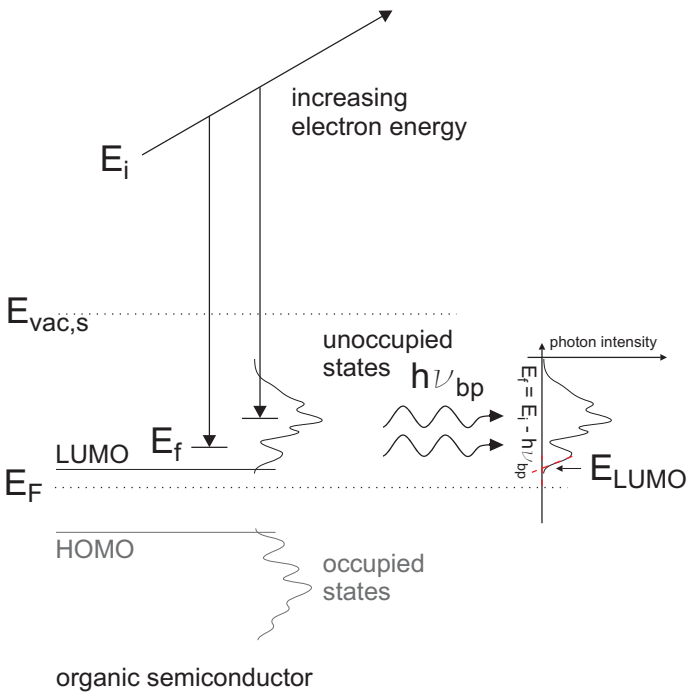

Figure 3.6: The principle of IPES in isochromat mode. Electrons with an energy E_i decay into various unoccupied states of the organic semiconductor. Only the transition into the final state with an energy E_f, leading to the emission of photons with an energy of $h\nu_{bp}$, is recorded by the detector. By increasing the electron energy, the entire distribution of the density of unoccupied states is determined. The "secondary" photon background has been neglected in this schematic. The dashed lines indicate the determination of E_{LUMO}.

were usually averaged from several spots on the sample surface. Furthermore, IPES was done in the isochromat mode, also known as Bremsstrahlung isochromate spectroscopy, using a fixed-energy photon detector based on a band-pass filter and varying the electron energy from 5 to 20 eV. The band-pass filter consists of a 1 mm thick SrF_2 window which is placed in front of an electron multiplier coated with an 80 nm thick layer of KCl [82]. Since SrF_2 acts as a low-pass filter for photon energies below its band gap of 9.7 eV and KCl generates electrons by photoexcitation with energies higher than its IE of 8.6 eV, the combination represents a band-pass filter around 9.1 eV with a resolution of 0.5 eV or ± 0.25 eV. Figure 3.6 demonstrates the principle of the IPES measurement in the isochromat mode for the analysis of an organic semiconductor. Only the photons with energy of $h\nu_{bp} = 9.1$ eV were detected. By increasing the electron energies during one measurement run, it is possible to map the distributed density of unoccupied states, represented by the kinetic energy-dependent photon intensities. Since the kinetic energy of the electrons only refers to the electron gun and not to the sample, it is important to determine the Fermi level E_F of the sample system by a metallic reference beforehand.

The same considerations, made for UPS regarding the determination of the HOMO level and the discussion about the time scales of photoemission and polarization in organic semiconductors, apply for IPES [29]. Accordingly, the nearly fully relaxed electron transport level as the final state of the generated anion is measured by IPES. The LUMO level E_{LUMO} is determined at its low kinetic energy cutoff by extrapolating from a tangent to the steepest segment of the LUMO peak, as indicated in Figure 3.6. Consequently, the electron affinity (EA) of the respective sample is determined from the difference between the work function derived from UPS and the energetic distance of the LUMO level to the Fermi level. Therefore, IPES and UPS spectra are usually plotted together in one energy diagram by aligning the Fermi levels of the separate energy scales.

3.3.2 Kelvin Probe Technique

The Kelvin probe is an analytical tool, allowing for the measurement of the contact potential difference between two electrodes. It is based on a vibrating parallel-plate capacitor setup, in which one plate is given by the Kelvin probe as reference electrode and the other plate is represented by the sample surface. The plates are held at a specific distance to each other during the measurement, so that this non-contact mode allows for a non-destructive analysis of the sample surface. The principle of measuring the contact potential difference is illustrated in Figure 3.7. The electrical connection of two electrode materials having different work functions leads to a Fermi level alignment and accordingly to a short current

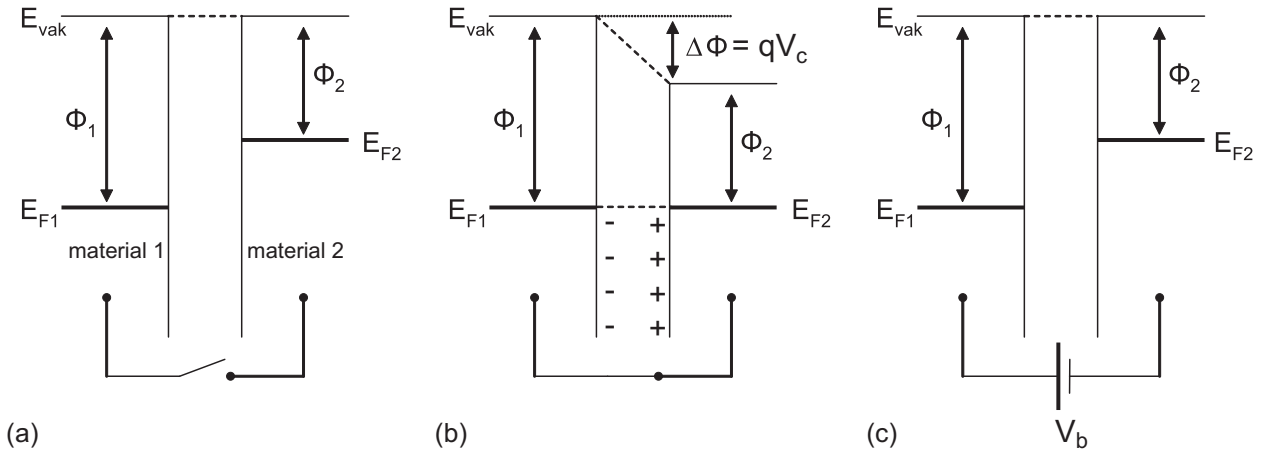

Figure 3.7: Principle of the contact potential difference arising between two materials with different work functions. (a) No contact between the two materials. (b) Electrical contact and Fermi level alignment, leading to contact potential difference V_c. (c) Application of an external voltage V_b equally to V_c.

flow causing a charge redistribution on the plates. The voltage arising between the two electrodes is denoted as the contact potential difference V_c, which is directly associated with the work function difference $\Delta\Phi$ according to $qV_c = \Delta\Phi$. The application of an external voltage equal to the contact potential difference reduces the electric field to zero. In order to detect this situation, the reference electrode is oscillated, leading to a periodic change of the parallel-plate capacitance value with a varying distance d and accordingly to a periodic current flow. Assuming a sinusoidal variation of the distance at a frequency ω and an arbitrary phase θ the current I_{KP} is given by

$$I_{KP} = -\epsilon_0 \epsilon_r A_{KP} \Delta V \frac{d_1 \cos(\omega t + \theta)}{[d_0 + d_1 \sin(\omega t + \theta)]^2}, \tag{3.10}$$

where A_{KP} is the area of the Kelvin probe, d_0 and d_1 are the initial parallel-plate distance and the amplitude of vibration, respectively, and ΔV is the sum of the contact potential difference and the applied voltage V_b. The current diminishes in the case where V_b = -V_c, indicating the work function difference between the sample surface and the reference electrode.

In this work, a KP6500 Digital Kelvin Probe from McAllister Technical Services was placed into the transfer system of the OMBD as shown in Figure 3.1. Figure 3.8 schematically illustrates the setup. The Kelvin probe head, 4 mm in diameter, was eccentrically inserted

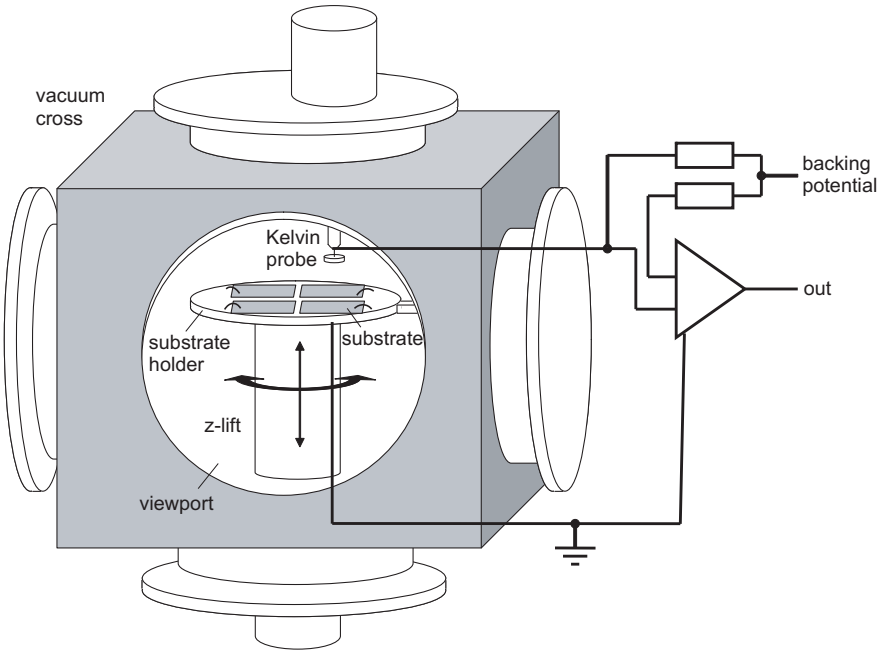

Figure 3.8: Kelvin probe setup in the OMBD system and schematic circuit diagram.

into the vacuum cross, allowing for the sequential measurement of four substrates on a holder which could be manually rotated on the z-lift. The samples have to be initially coated with a conductive layer, for which reason ITO coated glass substrates were used. Moreover, they were electrically grounded by a connection to the metallic substrate holder. The measurement was conducted in a short distance between the Kelvin Probe and the respective sample surface, which was indicated by the software. A frequency of 180.2 Hz and an amplitude of 80 (a.u.) were used. The external backing potential V_b was varied from -1 to +1 V. This sufficed to measure any work function difference, since the Kelvin probe takes advantage of the linear relationship between the current and the applied voltage, as demonstrated in equation 3.10. This allows for the interpolation or extrapolation of the current versus voltage characteristics to the null point, indicating the case of zero field. Accordingly, the contact potential difference can be measured with high accuracy unlike lock-in techniques that measure the null point directly, where the signal-to-noise ratio is far inferior to the other points [87]. The work function of the stainless-steel Kelvin probe head was determined prior to this study in another work, allowing for the calculation of the respective work function of the sample surface.

3.3.3 Electro-Optical Characterization

Considering the applications of OLEDs in displays and general lighting, it is important to characterize their properties in respect to the optical impression on the human eye. Ac-

Table 3.1: Photometric quantities for the OLED characterization.

quantity	symbol	specification	unit
luminous flux	Φ_v		lm
luminous intensity	I_v	luminous flux/ solid angle	cd (lm/sr)
luminance	L	luminous intensity/ luminous area	cd/m^2
current efficiency	η_{phot}	luminance/ current density	cd/A
power efficiency	η_{lum}	luminous flux/ electrical power	lm/W

cordingly, the radiometric quantities measured by photodiodes and spectrometers have to be weighted by the luminosity function and color matching functions that model human brightness sensitivity and color sensitivity, respectively. The spectral luminosity function at light conditions (photopic) *V(λ)* was empirically investigated and defined by the International Commission on Illumination (CIE, Commission internationale de l'éclairage) and implies that only the electromagnetic radiation from 380 to 780 nm is visible for the human eye. It allows for the conversion of the radiant flux Φ_r into the luminous flux Φ_v according to

$$\Phi_v = K_{ph} \int_{380\ nm}^{780\ nm} \Phi_{rs}(\lambda) V(\lambda) d\lambda, \tag{3.11}$$

where Φ_{rs} is the spectral power distribution and $K_{ph} = 683$ lm/W is a constant resulting from the normalization of the luminosity function at its maximum ($\lambda = 555$ nm). Assuming Lambertian emission from the OLED devices, their current efficiency η_{phot} and power efficiency η_{lum} are defined as follows:

$$\eta_{phot} = \frac{L}{J} \quad \text{and} \quad \eta_{lum} = \frac{\pi L}{VJ}, \tag{3.12}$$

where L denotes the luminance, J the current density, and V the applied voltage. Accordingly, the power efficiency denotes the ratio of total light output to the total electrical input power and is a measure for the performance of OLEDs compared to other light sources. Table 3.1 summarizes the most important photometric quantities for the characterization of OLEDs.

Three color matching functions, $\bar{x}(\lambda)$, $\bar{y}(\lambda)$, and $\bar{z}(\lambda)$ exist for the complete description of the color perception of the human eye which is based on three types of different photoreceptors,

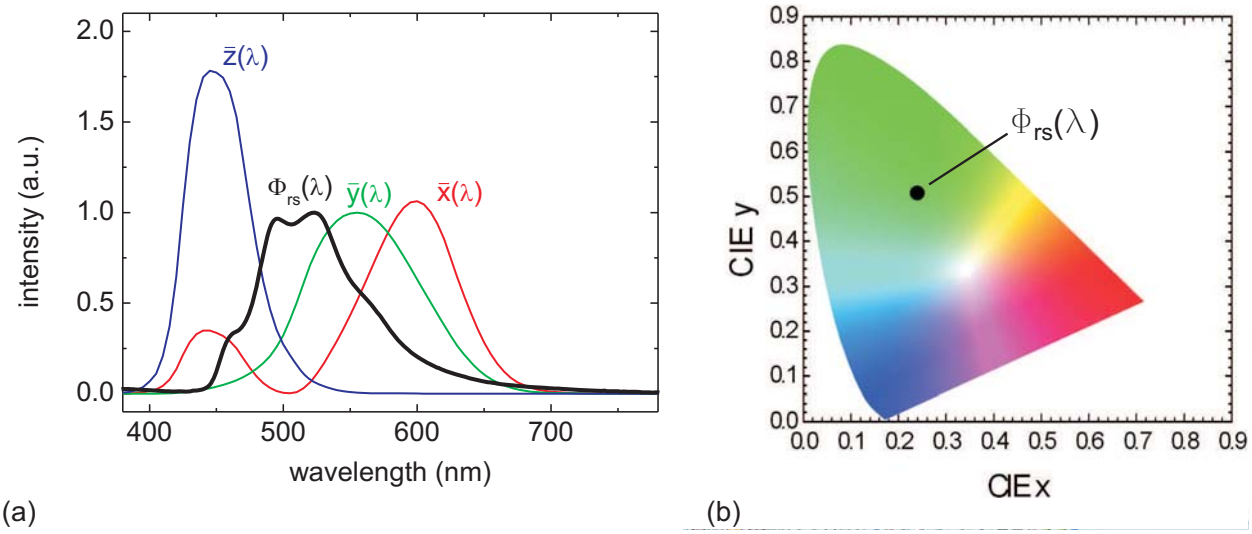

Figure 3.9: (a) Spectral color matching functions and an exemplary emission spectrum with a spectral power distribution $\Phi_{rs}(\lambda)$. (b) CIE color space diagram including the plotted CIE coordinates of the exemplary emission spectrum.

responding to different ranges of wavelengths. The functions were empirically investigated and defined by CIE in 1931 as the chromatic response of the average human eye viewing through a 2° angle [88]. The integration of the spectral power distribution weighted by the respective color matching function in the visible spectrum according to

$$X = \int_{380\ nm}^{780\ nm} \Phi_{rs}(\lambda)\bar{x}(\lambda)d\lambda, \quad Y = \int_{380\ nm}^{780\ nm} \Phi_{rs}(\lambda)\bar{y}(\lambda)d\lambda, \quad Z = \int_{380\ nm}^{780\ nm} \Phi_{rs}(\lambda)\bar{z}(\lambda)d\lambda, \tag{3.13}$$

leads to three values X, Y, and Z, describing the degree of response by the different photoreceptors. Their normalization according to

$$x = \frac{X}{X+Y+Z}, \quad y = \frac{Y}{X+Y+Z}, \quad z = \frac{Z}{X+Y+Z}, \tag{3.14}$$

allows for the two-dimensional illustration of the color perception by the CIE color space diagram. Figure 3.9a shows the spectral color matching functions along with an exemplary emission spectrum, which is converted into the two CIE coordinates x and y and plotted into the CIE diagram depicted in Figure 3.9b.

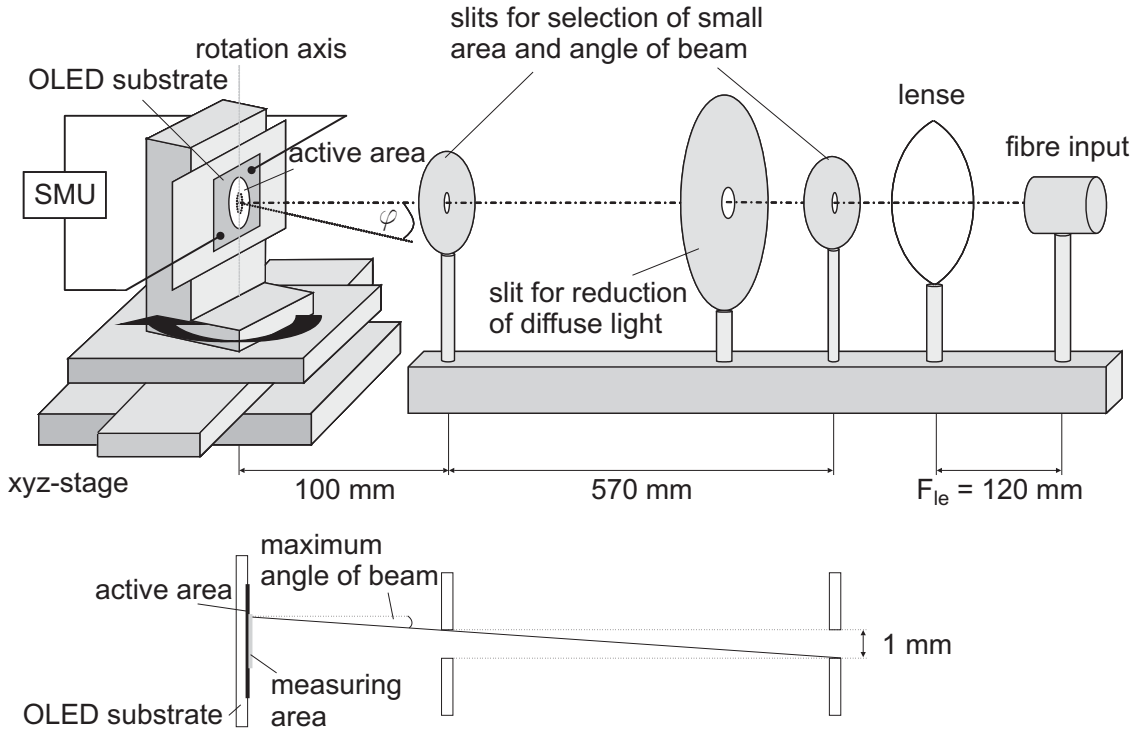

Figure 3.10: Schematic of the measurement setup for the analysis of the angular-resolved electroluminescence spectra of OLEDs. At the bottom: schematic top view on the essential slits and the OLED substrate for the illustration of the maximum angle of beam and the measuring area on the OLED.

L-I-V measuring station

The luminance-current density-voltage *(L-I-V)* measurements were conducted under ambient conditions using a Keithley 2400 source measure unit and a large-area Si-photodiode (Advantest TQ 82214) connected to an optical power meter (Advantest TQ 8221). The conversion to photometric quantities was based on a calibration with a luminance meter (Minolta LS-110), implying the consideration of the spectral properties of light emission and the geometrical properties of the measurement setup in respect to the areas of emission and detection and their distance to each other. The voltage-dependent electroluminescence spectra were obtained by a fibre-coupled spectrometer (TecFive MMS UV-VIS II).

Angular-resolved electroluminescence spectra

The measurement of the angular-resolved electroluminescence spectra is useful for the complete characterization of OLEDs, since weak microcavity effects are known to influence their angular-dependent spectral characteristics depending on the position of the emission zone

in relation to the reflective electrodes [72]. Thus, the knowledge about the devolution of the spectra with higher angles of view φ allows, in combination with optical device simulation, for the reliable determination of the emission zone within single or stacked OLEDs. Figure 3.10 schematically shows the realized measurement setup. OLED substrates were mounted on a xyz-stage, which is able to rotate the device by 360° around its center axis. They were electrically driven by a Keithley 2400 source measure unit (SMU). Two slits with an aperture of 1 mm in diameter were placed in a row with a distance of 570 mm to each other, in order to permit the measuring of only a small maximum angle of beam of 0.1°. This can be easily comprehended by the drawing at the bottom of Figure 3.10, showing the top view on the OLED substrate and the two essential slits. Additionally, they define a small circular measuring area of only 1.4 mm^2 on the respective light emitting (active) area of the OLED substrates, since the first slit was placed only 100 mm behind the rotation axis of the xyz-stage. An additional slit with an aperture smaller than 5 mm was placed between the two others to reduce diffuse light coming from reflections or other small light sources in the laboratory. Behind the three slits, a bi-convex lens (BK7, focal length F_{le} = 120 mm) was positioned, collecting the light and guiding it into the fibre input of the imaging monochromator system (Triax320, CCD4000, Jobin Yvon; grating of 150 lines/mm).

Optical device simulation

The optical device simulation was performed by the commercial software "ETFOS v. 1.4" from Fluxim AG. The modeling is based on the classical approach of electrodynamics, considering the light emission to originate from oscillating and thus radiating dipoles embedded in a multilayer device [89]. It is able to calculate radiometric as well as photometric quantities such as radiance and luminance of an OLED device as a function of viewing angle and dipole orientation. Moreover, it exhibits the possibility of simulating the angular-dependent electroluminescence spectra which can directly be plotted in the CIE diagram, offering a simple way of comparison with experimental results. The simulation program requires several input parameters such as the layer sequence and thicknesses of the device, the complex refractive index of each layer, the position, width, and distribution of the emission zone(s), and the intrinsic emission spectrum of the emitting layer(s). The refractive indices were obtained by ellipsometer measurements except for Al, ITO and SiO_2. The data for these layers were taken from the ETFOS data base. The refractive index of the glass substrate was assumed to be constant in the visible spectrum and was set to 1.51. The photoluminescence spectrum of the organic dye ($Ir(ppy)_3$) doped in the host material (TPBi) was used as the intrinsic spectral distribution of the emitter [71].

4 Fundamental Properties of Transition Metal Oxides

The introduction of transition metal oxides (TMOs) in organic devices such as organic light-emitting diodes (OLEDs) and organic solar cells (OSCs) led to first promising results referring to the device efficiency and lifetime, although the deeper understanding of their electronic structures is very limited so far. The knowledge of their electronic properties would further allow for their appropriate application within those devices, since the energy level alignment between the TMOs and their neighboring functional organic materials and inorganic electrodes is the key for highly efficient devices. For this reason, the electronic structure of MoO_3 and WO_3 will be studied first. Subsequently, a new model for hole injection by TMOs will be proposed and finally, their properties of electron-blocking and luminescence quenching in OLEDs will be studied.

4.1 Electronic Structure of MoO_3 and WO_3

Kelvin probe (KP) analysis offers one possibility to learn more about the electronic structure of TMOs by measuring their surface potential. Reynolds *et al.* used an oxygen plasma treatment of transition metal dichalcogenide MoS_2 to form a fully oxidized layer on top which corresponds to molybdenum trioxide (MoO_3). The KP measurements gave a value of 5.3 eV for its work function (WF, Φ), regardless of the duration of the plasma treatment [90]. By considering the optical band gap of MoO_3 of about 3-3.1 eV and assuming an electron affinity (EA) of 2.2-2.3 eV (in reference to [91]), an ionization energy (IE) of around 5.3 eV was calculated which would exactly correspond to the measured work function. This would mean that MoO_3 exhibits properties of a degenerated p-type semiconductor. However, first thickness-dependent measurements of the surface potential of MoO_3 via ultraviolet photoelectron spectroscopy revealed a different value for the work function of 5.7 eV which is obtained after the deposition of 10 nm of the TMO on indium tin oxide (ITO) [92, 93]. Finally, another KP study reveals values of work function for hyperthermal surface oxydized Mo and W at 6.5 eV and 6.3 eV, respectively [94]. Accordingly, it has to be assumed that the discrepancy of the measured values is caused by the deposition and measurement conditions. While the relatively small work function of around 5.3 eV has been obtained by KP analysis in ambient air [90], the higher values in the aforementioned study have been

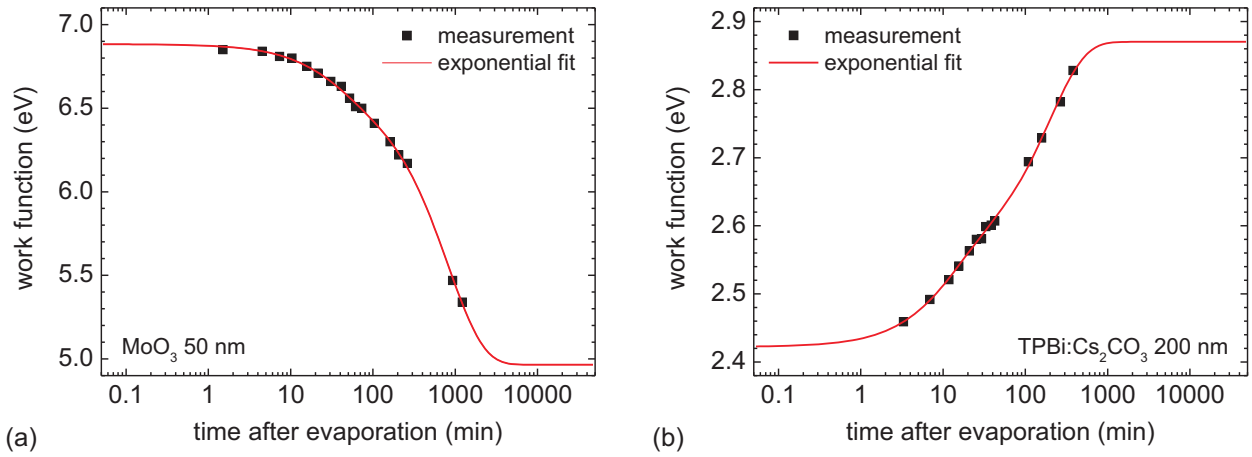

Figure 4.1: Time-dependent work function characteristics measured by KP of (a) a 50 nm thick MoO_3 film and (b) a 200 nm thick Cs_2CO_3 doped TPBi film deposited on ITO, respectively.

determined in an ultra high vacuum chamber with a base pressure of 10^{-10} mbar [94]. The deposition of MoO_3 with the work function around 5.7 eV measured by UPS was carried out in a UHV chamber with a base pressure of only 3 x 10^{-6} mbar [93]. Obviously, the base pressure and with it the amount of residual gases within the UHV system influences the work function of the TMOs due to adsorbates on the surface. Contaminants like hydrocarbons or molecular oxygen are known to change the surface potential of even inert metals such as Au and Pt [95, 96]. Figure 4.1a shows the time-dependent work function characteristics of 50 nm of MoO_3 deposited onto ITO and subsequently measured with KP at a base pressure of 5 x 10^{-7} mbar. The initial work function reaches a high value of about 6.85 eV which up to now had not been observed. After only thirty minutes of storage the surface potential drops to 6.65 eV and further decreases to 5.35 eV approximately 20 hours after evaporation. Thereby, the substrate has been removed from the KP tip after each measurement step, so that the influence of the alternating electric field could be excluded. The work function vs. time curve can be fitted by a second-order exponential decay indicating the influence of two main contaminants and showing up the value of the saturated work function of about 5 eV which would be obtained after more than 100 hours of storage in the UHV system. This value correlates quite well with the small work function which was measured by KP in ambient air [90] indicating the influence of oxygen and water. For comparison, Figure 4.1b displays a similar time-dependent devolution of work function of a 200 nm thin film of Cs_2CO_3 (molecular weight: 325.82 g/mole) doped TPBi (see Appendix for constitutional formula

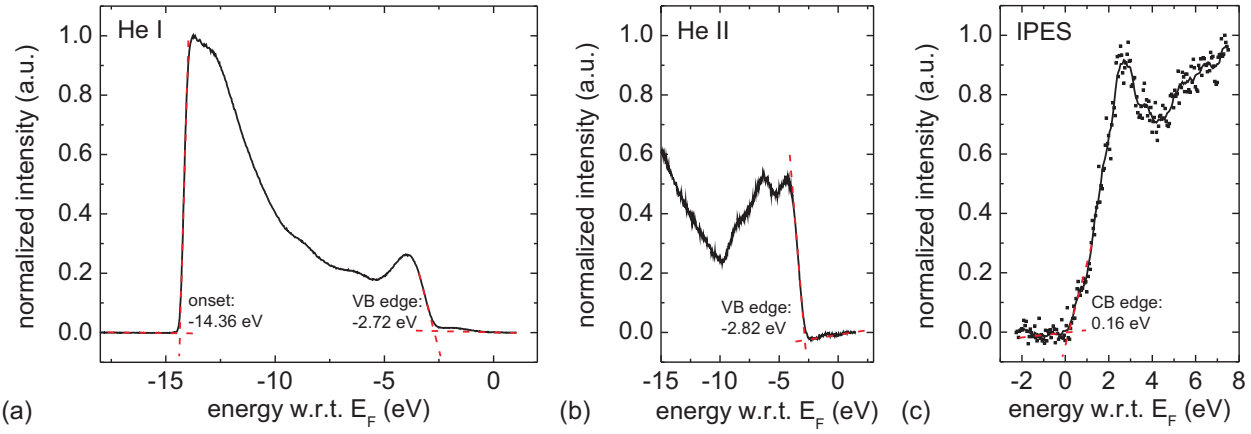

Figure 4.2: UPS spectrum of a MoO_3 film obtained by the use of (a) He I line and (b) He II line. (c) IPES spectrum of the MoO_3 film.

and molecular weight) as n-type organic electron transport material, starting at 2.45 eV for the freshly evaporated film and ending up at 2.87 eV as predicted by the exponential fit. This data make clear that depending on the base pressure within the measurement system, the time period between evaporation and measurement of the work function is essential and has to be kept short. Even in a UHV system with a base pressure of $<$ 2 x 10^{-10} mbar the surface of a cleaned Si substrate has been covered significantly with molecular oxygen, carbon-containing molecules, hydrogen atoms and hydroxyl-containing molecules [97]. Since WO_3 and MoO_3 are known for their hydrophilic property [98,99], mainly hydroxyl-containing molecules are assumed to be absorbed at the thin films. It has been shown that the immersion of MoO_3-like film in de-ionized water leads to a decrease of surface potential relative to that of MoO_3 [100], which is comparable to the observation made in this work.

In order to get information about the electronic structure of MoO_3 and WO_3, ultraviolet and inverse photoelectron spectroscopy (UPS and IPES) were conducted in a UHV system with low base pressures of $<$ 7 x 10^{-10} mbar and $<$ 7 x 10^{-9} mbar in the analysis and thermal evaporation chamber, respectively, keeping the influence of contaminants on the electronic structure low. This is all the more important, since high energetic photon and electron radiation could lead to chemical reactions between residual gases and the examined thin films. Initially, a 30 nm thick MoO_3 film was evaporated on Au and examined by the He I line. The resulting filled valence state spectrum is shown in Figure 4.2a. The photoemission onset lies at -14.36 eV with respect to the Fermi level E_F corresponding to a work function of 6.86 eV which coincide exactly with the value obtained by KP measurement shown above.

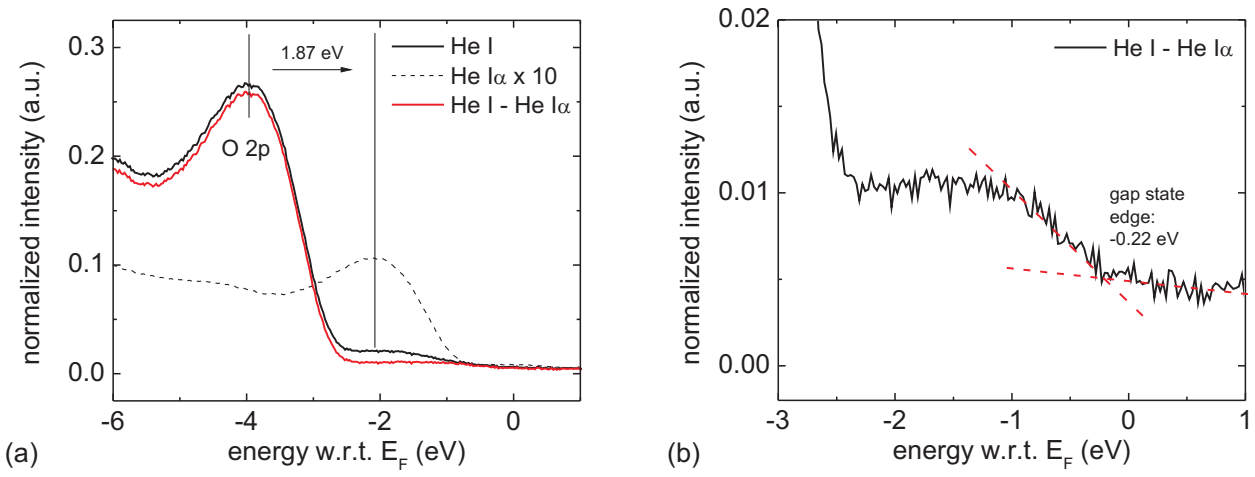

Figure 4.3: (a) UPS spectra of a MoO_3 film obtained by He I line (including parasitic effects of He Iα line), calculated for the exclusive radiation of He Iα line and shown for the situation after calculative elimination of the He Iα line. (b) Enlarged view on the gap states spectrum obtained after calculative elimination of the He Iα line.

The principal valence band (VB) spectrum near the Fermi level arises from the photoejection of O 2p electrons [9] and the linear extrapolation of its leading edge results in an energetic position at -2.72 eV corresponding to IE of about 9.58 eV. Since no monochromator is used in this work to separate the photon lines of the He plasma discharge lamp, significant parasitic background induced by the He Iα line has to be considered [101]. That is why the density of filled states of MoO_3 are also recorded by the He II line after changing the plasma pressure in the lamp. Figure 4.2b displays the resulting valence state spectrum with VB edge at -2.82 eV corresponding to IE around 9.68 eV. In the range of uncertainty of UPS measurements of about $\pm$ 0.1 eV, this value accords well with the result obtained by using the He I line. Finally, IPES measurements conducted on MoO_3 provides the energetic position of the conduction band (CB) edge lying at 0.16 eV with respect to Fermi level and indicating an EA of 6.7 eV. Note the energy resolution of IPES measurements amounts to $\pm$ 0.25 eV. In combination with the UPS results, a band gap of approximately 3 eV is defined which is in good agreement with the values around 3.1-3.2 eV determined by optical measurements on amorphous MoO_3 [102, 103].

Accordingly, these results draw a completely new picture of MoO_3 and its electronic structure. On the one hand, the IE and EA are more than 4 eV deeper than previously reported. On the other hand, the proximity of the Fermi level to the CB indicates characteristics of an n-type semiconductor of the TMO which is absolutely the opposite of the conception given

by previous reports [90, 104]. Thermoelectric power measurements on thermally evaporated WO_3 also indicated its n-type semiconducting properties [105]. The origin of the n-type character of the TMOs is assumed to be in the thermal evaporation process leading to oxygen-deficient films which is responsible for the n-type doping of the TMO and has been evidenced by x-ray photoelectron spectroscopy [102]. At the same time, thermally evaporated layers exhibit lower material density as compared to sputtered films which has been shown for tungsten trioxide [106]. The relation of the material densities for evaporated and crystalline WO_3 films allows for the estimation of the O/W ratio to be 2.7 [9]. Amorphous evaporated MoO_3 films possess a material density around 4.1 g/cm^3 as compared to 4.7 g/cm^3 for monocrystalline MoO_3 [107]. The formation of oxygen-deficient films is attributed to the decomposition and preferential evaporation of the lower vapor pressure constituent atomic species of the TMO [103]. However, different publications on the amount of deficiency exist ranging between $x < 0.1$ to $x = 0.3$ for MoO_{3-x} [102,103]. In a stoichiometric film of MoO_3 the molybdenum atoms would only exist in the form of fully oxidized sites, namely Mo^{6+}. Oxygen vacancies lead to the formation of Mo^{4+} and Mo^{5+} so that the TMO becomes photochromic. The discussion of its mechanism would by far exceed the scope of this work, since different controversial models exist for the explanation of photochromism [108]. Focusing on one of these models, the oxygen vacancies are considered as doubly positive charged structural defects V^{2+}. When they capture one or two electrons, they serve as color centers which are responsible for the deep blue coloration of TMOs. The illumination of MoO_3 films leads to an increase of such color centers to which a broad photochromic absorption band around 850 nm (corresponding to 1.46 eV) is attributed [103]. Consequently, the radiation by high energetic He photons during the UPS measurements should lead to an additional absorption spectrum within the band gap as indicator for the existence of non-stoichiometry which is already shown for deeply colored MoO_3 [9]. For this reason, Figure 4.3a displays the low binding energy section of the full UPS spectrum which has been shown in Figure 4.2a. The parasitic influence of the He Iα line on the UPS spectrum mentioned above is clearly visible: the O 2p states spectrum is reproduced after an energetic shift of 1.87 eV to lower binding energies which is given by the energetic difference of He I and He Iα line. However, even the calculative elimination of this effect leaves a weak residual signal as shown by Figure 4.3b in a further enlarged view. This broad spectrum with its center at approximately -1.5 eV indicates the partially occupied oxygen vacancies denoted as gap states and serving as evidence of the existence of non-stoichiometric MoO_3 film. Two other UPS studies also indicated the existence of gap states in MoO_3 relating the signals within the band gap to a partial occupation of "local" Mo 4d orbitals [109, 110]. Note however that the density of gap states is far below that of O 2p states and will be neglected in the further discussion.

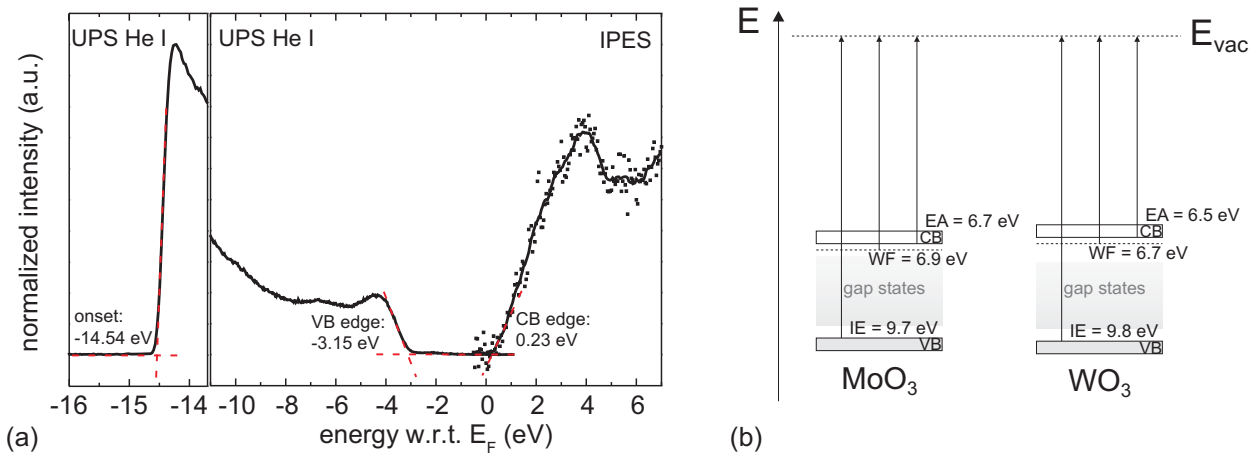

Figure 4.4: (a) UPS and IPES spectra of a WO_3 film. (b) Summary of the electronic properties of MoO_3 and WO_3. E_{vac} denotes the energy of the vacuum level.

The examination of WO_3 by UPS and IPES provides an electronic structure similar to that of MoO_3. Figure 4.4a shows the relevant parts of the UPS and IPES spectra of 10 nm thick WO_3 deposited on Au. The photoemission onset at -14.54 eV is slightly smaller than that of MoO_3 and indicates a work function of 6.68 eV. VB edge and CB edge have been measured to -3.15 eV and 0.23 eV, respectively, being equivalent to IE of about 9.83 eV and EA of about 6.45 eV. Accordingly, WO_3 also features properties of an n-type semiconductor caused by the existence of oxygen vacancies which lead to a substoichiometric thin film. However, the gap states signal of the UPS spectrum near the Fermi level was negligibly small compared to MoO_3 indicating only a slight deviation of the stoichiometry. Moreover, different measurement periods equivalent to different radiation dosages for the two TMOs could have led to unequal extents of photochromic effects reflected by differing signal strengths of the gap states spectra. Figure 4.4b summarizes the electronic structures of MoO_3 and WO_3 found by KP and photoelectron spectroscopy within this work and implies the possible existence of gap states.

4.2 Insertion of Neat TMO Layers into OLEDs

The results of the previous section necessitate a novel interpretation of the impact of TMOs, especially MoO_3 and WO_3, on OLEDs and OSCs. On the one hand, they have been found to enable efficient hole injection out of the anode into OLEDs. On the other hand, improved performance of OSCs has been attributed to an electron-blocking effect of TMOs. Both

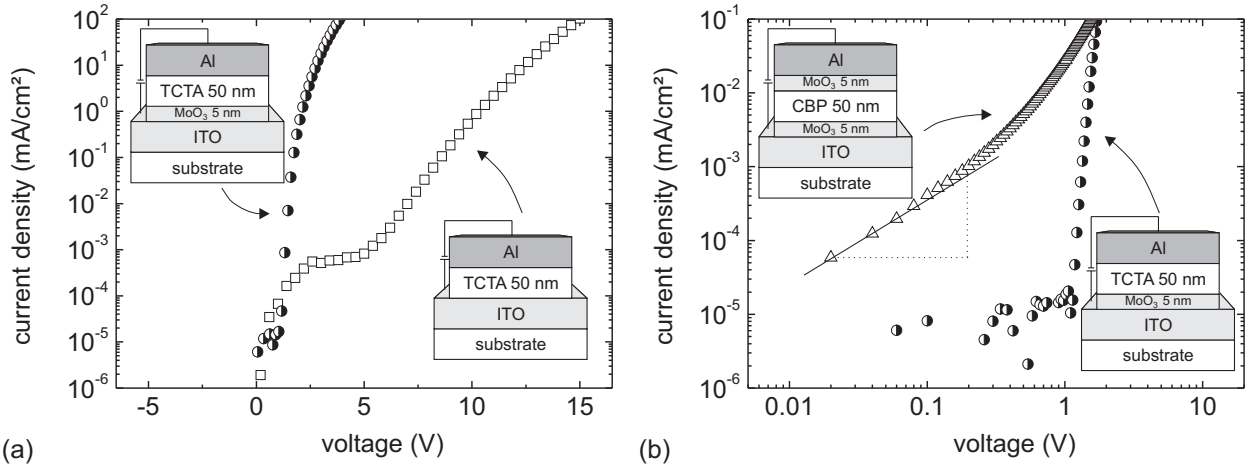

Figure 4.5: Characteristics of hole-only devices optionally employing MoO_3 interlayers at anode and/or cathode. Insets: respective scheme of the device structure. (a) Current density versus voltage characterstics of TCTA devices. (b) Magnified view on current density versus voltage characterstics of a TCTA device with MoO_3 interlayer compared to a CBP device sandwiched by two MoO_3 films. Insets: respective scheme of the device structure.

modes of operations will be analyzed in the following subsections within the revised picture of the electronic structures of MoO_3 and WO_3. According to their similarity the examinations of one of both TMOs respectively should lead to the same conclusions for the comparable use of the other one. However, the use of neat layers of TMOs does not necessarily implicate an improvement of device performance. In the final subsection of this chapter luminescence quenching by thin films of WO_3 in OLEDs will be shown and discussed.

4.2.1 Hole Injection

For lack of electrodes with sufficiently high work functions, interlayers are used to lower the hole injection barriers to organic hole transport materials with HOMO energy levels around 5.4 to 6.2 eV. Transition metal oxides inserted as neat films adjacent to the anode turned out to be a general instrument of improving hole injection. They were successfully used in organic transistors [104], OLEDs [15, 16, 90, 111, 112] and hole-only devices for admittance spectroscopy [113], apparently independent of the work function of the anode and the HOMO energy level of the successive organic material. If TMOs behaved like insulators as given for completely stoichiometric layers, they would only contribute to lower injection barriers as very thin films because the tunneling probability depends on interlayer thickness [114].

However, it has been shown that even thicker MoO_3 films up to 20 nm can be used without significant change of the overall device performance [16], so that a real charge carrier transport occurs through the interlayer. For this reason, it is all the more important to clarify the mechanism of hole injection using the example of MoO_3.

Figure 4.5a shows current density-voltage (*I-V*) characteristics of hole-only devices consisting of 50 nm TCTA deposited between an ITO anode and an Al cathode. An optional 5 nm thin MoO_3 interlayer has been included as depicted in the insets. Due to the potential barrier of more than 2 eV between TCTA and Al for the injection of electrons given by the difference of the LUMO energy level and work function of both materials, electron injection from the cathode into the organic layer is improbable. Obviously, the hole injection is significantly improved by the thin film of MoO_3, since higher current densities of more than five orders of magnitude are already obtained for low voltages around 2.5 V compared to *I-V* characteristics of the device without the interlayer. However, no current flow is detected for voltages up to 1 V even for the device with MoO_3 as displayed in a magnified view in Figure 4.5b. This is due to the existence of a built-in voltage which first has to be compensated by an external electric field prior to the initial current flow by intrinsic charge carriers. The magnitude of the built-in potential can not be determined a priori by the work function difference of the electrodes [115], since potential interface dipoles between the layers have to be considered. On the contrary, a 50 nm thick CBP film comprising a 5 nm MoO_3 interlayer at both electrodes as depicted in Figure 4.5b leads to an immediate Ohmic behavior at low voltages as indicated by the dashed line with a slope of nearly one. Obviously, MoO_3 enables comparable electronic conditions at both electrodes, so that the built-in voltage vanishes. This comparison illustrates that the examination of electrode interfaces are important in order to predict the internal electric field situation and the mechanism of charge injection. Inversely, a high work function electrode does not a priori lead to an efficient injection of charge carriers, as shown for the interface between Au and α-NPD [96]. For this reason, the interfaces between ITO and MoO_3 as well as between MoO_3 and TCTA have been examined by film thickness-dependent measurements of the work function via KP as depicted in Figure 4.6a. Starting with the work function of ITO of about 4.8 eV it increases sharply and reaches a value of 6.5 eV after only 2 nm of MoO_3 which coincide with the total coverage of the anode. However, it seemingly takes more than an additional 4 nm for the work function to saturate at around 6.8-6.9 eV. The orientation of the dipole formed between ITO and the TMO with the negative side directed to the vacuum indicates an electron transfer from the electrode to MoO_3 which has been evidenced by x-ray photoelectron spectroscopy [92]. The thin film deposition of TCTA onto 65 nm of MoO_3 shown in the right part of Figure 4.6a is in a similar manner correlated with the formation of an interface dipole within 2 to 4 nm

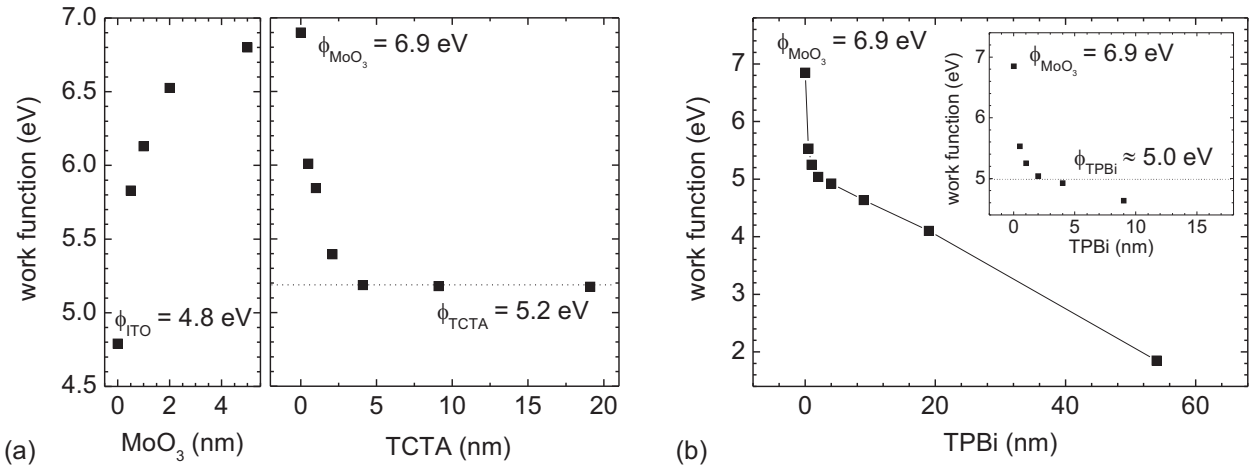

Figure 4.6: Thickness-dependent work function characteristics of (a) MoO_3 on ITO and TCTA on MoO_3 and of (b) TPBi on MoO_3. Inset: magnified view on the progression of the work function of TPBi on MoO_3 within the first 10 nm.

of TCTA directing again with its negative part to the TMO. Therefore, an electron transfer from the hole transport layer (HTL) to MoO_3 is expected [116]. The dipole Δ leads to a potential energy shift of 1.7 eV which is smaller than the shift at the anode. The latter is considered as the result of the Fermi level alignment between ITO and MoO_3. A comparison to the deposition of an electron transport layer (ETL) like TPBi on 65 nm thick film of MoO_3 indicates a similar value for the interfacial dipole of about 1.9 eV as clearly seen in the inset of Figure 4.6b. Assuming a thickness of the dipole layer around 2-4 nm comparable to the situation of TCTA, the work function saturates at 5.0 eV after the steep decrease from the initial value of about 6.9 eV for MoO_3. However, Figure 4.6b also displays the buildup of a giant surface potential for thicker layers of TPBi given by its linear increase and without any indication of saturation. The surface potential reached 3.1 V for an additional 50 nm thick film of TPBi after the interface dipole. This corresponds to a gradient of about 0.06 V/nm which is in good agreement to previous studies on TPBi and Alq_3 [117, 118]. The formation of this giant surface potential is explained by the preferential orientation of the organic molecules having a permanent dipole moment and has been shown to vanish by electronic excitation, so that no further consequences are expected within operating devices. In this case however, a slight interference between the interface dipole and the dipole within the bulk material takes place, giving rise to some uncertainty in the determination of their values. Nevertheless, it could be speculated that the deposition of non-doped organic materials onto MoO_3 leads to an interface dipole in the region of 1.5-2 eV as a general feature.

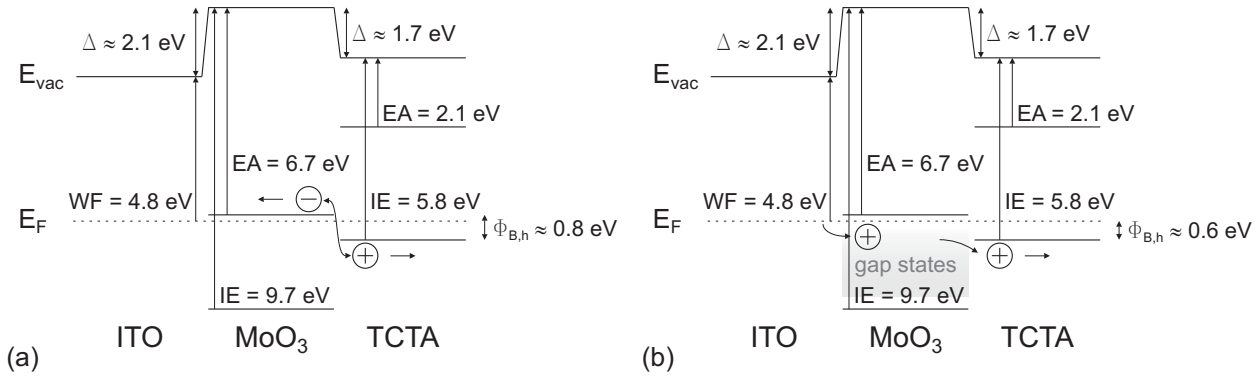

Figure 4.7: Schematics of the hole injection into TCTA assisted by MoO_3. (a) Proposed model of electron extraction and concomitant hole injection at the MoO_3/TCTA interface. (b) Model of gap states assisted hole injection through MoO_3 according to [109, 110].

Figure 4.7a summarizes schematically the results obtained for ITO/MoO_3/TCTA and allows for the interpretation of the hole injection mechanism. Due to the Fermi level pinning at the electrode, the position of the CB minimum of MoO_3 is only 0.2 eV higher than the work function of ITO. This suggests an efficient electron extraction from the CB into the electrode rather than a hole injection from the anode into the very deep-lying VB of the TMO, when positive bias is applied to ITO. The electrons, on the other hand, are generated at the interface between MoO_3 and TCTA with a concomitant injection of holes into the HOMO level of the HTL. The hole injection barrier $\Phi_{B,h}$ amounts to 0.8 eV which is significantly lower than the barrier between ITO and TCTA of about 1.0 eV by assuming no additional dipole formation at this direct interface [96]. For comparison, a difference in height of injection barriers of approximately 0.15 eV already leads to a significant change in the *I-V* characteristics of more than two orders of magnitude as shown for MoO_3/α-NPD compared to ITO/α-NPD [119]. Nevertheless, the hole injection via TMOs can not be denoted as Ohmic. The proposed model of hole injection implies the electron transport within the CB of MoO_3 which is self-evident due to the n-type character of the TMO. By following the argumentation of [109, 110], however, a gap state assisted hole injection into and transport through the TMO up to the HTL is suggested which is schematically displayed in Figure 4.7b for completeness. The hole injection barrier would amount to 0.6 eV and is slightly lower as stated above since the 0.2 eV higher-lying CB of MoO_3 is skipped by this mechanism. Admittedly, this alternative model presumes the existence of a sufficiently high gap state density throughout the TMO and additionally, all gap states have to be partially occupied by electrons for an efficient hole transport, which is at least questionable.

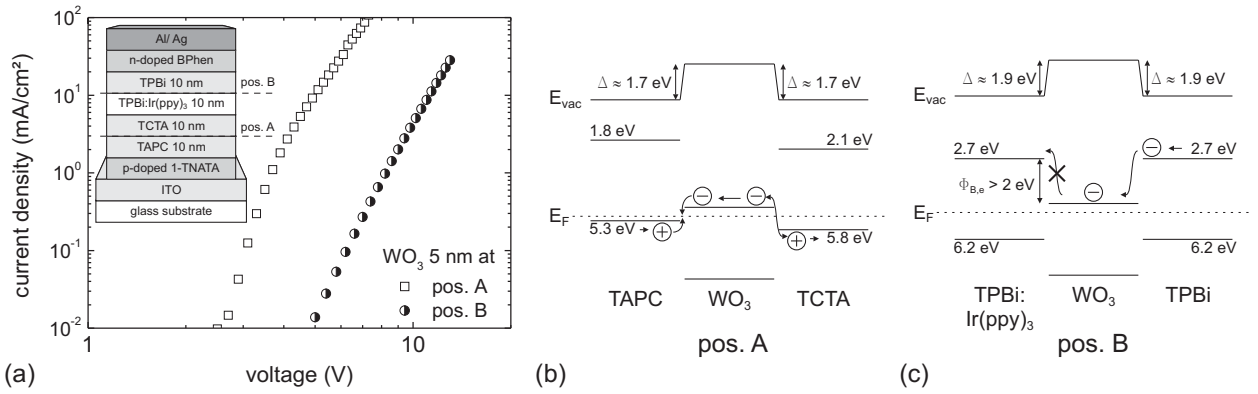

Figure 4.8: (a) Current density versus voltage characteristics of conventional OLEDs with a 5 nm thick WO_3 layer at two optional positions. Inset: device structure of the conventional OLED indicating the WO_3 positions. (b) Schematic of the hole transport through the TMO for WO_3 at position A. Values of electronic structure of TAPC are extracted from [122]. (c) Schematic of the electron-blocking mechanism for WO_3 at position B. Values of electronic structure of TPBi are extracted from [123].

4.2.2 Electron Blocking

In view of the obsolete values of the electronic structure of MoO_3 with EA at 2.3 eV and IE at 5.3 eV [16, 90, 120], several publications assumed an electron-blocking behavior of the TMO [90,93,121]. They report on the improvement of device performance by introduction of a thin film of MoO_3 between the active layer and the electrode for OLEDs as well as OSCs. The enhancement is ascribed to a lower rate of electron recombination at the electrode which would lead to charge imbalance and lower internal quantum efficiency. Accordingly, an electron-blocking effect is inferred for MoO_3 supposedly having a significant higher lying CB minimum compared to the LUMO level of the adjacent organic materials. It has been shown in the previous sections that MoO_3 and WO_3 exhibit very deep-lying transport levels and characteristics of n-type doped semiconductors, so that an electron-blocking effect is not expected.

In order to shed more light on this issue a 5 nm thin film of WO_3 has been inserted in two different positions of a conventional OLED whose layer sequence is shown in the inset of Figure 4.8a. First, the TMO has been deposited between the hole transport layers TAPC and TCTA denoted as position A. Assuming the formation of similar interface dipoles between TMO and organic layers as shown for MoO_3/TCTA in the previous section, the hole transport is barely affected by WO_3 according to the new model of hole injection. As schematically

depicted in Figure 4.8b, holes coming from the anode side through TAPC recombine with electrons from the WO_3 layer which in turn are generated at the TMO/TCTA interface. In this way, holes reach the $Ir(ppy)_3$ doped TPBi emission layer where they recombine with electrons from the cathode side causing the green light emission of the OLED. On the other hand, no light emission has been observed from OLEDs comprising a 5 nm thin film of WO_3 which is deposited between the doped and undoped TPBi layers at position B. Additionally, Figure 4.8a indicates that the current density is more than three orders of magnitude lower than in the OLEDs with WO_3 deposited at position A. Actually, electron-blocking occurs by the assumption of a similar dipole formation between WO_3 and the ETLs as discussed for the MoO_3/TPBi interface in the former subsection. Figure 4.8c schematically shows how electrons coming from the cathode side and drifting through the undoped TPBi film drop into the CB of WO_3 and accumulate at the interface to TPBi:$Ir(ppy)_3$. The electronic structure of the dopant has been excluded to simplify matters without loss of information. Obviously, the interface dipoles are not sufficient to move the LUMO level substantially closer to the CB minimum of the TMO and to significantly lower the barrier for an efficient electron injection. As a result, the electron barrier $\Phi_{B,e}$ amounts to more than 2 eV and precludes the injection of electrons into the emission layer so that no light emission results. Presumably, a leakage current of holes through the emission layer to WO_3 takes place and leads to a small recombination rate at this interface. Accordingly, it has been shown that not the TMOs but the organic layers adjacent to them are blocking the electrons due to the energetic offset between their LUMO level and the CB minimum of the oxide layers. Thus, it has to be checked again whether the explanation of the improvement of device performance as cited above is still valid. Besides electron-blocking by the combination of TMO and an organic layer, positive effects on the internal electric field could be considered as exemplarily shown in the former subsection.

4.2.3 Luminescence Quenching

As previously mentioned, it has been shown that thicker layers of TMOs in OLEDs can be used not only for efficient hole injection but also for charge carrier transport to the emission layer. In this way, organic hole transport materials can be substituted by comparably conductive TMOs. For instance, WO_3 exhibits conductivity on the order of 1 x 10^{-6} S/cm [124] which exceeds the low conductivities of intrinsic organic materials. Note, that the conductivity can be raised by more than four orders of magnitude via coloration [125] by varying the amount of W^{5+} or Mo^{5+} versus W^{6+} or Mo^{6+}. Figure 4.9a actually indicates higher current densities at equal voltages for thicker layers of WO_3 which successively substitute TCTA within the OLED structure as depicted in Figure 4.9b (device structure on the left

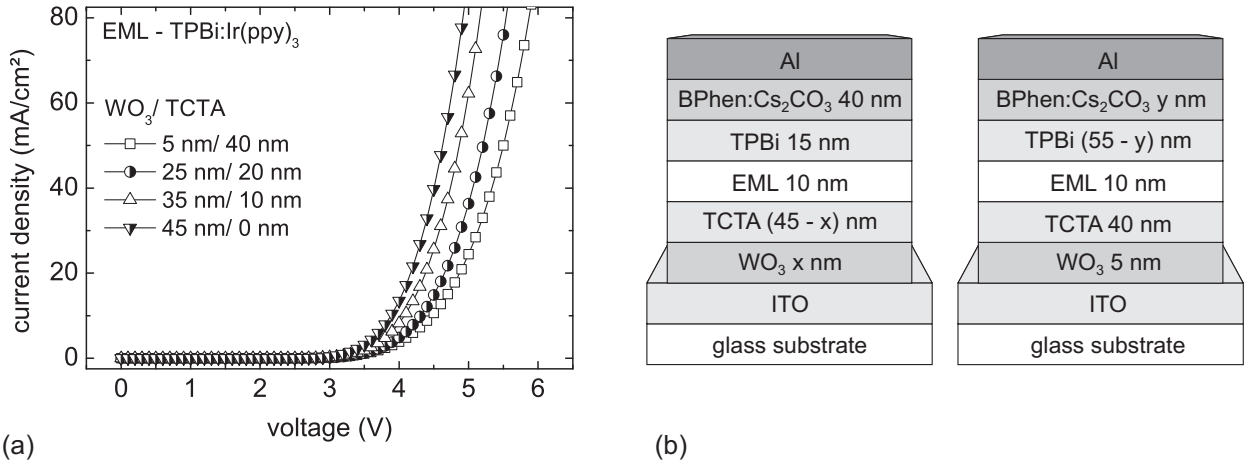

Figure 4.9: (a) Current density versus voltage characteristics of OLEDs employing different thicknesses of WO_3 layer. (b) Device structure of OLEDs with varying WO_3 and TCTA thickness (left) and varying BPhen:Cs_2CO_3 and TPBi thickness (right).

hand side). $Ir(ppy)_3$ doped TPBi has been used as emission layer (EML). On the other hand, the current efficiency of the OLEDs measured at 100 cd/m^2 decreases with increasing thickness of the TMO as depicted in Figure 4.10a. Initially, the efficiency amounts to approximately 35 cd/A at 5 nm of WO_3 and slowly decreases to 30 cd/A at a TMO thickness of 35 nm corresponding to a residual TCTA thickness of 10 nm. By further reducing the distance between WO_3 and TPBi:$Ir(ppy)_3$ the efficiency starts to drop dramatically to lower values and reaches 0.2 cd/A at direct contact between TMO and EML. To further analyze this mechanism the EML has been changed to TCTA:$Ir(ppy)_3$. Similar thickness dependent characteristics of the current efficiency are obtained, though it only drops to approximately 50 % of its initial value at 5 nm of WO_3, when again direct contact is established between the TMO and EML. Accordingly, WO_3 apparently leads to strong luminescence quenching. Though this mechanism is not fully understood in all details, it is assumed that especially polarons induced by photogeneration, charge injection, or electrochemical doping are responsible for exciton quenching in organic devices [126–129]. This mechanism could also be valid for WO_3, since the quenching-induced current efficiency characteristics obtained by thickness variation of the n-type doped BPhen layer are similar to those of the TMO as shown in Figure 4.10b. After the complete substitution of TPBi by the n-type doped layer according to the device structure on the right hand side of Figure 4.9b, the efficiency drops to almost 0 cd/A when TCTA:$Ir(ppy)_3$ is taken as EML. Using TPBi:$Ir(ppy)_3$ the efficiency ends up at approximately 50 % of its initial value.

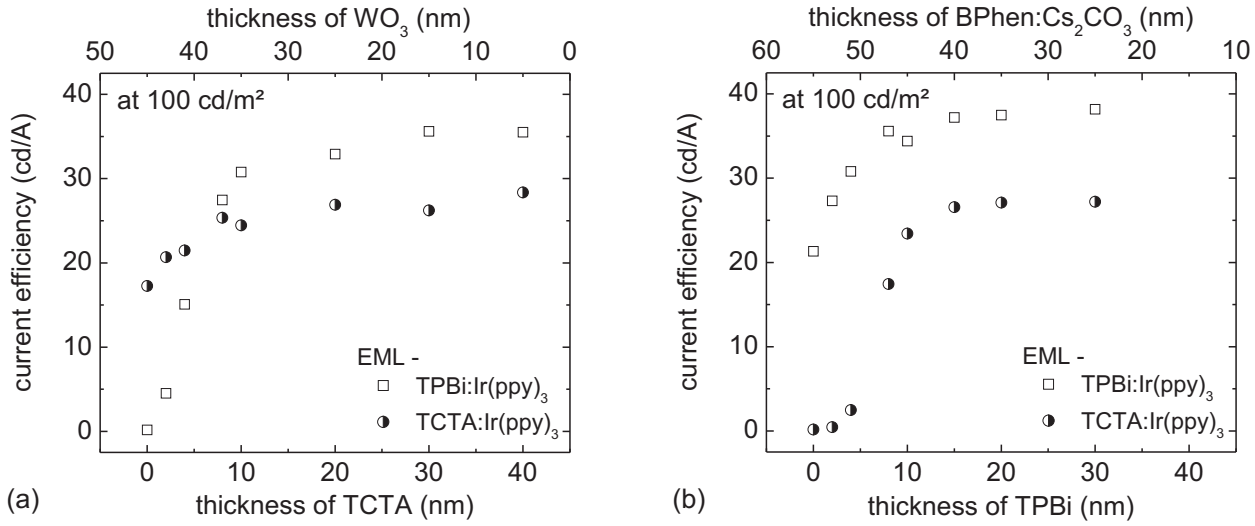

Figure 4.10: Current efficiency versus layer thickness characteristics of OLEDs employing different emission layers and with concomitant variation of (a) WO_3 and TCTA thickness (b) BPhen:Cs_2CO_3 and TPBi thickness.

Photoluminescence (PL) measurements on a neat layer of WO_3 also indicate luminescence quenching by the TMO. Figure 4.11a shows that the integral PL intensity starts to significantly grow at a layer thickness above 4 nm of TPBi:$Ir(ppy)_3$ deposited on top of WO_3 due to the quenching of excitons in the vicinity of the TMO. Only at a sufficient distance between interface and emissive layer the excitons decay radiatively and contribute to photoluminescence. The PL spectra were obtained by using a cw HeCd laser ($\lambda = 325$ nm) which simultaneously excited TPBi and $Ir(ppy)_3$ excitons. Still, only qualitative information about the distance dependence of quenching effects can be gained out of this measurement, since further analysis needs to be done regarding the exciton transfer rates between host and dopant on the one hand and between dopant as well as host molecules and quenching film on the other hand. Figure 4.11b displays selective PL spectra for different thicknesses of the emission layer. It is particularly noticeable that the quenching occurs without spectral selectivity, possibly indicating a direct transfer of TPBi excitons to WO_3 rather than to $Ir(ppy)_3$.

The comparison of the results obtained by the thickness variation of WO_3 and BPhen:Cs_2CO_3 with the sequential use of two different emission layers demonstrates that the actual emission zone is narrowed to only a few nanometers of the respective dye-doped layer and is located at the TCTA/TPBi interface within the OLED. That is why the current efficiency only drops

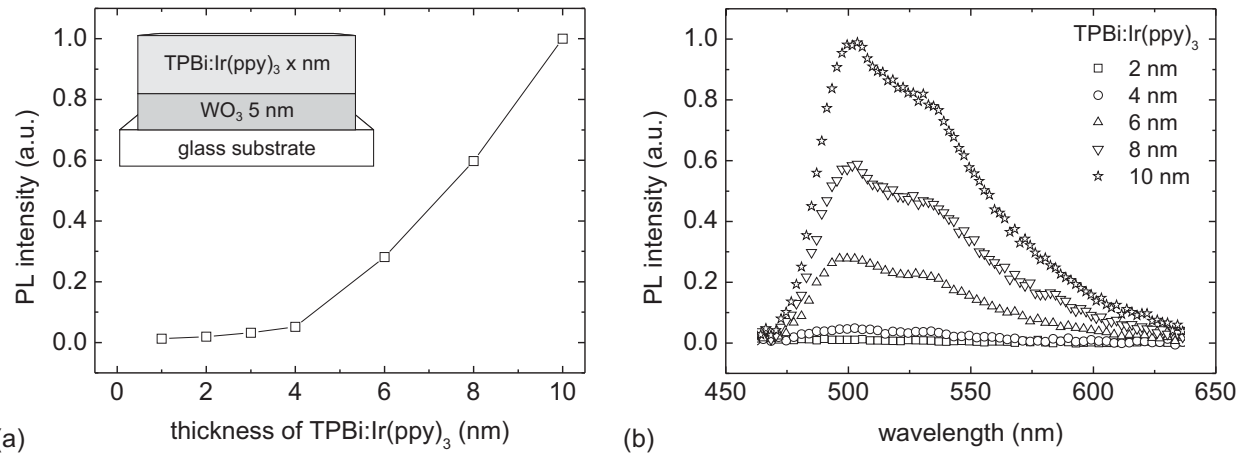

Figure 4.11: (a) Normalized integral PL intensity versus TPBi:$Ir(ppy)_3$ thickness of the displayed device structure. (b) Normalized PL spectra.

by 50 % when, for instance, WO_3 is contacting the TCTA:$Ir(ppy)_3$ emission layer. This is due to the fact that the emission zone at the interface of TCTA:$Ir(ppy)_3$ and TPBi is actually an additional 10 nm away from the interface to WO_3 as compared to the situation in which TPBi:$Ir(ppy)_3$ is used as EML. In summary, a distance of approximately 15 to 20 nm between emission zone and TMOs or electrochemically doped layers is needed to effectively avoid quenching effects. The energy transfer from excitons to polarons is considered to be mainly a Förster-type process [130, 131]. However, the distance dependence of the current efficiency from the quenching layer can not be directly correlated to the corresponding distance dependency of the Förster transfer mechanism. This can be explained in reference to the exciton formation zone which, by approximation, locally coincides with the emission zone at the TCTA/TPBi interface. Due to the offset between the HOMO and LUMO levels of the participating organic materials an accumulation of charge carriers is expected at the interface. As previously shown, TCTA exhibits a HOMO level at 5.8 eV compared to that of TPBi at 6.3 eV. Although $Ir(ppy)_3$ is known as hole transport material possessing a comparably high-lying HOMO level at 5.2 eV [132], a trapping and forming of excitons directly on the phosphorescent dopant can be estimated to 18 % of the overall recombination and therefore neglected in the following discussion [133]. Accordingly, the drop in efficiency within the last 2-4 nm of distance between quenching layer and emission zone must also be attributed to the decreased charge accumulation due to the absence of complete surface coverage by the organic spacer. Properties like film morphology and roughness play a role in these considerations. Interestingly, the current efficiency still amounts to 42 % of the

maximum value (35 cd/A) at a distance of 4 nm between WO_3 and emission zone using TPBi:$Ir(ppy)_3$. On the other hand, the efficiency drops to only 9 % of its maximum value for the same distance between BPhen:Cs_2CO_3 and the emission zone using TCTA:$Ir(ppy)_3$ as shown in Figure 4.10b. The result of this comparison is all the more surprising considering the existence of an interfacial dipole at the WO_3/TCTA interface as inferred in the previous sections. It could be speculated that this dipole layer leads to additional exciton quenching. On the other hand, this would have lowered the current efficiency at already higher distances between WO_3 and emission zone. Thus, further experiments are needed to shed more light on this issue. Finally, the influence of injected charge carriers on polaron quenching has to be taken into account. It has been shown that quenching of Alq_3 emission is caused by NPB^+ radical cations due the excessive hole injection and accumulation near the emission zone [134]. The same applies for thicker WO_3 layers leading to higher hole current densities and consequently a charge imbalance, since no simultaneous adaption of the BPhen:Cs_2CO_3 thickness is done. Accordingly, accumulation of excessive holes at the TCTA/TPBi interface has to be expected which additionally lowers the current efficiency.

4.3 Conclusion

In this chapter, the transition metal oxides, namely MoO_3 and WO_3, were studied referring to their electronic structure and functionality in OLEDs. UPS and IPES measurements revealed their IE and EA to be actually 4 eV deeper than previously published. MoO_3 and WO_3 exhibit an EA of about 6.7 eV and 6.5 eV and an IE around 9.7 and 9.8 eV, respectively. The dramatic discrepancy between the reported and measured values was attributed to varying deposition and measurement conditions. Different base pressures were expected to influence the work function of the TMOs due to the time dependent surface adsorption of contaminants demonstrated by KP measurements. In addition, it was clarified that MoO_3 and WO_3 represent n-type semiconductors due to the energetic proximity of their Fermi levels to the respective CB minimum. The n-type doping of the TMOs was explained by the existence of oxygen vacancies which arise out of the thermal evaporation process. They are also responsible for their photochromic properties.
Moreover, a new model of hole injection by neat layers of MoO_3 was inferred. The enhancement of hole injection by the TMO was explained by the formation of large interface dipoles between ITO anode and TMO as well as MoO_3 and the adjacent organic hole transport layer. Accordingly, evidence was provided for hole injection via electron extraction from the TCTA HOMO level through the MoO_3 conduction band. Furthermore, reports on apparent electron-blocking by TMOs in organic devices were revised. It was demonstrated that WO_3

alone can not block electrons. Electron blocking was achieved only in combination with organic materials possessing a low EA which, despite the formation of a large interface dipole, leads to an appreciable energetic offset between CB minimum and LUMO level. Finally, luminescence quenching by TMOs was studied with the variation of the WO_3 thickness in OLEDs and compared with exciton quenching by Cs_2CO_3 doped BPhen. It turned out that the real emission zone in those OLEDs using $Ir(ppy)_3$ as phosphorescent dopant is narrowed and located at the TCTA/TPBi interface so that strong luminescence quenching occurred in its immediate vicinity to the quenching layer. A minimum distance of 15 to 20 nm between emission zone and TMO was inferred to obtain high current efficiencies. However, additional studies are required to reveal the actual exciton quenching mechanism which could not be completely revealed due to interfering effects within the OLED structure.

5 Electrochemical Doping of Organic Semiconductors by MoO_3 and Cs_2CO_3

Electrochemical doping of organic materials is an important technique to increase the efficiency of OLEDs. In this way, not only the charge carrier injection properties of doped materials can be improved but also their bulk conductivity as explained in Section 2.2.3. After having clarified the electronic structure of TMOs and their functionality as neat layers in organic devices, their suitability for p-type doping of organic materials will be studied in this chapter. Specifically, MoO_3 will be investigated as p-type dopant. Since the doping efficiency not only depends on the acceptor but also on the respective host material and their interaction, different p-doped organic materials will be compared at the end of this chapter. Referring to ambipolar wide band gap organic materials, it is also necessary to study the possibility of their n-type doping. For that purpose, Cs_2CO_3 will be used as dopant in different host materials. Initially, the electronic properties of the p- and n-doped layers are investigated. Then, the impact of doping on electrical, morphological and optical characteristics is analyzed and finally, the doping-induced free charge carrier densities are measured.

5.1 P-Type Doping of CBP by MoO_3

P-type doping of organic hole transport materials by F_4-TCNQ is well-known. For instance, it has been shown that only a small mol % of dopant molecules is sufficient to achieve high free hole densities around 10^{19}-10^{20} cm^{-3} in starburst amines like TDATA or in zinc phthalocyanine (ZnPc) [44]. This is explained by the energy level alignment between the LUMO level of the acceptor molecule F_4-TCNQ lying at 5.24 eV and the HOMO level of the respective organic material. ZnPc exhibits a HOMO level at 5.28 eV, so that the transfer of an electron from the HOMO of the host molecule to the LUMO of the dopant molecule is energetically favorable [38]. The p-type doping of organic wide band gap materials with deeper-lying HOMO levels using F_4-TCNQ, however, is comparably inefficient as demonstrated by doping of TPD and TCTA which exhibit a HOMO level of 5.4 and 5.8 eV, respectively [44,135]. Only a partial electron transfer from these hosts to acceptor molecules takes place. On the

other hand, almost simultaneously with the introduction of neat TMO layers in OLEDs, first demonstrations of p-type doping by these oxides have emerged. Organic hole transport materials such as 2-TNATA, NPB and m-MTDATA were successfully doped by TMOs like WO_3, MoO_3 and ReO_3 [17,18,136–138]. All these hole transport materials, however, are known for their low IE around 5.1-5.2 eV [123,139]. Due to the deep-lying CB minimum of MoO_3 and WO_3 as revealed in the previous chapter, it should also be possible to p-type dope organic materials like TCTA with a considerably higher IE of about 5.8 eV. A carboxyl-derivate of TCTA, namely CBP, even exhibits a HOMO level at 6.3 eV according to literature [123]. It has been widely used as a host material for phosphorescent dopants like $Ir(ppy)_3$ and has led in this combination to the highest efficiencies of monochrome OLEDs to date [4]. Moreover, CBP is known as ambipolar material allowing for the transport of both holes and electrons. In addition, it possesses comparably high charge carrier mobilities around 10^{-4}-10^{-3} cm^2/Vs [140]. It is conceivable to use this organic material as an electrochemically doped injection and transport layer for holes and electrons, providing the possibility to reduce the complexity of organic devices. Thus, the p-type doping of organic host materials by TMOs will be exemplified by the study on MoO_3 doped CBP in the following sections.

5.1.1 Analysis of P-Type Doping via UPS and KP

KP analysis of electrochemically doped organic semiconductors is a proven tool for the determination of their Fermi levels [141]. The incremental shift of the Fermi level toward the transport state by higher doping concentrations indicates the sign and amount of the generated free charge carriers. Figure 5.1a exemplarily shows the results of the doping of TCTA by WO_3 (molecular weight: 231.85 g/mole). Different doping concentrations of WO_3 in TCTA were prepared by the co-evaporation onto ITO. The respective film thickness of the doped layers was kept constant at 30 nm (inset of Figure 5.1a). The work function of completely undoped TCTA apparently yields a value of 4.8 eV. Normally, the Fermi level of an intrinsic semiconductor should be expected in the middle of its band gap which, in this case, would be at 4 eV. Due to the fact that the organic material exhibits a very low charge carrier density it can be inferred that no Fermi level alignment between ITO and TCTA is achieved within a layer thickness of 30 nm [142]. Furthermore, the measured work function confirms the assumption made in Section 4.2.1 that no significant interface dipole arises between ITO and TCTA. Thus, the value represents the slightly modified work function of ITO which usually amounts to 4.7 eV. The low doping concentration of 0.3 vol % of WO_3 is already sufficient for Fermi level alignment as will be discussed in Section 5.3.2 and leads to an instant increase of the work function to 5.2 eV. This is a clear indication of p-type doping due to the Fermi level shift towards the HOMO level of TCTA. Higher doping

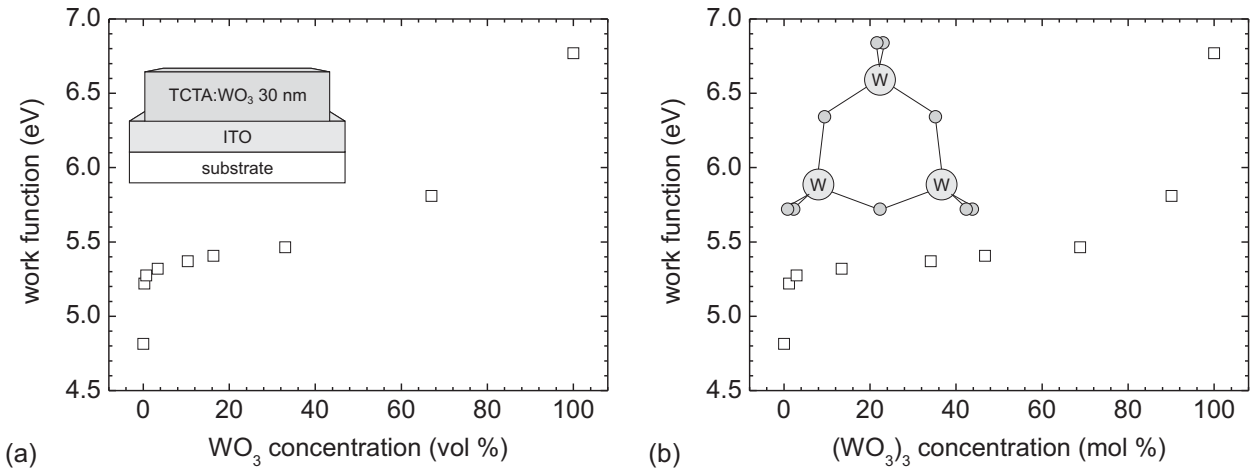

Figure 5.1: KP analysis of the doping concentration-dependent work function characteristics of TCTA:WO_3 on ITO. (a) WO_3 concentration given in vol %. Inset: layer sequence of analyzed structure. (b) $(WO_3)_3$ concentration given in mol %. Inset: geometry of WO_3 trimers according to [143, 144].

concentrations evoke an additional slight linear increase of the work function. At 67 vol % of the TMO within the doped layer, the work function characteristics, however, change due to the increasing interference with the bulk properties of WO_3. In the end, the work function again amounts to 6.75 eV for the neat TMO film.

In order to analyze the mechanism of doping, the knowledge of the respective amount of WO_3 incorporated into the organic film is of high importance. The thermal evaporation of MoO_3 from a Knudsen cell was analyzed by mass spectroscopy by Berkowitz *et al* [145]. They found that the major part of the vapor consists of $(MoO_3)_3$ clusters. That also applies to WO_3 due to the similar valence orbital structure of the transition metal atom and the preferential formation of trimers against other clusters as demonstrated by DFT calculations [143]. The inset of Figure 5.1b displays the energetically favored geometry of $(WO_3)_3$. Additionally, it was shown that the $(WO_3)_3$ clusters resemble the bulk oxide in its electronic structure independent of the level of clustering, and even the energetic band gaps of the tungsten and molybdenum anionic trimers correspond to those of the neutral bulk oxides so that no change in electronic structure is supposed [143,144]. Thus, in the following it is assumed that mainly $(WO_3)_3$ and $(MoO_3)_3$ clusters are incorporated in organic materials so that actually an electron transfer to trimers takes place by p-type doping. Accordingly, the abbreviations predominantly employed in this work, namely MoO_3 and WO_3 stand for the existence of trimers, which has to be considered in the declaration of the molar ratios. The material

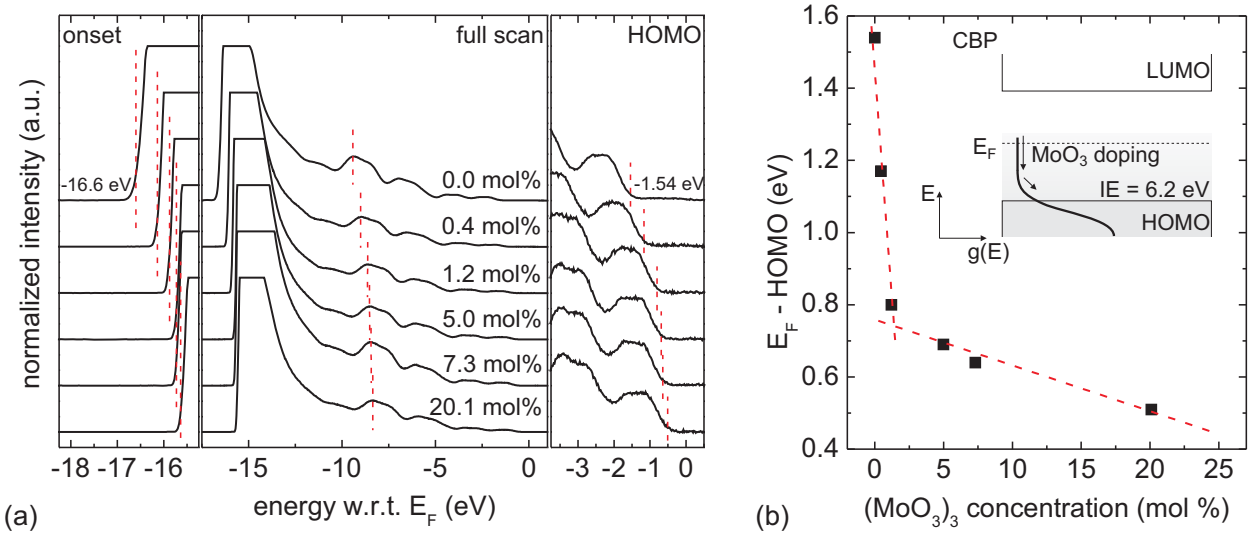

Figure 5.2: (a) UPS spectra of MoO_3 doped CBP layers deposited on ITO for various trimer concentrations. (b) Energy difference between Fermi level and HOMO edge versus trimer concentration. The dashed lines act only as visual guidelines. Inset: schematic of the Fermi level shift toward HOMO edge upon p-type doping of CBP.

density of evaporated WO_3 of about 6.5 g/cm^3 has been used for the calculation of the molar ratio [107], which is in this work generally expressed in terms of $[(WO_3)_3]/([(WO_3)_3] + [TCTA])$. As a result, Figure 5.1b displays the trimer concentration-dependent work function characteristic which is qualitatively the same as compared with the evolution shown in Figure 5.1a.

UPS measurements on MoO_3 (molecular weight[monomer]: 143.93 g/mole) doped CBP were done to further analyze the p-type doping and exclude the influence of bulk properties of the TMO on the Fermi level shift for increasing acceptor concentrations. The advantage over KP analysis is provided by the fact that not only the work function but also the valence states including the HOMO edge are recorded by UPS, telling more about the chemical constitution of the host material upon doping. A chemical reaction leading to the reorganization of the molecular orbital would be reflected in the UPS spectrum. Figure 5.2a shows the UPS spectra of 10 nm thick CBP layers doped by different concentrations of $(MoO_3)_3$ and deposited onto ITO. Thereby, the bulk density of amorphous evaporated MoO_3 was considered to be 4.1 g/cm^3 according to [9]. The center plot of 5.2a represents the full valence spectrum recorded on the He I line excitation. A magnified view on the photoemission onset region and the HOMO region of the spectra are displayed on the left and right side, respectively.

Again, the work function measured for the undoped organic film is attributed to the ITO layer and amounts to 4.62 eV corresponding to the secondary-electron cutoff at -16.6 eV with respect to the Fermi level. The HOMO edge is approximated to -1.54 eV and corresponds to a HOMO level at 6.16 eV which is in accordance with published values for CBP [123]. It can be observed that the whole valence spectrum shifts upon doping to lower energies indicating higher work functions and energetically constant HOMO levels. Furthermore, no significant change within the spectral features occurred upon doping so that a chemical reaction can be excluded. Even a molar doping concentration of 20.1 % does not convert the valence spectrum of CBP into that of the TMO which precludes the influence of bulk-like MoO_3 on the work function to this molar ratio. Figure 5.2b summarizes the results of the UPS measurements showing how the energy difference between the Fermi level E_F and the HOMO edge depends on the trimer concentration. Thereby, two different slopes have to be distinguished. For very low concentrations the Fermi level rapidly shifts to the hole transport level of the organic semiconductor. In the region between 1 and 2 mol % the slope decreases more or less abruptly, leading to a slower shift of the Fermi level for higher dopant concentrations. An explanation for this behavior is given by the consideration of the Gaussian-distributed density of states (DOS) at the HOMO level [101]. As discussed in Section 2.2.1, structural disorder in amorphous organic films causes energetic disorder due to locally varying polarization effects. This leads to the formation of the Gaussian-distributed DOS. The HOMO edge is usually positioned at the beginning of the tail states extending into the band gap as schematically depicted in the inset of Figure 5.2b. For this reason, holes generated by doping initially fill the tail states in the gap. Due to their low density *g(E)* they

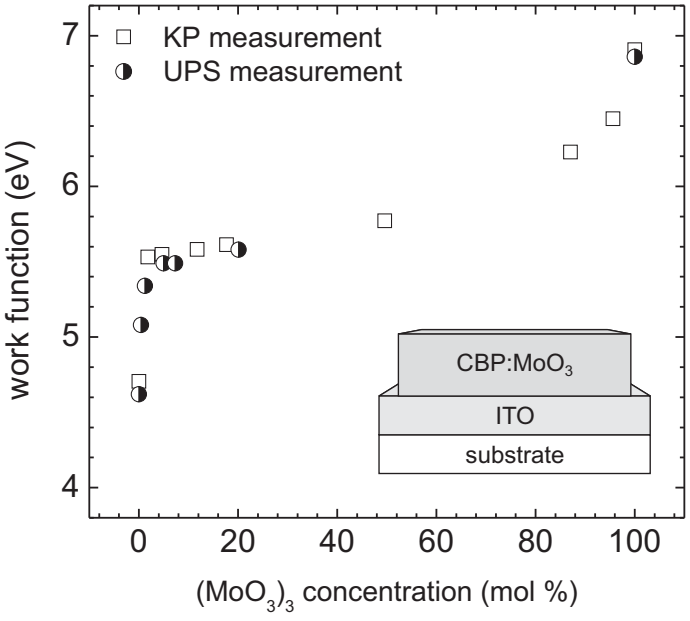

Figure 5.3: Work function of CBP:MoO_3 on ITO versus trimer concentration of the TMO analyzed by KP and UPS. Inset: layer sequence of analyzed structure. Note, the respective organic layer thickness was 10 nm at the UPS and exceeded 40 nm at the KP analysis.

are easily filled by the number of charge carriers. Consequently, the Fermi level rapidly shifts toward the HOMO edge. The density of tail states, however, shows a Gaussian increase upon approaching the HOMO level so that their filling requires an increasingly higher number of generated free charge carriers. Accordingly, the Fermi level shifts only slightly in the second part at higher doping concentrations. Thus, an apparent Fermi level pinning occurs at 0.5 eV above the HOMO edge of CBP.

Finally, Figure 5.3 compares the work function characteristics obtained by UPS and KP measurements, respectively. Note that the KP analysis was made on MoO_3 doped CBP layers having an integral thickness of more than 40 nm. The very good correlation of the results again certifies the KP analysis to be an appropriate tool for the examination of electrochemical doping.

5.1.2 Impact of P-Type Doping on the Properties of CBP

After the demonstration of p-type doping by MoO_3 via KP analysis and UPS, its impact on the electrical, morphological and optical properties of CBP will be discussed in the following. Most notably, an increase of the conductivity with higher doping concentrations has to be expected due to elevated free charge carrier densities. The device structure comprising a 50 nm thick CBP and two 5 nm thick MoO_3 layers (already shown in Figure 4.5b) has been used to analyze the relationship between $(MoO_3)_3$ concentration and conductivity. As discussed in Section 4.2.1, the deposition of the neat MoO_3 layers at both electrodes leads to a negligible built-in voltage in those hole-only devices. Accordingly, the *I-V* characteristics of the device directly correlate with the applied voltage. The voltage drop, thereby, has been completely attributed to occur at the (un)doped CBP layer. Figure 5.4a shows the resulting characteristics of current density versus electric field for various doping concentrations. Upon the addition of MoO_3, the current of the device is increased by about four orders of magnitude in the low bias regime. At low electric fields the doping-induced free hole density largely outnumbers the charges that are injected from the contacts leading to an Ohmic current. Accordingly, the value of the conductivity for each doping concentration can be simply obtained out of the slope of the current density characteristics. Figure 5.4b summarizes the conductivities including the value for the neat MoO_3 layer of around 4 x 10^{-7} S/cm. Similar to the work function characteristics discussed in the previous section, two different slopes can be distinguished. The inset of Figure 5.4b shows that at low doping concentrations the conductivity increases superlinearly as clearly indicated by the double-logarithm plot and the linear fit of the values yielding a slope of 2.7. In the second regime, from approximately 2 mol % up to higher doping concentrations of around 20 mol %, the conductivity increases

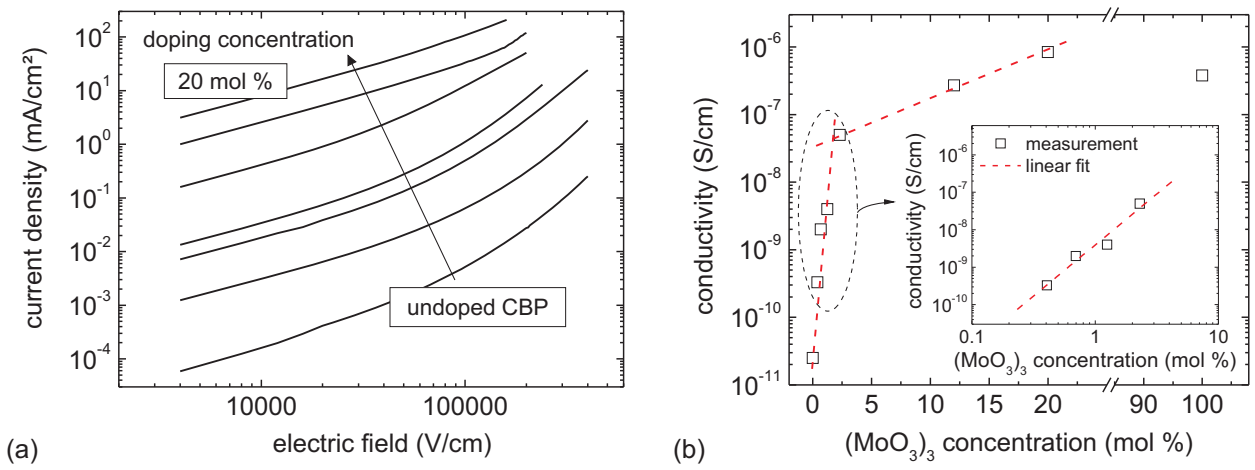

Figure 5.4: Electrical characteristics of hole-only devices comprising 50 nm thick CBP:MoO_3 layers for various doping concentrations (device structure shown in 4.5b). (a) Current density versus external electric field characteristics. (b) Conductivity versus $(MoO_3)_3$ concentration. The dashed lines are guidelines. Inset: double-logarithm plot and linear fit of the values for low doping concentrations.

only linearly and slightly exceeds the value of the neat TMO film.

The superlinear increase of the conductivity σ at low doping concentrations has been already shown for the p-type doping of organic small molecule materials and polymers and is mainly explained by the concomitant elevation of the free hole density and charge carrier mobility [146–148]. The filling of energetically deep-lying tail states by doping-induced holes lowers their influence on the current by trapping charge carriers and consequently leads to an increase of the overall mobility. Additionally, the Fermi level successively shifts toward the transport level as seen in the previous section, so that the hopping rate increases due to the increased density of states. The comparison of the mobilities for different doping concentrations in this examination indicates similar characteristics. In anticipation of the results of Section 5.3.2 regarding the free hole density p in CBP:MoO_3 it is possible to roughly estimate the mobility μ according to

$$\sigma = pq\mu. \tag{5.1}$$

For instance, the mobility yields 2 x 10^{-7} cm^2/Vs for a charge carrier density of about 1.5 x 10^{18} cm^{-3} at a doping concentration of 2.3 mol %, whereas the mobility only amounts to 3.3 x 10^{-10} cm^2/Vs for a charge carrier density of about 3 x 10^{17} cm^{-3} at 0.4 mol %. These values, however, are significantly lower than the hole mobility of the undoped CBP layer which was reported to be at 2 x 10^{-3} cm^2/Vs [140]. The comparison of the carrier

mobility in the organic polymer RR-P3HT by both field-effect and electrochemical doping indicated an additional lowering influence of more than three orders of magnitude on the mobility for the latter mechanism of charge carrier creation [149]. As opposed to the mere injection of charge carriers into the bulk material, Coulomb potentials of dopant ions are formed upon charge transfer from host to acceptor molecules. Accordingly, although charge carriers are induced by the doping mechanism, they possibly remain trapped at the host molecules due to the Coulomb attraction by the ionized dopants. This leads to the formation of charge transfer complexes rather than free carriers. The Coulomb trapping is facilitated by the low dielectric constant of organic materials of $\epsilon \approx 3$ hampering the dissociation of the charge transfer complexes due to the long range of the Coulomb potential. At higher doping concentrations, however, the Coulomb potentials increasingly overlap with each other leading to a smoothing of the "potential landscape" and accordingly, to a relaxed impact of charge trapping [39]. For this reason, the mobility starts to increase steeply. At very high molar doping ratios the mobility is expected to decrease, since the increasing amount of dopant molecules causes a larger distance between the host molecules which lowers the hopping rate of charge carriers. In summary, the mobility of doped CBP layers initially drops to significantly lower values and steeply increases for higher doping concentrations. The characteristics of the charge carrier density upon doping will be discussed in detail in Section 5.3.2 and 5.4.

The model of Coulomb trapping can also be expressed by the width of the DOS. The insertion and ionization of dopant molecules induces Coulomb potentials. Still, it depends on the nature of the intrinsic DOS of the host material whether the Coulomb potentials cause a broadening of the intrinsic DOS corresponding to the introduction of additional deep trap states which would lower the mobility. Amorphous organic materials already exhibit a DOS with a significant width due to energetic disorder. Thus, the effect of additional Coulomb trapping is expected to be lower than for crystalline materials possessing a narrow intrinsic DOS [39]. Actually, a neat layer of CBP deposited on ITO seems to be polycrystalline as indicated by the atomic force microscopy (AFM) image of its surface shown in Figure 5.5a. The rms roughness is approximately 3.1 nm. Additionally, the formation of grain-like domains in the dimension of 0.5 x 0.5 μm^2 is clearly observed. Figure 5.5b indicates that a doping concentration of 1.8 mol % by MoO_3 already leads to a significant change of the surface morphology. Though the rms roughness stays high at 3-4 nm, the grain structures shrink in the planar dimensions with a higher doping concentration as shown by the AFM images in Figure 5.5b and c where the molar ratio of dopant to host+dopant molecules reaches 17.7 %. In contrast, a neat MoO_3 layer is completely amorphous and exhibits a small rms roughness of approximately 1.4 nm as displayed in Figure 5.5d. Note that this

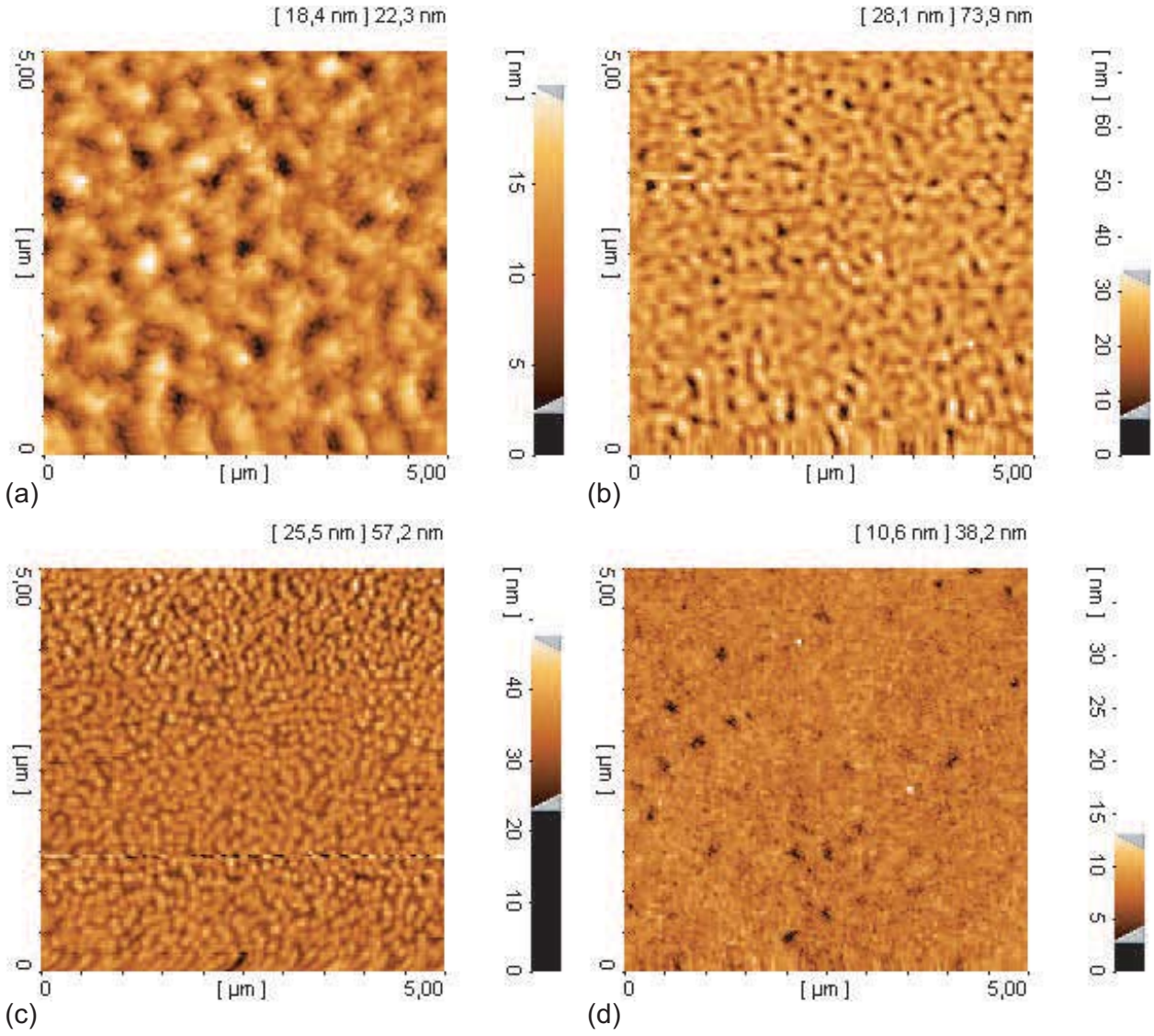

Figure 5.5: 5 x 5 μm^2 AFM images of (a) a neat CBP layer, (b) a CBP layer doped by 1.8 mol % of MoO_3, (c) a CBP layer doped by 17.7 mol % of MoO_3 and (d) a neat MoO_3 layer. All layers were deposited on ITO and measured in ambient air.

layer is also deposited onto ITO so that the surface structure is partially a consequence of the morphology underneath. Accordingly, the change in morphology could additionally influence the charge carrier mobility for different doping concentrations.

The change in morphology is accompanied by a change of the refractive index. In Figure 5.6a, the refractive indices at 550 nm spectral wavelength of CBP layers with varied doping concentrations including the neat CBP and MoO_3 films are summarized. All films

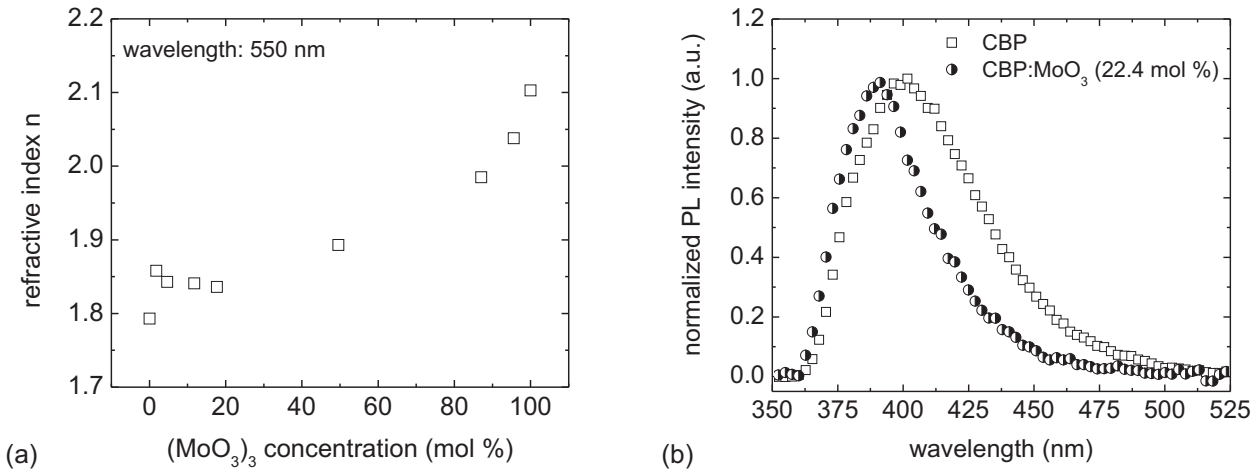

Figure 5.6: (a) Refractive index at 550 nm spectral wavelength versus doping concentration of CBP:MoO_3 layers on Si substrates. (b) Normalized PL spectra of a neat CBP layer and a MoO_3 doped CBP (22.4 mol %) film. Note that the absolute values of the PL intensity of the doped CBP layer decreased to around 2 % of the initial values given for the neat layer.

were deposited on cleaned Si substrates and measured by ellipsometry. The mutation of the morphology at already low doping concentrations of around 2 mol % observed in the AFM images is also expressed by the abrupt rise of the refractive index from 1.8 for the neat CBP film to 1.86. This change indicates the formation of a bulk material with a slightly higher density. The refractive index then remains constant for higher doping concentrations up to 20 mol % and again starts to increase at a molar ratio of 50 % due to the elevated amount of MoO_3 within the mixed layer. The refractive index of the neat TMO film has been determined to be 2.1 at 550 nm wavelength.

The p-type doping of CBP by MoO_3 also has an influence on the absorption and emission properties of the host material. As already discussed in Section 4.2.3, luminescence quenching is caused by doped organic layers or even neat TMO films deposited in the vicinity of the emission zone. Accordingly, their impact on the emission characteristics can be easily studied by PL analysis. Figure 5.6b compares the normalized PL intensities of a non-doped and doped CBP layer. Both have a thickness of 50 nm and were excited by a cw HeCd laser at $\lambda = 325$ nm in vacuum. The PL intensity of the neat CBP layer at its peak emission wavelength of around 402 nm decreases to 2 % of the initial value for the 22.4 mol % doped film. Moreover, the PL emission spectrum of CBP:MoO_3 appears to be slightly blue shifted and narrowed. Accordingly, an additional wavelength-dependent exciton quenching takes place which was also observed at early stages of electrochemical doping of polymers [126].

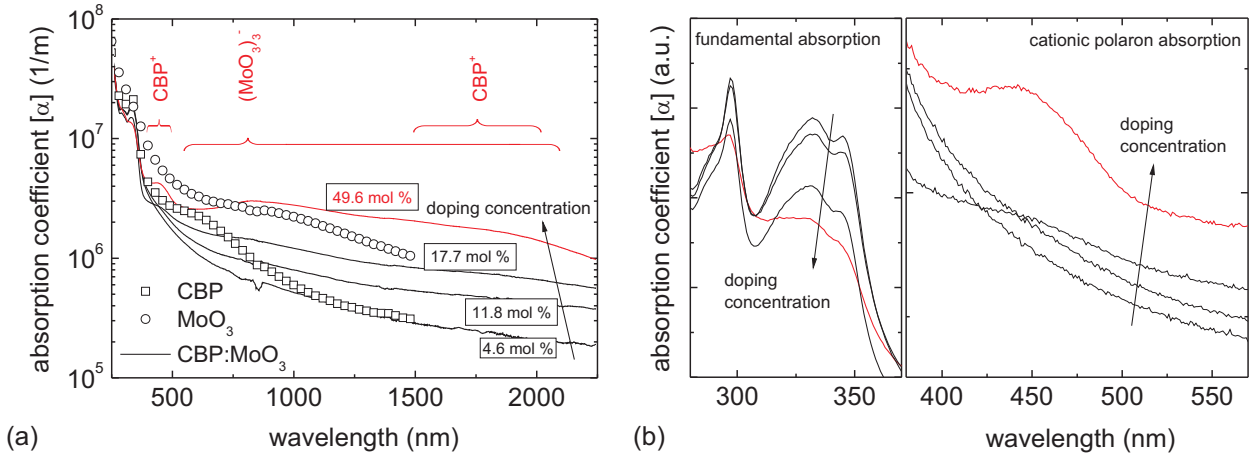

Figure 5.7: UV-Vis-NIR absorption spectra of MoO_3, CBP and MoO_3 doped CBP layers with varying doping concentration. The spectrum of the CBP layer with the highest doping concentration is highlighted by using another color. (a) UV-Vis-NIR spectra. The spectral absorption features of the sample with the highest doping concentration are assigned to the respective polarons. (b) Magnified view on the UV-Vis spectra from 280 to 570 nm.

This has to be attributed to the formation of charge transfer complexes between the host and acceptor molecules. The transfer of an electron from the HOMO level of CBP into the conduction band of MoO_3 corresponds to the generation of a cation and anion, respectively. These ions polarize the surrounding neutral molecules and concomitantly lower the potential energy of the charge carriers as discussed in Section 2.1. Considering the ion as a polaron, two different polaron absorption features arise and are usually located in the near-infrared and visible regions of the spectrum, respectively [128]. Assuming a Förster transfer between excitons and polarons [130, 131], it is evident that the spectral overlap of their emission and absorption spectrum determines the quenching efficiency. Accordingly, an additional polaron absorption band around 400 to 500 nm is supposed to be the reason for the qualitatively lower PL intensity in this region for the doped CBP layer.

To obtain more detailed information about the optical properties of the doped CBP layers compared to those of the neat films of CBP and MoO_3, their UV-Vis-NIR absorption spectra were measured. Figure 5.7a shows the spectra using the absorption coefficient as a measure which is free from variations due to slightly different film thicknesses around 40 to 60 nm. All layers were deposited on borofloat-glass substrates and their absorption spectra were obtained using an uncoated substrate as reference. First, Figure 5.7a demonstrates that the neat CBP layer exhibits a lower absorption coefficient than the TMO film for almost

all spectral wavelengths. Moreover, CBP seems to possess an additional absorption band between 500 and 1000 nm as opposed to the doped CBP layers. However, this should be attributed to a strong scattering due to its polycrystalline structure rather than being a real material absorption. As already demonstrated by the AFM measurements in Figure 5.5, its morphology abruptly changes upon doping by MoO_3 leading to an apparently lower absorption. By raising the doping concentration from 4.6 mol % to 49.6 mol %, the absorption coefficients increase within a broad spectral range from 500 nm to more than 2000 nm and partially exceed those of the neat MoO_3 film. At the same time, the fundamental absorption of CBP expectedly diminishes as indicated by the magnified view on the spectrum around 300 to 350 nm in Figure 5.7b. Addionally, a polaron absorption band can directly be observed around 400 to 500 nm for highly doped CBP layers with a doping molar concentration ratio of 17.7 and 49.6 % shown in the right part of Figure 5.7b. A similar absorption feature at these spectral wavelengths has been observed for several TMO doped organic hole transport layers and is attributed to the formation of charge transfer complexes [136–138]. The assignment of the respective absorption band to the cation or anion of the charge transfer complex is only possible with comparative polaron absorption measurements on hole-only or electron-only devices [150]. Such a measurement on S-2CBP, which is a derivative of CBP, delivered a polaron absorption feature with a maximum polaron cross section at approximately 500 nm [151] in the case of the injection of holes into the layer. Accordingly, the polaron absorption band around 400 to 500 nm observed in the UV-Vis-NIR measurements must be attributed to the cation of CBP. The existence of a second cationic absorption feature located in the NIR region of the spectrum has been also reported in several publications about TMO doped organic HTLs [135, 137, 138]. In the present case of MoO_3 doped CBP, such a signal is only weakly visible from 1500 to 2000 nm for the sample with the highest doping concentration due to the superimposition by the broad absorption spectrum of the counterion $(MoO_3)_3^-$. Its maximum wavelength is located at 825 nm and therefore could be attributed to the photochromic absorption band of MoO_3, which actually should increase in intensity with a higher doping concentration and concomitant electron transfer to the TMO molecules. A similar absorption spectrum of WO_3 doped 2-TNATA was shown by Chang *et al.* without discussing the three spectral features observed there [17]. Accordingly, the study of the optical absorption of MoO_3 doped CBP proved that a charge transfer upon p-type doping occurs leading to the formation of anionic $(MoO_3)_3$ and cationic CBP which additionally quenches the excitons in the range from 400 to 500 nm.

5.2 N-Type Doping of CBP by Cs_2CO_3

After having demonstrated the p-type doping of CBP by MoO_3 in the previous sections, the n-type doping of the same host material by Cs_2CO_3 will be discussed in the following. It has already been shown that ambipolar materials such as Pentacen and ZnPc allow for the p- and n-type doping by organic acceptors and donors, respectively [50, 52]. An unintentionally doped layer of Pentacen showing properties of a hole transport layer was successfully n-doped by $CoCp_2^*$ changing the polarity of majority carriers within the bulk material from positive to negative [82]. Moreover, it has been demonstrated by improved *I-V* characteristics of electron-only devices that MADN, as another ambipolar material, can be n-type doped by Cs_2CO_3 [152]. To further verify the mechanism of n-doping by the Cs salt, a short analysis of the electronic properties of CBP upon doping with Cs_2CO_3 will be given first. This is all the more important due to the controversial discussion going on about the origin of the doping effect by the Cs salt. Therefore, a further attempt to clarify this issue will be demonstrated by photoelectron spectroscopy, taking the current reports on the potential mechanism of the n-type doping into account. Finally, the impact on the properties of CBP upon doping with Cs_2CO_3 will be demonstrated.

5.2.1 Analysis of N-Type Doping by UPS, IPES and KP

According to the effects on the electronic characteristics upon p-type doping obtained in Section 5.1.1, a corresponding Fermi level shift toward the electron transport level should be expected by the donor insertion indicating the filling of the energetically deeper-lying tail states by electrons. Figure 5.8a shows the work function characteristics of a CBP layer measured by KP method depending on its thickness. The deposition of a non-doped CBP film on ITO provides a small work function shift from 4.6 to 4.8 eV within the first 5 Å which is attributed to a negligible interface dipole. Even thicker layers of CBP up to 140 Å do not induce a significant work function shift due to the small intrinsic charge carrier density within the bulk material. However, the subsequent evaporation of Cs_2CO_3 doped CBP leads to a thickness-dependent work function shift towards lower values. Considering the material density of the dopant of 4.07 g/cm^3 [153] the mixed layer exhibited a molar concentration of 10.2 %. The work function drops by 1.4 eV upon deposition of only 15 Å of the doped layer and saturates at around 2.3 eV after the evaporation of an additional 190 Å thick film. Apparently, the Fermi level shifts toward the vacuum level at 0 eV as a consequence of the n-type doping. Comparing the saturated work function with the commonly reported LUMO level of CBP of around 3.2 eV [123, 154], the discrepancy of these values becomes obvious. Such a relation between Fermi and electron transport level is only known for

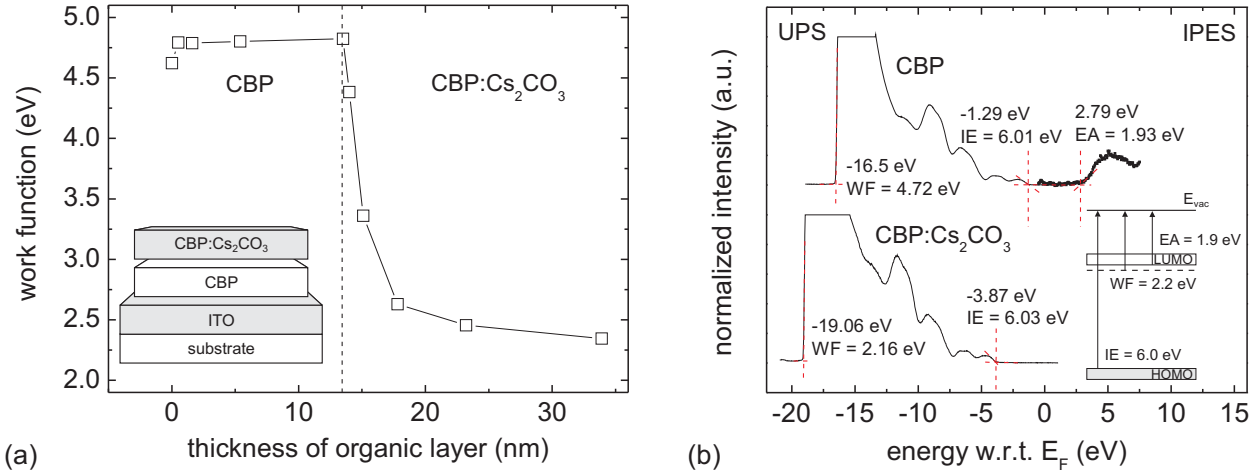

Figure 5.8: (a) Thickness-dependent work function characteristics of undoped and Cs_2CO_3 doped CBP layer on ITO measured by KP. Inset: layer sequence of analyzed structure. (b) UPS and IPES spectrum of undoped and UPS spectrum of Cs_2CO_3 doped CBP layer on ITO. Inset: schematic of the electronic structure of CBP:Cs_2CO_3.

inorganic semiconductors defined as degenerate due to very high doping concentrations [34]. The origin of this discrepancy originates from the erroneous calculation of the LUMO level by subtracting the optical band gap energy (3.1 eV) from the IE (6.3 eV) of CBP. Therefore, UPS and IPES measurements were conducted to clarify the energetic relation of Fermi und LUMO levels in Cs_2CO_3 doped CBP. Figure 5.8b displays the UPS spectra of 20 nm thick doped and 7.5 nm thick undoped CBP layer as well as the IPES spectrum of the latter film deposited on ITO. Referring to the neat film of CBP, the secondary-electron cutoff of the UPS spectrum at -16.5 eV corresponds to a work function of 4.72 eV which is again attributed to the ITO layer and the small dipole formed at its surface. The HOMO edge at -1.29 eV indicates an IE of 6.01 eV which is slightly lower than the value reported in Section 5.1.1, still lying in the range of uncertainty of UPS measurements as denoted in Section 3.3.1. The most interesting feature is given by the IPES spectrum. The LUMO edge is thereby determined at 2.79 eV w.r.t. E_F corresponding to an EA of about 1.93 eV. Accordingly, the transport band gap is approximately 1 eV larger than the optical band gap. Note however that UPS and IPES are surface sensitive techniques and do not reflect the polarization effects within the bulk material. Therefore the transport band gap energy is slightly larger at the surface than in the bulk material [63]. The whole UPS spectrum of the n-type doped layer with a molar ratio of 24 % of Cs_2CO_3 to CBP+Cs_2CO_3 is shifted by 2.56 eV to higher binding energies compared to that of the undoped layer indicating a strong n-type doping effect. The slightly

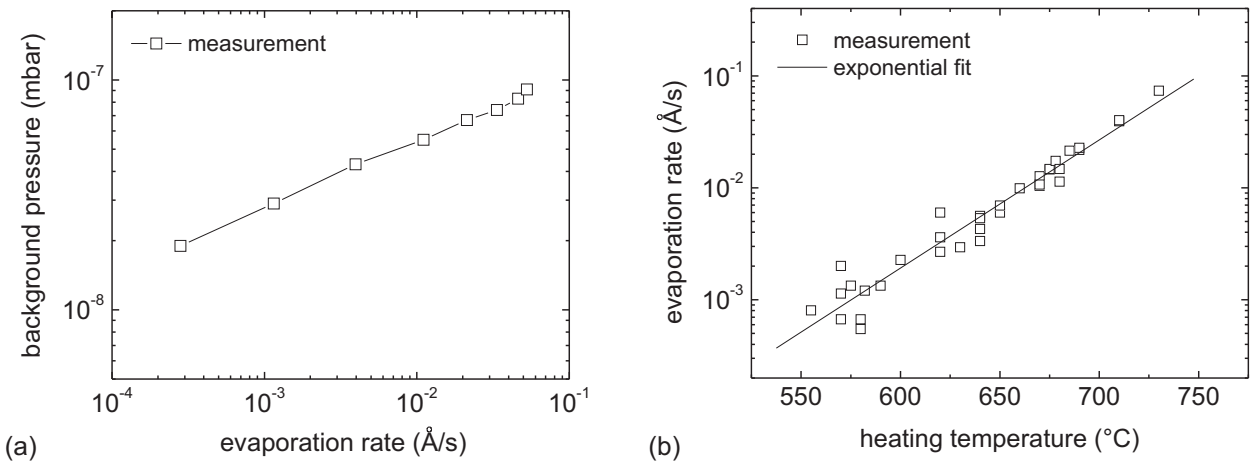

Figure 5.9: Thermal evaporation of Cs_2CO_3 in the UHV chamber. (a) Background pressure versus evaporation rate. (b) Heating temperature-dependent characteristics of the evaporation rate.

smaller work function obtained by photoelectron spectroscopy compared to that measured by KP is due to the higher doping concentration moving the Fermi level further toward the LUMO level. Accordingly, the Fermi level is pinned approximately 0.2-0.3 eV below the LUMO edge, assuming no change of its energetic position upon doping (similar to the HOMO edge of the doped film remaining almost constant at 6.03 eV). The schematic of the electronic structure of CBP:Cs_2CO_3 in the inset of Figure 5.8b summarizes the results.

Neither additional gap states as observed for high doping concentrations in BCP:Li or Alq_3:Cs layers [56, 59] nor other indications of spectral modification upon doping were observed within the UPS analysis. That raises the question of how the n-type doping by the Cs salt actually occurs. The Cs-derivative comprises two Cs cations (2 Cs^+) and one doubly charged carbonate anion ($CO_3{}^{2-}$) per molecule, so that an electron transfer could be only expected from the latter ion to the organic molecules. However, Li *et al.* demonstrated via quartz crystal microbalance analysis that the vacuum thermal deposition of Cs_2CO_3 leads to a decomposition of the Cs salt as opposed to the evaporation of other thermally stable electron injection materials such as LiF and CsF [155]. They proposed a reaction equation in which Cs_2CO_3 decomposes to metallic Cs and molecular oxygen as well as carbon dioxide. The metallic Cs is assumed to form a low electron injection barrier at the cathode interface when evaporated onto the organic layer. Figure 5.9a shows the relationship between the background pressure measured by a highly sensitive full-range vacuum gauge and the evaporation rate of Cs_2CO_3 determined by a calibrated quartz crystal microbalance in the evaporation

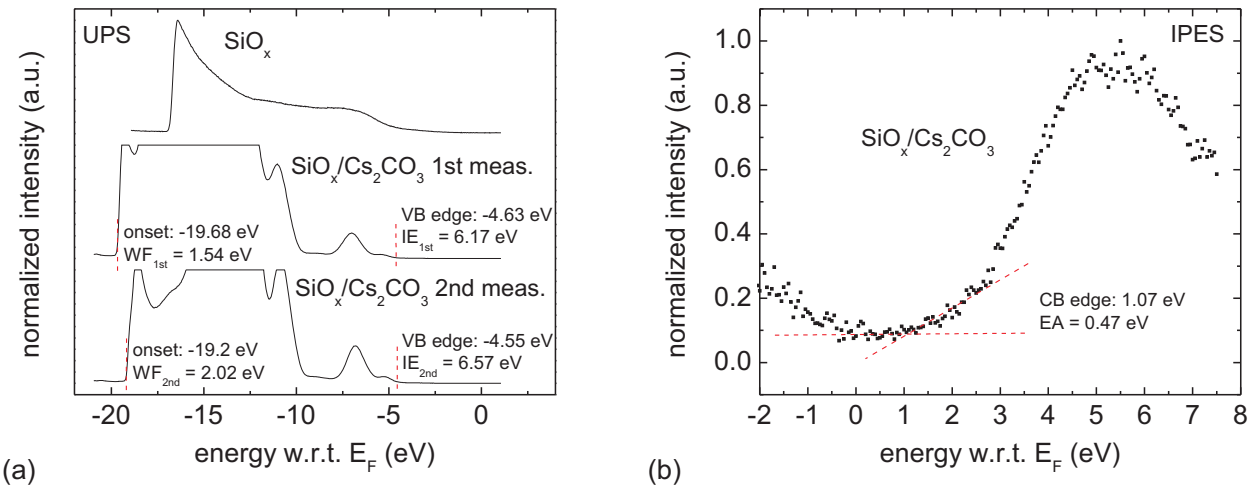

Figure 5.10: Thermal evaporation of Cs_2CO_3 on SiO_x. (a) UPS spectra of Si substrate and of a thin film of Cs_2CO_3 at two different points in time. (b) IPES spectrum of Cs_2CO_3. Note that EA has been calculated by using $WF_{1st} = 1.54$ eV.

chamber used for n-type doping in this work. Actually, the pressure increases by almost one order of magnitude for ascending evaporation rates from 3 x 10^{-4} Å/s to 5 x 10^{-2} Å/s . This increase in background pressure is significant and very high compared to the evaporation of organic materials or transition metal oxides and could also be seen as indicator for the decomposition of Cs_2CO_3 during thermal evaporation. Note that these characteristics are obtained within the same run and could slightly deviate quantitatively depending on the respective base pressure at the beginning and the conditions at the co-evaporation with organic materials. The temperature-dependent evaporation rate characteristics of Cs_2CO_3 are shown in Figure 5.9b. The characteristics have been found to follow an exponential growth given by the equation

$$y = A \times 10^{Bx} \tag{5.2}$$

where A and B represent constants obtained by the fit. The standard deviation of the measured evaporation rates increases at lower temperatures possibly indicating a change in the decomposition process or at least the measuring limit of the quartz crystal method. Therefore, UPS and IPES measurements were conducted on the evaporated species of Cs_2CO_3 to shed more light on this issue.

Figure 5.10a shows the UPS spectra obtained from the clean surface of a Si substrate and from a 22.5 Å thick film of the Cs_2CO_3 species deposited on this sample and recorded by the excitation with the He I line at two different points in time. The UPS spectrum of the

Si substrate basically stems from the native oxide which is inevitably formed prior to the insertion into the UHV system. It changes upon evaporation of the Cs_2CO_3 species, clearly indicating the sticking of and coverage by the n-type dopant. First of all, no signal around the Fermi level is observed in the two measurements. Assuming the decomposition into metallic Cs, an exponential signal characteristic corresponding to the Fermi edge would have been expected around the binding energy of 0 eV. Accordingly, the observation casts some doubt on the published hypothesis about the decomposition process. In fact, other groups reported on the decomposition of Cs_2CO_3 into Cs_2O and several suboxides such as cesium peroxide (Cs_2O_2) leading to an n-type doping of the cesium oxide semiconductor and very low work functions in the range of 1 and 2.2 eV [156,157]. Not only the evaporation but also the thermal annealing of solution-processed Cs_2CO_3 at 150°C supposedly causes its decomposition into the n-type doped semiconductor improving the performance of organic solar cells by the work function modification at the cathode [156]. The UPS spectra shown in Figure 5.10a also provide a low work function of $WF_{1st} = 1.54$ eV in the first measurement and $WF_{2nd} = 2.02$ eV in a further measurement conducted approximately 18 hours later after the storage of the sample within the analysis chamber. The variation in work function could be compared with observations made by Cs oxidation. Based on those experiments, the work function depends on the extent of O_2 exposure leading to different stages of Cs oxide formation and respective inclusion of oxygen below the layer surface [158]. Consequently, a degassing of the sample could have occurred overnight. Considering the UPS spectrum of the first measurement in Figure 5.10a, the valence band edge at -4.63 eV with respect to the Fermi level corresponds to an IE of 6.17 eV. At the same time, the IPES measurement shown in Figure 5.10b provides a conduction band edge at 1.07 eV. Referring to the first UPS spectrum of the Cs_2CO_3 layer with $WF_{1st} = 1.54$ eV, this value corresponds to an extremely low EA of 0.47 eV. For this reason, the electronic structure indicates a heavily n-type doped semiconductor in which the Fermi level lies only 1.1 eV below the EA. Huang *et al.* demonstrated by thickness and substrate variation that the low work function is an intrinsic property of the evaporated Cs_2CO_3 layer and not a surface phenomenon given by any interface dipoles [156]. On the other hand, using UPS on a Cs_2CO_3 layer deposited on a cleaned Ag surface, they found an IE of about 3.9 eV, which completely differs from the value obtained in this work. Additionally, not only was the work function apparently changed upon storage in the analysis chamber, but also the electronic structure since the determination of the IE afterwards provided a higher value by 0.4 eV as also shown in Figure 5.10a. Assuming instability of the Cs oxide species as indicated by this experiment, it is possible that the highly energetic photon and electron radiation used in the UPS and IPES could also influence the chemical bonds of Cs to oxygen. Finally, it has to be noted that Wu *et al.* found qualitative differences in the valence spectra

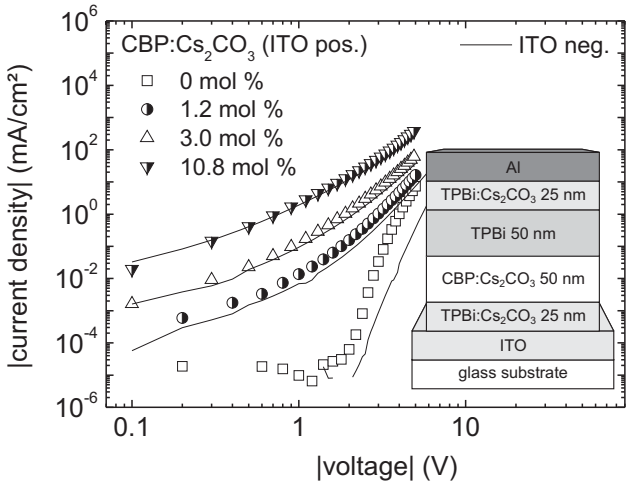

Figure 5.11: Current density versus voltage characteristics of an electron-only device comprising a Cs_2CO_3 doped CBP layer with various doping concentrations. The solid lines denoted as "ITO neg." correspond to the respective I-V characteristics for negative bias applied on ITO. Inset: layer sequence.

obtained for evaporated Cs_2CO_3 and Cs_2O by UPS and observed a clear signal from carbon in x-ray photoelectron spectroscopy measurements on evaporated Cs_2CO_3 layers as opposed to the analysis of oxidized Cs [155]. Thus, they concluded that no decomposition of Cs_2CO_3 takes place upon evaporation. The decomposition and formation of Cs cations would only occur in contact with organic molecules like Alq_3 leading to its n-type doping [155, 159].

In conclusion, it remains difficult to specify unambiguously the n-type doping mechanism upon co-evaporation with Cs_2CO_3. For reasons of simplicity, the molar doping concentrations of Cs_2CO_3 will be given by assuming no decomposition of the n-type dopant in the following. It is all the more important to further prove the n-type doping by the Cs salt with the help of additional analysis in the next sections.

5.2.2 Impact of N-Type Doping on the Properties of CBP

The influence of n-type doping on CBP can be simply demonstrated by I-V characteristics of electron-only devices. Its layer sequence is given in the inset of Figure 5.11. In this case, 25 nm thick Cs_2CO_3 doped layers of TPBi are deposited adjacent to the electrodes to reduce the built-in voltage, assuming the formation of sufficiently thin depletion layers which can be easily tunneled by electrons. The molar doping concentration ratio for the doped TPBi layers amounts to more than 13 %. Additionally, a 50 nm thick undoped film of TPBi is deposited onto the equally thick CBP film to ensure an electron-only charge transport through the device. As indicated by Figure 5.11 the current densities increase with higher doping concentrations of Cs_2CO_3 in CBP. In the case of an undoped CBP layer, the quasi-Ohmic region at low voltages up to 1.1 V is absent. This is in contrast to the situation of the electron-only devices comprising a doped CBP film. This can be explained by the concurrent absence of a Fermi level alignment at the interfaces of TPBi:Cs_2CO_3/CBP

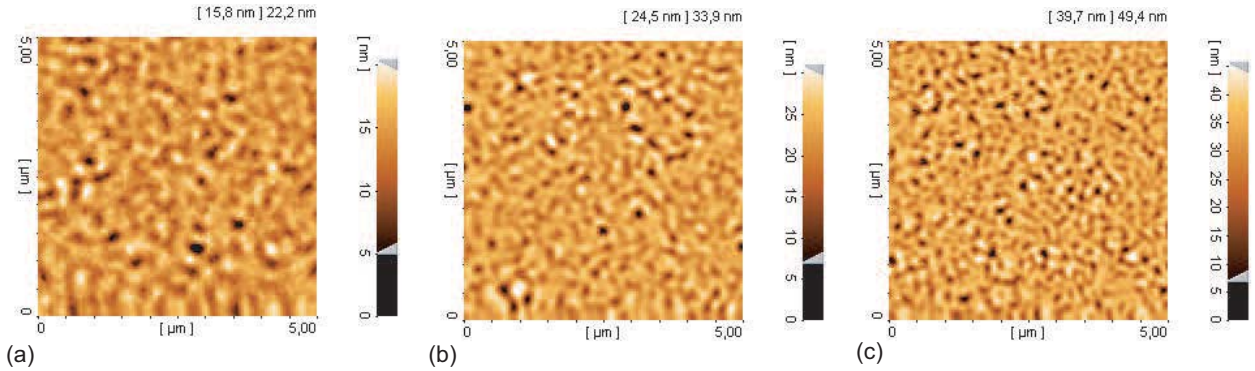

Figure 5.12: 5 x 5 μm^2 AFM images of CBP:Cs_2CO_3 layers having a doping concentration of (a) 1.1 mol %, (b) 3.1 mol % and (c) 11.9 mol %. All layers were deposited on ITO and measured in ambient air.

and TPBi/TPBi:Cs_2CO_3. The situation already changes for a low doping concentration of 1.2 mol % which seems to be sufficient for the formation and pinning of the Fermi level within the 50 nm thick CBP film. Furthermore, comparing the *I-V* characteristics for positive and negative bias applied to the ITO bottom contact, it is obvious that they become absolutely symmetric for higher doping concentrations.

The electrical measurements were conducted in a nitrogen-box, since the n-type doped electron-only devices tend to degrade very fast in ambient air leading to irreproducible *I-V* characteristics. The degradation originates from the hygroscopicity of Cs and its compounds such as cesium carbonate or cesium oxide [160, 161] and is also reflected in the surface morphology of the n-type doped layers. Figure 5.12 shows 5 x 5 μm^2 sized AFM images of 65 nm thick CBP:Cs_2CO_3 layers with various doping concentrations deposited on ITO coated glass substrates. The AFM images were taken in ambient air. Similar to the p-type doping by MoO_3, the polycrystalline appearance of the CBP surface slightly changes already at a small doping concentration of Cs_2CO_3 of only 1.1 mol %. Comparing Figure 5.12a with Figure 5.5a showing the surface of the undoped CBP layer, the grain-like domains obviously shrink to smaller dimensions below 0.25 x 0.25 μm^2. However, as opposed to the p-type doping, higher concentrations of Cs_2CO_3 additionally cause a higher roughness probably due to the adsorption of moisture. The rms roughness yielded values of about 2.4 nm, 3.5 nm and 6.4 nm for the CBP:Cs_2CO_3 layers having a molar doping concentration ratio of 1.1 %, 3.1 % and 11.9 %, respectively. Accordingly, the risk of leakage current and degradation of organic materials by moisture rises in ambient air and should be avoided by encapsulation.

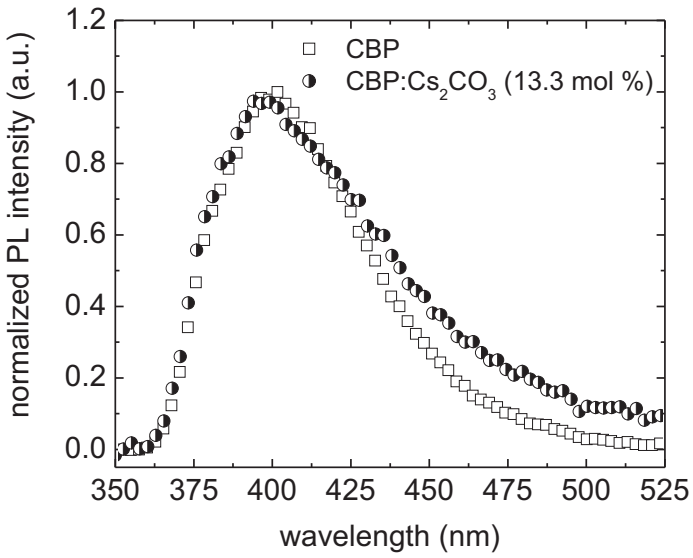

Figure 5.13: Normalized PL spectra of a neat CBP layer and a Cs_2CO_3 doped CBP (13.3 mol %) film. Note that the absolute values of the PL intensity of the doped CBP layer decreased to around 20 % of the initial values given for the neat layer.

Expectedly, the n-type doping of CBP by Cs_2CO_3 causes exciton quenching as observed in PL measurements. The PL intensity of the neat CBP layer decreased to 20 % of the initial value at its peak emission wavelength at 402 nm upon doping by Cs_2CO_3 with a concentration of 13.3 mol %. Compared to the p-type doping via MoO_3, the drop in intensity is low and hardly wavelength-dependent as indicated in Figure 5.13. Accordingly, the polaron absorption features induced by the formation of charge transfer complexes seem to be spectrally displaced compared to the p-doped CBP layer, where the cations evidently caused an additional exciton quenching around 400-500 nm as shown in Figure 5.7 in Section 5.1.2.

5.3 Determination of Excess Charge Carrier Densities in Doped Organic Semiconductors

The knowledge of the doping-induced excess charge carrier density in organic materials is of high importance for the determination of the respective doping efficiency. As demonstrated in the previous sections, not only electrical but also optical and electronic properties of CBP changed upon doping. Therefore, different methods for the determination of the free charge carrier densities exist in principal. Referring to the *I-V* characteristics of doped layers, the charge density could be extracted out of the slope of the conductivity versus the applied electric field if the mobility is known. However, as seen in Section 5.1.2, the mobility itself changes upon variation of the doping concentration and must be determined together with the respective conductivity. Recently, the dependency of the charge carrier mobility on the carrier density has been derived from a numerical solution of the master equation for hopping transport in a disordered material with Gaussian density of states [162]. The parameterization of the numerical data allows for the determination of the mobility and of

the charge carrier density from the characteristics of the space-charge limited current. On the other hand, the influence of the change in morphology on the electric characteristics upon doping is not included, though potentially playing a role in CBP and other organic semiconductors as discussed in Section 5.1.2.

Another possibility for the determination of charge carrier densities is to look at the electronic properties of the doped organic material. For instance, the energetic position of the Fermi level E_F relative to the conduction band minimum E_C is directly associated with the doping-induced free electron density in inorganic semiconductors according to

$$n = N_C \ \exp\left(-\frac{E_C - E_F}{kT}\right), \tag{5.3}$$

where N_C represents the effective density of states in the conduction band. This equation is only valid in Boltzmann-approximation for nondegenerate semiconductors and for the assumption of the ionization of all donors leading to the equal amount of electron density n [34]. Considering the Gaussian-distributed density of states *g(E)* for organic materials

$$g(E) = N_M \frac{1}{\sqrt{2\pi{\sigma_d}^2}} \ \exp\left(-\frac{E^2}{2{\sigma_d}^2}\right), \tag{5.4}$$

where σ_d represents the standard deviation and N_M the molecular density of the respective semiconductor, the electron density is given more precisely by

$$n = \int g_L(E)F(E)dE = \int N_M \frac{1}{\sqrt{2\pi{\sigma_d}^2}} \ \exp\left(-\frac{(E-E_L)^2}{2{\sigma_d}^2}\right)\left[1+\exp\left(-\frac{E-E_F}{kT}\right)\right]^{-1} dE \tag{5.5}$$

with *F(E)* as the Fermi-Dirac distribution and $g_L(E)$ as the Gaussian-distributed density of states at the LUMO level centered at E_L. However, the standard deviation corresponding to the energetic width of the density of states (DOS) could also change upon doping due to additional Coulomb potentials from ionized dopants leading to deep-lying trap states as discussed in Section 5.1.2. Moreover, it has been shown in a disordered conjugated polymer that only the core of the DOS function is Gaussian, while the low-energy tail has a more complex structure [163]. Finally, the determination of the energetic position of the LUMO level by IPES is afflicted with a comparably large uncertainty of ± 0.25 eV precluding the exact calculation of the free electron density with the help of equation 5.5. These considerations also apply to the determination of free hole densities.

Thus, in the following, other techniques for the determination of the doping-induced charge carrier densities will be discussed. First, the calculation of the densities out of the depletion

region formed at the point of contact between an electrode and the doped organic layer will be demonstrated. These results will be subsequently compared with the values obtained by capacitance-voltage measurements *(C-V)* on metal-insulator-(doped) semiconductor (MIS) structures and by polaron absorption measurements. Finally, the characteristics of the charge carrier density versus doping concentration will be discussed for different organic materials as well as for p- and n-type doping by MoO_3 and Cs_2CO_3, respectively.

5.3.1 Thickness-Dependent Work Function Characteristics of Doped Organic Semiconductors on ITO

Several reports exist on the doping-induced enhancement of charge carrier injection into organic materials. The formation of a thin depletion layer at the electrode/organic interface is supposed to enable an efficient tunneling of charge carriers through the space charge region [37, 38]. In analogy to the world of inorganic semiconductors, the width W of the depletion layer is given by

$$W = \sqrt{\frac{2\epsilon_0 \epsilon_r V_{bi}}{qn}} \tag{5.6}$$

in the case of n-type doping with n as the free electron density corresponding to the ionized donor density and V_{bi} as the built-in voltage derived from the difference between the work function of the electrode and the saturated work function of the doped semiconductor beyond the space charge region [34]. This relation is only valid for the assumption of a uniform distribution of fully ionized donors and it results from the Fermi level alignment at thermal equilibrium at the metal-semiconductor contact as well as at the one-sided abrupt p-n junction in which the space charge region predominantly extends into the weaker doped semiconductor. ITO is considered as a degenerate n^+-type semiconductor [164] with a measured free electron density of 1.5 x 10^{21} cm^{-3}, leading to the formation of a space charge region in the adjacent organic material. It has been already shown for unintentionally doped organic semiconductors deposited at several metal contacts that a Fermi level alignment could be achieved by bending their energy levels near the interface similar to the band bending in inorganic semiconductors [165]. By several cycles of alternating evaporation and measurement steps in-vacuo and by using equation 5.6, an impurity concentration of N_d = 4.2 x 10^{14} cm^{-3} in C_{60} was calculated for a space charge layer width of W = 495 nm after which the work function reached a constant value [26]. The measurement of the work function was conducted by KP method, since the influence of screening effects by electronic polarization especially for thin organic layers deposited on metal contacts, which may appear

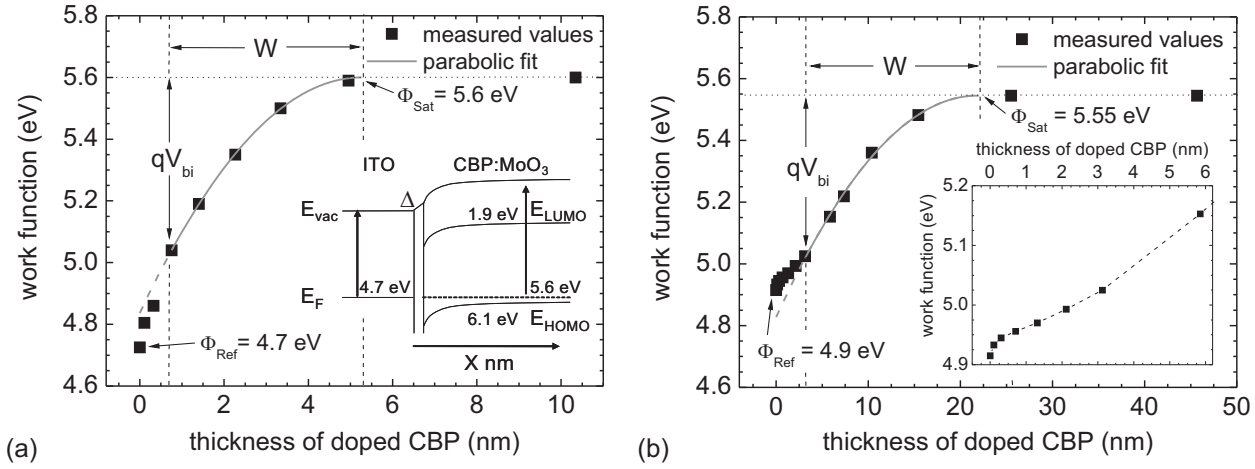

Figure 5.14: (a) Work function of $(MoO_3)_3$ (17.3 mol %) doped CBP deposited stepwise on ITO. Inset: energy level alignment at the n^+-p junction. (b) Work function of $(MoO_3)_3$ (2.2 mol %) doped CBP deposited stepwise on ITO. Inset: magnified view of the progression of the work function within the first 6 nm of CBP:MoO_3.

in UPS experiments, can be excluded. Additionally, the charging of the sample, caused by the emission of electrons and generation of holes which possibly accumulate on the surface of the generally insulating organic materials at higher thicknesses, hampers the analysis by UPS [26].

Therefore, p- and n-type doped CBP layers were prepared by a stepwise deposition on ITO and repetitive measurement of their work function with the Kelvin probe system. The progression of the work function is shown in Figure 5.14a for a MoO_3 doped CBP layer with a doping concentration of $(MoO_3)_3$ of 17.3 mol %. For this substrate, the work function of ITO has been determined to 4.7 eV before the deposition of the organic layer. An abrupt increase in the work function by 0.3 eV is observed within the first 0.8 nm of the doped CBP layer. This has to be attributed to the formation of an interfacial dipole on ITO and is not considered as part of the depletion layer. Similar observations were made by the deposition of the unintentionally doped C_{60} on different metal contacts such as Au, Cu and Ag where the characteristics similar to band bending appeared after an interface dipole of 2 nm in thickness [142]. Accordingly, after this dipole the evolution of the work function can be assigned to the formation of a space charge region. Following a section of parabolic increase, the work function saturates at 5.6 eV for a thickness of the p-type doped CBP larger than 5 nm. Taking the width of the interface dipole between the organic semiconductor and ITO

into account and fitting the typical parabolic function of band bending to the measured values of the work function [34], according to

$$V(x) = -\frac{qp}{2\epsilon_0\epsilon_r}(W - x)^2 \tag{5.7}$$

the built-in voltage V_{bi} and the depletion width W are determined to 0.56 V and 4.5 nm, respectively. The dielectric constant of CBP has been measured to $\epsilon_r = 2.84$ via MIS structures as will be discussed in the next section. Accordingly, the density of free holes p amounts to 8.7 x 10^{18} cm^{-3}. Figure 5.14a demonstrates the corresponding measurement data for a significantly weaker doped CBP layer with only 2.2 mol % of $(MoO_3)_3$. In this case, the work function of the neat ITO layer has been determined to 4.9 eV. The formation of the interface dipole occurs within a thicker layer of almost 3 nm as compared to the first sample and indicated in the inset of Figure 5.14b. The origin of the dipole, however, is not clear. Either an electron transfer from ITO to MoO_3 takes place as already discussed in Section 4.2.1, leading to a thicker dipole layer in the case of lower doping concentration. Or the energetically small interface dipole originates from the contact of CBP molecules with ITO as observed in Section 5.2.1 so that the doping by the TMO is hampered and only occurs in a specific distance from the dipole layer depending on the doping concentration. It is also possible that the charge transfer complexes themselves cause a specific dipole at the ITO interface. As a consequence, the dipole layer would be completed within a thinner layer at a higher concentration of charge transfer complexes. In any case, the work function saturates after its parabolic increase beyond the interface dipole at a value around 5.55 eV. A built-in voltage of $V_{bi} = 0.53$ V and a depletion width $W = 18.7$ nm are derived by the parabolic fit. The resulting density of free holes is $p = 4.7$ x 10^{17} cm^{-3}. The schematic in the inset of Figure 5.14a summarizes the conditions of energy level alignment at the ITO/CBP:MoO_3 interface.

The examination of the n-type doping of CBP is also possible in this way. Figure 5.15a shows the thickness-dependent work function characteristics of CBP:Cs_2CO_3 with a doping concentration of 14.6 mol %. The formation of a very thin interfacial dipole layer within the first 0.5 nm is again observed. However, its termination can not be specified unambiguously due to the similar slope compared with the initial band bending assumed beyond the dipole shift. The parabolic fit of the measured work function values provides a built-in voltage of 1.85 V and a depletion width of 8.4 nm corresponding to an electron density of $n = 8.3$ x 10^{18} cm^{-3}. The fit, however, is subject to an increased uncertainty especially in the region of higher layer thickness. Only a small change in doping concentration to 17.8 mol % leads to an even larger uncertainty in the parabolic fit. As indicated in Figure 5.15b, the measured values significantly deviate from the fit at a layer thickness of 6 nm and above.

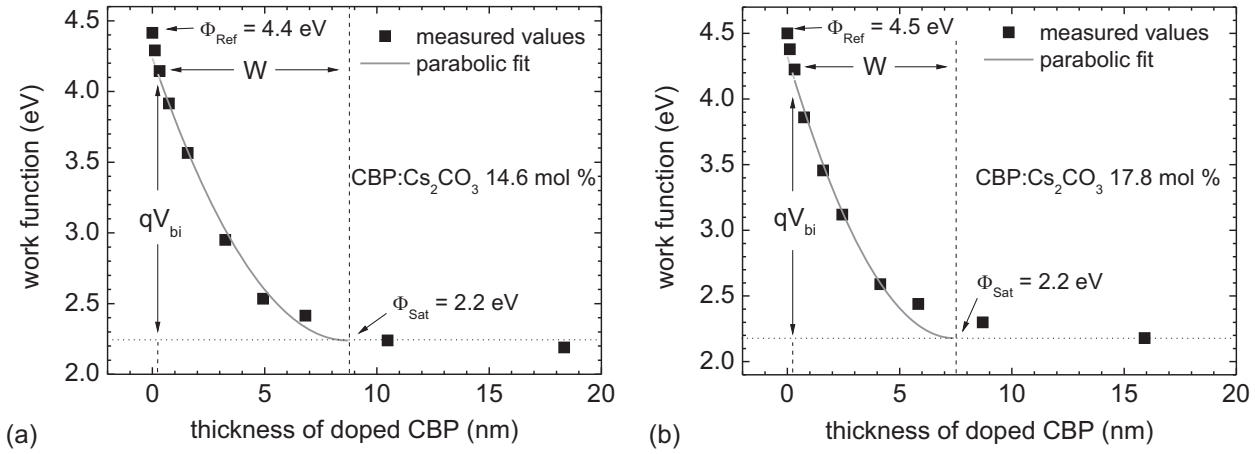

Figure 5.15: Thickness-dependent work function characteristics of Cs_2CO_3 doped CBP deposited stepwise on ITO. (a) Doping concentration at 14.6 mol %. (b) Doping concentration at 17.8 mol %.

The electron density amounts to n = 1.2 x 10^{19} cm^{-3}. Several factors could be the reason for the poorer fits for n-type doped organic layers. For instance, the surface coverage by adsorbates from residual gases in the UHV system has already been shown to increase the work function of n-type doped TPBi in Section 4.1. Additionally, the adjustment of the doping concentration between two successive evaporation steps is not fully reproducible by using Cs_2CO_3 as dopant as discussed in Section 5.2.1. Finally, it has been recently argued that the reconstruction of the potential profile in a thick insulator layer on the basis of stepwise Kelvin probe measurements of the surface work function is not fully correct [166]. A difference between the thickness-dependent surface potential and the real bulk potential distribution arises due to the KP-induced condition of zero field at the surface. This is assumed to lead to a modification of the space charge region at the metal/organic interface and with it to a charge redistribution within the probed layer. Although the KP system used in this work does not attempt to measure the null point directly, but rather inter- or extrapolates the contact potential difference depending on the settings of the backing potentials [87], the influence on the bulk potential profile by the measurement method itself remains somewhat unclear. Therefore, it is necessary to compare these results with those obtained by other measurement techniques. In the following section, the capacitance-voltage (C-V) measurements will be introduced as a further possibility of the charge carrier density determination.

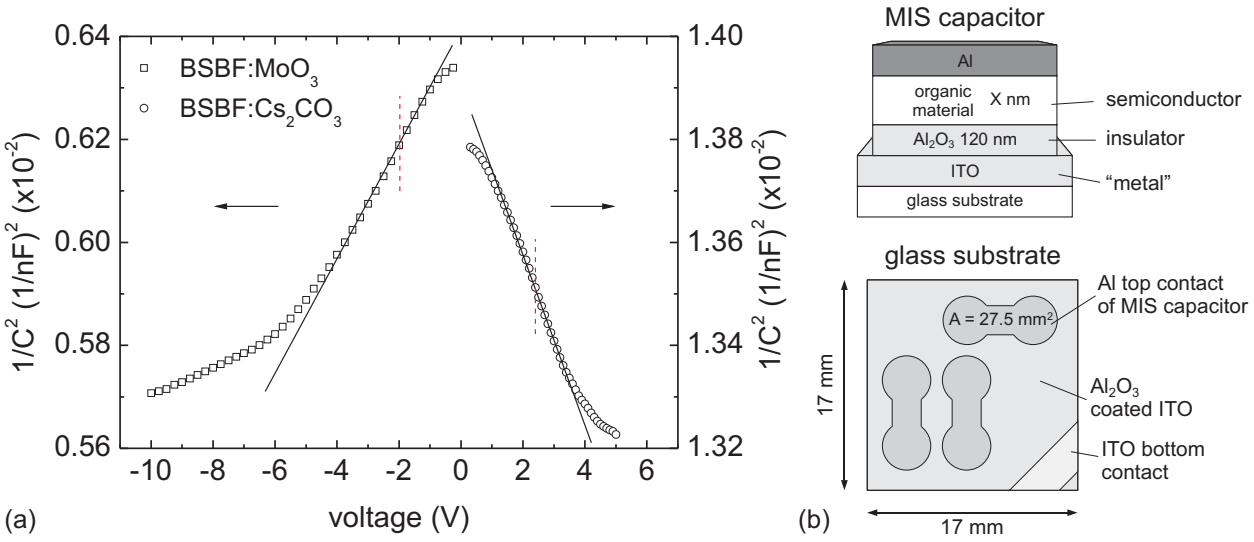

Figure 5.16: (a) Capacitance-voltage measurements of 50 nm thin MoO_3 doped BSBF (10 mol %) and a 200 nm thick Cs_2CO_3 doped BSBF (3.2 mol %) MIS structures. The dashed lines indicate the respective inflection point and the solid lines represent the respective linear part of the curves. Note that the scales for the two $(1/C)^2$-V curves are different. (b) Schematics of the principle layer sequence of the MIS devices and their dimensions on the ITO coated glass substrates.

5.3.2 Capacitance-Voltage Measurements on Metal-Insulator-Semiconductor Structures

Capacitance-voltage (C-V) measurements on metal-insulator-semiconductor (MIS) structures exhibit two technological advantages for the determination of charge carrier densities over the KP method which has been demonstrated in the previous section. First, no evaporation break is necessary due to the omitted determination of the thickness-dependent work function characteristics, minimizing the time of deposition and measurement and lowering the fluctuations in the processing of the doped organic semiconductors. Second, the organic material is deposited on an insulator as shown in Figure 5.16b. Therefore, one can assume that no interface dipoles are formed between the inert insulator material and the doped semiconductor which would interfere with the measuring principle. In this case, the insulator consists of a 120 nm thick layer of aluminum oxide (Al_2O_3) prepared by atomic layer deposition (ALD) at 120°C on 17 x 17 mm^2 sized ITO coated glass substrates. A small

area at one of the corners of the glass substrate is capped by Kapton[1] polyimide film during the ALD process keeping the ITO bottom contact free. The layer thickness of Al_2O_3 d_{iso} has been verified by profilometer measurements. Three parallel-plate capacitors each with an area of $A = 27.5$ mm^2 are obtained on one substrate after the thermal evaporation of Al directly on Al_2O_3 through a shadow mask as schematically indicated by Figure 5.16b at the bottom. Accordingly, using an LCR meter (SR715/720) in which the quasi-static signal was varied by a sinusoidal ($\pm$ 1.0 V at a frequency of 100 Hz), a relative permittivity of $\epsilon_{iso} = 7.44$ has been obtained on average. By inserting an undoped organic layer of specific thickness between the Al_2O_3 film and the Al top contact, it is also possible to measure its permittivity from the serial connection of the two formed capacitors. In this way, in addition to the relative permittivity of CBP given in the previous section, the dielectric constants ϵ_{sem} of S-2CBP, TPBi and TCTA have been determined to 2.7, 3.11 and 2.94, respectively.

In the following, the concept of the determination of charge carrier densities in organic materials by C-V measurements on ideal MIS structures will be briefly explained using the example of a p-type doped semiconductor deposited between the insulator and the metallic top contact of the structure shown in Figure 5.16b. In the case of a negative bias applied on the metallic bottom contact, holes are injected from the top contact into the doped semiconductor. By increasing the negative bias, they are pushed toward the insulator-semiconductor interface and accumulate there. In this case denoted as the accumulation mode, the capacitance of the MIS structure simply equals that of the oxide layer and reaches its maximum value according to

$$C_{iso} = \frac{\epsilon_0 \epsilon_{iso} A}{d_{iso}}. \tag{5.8}$$

In the depletion mode the total capacitance C_{ges} is given by the series capacitances of the insulator C_{iso} and the doping concentration-dependent depletion layer within the semiconductor C_{sem} which is formed in the vicinity of the insulating oxide layer. The width of the depletion layer w depends on the bias voltage V according to

$$w = \sqrt{\frac{2\epsilon_0 \epsilon_{sem} V}{qp} + \left(\frac{d_{iso}\epsilon_{sem}}{\epsilon_{iso}}\right)^2} - \frac{d_{iso}\epsilon_{sem}}{\epsilon_{iso}}, \tag{5.9}$$

derived by the consideration of the respective voltage drop partly across the insulator and partly across the semiconductor [34]. Assuming a δ-distribution of the induced charges corresponding to the situation that the induced charges are located at the metal-insulator

[1] registered trademark of DuPont

interface and at the edge of the depletion region on the semiconductor side [82], the total capacitance is given by the series connection of two parallel-plate capacitors according to

$$\frac{1}{C_{ges}} = \frac{1}{C_{iso}} + \frac{1}{C_{sem}} = \frac{d_{iso}}{\epsilon_0 \epsilon_{iso} A} + \frac{w}{\epsilon_0 \epsilon_{sem} A}. \tag{5.10}$$

Squaring this equation and substituting w with equation 5.9 gives the basic relation between the inverse-square of the total capacitance and the applied voltage V by

$$\frac{1}{C_{ges}^2} = \frac{2V}{qp\epsilon_0 \epsilon_{sem} A^2} + \frac{d_{iso}^2}{(\epsilon_0 \epsilon_{iso} A)^2}. \tag{5.11}$$

Thus, the charge carrier density p is simply obtained by the differentiation of the inverse-square of the total capacitance according to

$$p = \frac{2}{q\epsilon_0 \epsilon_{sem} A^2} \cdot \frac{\partial V}{\partial \left(\frac{1}{C_{ges}^2}\right)}. \tag{5.12}$$

Note that these considerations are based on an ideal MIS structure in which the work function of the bottom metal contact corresponds to the work function of the probed semiconductor. In the real case, however, the work function of the ITO contact never equals that of the doped organic materials so that the experimental *C-V* and *(1/C)²-V* characteristics are always displaced from the ideal theoretical curve in which the y-intercept would clearly separate the accumulation from the depletion mode by the polarity of the applied voltage [34].

Figure 5.16a shows the results of the *C-V* measurements on p- and n-type doped BSBF as a function of *(1/C)²* measured by the LCR meter of which the quasi-static signal was varied around the bias potential by a sinusoidal ± 1.0 V. The polarity of the applied bias voltage refers to the ITO bottom contact. BSBF is a homologous oligofluorene with two fluorene units and is known as an amorphous ambipolar organic semiconductor with high intrinsic electron and hole carrier mobilities around 3-5 x 10^{-3} cm^2/Vs [167]. Cyclic voltammetry measurements yielded a HOMO level at 6.4 eV and a LUMO level at 2.7 eV [168] suggesting the possibility of doping with MoO_3 and Cs_2CO_3, respectively. The left plot shows the characteristics of a 50 nm thick MoO_3 doped BSBF film with a doping concentration of 10 mol % deposited into the MIS structure with the above-mentioned layer sequence. The accumulation and depletion regimes are clearly observed for very high and very low voltages according to their amounts, respectively. Accordingly, the positive slope of the *(1/C)²* plot is a clear indication of the existence of holes as majority carriers which are increasingly pushed away from the insulator interface with increasing bias voltage. The almost linear curve is also given and allows to derive the hole density to p = 4 x 10^{18} cm^{-3}, assuming a

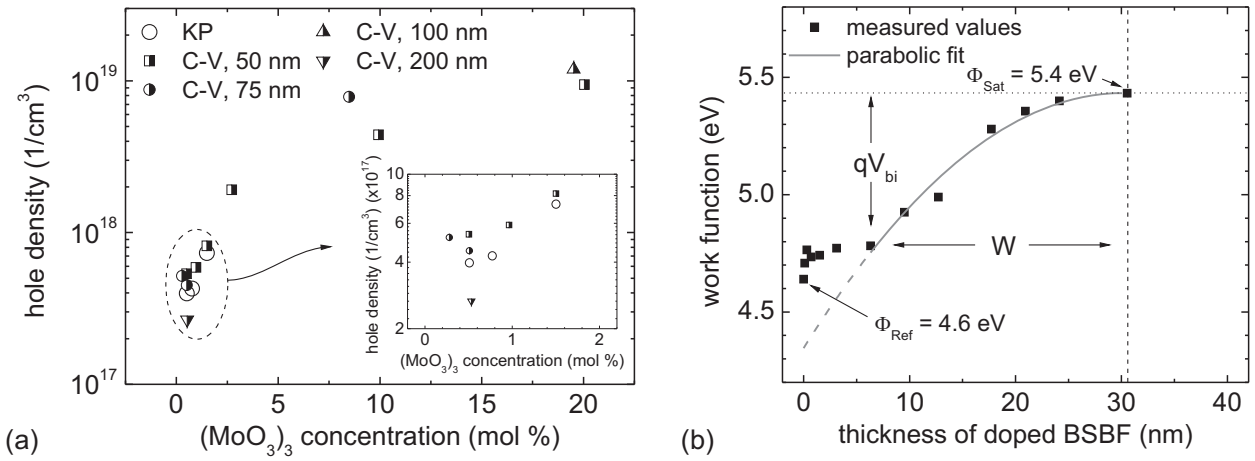

Figure 5.17: (a) Hole density versus doping concentration of BSBF:MoO_3 measured by KP and *C-V* method on MIS structures with various layer thicknesses of the doped semiconductor. Inset: magnified view of the range of low doping concentrations. (b) Thickness-dependent work function characteristics of MoO_3 doped BSBF with a doping concentration of 0.51 mol % and deposited on ITO.

relative permittivity of BSBF of $\epsilon_{sem} = 3$ according to the above-mentioned values for the organic semiconductors. For reasons of consistency, the inflection points of the $(1/C)^2$ curves were always extracted for the determination of the respective charge carrier densities. They are marked by the vertical dashed lines in Figure 5.16a. The right plot demonstrates the characteristics of a 200 nm thick Cs_2CO_3 doped BSBF layer with a doping concentration of 3.2 mol %. This time, a negative slope appears indicating the existence of electrons as majority carriers induced by n-type doping. The gradient at the inflection point yields an electron density of $n = 3.2 \text{ x } 10^{18}$ cm^{-3} by using equation 5.12.

To further verify the *C-V* method as a reliable technique for the determination of charge carrier densities, its results are compared to those obtained by the KP analysis. Figure 5.17a comprises the hole densities measured by both methods for various doping concentrations of BSBF:MoO_3. The hole density expectedly increases for higher concentrations of MoO_3 within the mixed layer. Moreover, the values obtained by KP analysis of the thickness-dependent work function characteristics are consistent with the results of the *C-V* measurements as indicated by the inset of Figure 5.17a. Note for low doping concentrations, it becomes clear that the results obtained by the *C-V* method tend to depend on the thickness of the probed organic semiconductor within the MIS structure. Using only 50 nm of BSBF:MoO_3 at 0.5 mol % leads to an apparent hole density of $p = 5.4 \text{ x } 10^{17}$ cm^{-3} whereas the measurements

on thicker layers of the same doping concentration yield a lower hole density of 4.5 x 10^{17} cm^{-3} and 2.7 x 10^{17} cm^{-3} for 75 nm and 200 nm in thickness, respectively. Obviously, the hole densities obtained by using too thin semiconductor layers can only be considered as an upper limit of the real density, since the width of the depletion layer would be in the range of the thickness of the doped material [169]. Actually, Figure 5.17b shows the thickness-dependent work function characteristics of BSBF:MoO_3 (0.51 mol %) deposited on ITO and measured by KP. The depletion width W is estimated to approximately 25 nm. Taking the width of the interface dipole into account, the work function saturates only after the deposition of more than 30 nm of BSBF:MoO_3. According to the parabolic fit, the density of free holes p amounts to 4.0 x 10^{17} cm^{-3}. Although no formation of an interface dipole is assumed between the doped semiconductor and Al_2O_3 in MIS structures, and though the voltage-dependent depletion width would not extend over the whole semiconducting layer in the case of using only 50 nm of BSBF:MoO_3, the influence of an additional depletion layer or at least an interface dipole at the metallic top contact must be considered. Ideal MIS structures exhibit an Ohmic contact on this side, which is obviously not given for the contact between the organic semiconductor and Al especially at low doping concentrations [170]. Therefore, it is highly important to use sufficiently thick layers of the probed semiconductor. Note however that due to these considerations the simplified circuit model for the C-V measurements used in this work is not applicable for very low doping concentrations. The circuit model of a series capacitance of insulator and depletion layer at its interface has to be extended. For example, the treatment of the bulk semiconductor as an additional RC circuit in series to the capacitance of interest becomes necessary. This complicates the determination of the charge carrier density and requires additional frequency-dependent measurements as shown by Zhang *et al.* for the determination of hole densities in the range of 10^{16} cm^{-3} [148].

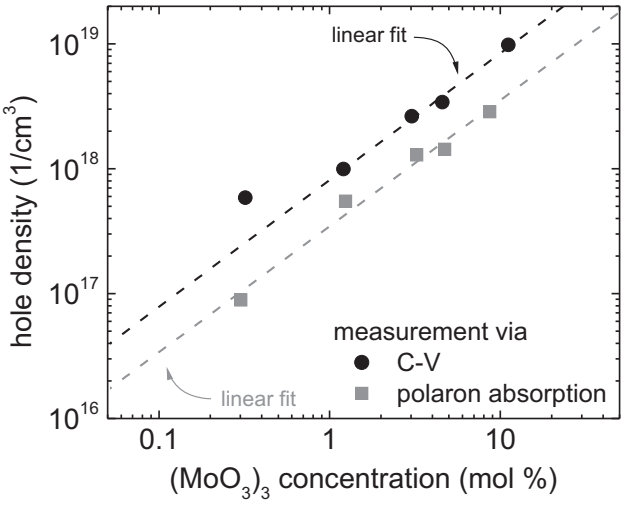

Figure 5.18: Hole carrier density vs. $(MoO_3)_3$ doping concentration. The squares and circles indicate the measurement via polaron absorption and C-V technique, respectively. The dashed lines represent the linear fit of the double-logarithm plots in which the value of the lowest hole carrier density measured by C-V is not included.

Finally, for both techniques, KP and *C-V*, it remains questionable whether the models known from the world of inorganic semiconductors may be simply transferred to their organic counterparts. Therefore, a further investigation of the results obtained by *C-V* measurements has been made by comparing them with the charge carrier densities obtained by polaron absorption measurements of doped semiconductors. Since this measurement technique does not represent a focus of this work, its principle should be only briefly discussed in the following. Details about the methods and device structures used therein for the determination of the charge carrier density are found elsewhere [150,151,171]. As already seen in Section 5.1.2 specific polaron absorption bands appear upon doping due to the formation of charge transfer complexes. Accordingly, it is possible to establish a connection between the intensity of absorption and the doping concentration. In order to obtain absolute values for the charge densities, the specific polaron absorption cross section of the undoped organic material has to be measured first. For reasons of high accuracy in the course of the absorption measurements, it is important to find a material with comparably high values of polaron absorption cross section. This is given for S-2CBP: at a wavelength of $\lambda = 510$ nm, corresponding to the maximum of the cationic polaron absorption spectrum, the polaron absorption cross section amounts to $\sigma_{pol} = 3.7 \text{ x } 10^{-16}$ cm^2 [151]. The value has been determined with a highly sensitive method using a waveguide structure which enables the propagation of the second transverse electric mode through the undoped organic semiconductor causing only very low waveguide losses [151, 171]. Simple UV-Vis absorption measurements through a coated glass substrate would not provide the accuracy needed for precise determination. By enabling a hole-only current and light propagation through the probed semiconductor within the waveguide, the cationic polaron absorption can be determined by the comparison of the edge emission spectra with and without the hole current [150]. A space charge limited current is considered for the relation of the density of charge carriers to the measured polaron absorption, in order to determine the polaron absorption cross section. The polaron absorption of the electrochemically p-type doped film has been measured by the variable stripe length method. The hole density induced by electrochemical doping can then be derived by comparing the absorption spectra obtained in both ways [151]. The large value of the polaron absorption cross section of S-2CBP ensures a direct relation to the doping concentration due to the limited potential influence of the additional polaron absorption induced by the MoO_3 anions as decribed in Section 5.1.2.

Figure 5.18 shows the results of the polaron absorption measurements on MoO_3 doped S-2CBP for varying doping concentrations. They are plotted together with the hole densities determined by *C-V* measurements on MIS structures comprising 150 nm thick S-2CBP layers. The hole carrier density characteristics correlate quite well with each other as indicated

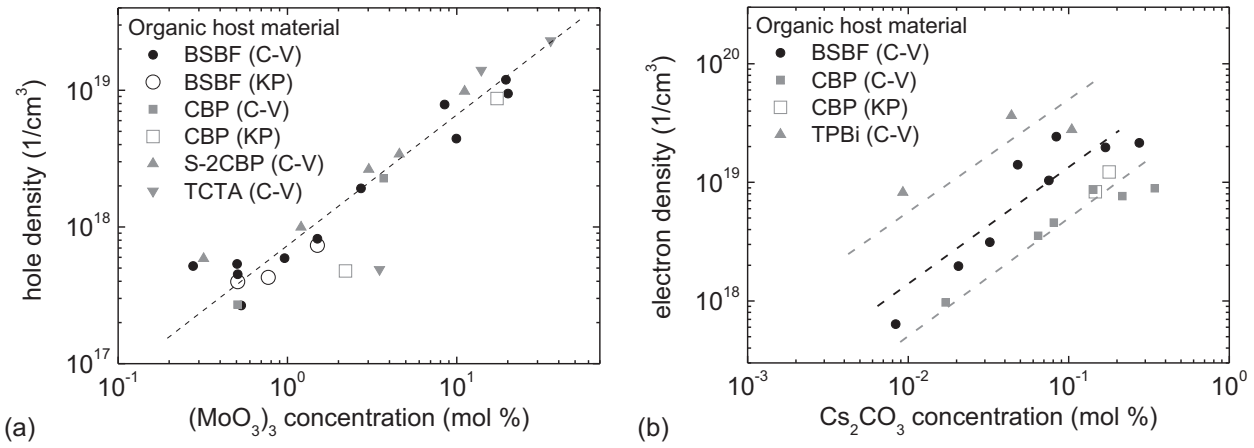

Figure 5.19: Charge carrier densities versus doping concentration determined by *C-V* and KP measurements for several organic semiconductors which are (a) p-type doped by MoO_3 and (b) n-type doped by Cs_2CO_3. The dashed lines are only guides for the eye.

by the parallel evolution of the linear fits of the double-logarithm plots. Accordingly, the comparison verifies the model of the formation of space charge regions in organic semiconductors similar to the characteristics of their inorganic counterparts. Interestingly, a difference exists between the hole carrier densities measured by the two techniques and amounts to an almost constant factor of 2.3. Thereby, the lower values of hole densities are given by the optical technique. This is all the more surprising, since the polaron absorption should not be limited whether free charge carriers are actually generated by doping-induced charge transfer complexes or remain bound to them. In other words, one would expect that the optical measuring method delivers an upper limit for the number of doping-induced charge carrier densities as compared to other measurement techniques, even if those methods supported an additional dissociation of charge transfer complexes into free carriers by the application of an external electric field [39]. Thus, it is assumed that some uncertainties add up in the context of the absorption measurements referring to the determination of the polaron absorption cross section [151]. Admittance spectroscopy, used to determine the field-dependent mobility of the organic material for the estimation of the charge densities from the SCL current, may account for some deviation. Moreover, the modeling of the spatial variation of the carrier density in the waveguide structure could have led to additional uncertainties. Nevertheless, in view of the two essentially different measurement techniques, the very good agreement of the results puts strong credibility on the derived charge carrier densities.

Most notably, the linearity with the slope of approximately one between the charge carrier density and the doping concentration as a common result of both methods is subject of further discussion in the following. Maennig *et al.* reported on a superlinear increase of hole density obtained by Seebeck measurements upon doping of amorphous ZnPc by F_4-TCNQ. The hole density rose by three orders of magnitude upon increasing the molar doping ratio of F_4-TCNQ/ZnPc from 0.002 to 0.02 [147]. They concluded that the hole mobility should be independent of the doping density so that the superlinear increase of conductivity originated solely from the similar increase of charge carrier density. Gregg *et al.* also assumed constant free carrier mobility in their discussion and explained the superlinear increase of conductivity by a decrease of the dopant activation energy upon higher doping concentrations. Referring to the example of n-type doping, they argued that one of the main reasons would be the attraction of free electrons to ionized dopants lowering their potential energy and with it the "conduction band" toward the donor level which would lead to a superlinear increase of electron density upon doping [146]. It is however questionable whether the LUMO level of the non-ionized host molecules is similarly affected by the dopants as in the case of the already ionized ones. Additionally, in Section 5.1.2, it was demonstrated that the superlinear increase of conductivity in CBP upon p-type doping by MoO_3 must be mainly attributed to a significant change of hole mobility rather than to the increase in hole density. In order to confirm the assumption of the linear increase of charge carrier densities at least within the examined range of doping concentrations, Figure 5.19 summarizes all hole and electron densities of several organic semiconductors induced by doping with MoO_3 and Cs_2CO_3, respectively, and determined by *C-V* and KP measurements in this work. Referring to the results of p-type doping shown in Figure 5.19a, all values of BSBF:MoO_3 are transferred from Figure 5.17a irrespective of the variation in layer thickness as discussed above. The hole densities of CBP:MoO_3 measured by KP in the previous section are also included. Additionally, *C-V* measurements on MIS structures comprising 200 nm thick MoO_3 doped CBP and 100 nm thick TCTA layers, respectively, were done and amend the data in Figure 5.19a. The dashed line is only guideline and demonstrates the almost linear relationship between the hole density and doping concentration in the double-logarithm plot. The same scenario is given for the characteristics of the electron density in Cs_2CO_3 doped organic semiconductors. All layers were 200 nm in thickness and measured by *C-V* technique in a nitrogen-box due to the hygroscopicity of the dopant as discussed in Section 5.2.2. A very good agreement is observed between the electron densities of CBP:Cs_2CO_3 determined by KP and *C-V* analysis. However, the magnitudes of the electron densities significantly differ for the three organic semiconductors for n-type doping. While TPBi:Cs_2CO_3 exhibits an electron density of 3.5 x 10^{19} cm^{-3} at 4.5 mol %, BSBF:Cs_2CO_3 possesses only a carrier density of 1.5 x 10^{19} cm^{-3}. An even lower electron density is obtained in Cs_2CO_3 doped

CBP around 3.5 x 10^{18} cm^{-3} despite a slightly higher doping concentration of 6.5 mol %. The inevitable question arises about the general and specific doping efficiencies in organic semiconductors which will be examined in the following section.

5.4 Doping Efficiencies of MoO_3 and Cs_2CO_3 in Organic Semiconductors

The doping efficiency is meant as the relation between the charge carrier density obtained upon electrochemical doping and the dopant density within the mixed layer $n_{dop,mix}$. A simple calculation of the dopant density is possible, assuming no aggregation or phase separation of molecules within the mixed layer and a linear increase of the total volume upon co-evaporation of dopant and host molecules corresponding to the addition of the their separate volumes. Accordingly, $n_{dop,mix}$ is derived by the multiplication of the doping concentration X_{mol} and the particle density of the mixed layer n_{mix} which is given by the total number of host and dopant molecules divided by the resulting volume of the layer. Since the area is the same for all layers, it is sufficient to use the layer thicknesses of the dopant and host molecules d_{dop} and d_{host} as measured by the quartz crystal monitors and their densities for neat layers n_{dop} and n_{host} to calculate the dopant density according to

$$n_{dop,mix} = n_{mix} X_{mol} = \frac{n_{dop} d_{dop} + n_{host} d_{host}}{d_{dop} + d_{host}} \cdot \frac{n_{dop} d_{dop}}{n_{dop} d_{dop} + n_{host} d_{host}} = \frac{n_{dop} d_{dop}}{d_{dop} + d_{host}}. \quad (5.13)$$

Thus it appears out of this equation that the dopant density is simply given by the division of the total number of dopant molecules to the total volume of the mixed layer. Figures 5.20 a and b show the doping efficiencies of the doped organic semiconductors studied in the previous section for the p- and n-type doping with MoO_3 and Cs_2CO_3, respectively. Referring to the p-type doping, the doping efficiency clearly ranges between 2 and 5 %. The values around 10 % doping efficiency obtained for BSBF and S-2CBP at 0.3 mol % doping concentration have to be handled with care due to the limitations of the simplified *C-V* measurements leading to higher values of charge carrier density as discussed in the previous section. In order to make reliable statements about the p-type doping efficiency in the two organic materials at least for the considered concentration range of $(MoO_3)_3$, some more data would be necessary. Nevertheless, it is obvious that the doping efficiency in S-2CBP exceeds that of CBP by almost 3 percentage points. One reason could be the difference in morphology between CBP and its spiro-derivative. It is known that the morphological

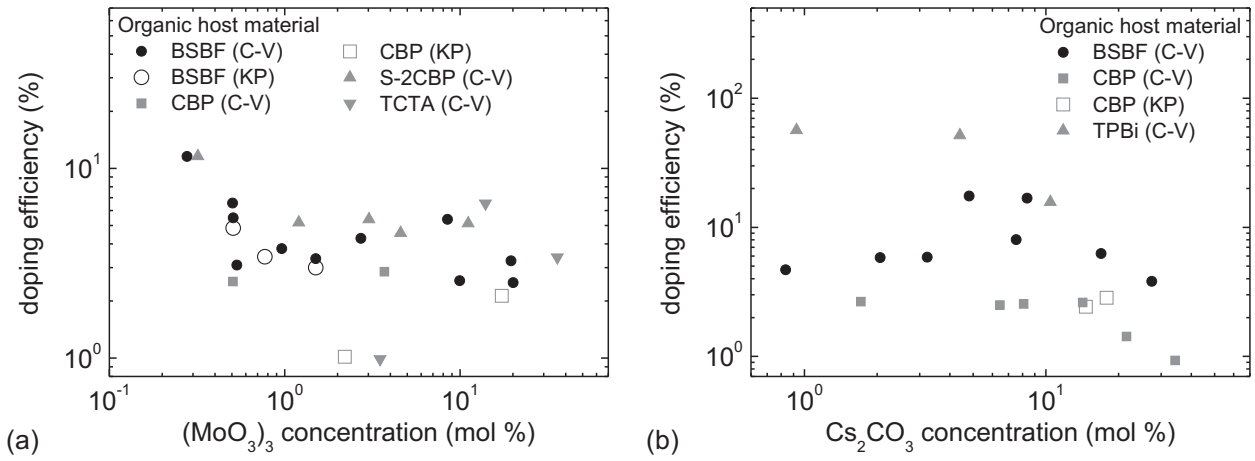

Figure 5.20: Doping efficiency versus doping concentration determined by *C-V* and KP measurements for several organic semiconductors which are (a) p-type doped by MoO_3 and (b) n-type doped by Cs_2CO_3.

stability of low molar mass organic materials is enhanced by the spiro concept [172]. Accordingly, S-2CBP with its slightly modified molecular structure compared to CBP shown in the appendix exhibits a glass transition temperature of 174°C[2] just like BSBF (another spiro-compound) [172]. Accordingly, both materials form amorphous layers at room temperature. Contrary to that, CBP exhibits a polycrystalline structure as already discussed in Section 5.1.2. Figure 5.21 shows the results of a combined measurement of the topology and spacially-resolved surface work function on a 2.5 x 2.5 μm^2 section of a 30 nm thick CBP:MoO_3 (22.8 mol %) layer deposited on ITO coated glass substrate. This has been achieved by the operation of an AFM as a Kelvin probe force microscope (KPFM) in a nitrogen-box.[3] The AFM image in Figure 5.21a again indicates the formation of crystallites as already shown in Section 5.1.2. Their planar dimensions are smaller as compared to those in a neat CBP film due to the high doping concentration. The KPFM image of the same section demonstrates a high correlation between the topography and the spacially resolved surface work function as shown in Figure 5.21b. The longitudinal section of one crystallite on this area indicated by the circle reveals an inhomogeneous potential difference corresponding to a differing work function depending on the measurement position on the grain. The potential difference is lower at the center of the crystallite as compared to that at

[2]quoted by one producer of this material, Luminescence Technology Corp.

[3]the measurements were conducted together with Dr. Frank Hitzel from Danish Micro Engineering, DME and Dipl.-Ing. Markus Tilgner

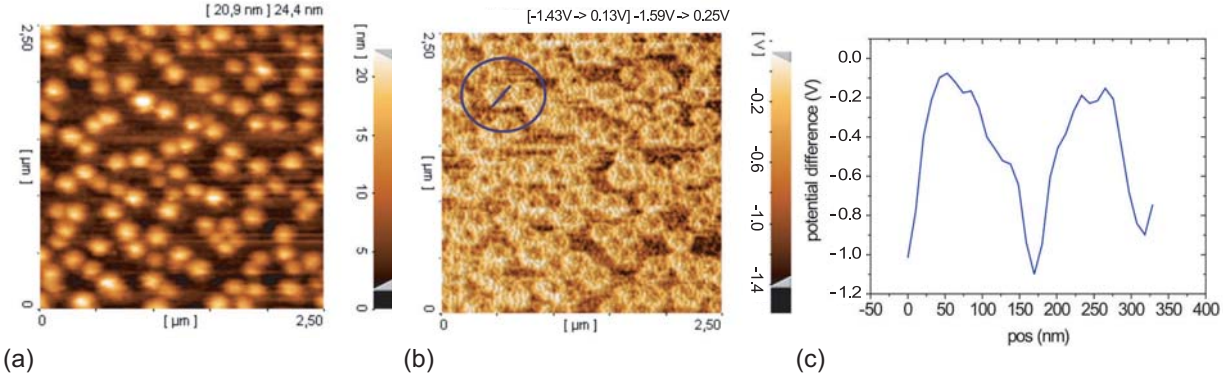

Figure 5.21: 2.5 x 2.5 μm^2 section of a 30 nm thick layer of CBP:MoO_3 (22.8 mol %) deposited on ITO. (a) AFM image. (b) KPFM image. The circle highlights a crystallite whose characteristics of the potential difference are shown in a longitudinal section in (c).

the grain boundary (Figure 5.21c). Accordingly, it could be assumed that the crystallization of CBP leads to an accumulation of MoO_3 trimers at the grain boundaries and therefore to an ineffective doping compared to the case of amorphous layers such as S-2CBP and BSBF. Note however that the comparison of the specific doping efficiencies lying in the same order of magnitude is only possible if the material densities for neat and mixed layers are completely clarified. The assumption of a material density of 1.7 g/cm^3 for all organic layers can only be seen as a rough estimate. Additionally, it has to be considered that the material density of an evaporated layer can deviate from the original powder. Aside from that, it is even more challenging to reliably declare doping efficiencies for the Cs_2CO_3 doped layers as summarized in Figure 5.20b due to the open questions about the decomposition process of the dopant during thermal evaporation. Based on the material density of Cs_2CO_3 and the assumption made for equation 5.13, one obtains a high doping efficiency in TPBi of around 50 % for lower doping concentrations and 15 % at 10.5 mol %. Again, the doping efficiency in CBP at 2.5 % on average is considerably lower than the efficiency in BSBF ranging between 4 and 17.5 %.

Despite some uncertainties, it can be concluded that the doping efficiency of MoO_3 around 2-5 % is unexpectedly low, though the conduction band minimum of the TMO lies considerably lower than the HOMO level of all organic materials studied in this work. More surprisingly, even the doping efficiency of MoO_3 in NPB has been found to be as low as 2.3 % (determined for 14.8 mol % doping concentration, considering the formation of $(MoO_3)_3$ clusters) [137]. This value is in the same order of magnitude as the results of this work,

although the IE of NPB is 1 eV smaller than that of CBP, making the electron transfer to the TMO even more favorable. A similar doping efficiency of 1.5 % is derived for MoO_3 doped 2-TNATA (calculated for 5.6 mol % doping concentration, considering the formation of $(MoO_3)_3$ clusters) [138]. In conclusion, the doping efficiency of MoO_3 in organic materials does not significantly depend on the position of the HOMO level of the host material. Thus, additional factors have to be considered to explain the low doping efficiencies. Possibly, a further macroscopic clustering of the TMO molecules occurs within the organic matrix, which would be expected to significantly lower the amount of transferred charges from host to dopant. Similar speculations have been made for the p-type dopant TNCQ in CuPc or the n-type dopant $CoCp_2^*$ in MEH-PPV [173,174]. From UPS measurements of TCNQ on CuPc and vice versa, it has been concluded that a phase separation of both moieties takes place in the composite. This lowers the effective volume which can be doped, since a charge transfer would only occur at the borderline of the two phases. An additional interface dipole observed between TCNQ and CuPc is considered to further limit the doping efficiency [173]. On the other hand, this example demonstrates that p-type doping in terms of a Fermi level shift toward the HOMO level is possible, although the IE of the CuPc host is about 1.6 eV higher than the EA of the TCNQ dopant. This can be explained by an energetically broadened density of states extending deeply into the band gap of the semiconductor materials. Accordingly, electrons from filled gap states of CuPc are assumed to be transferred to depleted gap states in TCNQ until Fermi level alignment [173].

Besides material-related morphological aspects, there are more general considerations concerning the doping efficiency. As addressed in the basics at the beginning of this work and more deeply discussed in Section 5.1.2, charge trapping by ionized dopants could reduce the number of free carriers. The situation is well summarized by the following reaction equation for p-type doping

$$H + \tilde{H}A \Leftrightarrow H + [\tilde{H}^+A^-] \Leftrightarrow H^+ + \tilde{H}A^-, \tag{5.14}$$

where H is the host molecule and $\tilde{H}$ the one adjacent to the acceptor A [175]. The center section of the equation describes the formation of charge transfer complexes as the first step of the doping process, in which the charge carriers are strongly bound to the host molecules. A high doping efficiency will only be achieved if the charge transfer complexes dissociate and lead to free carriers corresponding to the right part of equation 5.14. For instance, although the favorable energy level alignment between MeO-TPD and F_4-TCNQ is reflected by the high fraction of charge transfer of 73 % verified by infrared spectroscopy, Olthof *et al.* report on low doping efficiencies of only 5 % for this material system [176].

Moreover, high resolution scanning tunneling microscopy (STM) on F_4-TCNQ sandwiched by Pentacen molecules revealed that the acceptor-induced hole hops between neighboring molecules while still being localized in the vicinity of the ionized dopant [177]. The same situation could apply for the p-type doping of MoO_3 in organic semiconductors. However, a comprehensive model concerning the relation between charge transfer complexes and the amount of free carriers does not exist to date. Since the field of Coulomb attraction is proportional to $1/r^2$, it is generally assumed that small dopants such as Li or Cs lead to lower efficiencies as compared to larger molecular n-type dopants apart from the energy level situation. However, only complex calculations of the molecular density function could deliver the respective center of charges. This is important to know for the estimation of the Coulomb attraction between two ionized molecules. The same considerations could also apply for the charge transfer probability between the neutral host and dopant molecule leading to the charge transfer complex in the first step. Due to usually localized HOMO and LUMO levels on the molecules, the transfer of electrons could be sterically hindered. For instance, it has been observed that the n-type doping of NBPhen by Cs_2CO_3 does not significantly elevate the conductivity as compared to the doping of BPhen [178], although the molecular structures resemble each other except for two additional ligands in NBPhen. Similar argumentation has been given by Kido *et al.* referring to the n-type doping of Alq_3 and BPhen by Sr and Sm. In particular, the planar structure of BPhen has been considered to promote the doping by these metals compared to Alq_3 [53].

Despite these considerations, higher doping efficiencies with the help of other dopants are not excluded per se for the organic semiconductors investigated in this work. CsOH has been found to be a good candidate for n-type doping, leading to higher electron densities as in the case of Cs_2CO_3 in Alq_3 [179]. Additionally, ReO_3 has been shown to generate significantly higher hole densities in 2-TNATA than MoO_3 did at the same doping concentrations [138]. Still, the real dopant densities have to be verified first, in order to specify the actual doping concentration and efficiency. For instance, ReO_3 probably does not form trimers like MoO_3 or WO_3, actually leading to a tripled amount of effective dopant density at similar evaporation rates.

5.5 Conclusion

In this chapter, the electrochemical doping of organic semiconductors via MoO_3 and Cs_2CO_3 has been analyzed. Taking into account that the TMO mainly forms $(MoO_3)_3$ clusters, the characteristics of the Fermi level shift toward the HOMO level upon higher doping concentrations was shown to be based on the energetic properties of the density of states of

CBP. UPS and KP analysis demonstrated a rapid shift at very low doping concentration and a moderate further increase of the work function at higher doping concentrations until a Fermi level pinning at 0.5 eV above the HOMO level at 20 mol %. At the same time, the electrical conductivity increased by several orders of magnitude, mainly given by the super-linear increase of the hole mobility at low doping concentrations which is due to the filling of energetically deep-lying trap states in the band gap by the doping-induced charge carriers. They were also responsible for the change in the absorption and emission characteristics of CBP. UV-Vis-NIR absorption and PL measurements on doped layers demonstrated polaron absorption bands around 400-500 nm and 1500-2000 nm which were attributed to the CBP cations. Another broad absorption band with a maximum at 825 nm could be attributed to the chromic absorption of MoO_3. Finally, it was shown that the morphology of the poly-crystalline CBP gradually changed to amorphous layers at higher doping concentrations.
After finding the evidence of p-type doping via MoO_3, combined measurements conducted by UPS and IPES as well as KP proved the n-type doping of CBP by Cs_2CO_3. Thereby, the Fermi level shifted toward the electron transport level and was pinned at approximately 0.3 eV lower than the LUMO level of the organic semiconductor. Although UPS and IPES measurements could prove no decomposition into metallic Cs and a work function between 1.5 and 2 eV of the evaporated Cs_2CO_3 species allowing for the n-type doping of organic materials, the analysis was not able to further specify the assumed oxidic components due to instability of the compound during the measurement. For reasons of simplicity, the doping concentrations were therefore given by the assumption of no decomposition of the n-type dopant in the subsequent sections. Similarly to the p-type doping, higher electrical conductivities were proven by electron-only devices.
Two different measurement techniques known from the world of inorganic semiconductors were presented for the determination of the doping efficiencies of MoO_3 and Cs_2CO_3 in several organic semiconductors. Assuming the formation of a space charge region by the deposition of a doped organic layer on a metallic contact like ITO, the resulting surface work function characteristics were measured by KP depending on the layer thickness. The typical parabolic function of the potential characteristics could be fitted for p- and n-type doped CBP layers allowing for the determination of charge carrier densities in the range from 5×10^{17} to 1×10^{19} cm^{-3}. A second way of charge carrier determination was demonstrated by *C-V* measurements on MIS structures and compared to values obtained by specific polaron absorption measurements as a novel technique of charge carrier determination. As a result, a good correlation of the hole density characteristics could be demonstrated, confirming the approach of charge carrier determination by KP and *C-V* measurements. Moreover, it was verified that the hole and electron densities of several doped organic semiconductors

increased almost linearly with higher doping concentrations of MoO_3 and Cs_2CO_3 at least in the range from 0.5 to 20 mol %.
As a summary, the doping efficiencies were plotted for MoO_3 and Cs_2CO_3 doped in different organic semiconductors. The doping efficiency in CBP yielded only 2-3 % for the two dopants. A possible explanation was given by the results of the combined measurements of AFM and KPFM on MoO_3 doped CBP, showing an inhomogeneous potential landscape indicating the accumulation of the dopant at the grain boundaries of the polycrystalline surface. Most strikingly, it seemed that the low doping efficiency of MoO_3 does not depend on the position of the HOMO level of the host materials. The influence of additional factors were discussed such as phase separation and Coulomb trapping by ionized dopants which lower the free charge carrier density in general and not only in the case of MoO_3. The p-type doped spiro molecules BSBF and S-2CBP showed higher doping efficiencies by 2-3 percentage points above the values for CBP which was attributed to their amorphous structure. N-type doping of TPBi led to very high doping efficiencies of around 50 %.

6 Stacked OLEDs with Charge Generation Layers

OLEDs have attracted much interest in research and development in the last two decades. A long operating lifetime must be ensured however, before mass-production of OLEDs for the consumer market can start. An elegant way to meet this requirement using present organic materials and devices is to stack a number of OLEDs on top of each other, so as to significantly reduce the stress on each light-emitting unit while still achieving a given luminance level. Interconnecting units that serve as charge generation layers (CGL) are required when driving OLED stacks as two-terminal devices. The first studies by Kido *et al.* suggested that ITO or F_4-TCNQ adjacent to a hole transport layer (HTL) may lead to the generation of holes and electrons upon application of an electric field [6]. Since this early work, various concepts for CGL structures have been published, including the insertion of thin metal or transparent conductive oxide (TCO) layers [6, 180], junctions between chemically p- and n-doped charge transport layer [77, 181, 182], and the insertion of transition metal oxides (TMOs) [19, 20, 183–185]. It was recently shown that the charge generation mechanism when using a doped organic p–n heterojunction is based on a temperature-independent field-induced charge separation supported by a large band bending at the interface. This interpretation was proven by results from Kelvin probe measurements [118]. In the following section, an in depth analysis on the minimum thickness of the CGL components required in these structures will be presented using the example of CBP based complementarily doped homojunctions. In the second section of this chapter, the role of neat TMO films in CGLs will be clarified for stacked OLEDs.

6.1 Mechanism of Charge Generation in p-n Homojunctions

The mechanism of charge generation between highly doped organic layers is still not clarified in all details. In particular, the influence of the CGL thickness on its performance has not yet been studied. Assuming the formation of a space charge region close to the interface and with it a band bending-like energy level variation, an electric field-assisted tunneling of electrons is considered from the HOMO level of the p-doped layer into the LUMO level of the n-doped film leaving a hole at the other side [118]. Taking the results of the previous chapter into account, it is important to consider the low doping efficiency and the actual charge carrier

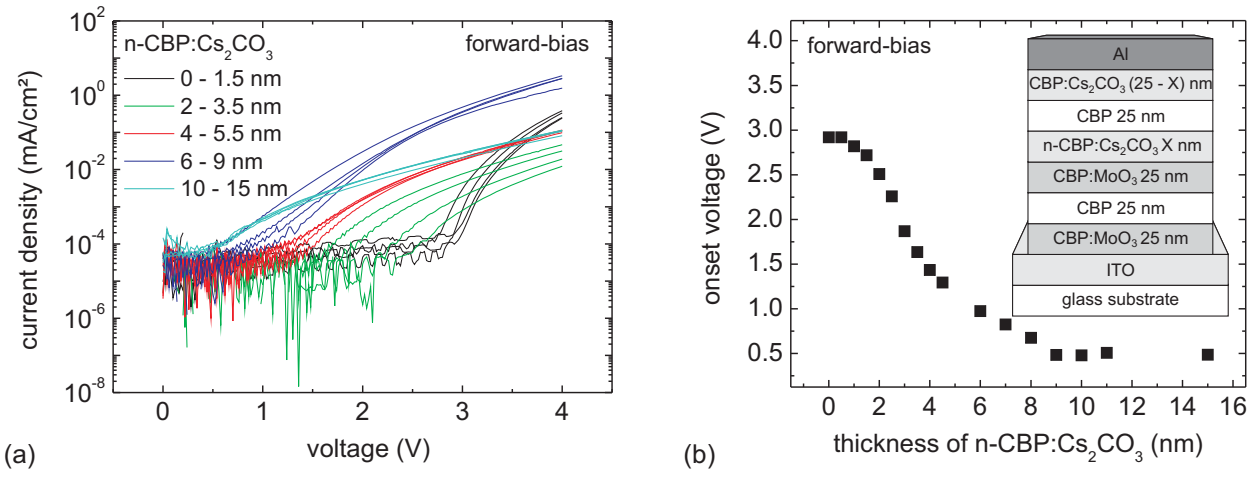

Figure 6.1: Electrical characteristics of the p-n homojunction-CGL devices operated in forward-direction with varying layer thickness of n-CBP:Cs_2CO_3. (a) Current density versus voltage characteristics. (b) Onset voltage versus layer thickness of n-CBP:Cs_2CO_3. Inset: device structure of the homojunction-CGL devices.

densities in doped organic semiconductors. That is why and for reasons of simplicity, a complementarily doped p-n homojunction-CGL based on CBP was analyzed referring to the correlation between the charge carrier density, the depletion width, and onset voltage for charge generation and separation. In order to reflect the electronic situation within the p-n homojunction-CGL, the electro-optical characteristics of the device structure shown in the inset of Figure 6.1b were measured for increasing layer thicknesses of the n-type doped CGL-component denoted as n-CBP:Cs_2CO_3. This device structure allows to examine the CGL characteristics without any electronic interference with the electrodes given by the insertion of neat CBP layers between the CGL-components and the outer doped layers. Only in this case, it is possible to learn more about the minimum thickness of the CGL-components required for a fully functional charge generation mechanism. Consequently, those layers as well as the 25 nm thick neat films of CBP assured that the examination of the energetics in the middle of the device was independent from the injection or extraction mechanism at the electrodes. Moreover, the thickness of the initially 25 nm thick Cs_2CO_3 doped layer at the Al cathode was reduced by the thickness of n-CBP:Cs_2CO_3 in each device. The doping concentrations amounted to approximately 16 mol % for the MoO_3 as well as Cs_2CO_3 doped CBP layers, corresponding to a free hole and electron density of almost 1 x 10^{19} cm^{-3} and 8 x 10^{18} cm^{-3}, respectively. Figure 6.1a shows the *I-V* characteristics of the devices at forward-bias upon variation of the n-CBP:Cs_2CO_3 thickness. Thereby, the

forward-direction of the current corresponds to the application of a positive bias to the ITO bottom electrode leading to the injection of holes and electrons into the device. Clearly varying onset voltages are observable at the respective points of steep increase in current density. Figure 6.1b summarizes the onset voltage characteristics in dependence of the n-CBP:Cs_2CO_3 layer thickness. The onset voltage starts at 2.9 V, gradually decreases for thicker layers of n-CBP:Cs_2CO_3, and saturates at 0.49 V for a thickness of more than 9 nm.

Obviously, an internal electric field has to be compensated first by an external forward-bias to inject charge carriers. It gradually decreases for thicker layers of n-CBP:Cs_2CO_3. The injected holes and electrons recombine in that intrinsic CBP layer which is closer to the Al cathode and cause the emission of violet light. Figure 6.2 summarizes the normalized electroluminescence spectra which were only observed for those devices comprising thin films of the n-CGL component up to 3.5 nm in thickness. The maximum wavelength at 430 nm energetically corresponds to the onset voltage of 2.9 V. Thereby, the EL spectra resemble that of the photoluminescence of a neat CBP film shown in Figure 5.6b except for the peak wavelengths. The shift of the maximum wavelength is mainly attributed to the weak microcavity effects within these devices leading to a varied out-coupling efficiency for the different spectral wavelengths. A further analysis of the properties of p-i-n homojunction devices based on CBP will be given in the next chapter. However, in the course of the CGL-investigation it is interesting to make a note of the spectral change upon thicker layers of n-CBP:Cs_2CO_3. A second local maximum wavelength apparently emerges at around 560 nm. At the same time, the intensity of the EL spectra gradually diminishes so that weak light emission could be only detected at very high voltages up to 9 V. Accordingly, it is concluded that the recombination zone moves from the intrinsic layer adjacent to the outer CBP:Cs_2CO_3 film into the p-n homojunction for an increasing thickness of the n-CGL

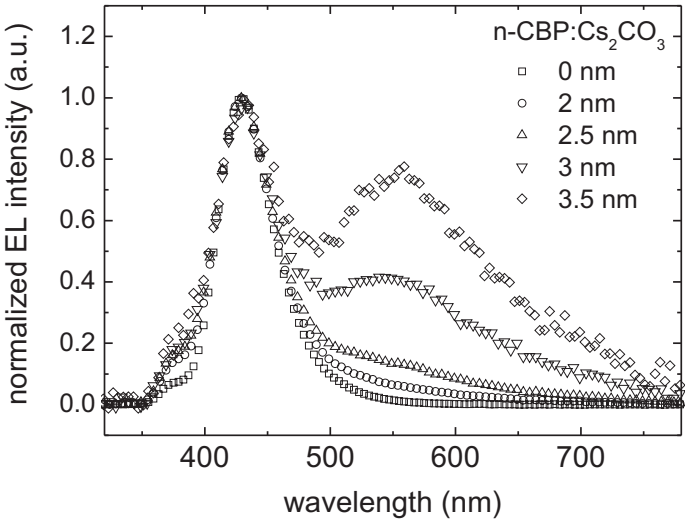

Figure 6.2: Electroluminescence spectra of the p-n homojunction devices for various thicknesses of the n-CBP:Cs_2CO_3 layer.

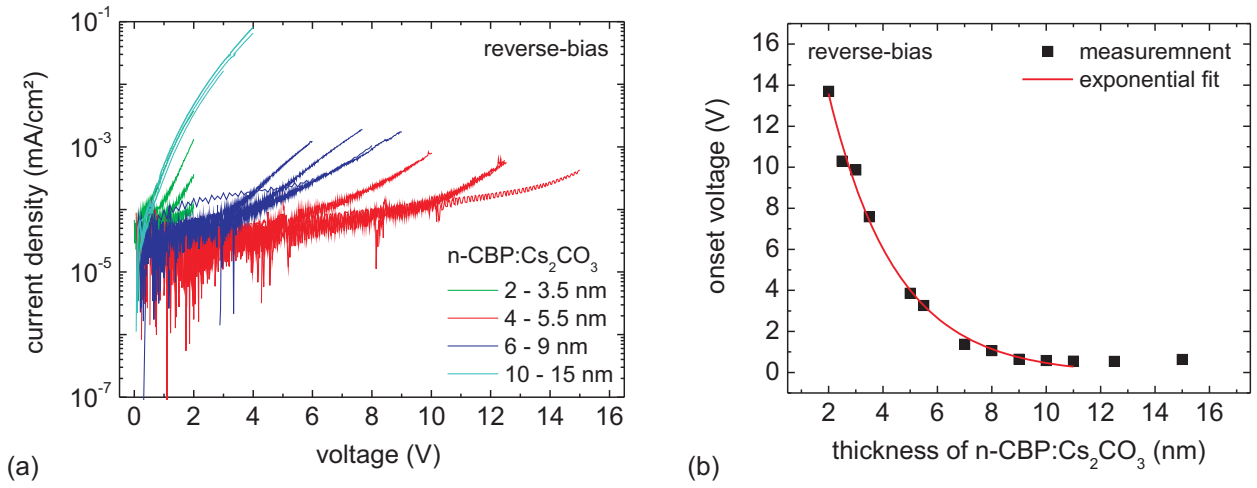

Figure 6.3: Electrical characteristics of the p-n homojunction-CGL devices operated in reverse-direction with varying layer thickness of n-CBP:Cs_2CO_3. (a) Current density versus voltage characteristics. (b) Onset voltage of charge generation versus layer thickness of n-CBP:Cs_2CO_3.

component, leading to a high exciton quenching rate induced by polarons. Actually, the shape of the EL spectrum of the device, comprising the 3.5 nm thick n-CBP:Cs_2CO_3 layer, possibly indicates an increased cationic polaron absorption leading to the specific collapse of the spectral intensity between the two spectral maxima.

While the onset voltages for the device operation in forward-direction reflect the internal potential drop across the intrinsic layer which is sandwiched by the two n-type doped films (as will be discussed below), the onset voltage characteristics for reverse-bias are indicative for the CGL performance. Figure 6.3a shows the *I-V* characteristics for reverse-bias corresponding to the application of a negative bias on the ITO bottom contact. In this case, a significant increase in current density is only given via the electric field-assisted charge generation at the p-n junction in the middle of the device and the subsequent carrier transport to the electrodes. However, the determination of the onset voltages of charge generation is less clear than for the forward-bias situation due to the generally higher voltages required for charge generation causing higher leakage currents through the device. In Figure 6.4, the derivation of the onset voltages is exemplified for two cases with different thicknesses of the n-CBP:Cs_2CO_3 film. As seen in Figure 6.4a, a smooth transition from the leakage to the charge generation-induced current density characteristics occurs, hindering the precise determination of the onset voltage. By adjacent averaging of the measurement points and

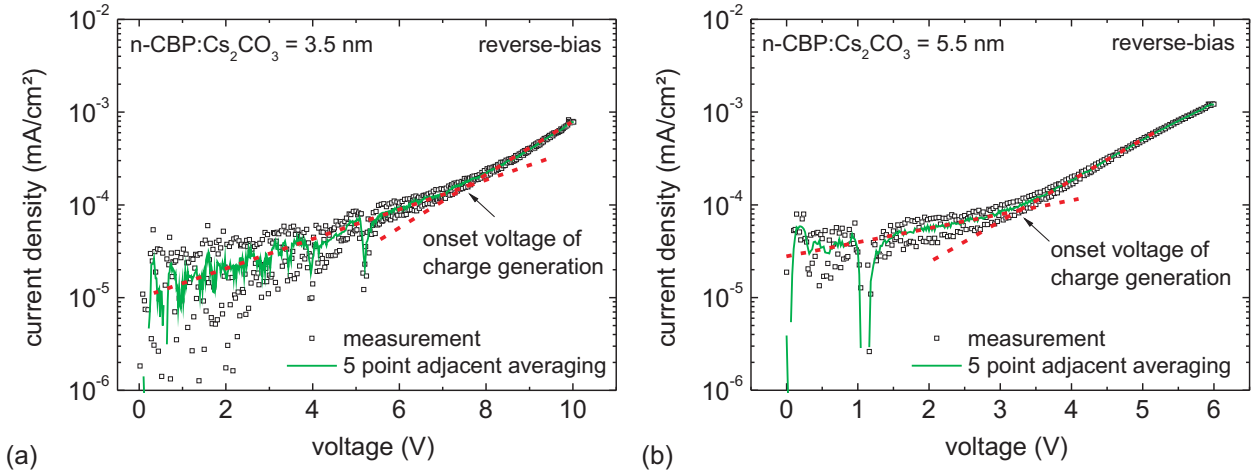

Figure 6.4: Determination of the onset voltage of charge generation under reverse-bias for two p-n homojunction devices with (a) a 3.5 nm thick n-CBP:Cs_2CO_3 layer and (b) a 5.5 nm thick n-CBP:Cs_2CO_3 layer. The dashed lines represent the respective slope of the current density characteristics.

extrapolation of the current density characteristics of the two different regimes, it is possible to define the onset voltage, lying at 7.5 V in the case of a 3.5 nm thick n-CBP:Cs_2CO_3 film. The determination of the onset voltages becomes easier for thicker layers of n-CBP:Cs_2CO_3 due to an improved signal-to-noise ratio for the current density and lower voltages needed for charge generation. The device comprising a 5.5 nm thick n-CBP:Cs_2CO_3 layer exhibits an onset voltage of charge generation at 3.3 V determined by the intersection of the two current density curves which are reproduced and extrapolated by the dashed lines (Figure 6.4b).

Figure 6.3b summarizes the onset voltage characteristics of charge generation depending on the layer thickness. The values at a thickness below 2 nm could not be determined due to low signal-to-noise ratio and electric field-induced breakdown causing irreversible damages of the organic devices. The onset voltages decrease exponentially from almost 14 V for the 2 nm thick n-CBP:Cs_2CO_3 layer to 0.6 V at 9 nm. Accordingly, the CGL performance is improved by increased thicknesses of the n-CGL component referring to the decreasing field needed for charge generation. The characteristics resemble the onset voltage curve for the operation in forward-direction concerning the point of saturation at 9 nm and its value around 0.5 V. Accordingly, it is concluded that the space charge region formed at the p-n junction is completed by 9 nm of the n-type doped film. This corresponds to the situation in which the internal potential (in the amount of the entire built-in voltage V_{bi}) drops across the total depletion width W_{tot}.

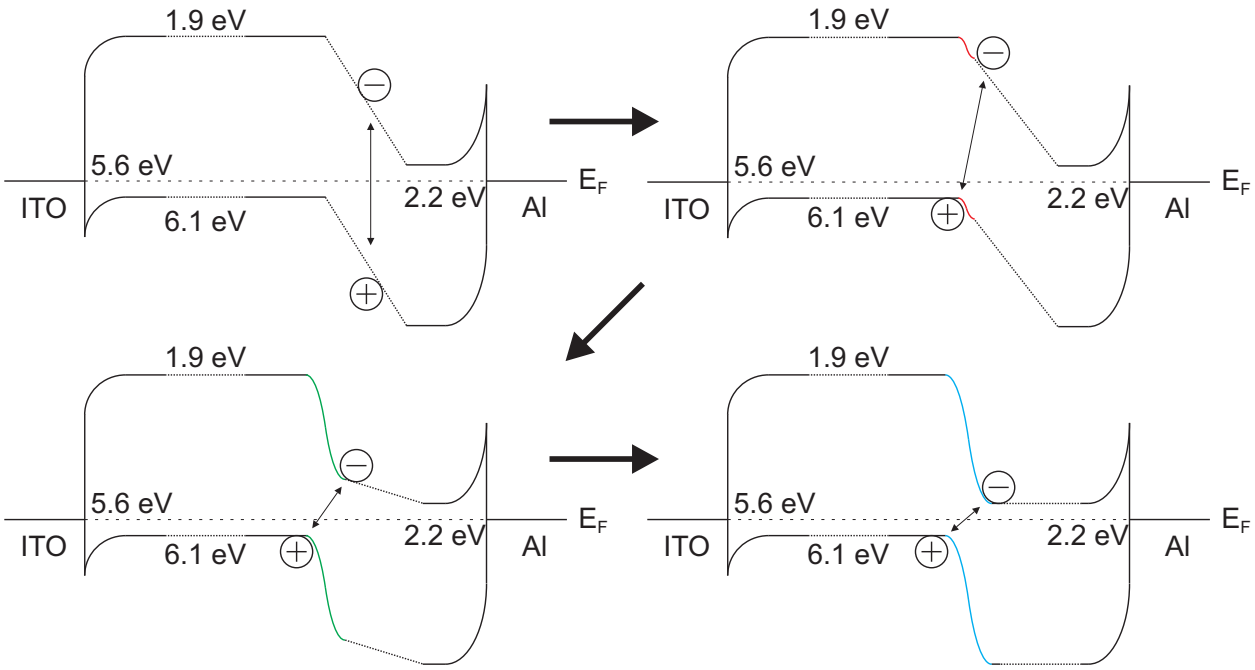

Figure 6.5: Schematics showing the evolution of the energy level situation in the p-n homojunction devices under zero bias and thermal equilibrium for an increasing thickness of the n-CBP:Cs_2CO_3 layer. Top-left: absence of n-CBP:Cs_2CO_3 layer. Top-right: very thin film of n-CBP:Cs_2CO_3 layer. Bottom-left: thicker film of n-CBP:Cs_2CO_3 layer. Bottom-right: thickness of n-CBP:Cs_2CO_3 layer exceeds that of the depletion layer within the n-doped film.

In Figure 6.5, the variation of the energy level in the device under zero bias and thermal equilibrium is schematically shown for an increasing thickness of the n-CBP:Cs_2CO_3 layer. Each diagram contains the same parabolic potential variation of the HOMO and LUMO levels of the doped materials at the electrodes caused by the Fermi level alignment. Accordingly, the position of the Fermi level E_F to the respective transport level distinguishes the p-doped from the n-doped layers. The work function of CBP:MoO_3 and CBP:Cs_2CO_3 at 5.6 eV and 2.2 eV, respectively, are taken from the results of this work for similar doping concentrations. The dotted lines represent the HOMO and LUMO levels of the intrinsic layers. It is assumed that the intrinsic CBP layer which is closer to the ITO anode exhibits comparable energy levels as the p-doped layers due to its very low charge carrier density. Accordingly, the entire built-in voltage drops across the other intrinsic layer without n-CBP:Cs_2CO_3 layer in the middle of the device (shown in the top-left diagram). Note that the built-in voltage normally corresponds to the work function difference of the doped layers yielding 3.4 V. On the other hand, the onset voltage under forward-bias only amounts to 2.9 V. By inserting

a thin film of n-CBP:Cs_2CO_3 into the device, the onset voltage decreases slightly according to the potential drop at the p-n junction in the middle of the device (shown in the top-right diagram). Thus, it is assumed that the charge carriers recombine through the small space charge region formed at the interface as indicated by the diagonal bidirectional arrows. In this case, a charge generation in reverse-bias is only possible at very high voltages due to the large barrier height for electron tunneling under zero bias between the HOMO level of the p-doped layer and the LUMO level of the n-doped film. The onset voltage under forward-bias further decreases for increasing thickness of the n-CGL component until the whole built-in potential only varies parabolically at the p-n junction and does not drop across the intrinsic layer any more (shown in the bottom-left and bottom-right diagrams, respectively). The onset voltage of charge separation concomitantly drops to very low values due to the high electric field at the p-n junction and the approximate energy level alignment between the HOMO level of the p-doped layer and the LUMO level of the n-doped one.

According to the energetic situation and Fermi level alignment at thermal equilibrium of inorganic p-n junctions, the total depletion width W_{tot} is given by [34]

$$W_{tot} = \sqrt{\frac{2\epsilon_0\epsilon_r}{q}\left(\frac{p+n}{pn}\right)V_{bi}} \tag{6.1}$$

and amounts to 13.9 nm, taking the free charge carrier densities as above-mentioned and assuming the built-in voltage V_{bi} of 3.4 V. Due to the similar values for holes and electrons, it can be concluded that the depletion width in the n-doped layer should be 7 nm in thickness which is in good agreement with the experimental value of 9 nm corresponding to the minimal thickness of the n-CGL component. Nevertheless, the origin of the residual onset voltage of charge generation of 0.6 V in spite of a completed space charge region remains questionable.

The energy difference between the HOMO level of the p-doped layer and the LUMO level of the n-doped one at the completed p-n junction amounts to 0.8 eV which could be one reason explaining a non-efficient charge generation mechanism. On the other hand, such an energy level situation will always be subject to an organic charge generation layer due to the Fermi level pinning above the HOMO and below the LUMO of p- and n-type doped layers. Nevertheless, it has been demonstrated that similar p-n heterojunction-CGL devices exhibit a negligible onset voltage of charge generation for sufficiently thick doped organic layers [118]. This could be explained by the fact that a charge transfer is not directly bound to the HOMO and LUMO levels of the organic semiconductors due to the Gaussian distribution of the density of states into the band gap. Therefore, there must be another reason for the existence of a residual onset voltage in spite of the completion of the space

charge region at the CBP homojunction. Figure 6.6 displays the *I-V* characteristics of a simplified p-n diode comprising a 25 nm thick CBP:MoO_3 layer deposited on ITO and capped by a 25 nm thick CBP:Cs_2CO_3 layer as well as completed by an Al top contact. The results of several measurement steps on the same device were listed including the application of reverse- and forward-bias with different voltage ranges. It is clearly observed that the *I-V* characteristics change from measurement to measurement, especially after the application of voltages considerably higher than the onset voltages of charge generation as demonstrated by the curves of measurement step no. 3, 4, and 5. The onset voltages apparently increase indicating an incrementally inefficient charge generation mechanism due to a non-completed space charge region at the p-n interface. This could be explained by the interdiffusion of dopants at the interface at high electric fields leading to the formation of a small non-doped region hampering the charge separation at low external fields. Such diffusion could have partially occurred already after the deposition of the materials so that a residual onset voltage of charge generation follows as a result. Particularly, the polycrystalline structure of CBP is supposed to be the main reason for the interdiffusion of the dopants. This could be prevented in homojunction-CGLs based on amorphous ambipolar materials like S-2CBP.

6.2 Mechanism of Charge Generation in TMO based Interconnecting Units

It has been recently shown that the insertion of a 1 nm thick film of ReO_3 between the p- and n-component of a CGL significantly improved the efficiency of the stacked OLEDs [185]. Therefore, the role of neat TMO films in CGLs will be analyzed in the following section

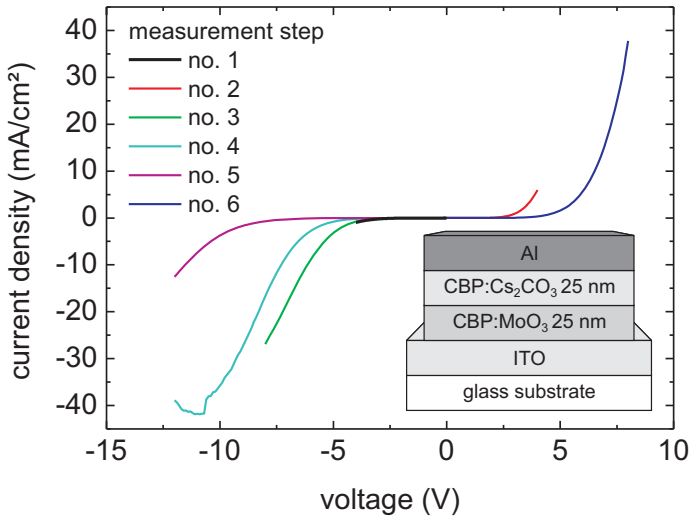

Figure 6.6: Current density versus voltage characteristics of a simplified p-n homojunction device as a result of several measurement steps in forward- and reverse-bias. Inset: layer sequence.

since speculation remains about the mechanism operating at TMO based CGLs. Terai *et al.* proposed a thermal stimulation model in which the charge generation is claimed to be thermally assisted. Based on the assumption of impurity levels within the bandgap of V_2O_5, electrons are supposed to diffuse from the valence band of the TMO to the LUMO of the adjacent n-type doped electron-transport layer (ETL), which is regarded as the charge generation mechanism [186]. Very recently, Qi *et al.* suggested a specific energy-level alignment between Li doped BCP and MoO_3 to explain the charge generation mechanism. The assumption made is that of a thermally assisted tunneling injection of electrons into the ETL and a concomitant hole generation within the TMO layer [187]. In that model, MoO_3 is assumed to be a p-type semiconductor with the valence band and conduction band located at 5.7 and 2.3 eV below vacuum level *(E_{vac})*, respectively. However, the electronic structure of MoO_3 must be revised as has been proved in Chapter 4 of this work. Based on the results obtained by UPS and IPES, MoO_3 exhibits a deep-lying conduction band at 6.7 eV and a high work function of 6.9 eV and therefore shows properties of an n-type semiconductor. Similar results have been shown for WO_3 exhibiting a conduction band minumum at 6.5 eV and a work function at 6.7 eV. Consequently, the CGL model mentioned above, in which holes are claimed to be generated within the TMO and subsequently drift towards the HTL, must be revised entirely [188].

To clarify the TMO-based CGL mechanism, a detailed study of the interconnecting unit placed in a stacked double OLED structure will be presented in the following. By conventional vertical stacking, an abrupt heterointerface is automatically formed between a Cs_2CO_3 doped BPhen layer as the topmost ETL of the bottom light-emitting unit, and WO_3 as the lowermost constituent of the top OLED depicted in Figure 6.7a. To analyze the functionality of the interconnecting unit, the thickness of its components are varied and the electro-optical properties of the stacked OLEDs are measured. With the help of luminance–current density–voltage *(L–I–V)* measurements, the analysis of the angular resolved spectral emission characteristics, and simultaneous optical device simulation, the minimum required thickness will be unambiguously identified that makes each individual constituent of the interconnecting unit fully functional [188]. Using the energetics determined via UPS and IPES for the interfaces between the interconnecting unit and adjacent charge transport layers [54], it will be demonstrated that the actual charge generation process takes place at the interface between the thin film of WO_3 and the neighboring HTL. A large interface dipole between these two layers is found. These results prove former assumptions of a thermally assisted charge generation mechanism within the TMO to be invalid. Based on these findings, a general design rule for CGLs involving TMOs will be suggested [188].

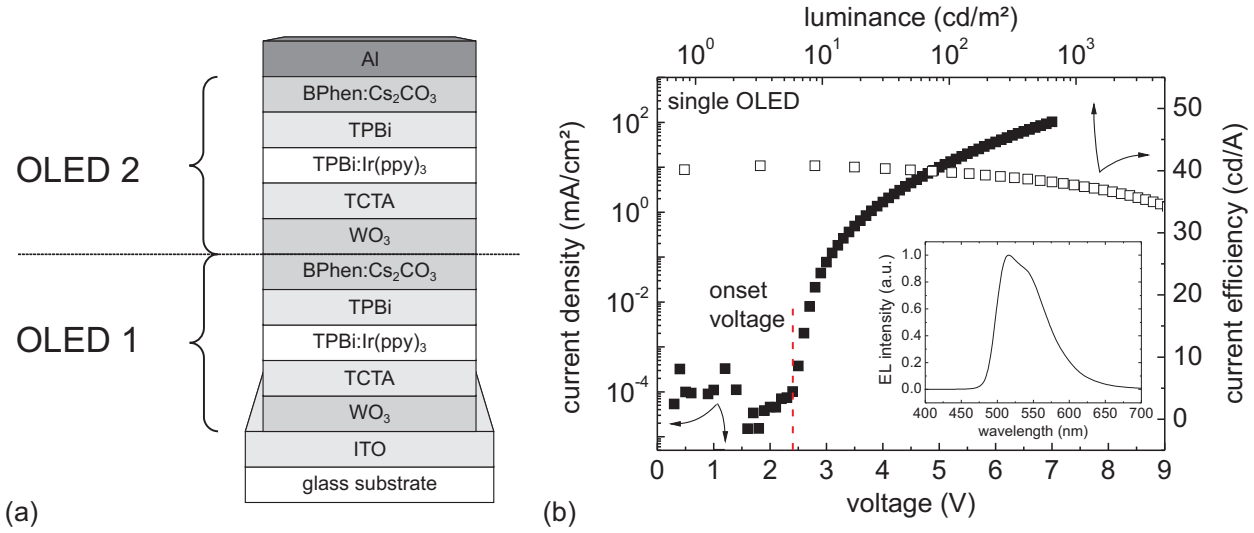

Figure 6.7: (a) Layer sequence of the twofold stacked OLED. (b) Luminance–current density–voltage and current efficiency characteristics of single OLED comprising the layer sequence and thicknesses of OLED 1 of series A given in Table 6.2. Inset: electroluminescence spectrum of the single OLED.

Table 6.1: Layer sequence and thicknesses (given in nm) of the two OLED series A and B.

OLED No.	Layer \ Series	A	B
		Al top electrode	
OLED 2	$BPhen:Cs_2CO_3$	20	20
	TPBi	30	30
	$TPBi:Ir(ppy)_3$	10	10
	TCTA	(45 - X)	40
	WO_3	X	5
OLED 1	$BPhen:Cs_2CO_3$	20	Y
	TPBi	30	(50 - Y)
	$TPBi:Ir(ppy)_3$	10	10
	TCTA	40	40
	WO_3	5	5
		ITO bottom electrode	

The twofold stacked OLEDs were prepared by stacking two green light emitting organic diodes with identical layer sequence on top of each other (Figure 6.7a). Each OLED comprises a thin film of WO_3 followed by TCTA as the HTL and TPBi as the ETL. The emission layer is formed by $Ir(ppy)_3$ doped TPBi (7 vol %) located between the HTL and the ETL. Finally, each OLED unit is capped by Cs_2CO_3 doped BPhen (16 wt %) as an efficient

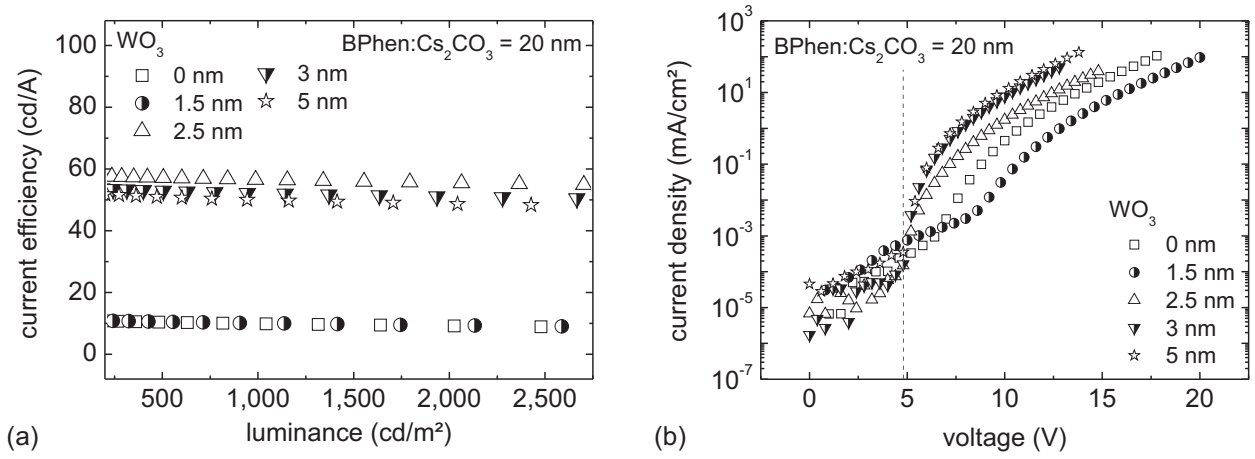

Figure 6.8: (a) Current efficiency versus luminance characteristics and (b) current density versus voltage characteristics of the twofold stacked OLEDs upon variation of the WO_3 layer thickness with constant thickness of the BPhen:Cs_2CO_3 component (series A).

electron-injecting layer (EIL). A 140 nm thick ITO bottom electrode and an Al top electrode are used. Table 6.2 summarizes the thicknesses for the two OLED series used in this analysis. Figure 6.7b shows the *L-I-V* data and the current efficiency characteristics of a single OLED comprising the layer sequence and thicknesses given for the bottom OLED (denoted as OLED 1) of the stacked OLEDs of series A and being capped by the opaque Al top electrode. The onset voltage of this diode amounts to 2.4 V, which exactly corresponds to the maximum wavelength of the greenish electroluminescence (EL) at 516 nm shown in the inset of Figure 6.7b. The current efficiency yields approximately 40 cd/A at 100 cd/m^2 and decreases for higher luminance values due to the efficiency roll-off caused by the increasing triplet-triplet annihilation and triplet-polaron quenching [131].

Critical layer thickness

As a first step to study the heterointerface between the two stacked sub-OLEDs, the thickness of the WO_3 layer in OLED 2 was varied from 0 to 5 nm and the thickness of the neighboring HTL was simultaneously changed from 45 to 40 nm, keeping the overall thickness of the stacked OLEDs as well as the distance between the emission layers and the electrodes constant (Table 6.2, series A). The current efficiency versus luminance characteristics are shown in Figure 6.8a. Without WO_3, or for a TMO thickness less than 1.5 nm, the stacked OLEDs only exhibit low current efficiencies of about 10 cd/A. This changes abruptly for a thickness of the TMO layer of 2.5 nm and beyond, for which the current efficiencies jump to values between 50 and 56 cd/A (at 1.000 cd/m^2). Furthermore, the *I-V* characteristics of the stacked

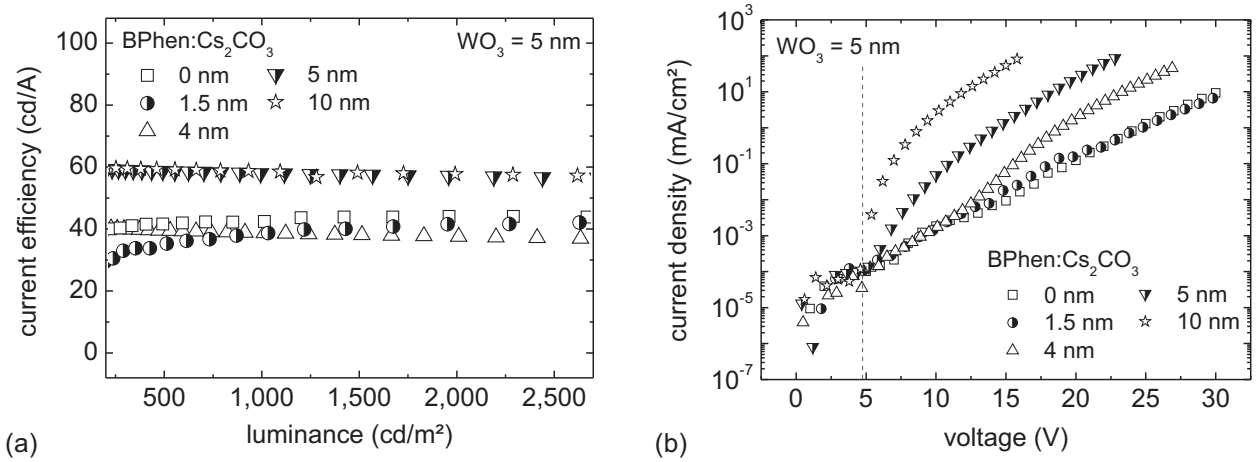

Figure 6.9: (a) Current efficiency versus luminance characteristics and (b) current density versus voltage characteristics of the twofold stacked OLEDs upon variation of the BPhen:Cs_2CO_3 layer thickness with constant thickness of the WO_3 component (series B).

OLEDs shown in Figure 6.8b indicate that only for devices with a WO_3 layer thickness larger than 2 nm the onset voltage is less than 5 V. This suggests an efficient charge generation mechanism, since the onset voltage is only twice that of each individual sub-OLED of similar structure as demonstrated for the single OLED in Figure 6.7b. In this case, no significant potential drop occurs within the CGL to generate and separate the charge carriers. The first result of this experiment is therefore that the CGL interconnecting architecture is not fully functional in stacked OLED devices as long as the WO_3 layer thickness is below a critical value of 2.5 nm [188].

A further set of experiments leads to a similar conclusion regarding the EIL, in that the efficiency of stacked OLEDs is significantly lower than 60 cd/A when using insufficiently thick films of Cs_2CO_3 doped BPhen at the heterointerface. The thickness of the n-doped ETL of OLED 1 (Figure 6.7a) is varied from 0 to 10 nm while simultaneously changing the thickness of the neighboring layer of TPBi from 50 to 40 nm and keeping the thickness of WO_3 at 5 nm as well as the overall thickness of the stacked OLEDs constant (Table 6.2, series B). Starting at a doped BPhen thickness below 5 nm, a current efficiency of around 40 cd/A was obtained as shown in Figure 6.9b. As the layer thickness increases to 5 nm and beyond, the current efficiency again jumps to higher values of around 55 to 60 cd/A, indicating full functionality of the stacked device [188]. Additionally, the *I-V* characteristics of the stacked OLEDs shown in Figure 6.9b exhibit an onset voltage of less than 5 V only in devices with a BPhen:Cs_2CO_3 layer thickness larger than 5 nm. A thickness of exactly 5 nm

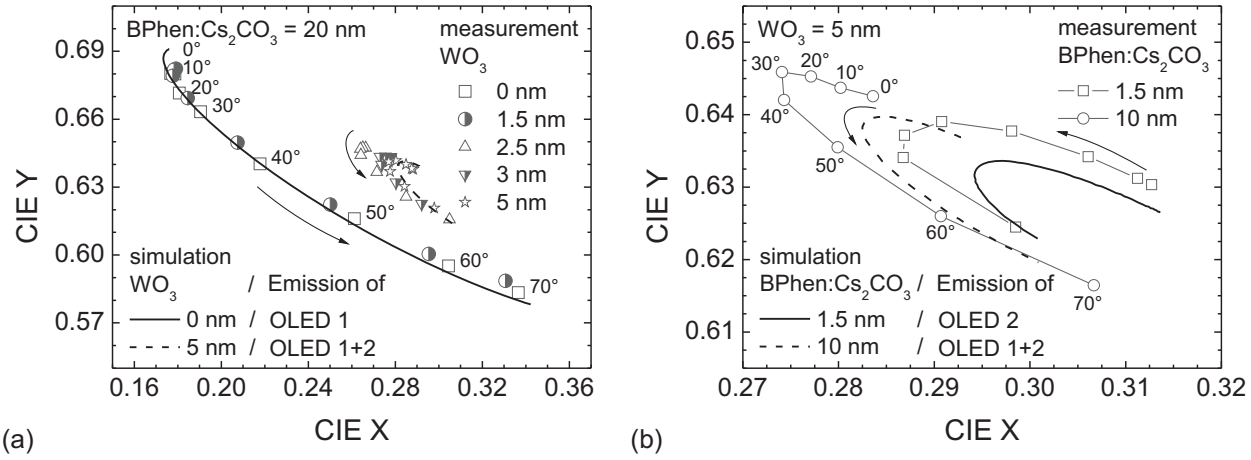

Figure 6.10: CIE characteristics of angular resolved EL spectra obtained by measurement and optical device simulation for (a) series A and (b) series B.

seems to be the limit for efficient charge generation mechanism, since the onset voltage is slightly higher than 5 V despite the jump in current efficiency to significantly higher values.

To clarify the nature of an incomplete interconnecting unit and its impact on the operation of the stacked OLEDs, angular-dependent measurements of the electroluminescence spectra were conducted and compared with optical device simulation. For a better illustration, the EL spectra are converted to CIE coordinates and summarized within respective sections of the CIE color space diagrams depicted in Figure 6.10. Thereby, the stacked OLEDs were operated at current densities from 10 to 80 mA/cm^2. The stacked OLEDs with a WO_3 layer below the critical thickness showed highly angular-dependent CIE characteristics. As shown in Figure 6.10a, the CIE values started at X = 0.18 and Y = 0.68 for the emission in forward direction and ended at X = 0.33 and Y = 0.59 at a viewing angle of 70°. The situation changed with increased thickness of the TMO layer. There, the CIE values only ranged from X = 0.64 to 0.62 and from Y = 0.28 to 0.30 for the same range of angles. The same characteristics are obtained with optical device simulation by assuming full operation of both light-emitting units. However, in the case of stacked OLEDs with an incomplete heterointerface (with WO_3 thickness below 2 nm), the CIE characteristics can only be reproduced if it is assumed that only OLED 1 emits light. As a result it is essential to note, that the low efficiency of the entire stack cannot be explained by two partially functional sub-OLEDs. On the other hand, this result indicates that the contribution of sub-OLED 1 to the total current efficiency is considerably less than that of sub-OLED 2 operated under similar conditions, as reflected by the *L*–*I*–*V* measurements above (Figure 6.8a). Thereby, the asymmetric contri-

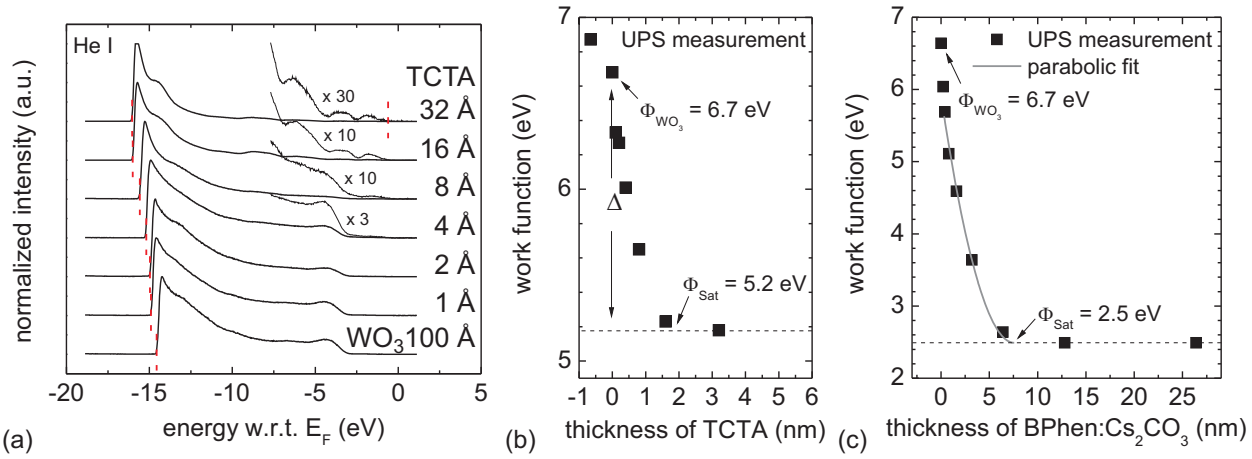

Figure 6.11: (a) UPS spectra of TCTA layers deposited on 10 nm thick WO_3 and their thickness-dependent work function characteristics (b). (c) Thickness-dependent work function characteristics of Cs_2CO_3 doped BPhen (9 wt %) deposited on 10 nm of WO_3 and measured by UPS.

bution of both light-emitting units to the luminance must be attributed to the non-optimal distance of the emission layer of sub-OLED 1 to the metallic top contact, which leads to a substantially lower out-coupling efficiency for this light-emitting unit. At the same time, the distance of the emission layer of OLED 2 of the stacked OLED to the Al cathode resembles the distance of the emission layer of the single OLED to the electrode as shown in Figure 6.7b. Therefore, similar values of current efficiency around 40 cd/A were achieved for both OLEDs. Consequently, the comparison between experiment and simulation upon variation of the thickness of the Cs_2CO_3 doped BPhen film demonstrates the following. Full operation of both light-emitting units is achieved for thick layers of BPhen:Cs_2CO_3, whereas light emission from only sub-OLED 2 is obtained for a BPhen:Cs_2CO_3 thickness below 5 nm (illustrated by two different CIE characteristics in Figure 6.10a). As a first result of these electro-optical studies, it is concluded that 5 nm of n-type doped BPhen and 2.5 nm of WO_3 represent the critical thicknesses for full operation of both sub-OLEDs of the entire stacked device. When only one sub-OLED is actually emitting, a leakage current through the non-emitting sub-OLED must supply charge carriers for the emitting sub-OLED, leading to comparatively high operating voltages for these stacked OLEDs as demonstrated by the *I-V* characteristics above [188].

CGL: Principle of operation

All reports on CGL units published so far emphasize the requirement of an n-type doped organic semiconductor layer adjacent to a p-type doped layer, a TCO layer, or a TMO layer. This is strong evidence of the essential role played by such a layer in the mechanisms operating in the CGL. In the previous section, it has been demonstrated that a sufficiently thick n-type doped layer is essential for the charge generation mechanism, leading to a high electric field at the interface which assists the charge generation and separation upon additional application of an external field. In the following, it is shown that the n-type doped organic semiconductor serves as EIL, while the actual process of charge generation occurs at the interface between the TMO and TCTA. The electronic structure of the interfaces between Cs_2CO_3 doped BPhen and WO_3 as well as WO_3 and TCTA were determined via UPS and IPES. Figure 6.11a summarizes the UPS spectra (recorded by He I line) of increasingly thicker TCTA layers deposited on 10 nm thick WO_3 [54]. As clearly observed, the UPS spectra shift to higher binding energies already at very small amounts of TCTA. From 8 Å on to higher thicknesses of TCTA, its signature becomes observable by highlighting the HOMO onset region. After the deposition of a total of 16 Å of TCTA on WO_3, no significant shift in work function is noticed for even thicker layers of the HTL. Figure 6.11b summarizes the thickness-dependent work function characteristics indicating the formation of an interface dipole Δ similar to the deposition of TCTA on MoO_3 which was demonstrated in Section 4.2.1. In this case, the interfacial dipole amounts to 1.5 eV and is completed within only 1.6 nm of the organic material. During the gradual deposition of Cs_2CO_3 doped BPhen (9 wt %) onto WO_3, the work function of the film decreases with almost parabolic characteristics, indicating the formation of a space charge region within the organic ETL as summarized in Figure 6.11c. Starting with the large value corresponding to the neat layer of WO_3, the surface work function drops and finally saturates at 2.5 eV for thicknesses of 13–26 nm. The saturation actually occurs at approximately 7.5 nm layer thickness when considering the parabolic characteristics of the work function indicated by the fit. Taking into account the IE (6.8 eV) and EA (2.4 eV) of BPhen:Cs_2CO_3 measured by UPS and IPES [54], the energy level alignment at the interface with the TMO can be represented as shown in Figure 6.12, which corresponds to the heterointerface between the bottom OLED 1 and the top OLED 2 [188].

It is evident from this schematic that no charge generation occurs between the n-type doped BPhen and the TMO layer. On the other hand, electrons reaching this interface can tunnel from the conduction band (CB) of WO_3 through the narrow potential barrier into the LUMO of the n-doped organic ETL. The higher tunneling probability is strongly supported by the fact that the high work function difference of the TMO and BPhen:Cs_2CO_3 amounts to 4.2 eV, leading to comparably high electron transport levels in the CB of WO_3 and LUMO of the ETL. These results also explain that below the minimum thickness of n-type doped

BPhen layer, an incomplete space charge region forms, the work function does not reach saturation in the BPhen covered WO_3, and the built-in potential remains too low to allow for efficient tunneling of electrons. In that case, the energy difference between the CB of WO_3 and the LUMO of BPhen:Cs_2CO_3 increases as the thickness of the n-type doped layer decreases. At the same time, the shape of the tunnel barrier for electrons changes unfavorably into a rectangle and becomes broader. Taking into account the fact that the n-type doping concentration used in the stacked OLEDs was higher than in the samples studied by UPS/IPES, the minimum thickness of 5 nm found above is in favorable agreement with the characteristic width of the space charge region derived here. On the other hand, the 2.5 nm minimum thickness of WO_3 found in the electro-optical study is believed to be simply related to the required amount of deposited material necessary to form a continuous layer of TMO. From the study of the heterointerface between the stacked OLEDs, it can be unambiguously concluded that the Cs_2CO_3 doped BPhen only acts as an EIL and is not directly involved in the charge generation process. Consequently, the actual charge generation mechanism is attributed to the heterointerface between WO_3 and TCTA within OLED 2 where the interfacial dipol leads to a small energy barrier between the HOMO of TCTA and the CB minimum of WO_3 of about 0.8 eV. This electronic configuration allows therefore electrons to be injected into the CB of the TMO from the HOMO level of the HTL, resulting in a hole in the HTL [188].

Accordingly, the findings cast some doubt on the recently published hypothesis about a two-step process of a charge generation directly within the TMO and an electron injection afterwards based on a tunneling-assisted thermionic emission into the n-type doped ETL, since that explanation neglects recent results concerning the electronic structure of

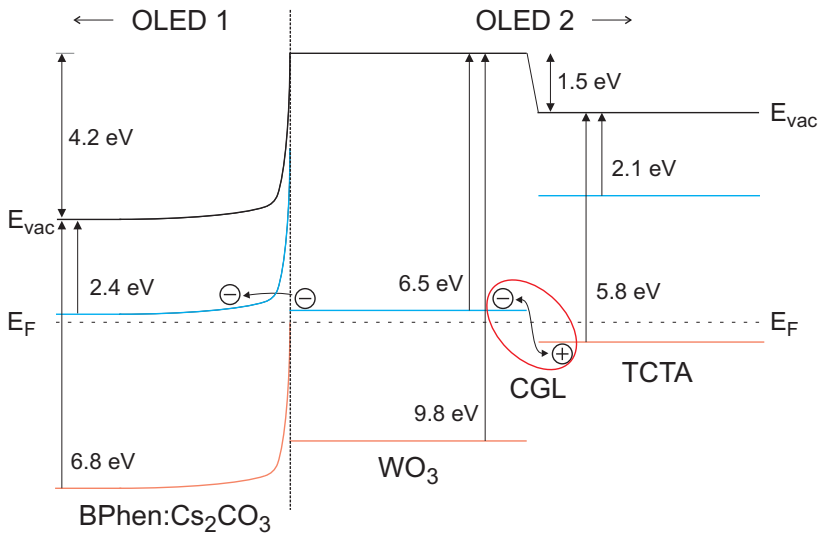

Figure 6.12: Energy level diagram of the BPhen:Cs_2CO_3/WO_3/TCTA junction determined by UPS and IPES [188].

TMOs [187]. The resulting misconception denotes the combination of n-type doped ETL and TMO as the essential components of a CGL. According to the study of this work, the combination of the TMO and HTL films can be regarded as the actual CGL, given the high work function and the deep-lying CB of the TMOs on the one hand, and the energy level alignment with the HOMO of the adjacent HTL on the other. It is also worth noting that the role of TMOs in CGLs can be compared, for example, with that of HAT-CN which also exhibits a high work function at 6 eV and a deep-lying LUMO level. This leads to the same electric field-assisted charge generation mechanism at the interface between HAT-CN and a hole transport material [189, 190]. As a consequence, the n-type doped BPhen is only required to enable an efficient electron injection into the bottom OLED unit [188].

At this stage, it can be noted that the formation of an interfacial dipole is also likely at the interface between TMO and a non-doped ETL as already demonstrated in Section 4.2.1 between MoO_3 and TPBi. This could possibly explain the steep decay of the work function within the first few monolayers of BPhen:Cs_2CO_3 deposited on top of the TMO, leading to some local deviation from the ideal parabolic fit (Figure 6.11c, first few nanometers). However, the value of the dipole is supposed to amount between 1.5 and 2 eV, which is not sufficient for an electron injection from the deep-lying CB of the TMO into the LUMO of a non-doped ETL like TPBi as has been shown by the electro-optical studies. At the same time, the interfacial dipoles at organic/organic interfaces are generally small. Figure 6.13a shows the thickness-dependent work function characteristics of a TCTA layer deposited on a 20 nm thick BPhen:Cs_2CO_3 film (16 wt %). The interface dipole amounts to only 0.3 eV and extends approximately 3 nm into the TCTA layer. Obviously, no band bending-like potential characteristics follow the work function saturation at 2.6 eV, indicating a low charge carrier density within the intrinisic hole transport material and concomitantly a negligible space charge density. Therefore, the work function at the surface is governed by that of the underlying BPhen:Cs_2CO_3 layer. Assuming a similar interface dipole between BPhen:Cs_2CO_3 and TPBi and neglecting further interface dipoles between intrinsic semiconductors, it is possible to reconstruct the electronic situation in the stacked OLEDs of series A and series B. Figure 6.13b schematically shows the energy level situtation in the entire stacked OLED without BPhen:Cs_2CO_3 (top illustration) as well as for the device without WO_3 (bottom illustration). For simplicity, it is assumed that the dipole between WO_3 and TPBi is of the same dimension as at the WO_3/TCTA interface. The energy level diagrams for both stacked OLEDs reflect the situation under zero bias voltage and explain why, in the case of series A, only OLED 2, and in the case of series B, only OLED 1 emits light for a non-completed CGL structure. It can be derived out of the schematics that a hole leakage current through the non-emitting OLED 1 is preferred in the case of the stacked OLEDs of series A, though

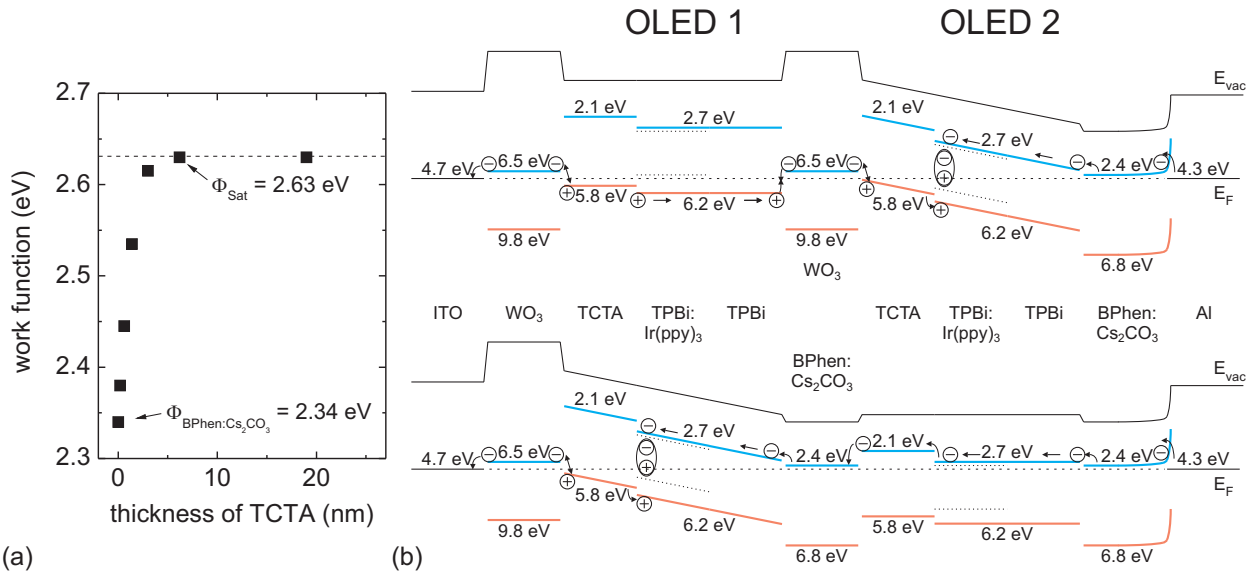

Figure 6.13: (a) Thickness-dependent work function characteristics of TCTA deposited on 20 nm thick BPhen:Cs_2CO_3 (16 wt %) layer. (b) Schematics demonstrating the energy level situations of stacked OLEDs of series A (top) and series B (bottom) for a non-functional charge generation mechanism. The dotted lines indicate the energy levels of $Ir(ppy)_3$.

leading to high operation voltages due to the forced drift of holes through the electron transporting material TPBi. In the second case, an electron leakage current through OLED 2 is preferred against a hole current, since both BPhen:Cs_2CO_3 layers surrounding the intrinsic layers of OLED 2 cause low work functions and comparably small electron injection barriers between them. Note however that TPBi and TCTA are no ambipolar materials and are not chemically stable against the hole and electron current over a longer period of operation, respectively.

6.3 Conclusion

In summary, it has been demonstrated that the charge generation mechanism in organic p-n homojunctions based on CBP relies on the formation of a space charge region due to the Fermi level alignment, leading to a strong electric field at the interface. The depletion width depends on the built-in voltage and charge carrier densities of the doped layers and determines their minimum thicknesses for an efficient electric field-assisted charge generation. An interdiffusion of dopants into the complementarily doped layers close to the interface is sup-

posed to lower the CGL performance leading to a residual onset voltage of charge generation of 0.6 V.

The charge generation in TMO-based interconnecting units of stacked OLEDs has been shown to occur at the heterointerface between the TMO and the adjacent non-doped hole-transporting layer. In spite of a substantial interfacial dipole of 1.5 eV, the energetic difference between the conduction band of WO_3 and the HOMO of TCTA only amounts to 0.8 eV, allowing for an efficient charge generation and separation at this interface. Consequently, the combination of TMO and HTL states the actual CGL. This is due to the nature of TMOs like WO_3 and MoO_3 having a deep-lying conduction band and a high work function. Accordingly, an electric field-assisted charge generation process takes place similar to the mechanism in the organic p-n junctions. Consequently, the adjacent n-type doped electron transport layer is only used to facilitate the electron injection from the TMO into the adjacent sub-OLED. These results have been used to explain the experimental results on twofold stacked OLEDs with a corresponding CGL architecture. In order to find both sub-OLEDs fully functional, a critical thickness of the doped ETL and the TMO has been determined to be 5 and 2.5 nm, respectively.

7 P-I-N Homojunction Device as Violet LED and Visible Blind Photodiode in One

Until now p-i-n homojunction devices have been extensively analyzed within the world of inorganic semiconductors, e.g. based on germanium, silicon or III-V compounds [34]. On the other hand, countless advances in terms of efficiency and lifetime have been achieved using heterojunction OLEDs since the first organic bilayer structure reported in 1987 [2]. These perpetual improvements mainly driven by the insertion of special additional charge injecting and exciton blocking layers led to complex multilayer devices. Accordingly, there is a need for simplified OLED structures not only for the ease of production but also for the preparation of model systems to study fundamental device properties [112,191,192]. Electrochemical doping of organic materials permits further simplification of OLEDs leading to p-i-n structures with high efficiencies while reducing the number of layers required for charge injection [61]. Furthermore, it is possible to use an ambipolar matrix material for both hole and electron injection [152]. Very recently, organic p-i-n homojunction diodes based on ZnPc, pentacene or bis(carbazolyl)benzodifuran (CZBDF) have been reported [52,193,194]. However, none of these devices have been shown to behave as LED and photodiode in one device as expected from their inorganic counterparts based on direct semiconductors. In the following, CBP will be used as single organic material for the preparation of p-i-n homojunctions serving as violet light-emitting devices as well as visible blind photodiodes. Consequently, the study is divided into two parts. In the first part, the generation of photocurrent by optical excitation will be analyzed. Most notably, the observation of a superlinear increase of the short-circuit current with higher optical power densities will be the focus of the following section. In the second part, the properties of light emission of the p-i-n homojunction will be discussed referring to the electrochemical doping and its impact on the emission zone.

7.1 Operation as Visible Blind Photodiode

The inset of Figure 7.1a shows the simple layer sequence of the homojunction device based on CBP. The conventional structure comprises a 35 nm thick MoO_3 doped CBP layer (14.1 mol %), followed by a 85 nm thick non-doped CBP film and completed by a 35 nm

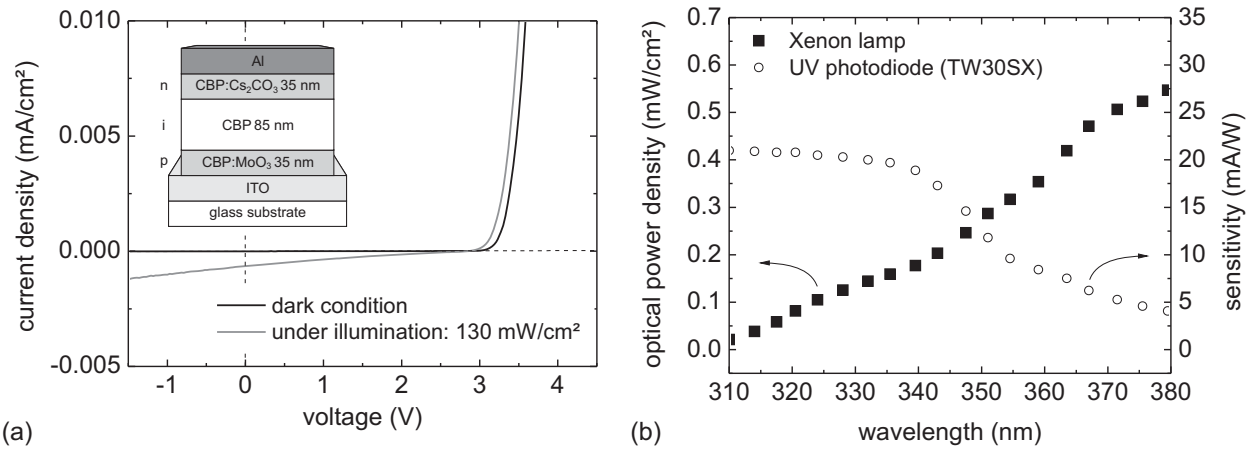

Figure 7.1: (a) Current density versus voltage characteristics of the p-i-n homojunction under dark condition and under illumination of light from sun simulator. Inset: layer sequence of device structure. (b) Spectral characteristics of the optical power density of the Xenon lamp after transmission through ITO coated glass substrate compared to the spectral sensitivity of the reference UV photodiode (TW30SX). The light emission of the Xenon lamp has been made almost monochromatic with a full width at half maximum of 10 nm.

thick Cs_2CO_3 doped layer (16.1 mol %). A 130 nm thick ITO bottom electrode and an Al top cathode were used. In analogy to inorganic semiconductor device physics, operating the organic p-i-n homojuncton in reverse-direction, one would expect the device to function as a photodiode. Figure 7.1a shows the I-V characteristics of the corresponding organic p-i-n device at dark condition and under illumination from a 300 W solar simulator (Newport) with an AM1.5G filter corresponding to an optical power density of 130 mW/cm^2. The device exhibits an extremely high open-circuit voltage V_{oc} of about 2.85 V which is slightly lower than the onset voltage of charge injection at 2.95 V under dark condition. According to the absorption characteristics of CBP, only the short-wavelength portion outside the visible spectrum is expected to generate excitons in the CBP p-i-n diode. This will be studied in more detail below. Additionally, Figure 7.1a demonstrates that for the applied voltages lower than the open-circuit voltage, the photocurrent depends almost linearly on the voltage, indicating charge carrier dissociation by the electric field as the dominant mechanism of separation, which is comparable to the behavior of common photodiodes. Note, as opposed to organic solar cells no donor-acceptor system is present, which would facilitate exciton dissociation due to dedicated heterointerfaces. In this device, the short-circuit current density amounts to 0.65 μA/cm^2. Interestingly, for voltages above the open-circuit voltage, the pho-

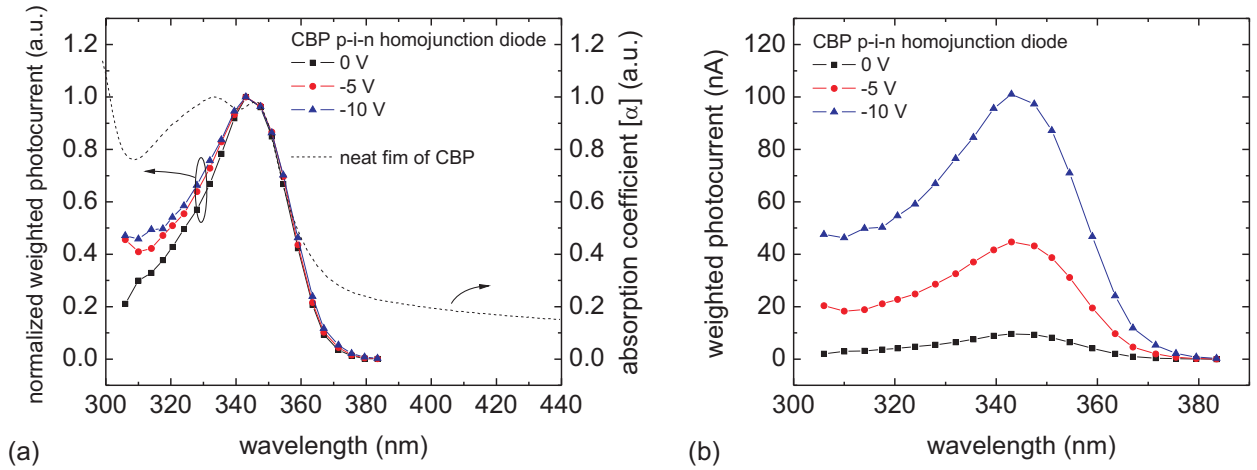

Figure 7.2: Spectral photocurrent characteristics of the p-i-n homojunction at different voltages. The photocurrent is weighted by a correction factor due to the wavelength-dependent characteristics of the Xenon lamp after transmission through an ITO coated glass substrate. (a) Normalized weighted photocurrent characteristics. The dashed line shows the normalized spectral absorption coefficient of a neat CBP film for comparison. (b) Weighted photocurrent characteristics.

tocurrent is clearly higher at each point than the dark current, probably due to an increased photoconductivity.

To further study the impact of this effect, the spectral characteristics of the photocurrent were analyzed by the illumination with quasi-monochromatic light. For the determination of the photocurrent spectrum, the spectral intensity characteristics of a Xenon lamp used in this investigation and the absorption spectrum of the ITO coated glass substrate had to be considered. For that reason, the spectral optical power density characteristics of the Xenon lamp (LTI A1020) were measured by a reference UV photodiode (TW30SX) after light dispersion by a monochromator (grating of 1200 lines/mm, Amko Light Technology Instruments) providing an almost monochromatic light with a spectral full width at half maximum of 10 nm. Note that only the spectral characteristics after transmission through an additional ITO coated glass substrate were recorded and provided as basis, in order to obtain the optical conditions within the CBP layers of the homojunction device. Figure 7.1b displays the resulting spectral characteristics of the Xenon lamp in comparison to the spectral sensitivity of the reference UV photodiode (extracted from the datasheet) in the specific region of fundamental light absorption of CBP.

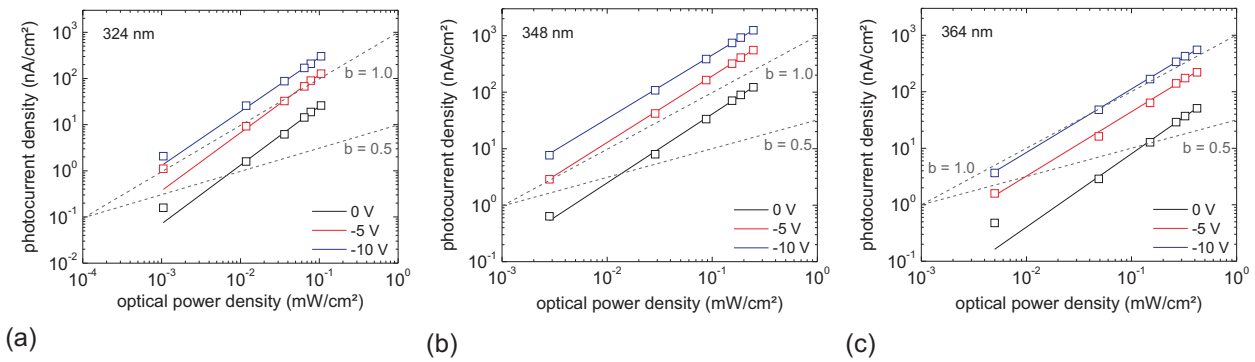

Figure 7.3: Photocurrent density versus optical power density of the p-i-n homojunction at three different wavelengths of illumination and at three different bias. The open squares represent measurement points whereas the solid lines stand for the respective fit according to the power law proportionality $J_{ph} \propto {P_{op}}^{b}$. The dashed lines with $b = 0.5$ and $b = 1.0$, respectively, are shown for comparison. (a) Illumination at 324 nm, leading to scaling factors of $b = 1.27$ at 0 V, $b = 1.26$ at -5 V, and $b = 1.17$ at -10 V. (b) Illumination at 348 nm, leading to scaling factors of $b = 1.22$ at 0 V, $b = 1.18$ at -5 V, and $b = 1.13$ at -10 V. (c) Illumination at 364 nm, leading to scaling factors of $b = 1.30$ at 0 V, $b = 1.14$ at -5 V, and $b = 1.12$ at -10 V.

Assuming a linear correlation between the light intensity and the short-circuit current, one would expect spectral characteristics of the photocurrent in accordance with the absorption spectrum of CBP. However, Figure 7.2 demonstrates an increasing deviation between the photocurrent and the absorption characteristics at wavelengths shorter than 340 nm. As can be seen in Figure 7.2a, the absorption spectrum of CBP down to the first peak at 346 nm is reproduced quite well by the photocurrent spectrum whereas the sequel including the second local maximum of absorption at 333 nm is not obvious in the spectral current characteristics. Remarkably, at shorter wavelengths the current drops steeper than expected from the absorption spectrum of CBP, even though the intensity drop of the light source has been accounted for by weighting the photocurrent at lower wavelengths with increasing correction factors, corresponding to the assumption of an illumination by a light source with a constant light intensity in the entire spectral range. This is a clear indication of a superlinear relationship between the photocurrent of the p-i-n homojunction and the light intensity. By setting a reverse-bias of -5 V and -10 V, respectively, the photocurrent considerably increases in all wavelengths as displayed in Figure 7.2b, slightly approaching the shape of the actual absorption spectrum of CBP towards shorter wavelengths.

To shed more light on the specific relationship of photocurrent and optical power density, measurements of the photocurrent density were conducted under varied illumination intensity and at varied reverse-bias. Figure 7.3 exhibits the results of the measurements for the irradiation at 324 nm (a), 348 nm (b), and 364 nm (c), with a respective variation of light intensity of more than two orders of magnitude. The optical power density-dependent measurements of the photocurrent at different wavelengths were conducted using optical neutral density filters (Melles Griot) between the Xenon lamp and the monochromator. At 0 V as well as at a reverse-bias of -5 V and -10 V a relation between the photocurrent density J_{ph} and optical power density P_{op} according to $J_{ph} \propto {P_{op}}^{b}$ with $b > 1$ can be inferred. It is known that in photovoltaic systems the scaling factor b of a power law $J_{ph} \propto {P_{op}}^{b}$ ranges from 0.5 to 1, depending on the carrier recombination mechanism [193]. A scaling factor of $b = 0.5$ implies a bimolecular recombination of statistically independent and oppositely charged carriers, leading to a sublinear increase of the photocurrent at higher light intensities. On the other hand, a scaling factor of 1 indicates a monomolecular mechanism normally given by the trapping of one sort of charge carriers and recombination with the oppositely charged moiety. A linear relationship between J_{ph} and P_{op} results, since the effect of immobilization is not influenced by the magnitude of light intensity. In this case however, the short-circuit photocurrent exhibited a scaling factor of $b = 1.22$ for the illumination at 348 nm by fitting the measurement points according to the power law.

This could be explained by a light intensity-dependent photoconductivity in CBP superimposing the charge carrier recombination process and leading to the observed scaling factors. Accordingly, the irradiation with UV light generates excitons which dissociate to charge carriers that are partially immobilized by occupying deep-lying trap states so that they can not contribute to photocurrent. On the other hand, the small density of these tail states is filled rapidly at moderate light levels, and as a result, a superlinear increase of the photocurrent due to higher conductivities for elevated intensities is evidenced (Figure 7.3). The difference to the monomolecular recombination despite similar trapping mechanism in this p-i-n homojunction is probably due to the fact that both species of charge carriers account for the filling of the respective tail states of the HOMO and LUMO level. As a result, the mobility of both holes and electrons is increased. This assumption is supported by the photocurrent characteristics at higher levels of reverse-bias. While in the short-circuit case the scaling factor amounts to $b = 1.22$, its value decreases to $b = 1.18$ and $b = 1.13$ at -5 V and -10 V, respectively. This is due to the fact that a stronger electric field leads itself to higher mobilities so that the dissociation of excitons and the transport of the resulting charge carriers to the electrodes are more effective. In addition, field-induced de-trapping of carriers leads to an overall increased photocurrent. As a result, b becomes smaller and is ultimately expected to approach 1 for high electric field levels. Additionally, the superlinear relationship between

photocurrent and optical power density seems to be wavelength-independent. The values of the scaling factor for the illumination at 324 nm and 364 nm are listed in the caption of Figure 7.3.

Another possible explanation for the slightly disproportionate increase in the photocurrent with higher light intensities could be provided by the assumption of additional multi-photon absorption processes [195]. According to this, the probability of charge generation by the dissociation of the photoinduced singlet excitons increases for excitons reaching a higher-lying energy state due to a multi-photon excitation. Such an observation was reported for organic photodiodes consisting of a single polymer layer of PFO, in which a quadratic intensity dependence was determined by the resonant excitation at 390 nm [196]. In the first step, a transition from the ground state S_0 to the first excited singlet state S_1 occurs after the absorption of one photon, followed by the transition from S_1 to a higher-lying state S_n by the absorption of another photon. That involves a long lifetime of the S_1 state so that the probability of dissociation into free charge carriers or transition to a triplet state by intersystem crossing should be low. Actually, it has been shown by spectrally resolved photoluminescence quenching experiments that CBP exhibits a comparably high singlet diffusion length of 16.8 nm [197], corresponding to a longer lifetime which possibly increases the probability of a multi-photon absorption. Moreover, the probability of charge generation by exciton-exciton collision ionization would increase in that way, which has also been proposed as the explanation for a quadratic intensity dependence of the photocurrent [198].

7.2 Operation as Violet Light Emitting Diode

Compared to the structure used in the previous analysis (also depicted in the inset of Figure 7.4b), the layer sequence, film thicknesses, and the MoO_3 doping concentration of the p-doped CBP layer were kept constant for the operation of the p-i-n homojunction device as light emitting device. Figure 7.4a summarizes the electro-optical characteristics of two homojunction devices under foward-bias, with 2.3 mol % and 15.5 mol % of Cs_2CO_3 concentration in the 35 nm thick n-doped layer, respectively. It can be clearly seen, that both the current density and the optical power density of the device with the higher n-type doping concentration show steeper characteristics.

At the same time, the EL spectra of both devices were recorded and compared with each other for different voltages (Figure 7.5a and b). The violet light emission from CBP is clearly identified. Compared with the spectra obtained from the p-n CGL-homojunction devices shown in Section 6.2, the shape and maximum wavelength of the EL is modified due to the

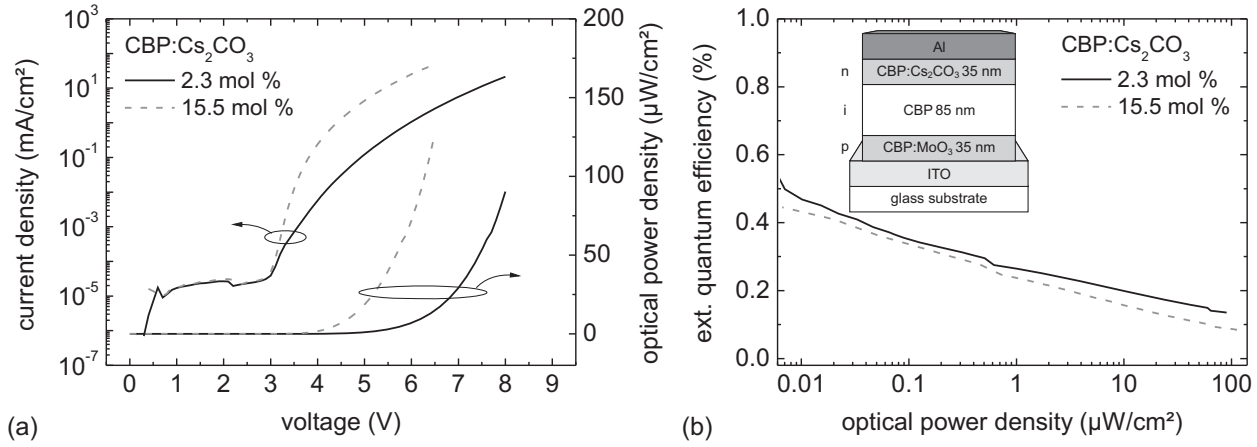

Figure 7.4: Electro-optical characteristics of two p-i-n homojunction devices exhibiting different n-type doping concentrations. (a) Current density and optical power density versus voltage characteristics. (b) External quantum efficiency characteristics. Inset: layer sequence.

varied layer sequence and altered overall thickness of the device. On the other hand, both p-i-n homojunction devices exhibit very similar EL spectra, slightly varying with the applied voltage. Therefore, it can be concluded that the electrochemically doped injection layers of the homojunction devices hardly influence the electrical characteristics which determine the shape and position of the recombination zone. This is remarkable, as the electron densities are estimated to be 7.8 x 10^{18} cm^{-3} and 1.1 x 10^{18} cm^{-3} for the higher and lower n-type doped layer, respectively, indicating a lower electron conductivity for the latter.

On the other hand, the external quantum efficiency shown in Figure 7.4b is slightly lower for the device with the substantially stronger n-type doping. Moreover, the values seem to be very low for both devices starting at 0.5 % for an optical power density of 0.01 $\mu W/cm^2$ and decreasing to 0.1 % at 100 $\mu W/cm^2$. For comparison, the single green light emitting organic diode based on the phosphorescence of $Ir(ppy)_3$ (shown in Section 6.2) yielded an external quantum efficiency of around 7 %. This is more than 25 times higher on average than the efficiency of the homojunction devices. The fact that CBP is only a fluorescent emitter would only quarter the efficiency to 1.7 % compared to that of the green light emitting device, assuming the same intrinsic photoluminescence quantum efficiency for both emitters. Therefore, further effects are supposed to lower the efficiency. Particularly, the absence of carrier confining layers in the device is supposed to lower the efficiency. Accordingly, a large number of charge carriers drifts through the device to the opposite electrodes without forming

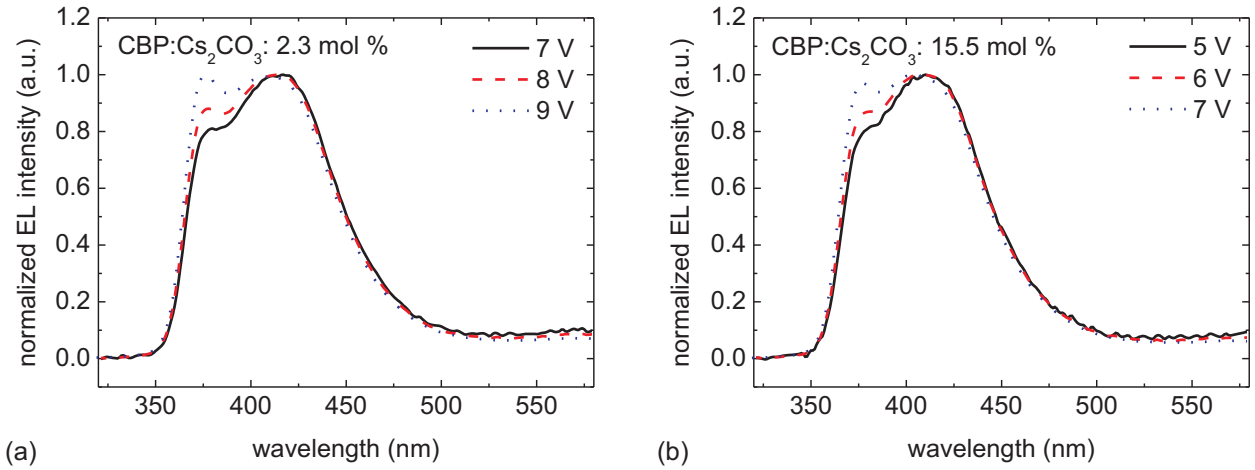

Figure 7.5: Voltage-dependent EL spectra of two p-i-n homojunction devices comprising an n-type doped layer with a Cs_2CO_3 concentration of (a) 2.3 mol % and (b) 15.5 mol %.

excitons. Additionally, the recombination zone could be distributed over the intrinsic layer. This would additionally lower the outcoupling efficiency due to the non-optimal position of a bigger part of the emission zone in respect to the metallic top contact.

That is why it is important to learn more about the characteristics of the recombination and emission zone. However, the electrical simulation of the conditions within the p-i-n homojunction affords many input parameters such as the electric field-dependent and charge carrier density-dependent mobility for holes and electrons or the exciton density-dependent energy transfer rates to positive and negative polarons. That is why it would be sufficient to study the emission zone by optical measurements and simulation in the first step. In a recent report, the profile of the emission zone in the emissive layer of polymeric OLEDs has been studied via comparison of measured and simulated EL spectra. It has been demonstrated that in those devices the main part of the emission zone was in the immediate vicinity of the ITO/PEDOT:PSS anode. This has been explained by the electron mobility μ_e of the emissive polymer being two to three orders of magnitude higher than its hole mobility μ_h [199]. In principle, the p-i-n homojunction device based on CBP would also allow for the determination of the recombination/ emission zone. Thereby, the measurement of the angular-resolved emission characteristics of the p-i-n homojunctions offers a good technique for the determination of the emission zone. Still, the polycrystalline morphology of CBP leads to a certain lack of reproducibility. Therefore, it is advisable to use amorphous ambipolar wide band gap materials like S-2CBP as basis for the p-i-n homojunction devices for future experiments.

7.3 Conclusion

For the first time, an organic p-i-n homojunction device based on CBP has been presented that operates both as a violet light emitting device and as a visible blind photodiode. A remarkable superlinear relationship between the spectral photocurrent and the irradiated optical power density was found by operation as photodiode according to the power law $J_{ph} \propto {P_{op}}^{b}$ with b of about 1.2. Light intensity-dependent photoconductivity of the p-i-n homojunction based on the dynamics of filling tail states, causing an increase of the charge carrier mobilities, was discussed as one reason. Aside from that it could be speculated about a partial multi-photon absorption process as a further possible explanation, leading to singlet excitons of higher energetic states and a higher probability of dissociation into charge carriers.
In the second part, the electro-optical characteristics of the p-i-n homojunction device operated as light emitting unit were demonstrated. The EL spectra indicated a violet light emission in agreement with the photoluminescence of CBP, modified by weak microcavity effects in the device and exhibiting a voltage dependence. The external quantum efficiency was low and yielded 0.25 % on average which was explained by the absence of carrier confining layers in the device. The comparison of two homojunction devices with differently high n-doped layers showed no influence on the spectral emission characteristics. Therefore, the optical analysis of the shape and position of the emission zone was proposed by the measurement of angular-resolved emission characteristics in order to further clarify the electrical conditions within this device. As a result, this study encourages further research on this class of organic devices for a better understanding of organic semiconductors.

8 Summary

Organic light emitting diodes are considered as the next generation of solid-state lighting and as the future of display technology. They exhibit several technological and economical advantages compared with their inorganic counterparts and are currently on the verge of mass-production. However, OLEDs still exhibit shorter lifetimes and lower efficiencies compared to inorganic LEDs. Very recently the introduction of transition metal oxides as funcional layers and electrochemical dopants has been shown to increase the efficiency and lifetime of OLEDs. In the present study, the electronic properties of these TMOs and their particular impact on OLEDs were investigated and clarified with regard to the device concepts such as charge injection, electrochemical doping and charge generation between stacked OLEDs.

Although MoO_3 and WO_3 are increasingly used in OLEDs, the previous conception of their electronic structure has to be thoroughly revised. The common belief of a EA = 2.3 eV and an IE = 5.3 eV of MoO_3 led to the concept of a p-conductor with electron-blocking properties. On the other hand, these values could not be used to explain their use as p-type dopant of organic semiconductors. Therefore in the course of this work, UPS and IPES as well as KP measurements in UHV were conducted on MoO_3 and WO_3 to reveal their actual energy levels. It could be demonstrated that their EA and IE are actually located 4 eV deeper than previously published. MoO_3 and WO_3 exhibit an EA of about 6.7 and 6.5 eV and an IE of 9.7 and 9.8 eV, respectively. Their initial work function yields approximately 6.9 and 6.7 eV, implying that these TMOs can be seen as n-type semiconductors.
In view of these novel results, it was important to further clarify the mechanism of hole injection from the anode into an organic hole transporting layer by using a TMO layer. It was demonstrated that energetically large interface dipoles between an ITO anode and MoO_3 as well as MoO_3 and HTL allowed for an efficient electron extraction from the HOMO of the HTL into the CB minimum of the TMO and a subsequent transfer of the electron to the anode. Thus, the mechanism of hole injection can be considered as a charge generation at the TMO/HTL interface leaving a hole within the HOMO of the hole transport layer. Due to the deep-lying CB of the TMOs, they do not exhibit electron-blocking properties. Only in combination with organic semiconductors having a small EA the electrons can be trapped

at the TMO/ETL interface, since the dipole between the two layers is not sufficiently large to permit efficient transfer of electrons from the CB minimum of the TMO into the LUMO.

In the next part of this study, the chemical doping of organic semiconductors by MoO_3 and Cs_2CO_3 was analyzed using UPS, IPES and KP. Clear indications of actual p-type doping by MoO_3 and n-type doping by Cs_2CO_3 could be given by the demonstration of a Fermi level shift towards the respective transport level of the ambipolar organic semiconductor CBP. Higher electrical conductivities were achieved for p- and n-type doping which was attributed to both elevated charge carrier densities and a superlinear increase of charge carrier mobility with higher doping concentrations. Most notably, the p-type doping by MoO_3 was shown to cause higher absorption of CBP due to the appearance of additional polaron absorption bands.
The efficiency of the n- and p-type dopants in several organic semiconductors was determined. The charge carrier densities were determined out of the depletion width and built-in potential, extracted from the thickness-dependent work function characteristics measured by KP. Moreover, capacitance-voltage *(C-V)* measurements of metal-insulator-semiconductor structures were shown to be an alternative to the elaborate analysis by KP, yielding similar results of charge carrier densities for doping concentrations in the range of 0.5 to 20 mol %. This was also confirmed by the comparison to a novel technique of quantitative polaron absorption measurements using the example of the determination of hole densities in MoO_3 doped S-2CBP. In general, an almost linear increase with higher p- and n-doping concentrations was found for all organic semiconductors. On the other hand, it was shown that the doping efficiency of MoO_3 is unexpectedly low despite of its favorable electronic properties with respect to the HOMO level of the organic semiconductors. Besides specific reasons concerning the polycrystalline morphology of CBP which lowers the efficiency to only 2-3 % due to a possible agglomeration of MoO_3 at the grain boundaries, there are more general factors reducing the effectiveness of all dopants in organic semiconductors. Most notably, the emergence of Coulomb potentials by the ionized dopants was discussed as the main reason for low free charge carrier densities.

Interconnecting units based on organic p-n heterojunctions or based on the insertion of neat TMO films were used for the charge generation in stacked OLEDs. In order to clarify the mechanism of charge generation and to find the minimum thickness of the used layers as a design rule, an organic p-n homojunction-CGL based on CBP and established by doping with MoO_3 and Cs_2CO_3 was analyzed. The experimental results confirmed the model of the formation of a free charge carrier density-dependent space charge region, causing a high electric field and a small energy difference between the HOMO and LUMO level of the p- and n-doped layer at the p-n interface. A partial interdiffusion of the dopants at the inter-

face, however, is supposed to lower the efficiency of the p-n homojunction-CGL expressed by higher onset voltages of charge generation in reverse-bias.
The role of a neat TMO film in interconnecting units was analyzed by angular-resolved measurements of the emission characteristics of twofold stacked OLEDs combined with optical simulation. A critical thickness of the Cs_2CO_3 doped BPhen layer and WO_3 film, together forming the interface between the two sub-OLEDs, was determined to be 5 and 2.5 nm, respectively. Photoelectron spectroscopy and KP analysis revealed the formation of an interface dipole between the two layers, followed by a subsequent space charge region within BPhen:Cs_2CO_3, leading to an energy level alignment between its LUMO level and the CB minimum of WO_3. Very similar to the results of hole injection assisted by MoO_3, it was demonstrated that the energetic difference between the CB minimum of WO_3 and the HOMO level of the neighboring TCTA layer only amounts to 0.8 eV. Consequently, an electric field-assisted charge generation was attributed exclusively to the WO_3/TCTA interface. In contrast to previous publications attributing the charge generation to the interface between the n-doped ETL and the TMO, it could be demonstrated that the neighboring BPhen:Cs_2CO_3 layer is only necessary for the efficient electron injection from the TMO into the adjacent sub-OLED after the actual charge generation at the TMO/HTL interface.

Finally, a novel p-i-n homojunction OLED based on CBP was presented which operates both as a violet light emitting diode and a visible blind photodiode. P- and n-type doping of the thin injection layers was established by MoO_3 and Cs_2CO_3, respectively. Operating as photovoltaic device, a very high open circuit voltage around 2.9 eV was found. Additionally, a superlinear relationship was demonstrated between the spectral photocurrent and the irradiated optical power density, independent of the wavelength of illumination in the range of the fundamental absorption of CBP. A superlinear increase of photoconductivity due to the filling of tail states by the photogenerated charge carriers as well as a partial multi-photon absorption process by excitons were given as possible explanations. Operating the p-i-n homojunction as light emitting diode, a violet light emission was shown corresponding to the photoluminescence of CBP. The low external quantum efficiency of 0.25 % on average was attributed to the absence of charge confining layers within the device. Nevertheless, this novel class of organic devices is supposed to give a new insight into the mechanisms of organic semiconductors.

A Molecular Structures

Organic materials mentioned in this work are listed by their commonly cited abbreviations together with their constitutional formula. The organic materials employed for this work are illustrated in Figure A.1 together with the indication of their molecular weight.

1-TNATA	:	4,4',4"-Tris(N-(1-naphthyl)-Nphenylamino)-triphenylamine
2-TNATA	:	4,4',4"-Tris(N-(2-naphthyl)-Nphenylamino)-triphenylamine
Alq_3	:	Tris(8-quinolato)aluminum
BCP	:	2,9-dimethyl-4,7-diphenyl-1,10-phenanthroline
BPhen	:	4,7-diphenyl-1,10 phenanthroline
BSBF	:	2-(9,9'-spirobifluoren-2-yl)-9,9'-spirobifluorene
C_{60}	:	buckminsterfullerene
CBP	:	4,4'-bis(carbazol-9-yl)biphenyl
$CoCp_2$	:	bis-(cyclopentadienyl)cobalt(II)
$CoCp_2^*$	:	decamethylcobaltocene
CZBDF	:	Bis(carbazolyl)benzodifuran
DDQ	:	dichlorodicyanoquinone
F_4-TCNQ	:	2,3,5,6-tetrafluoro-7,7,8,8-tetracyano-quinodimethane
HAT-CN	:	1,4,5,8,9,11-hexaazatriphenylene-hexacarbonitrile
$Ir(ppy)_3$	:	fac tris(2-phenylpyridin)iridium
m-MTDATA	:	4,4',4"-tris(3-methylphenylphenylamino)triphenylamine
MEH-PPV	:	poly(2-methoxy-5-(2-ethylhexyloxy)-1,4-phenylenevinylene)
MeO-TPD	:	N,N,N',N'-tetrakis(4-methoxyphenyl)-benzidine
NBPhen	:	2,9-Bis(naphthalen-2-yl)-4,7-diphenyl-1,10-phenanthroline
NPB	:	N,N'-diphenyl-N,N'-bis(1,1'-biphenyl)-4,4'-diamine
PEDOT	:	Poly(3,4-ethylenedioxy)thiophene
Pentacen		
PFO	:	poly(9,9dioctylfluorene)

PSS	:	Poly(styrenesulfonate)
RR-P3HT	:	regioregular poly(3-hexylthiophene)
$Ru(terpy)_2$	:	transition metal complex bis(terpyridine)ruthenium(II)
S-2CBP	:	2,7-Bis(9-carbazolyl)-9,9-spirobifluorene
TAPC	:	1,1-bis(di-4-tolylaminophenyl)cyclohexane
TCNQ	:	tetracyanoquinodimethane
TCTA	:	4,4',4"-Tri(N-carbazolyl)-triphenylamin
TDATA	:	4,4',4"-tris-N,N-diphenyl-amino-triphenylamine
TPBI	:	1,3,5-tri(phenyl-2-benzimidazole)-benzene
TPD	:	N,N-bis(3-methylphenyl)-N,N-diphenylbenzidine
ZnPc	:	zinc phthalocyanine

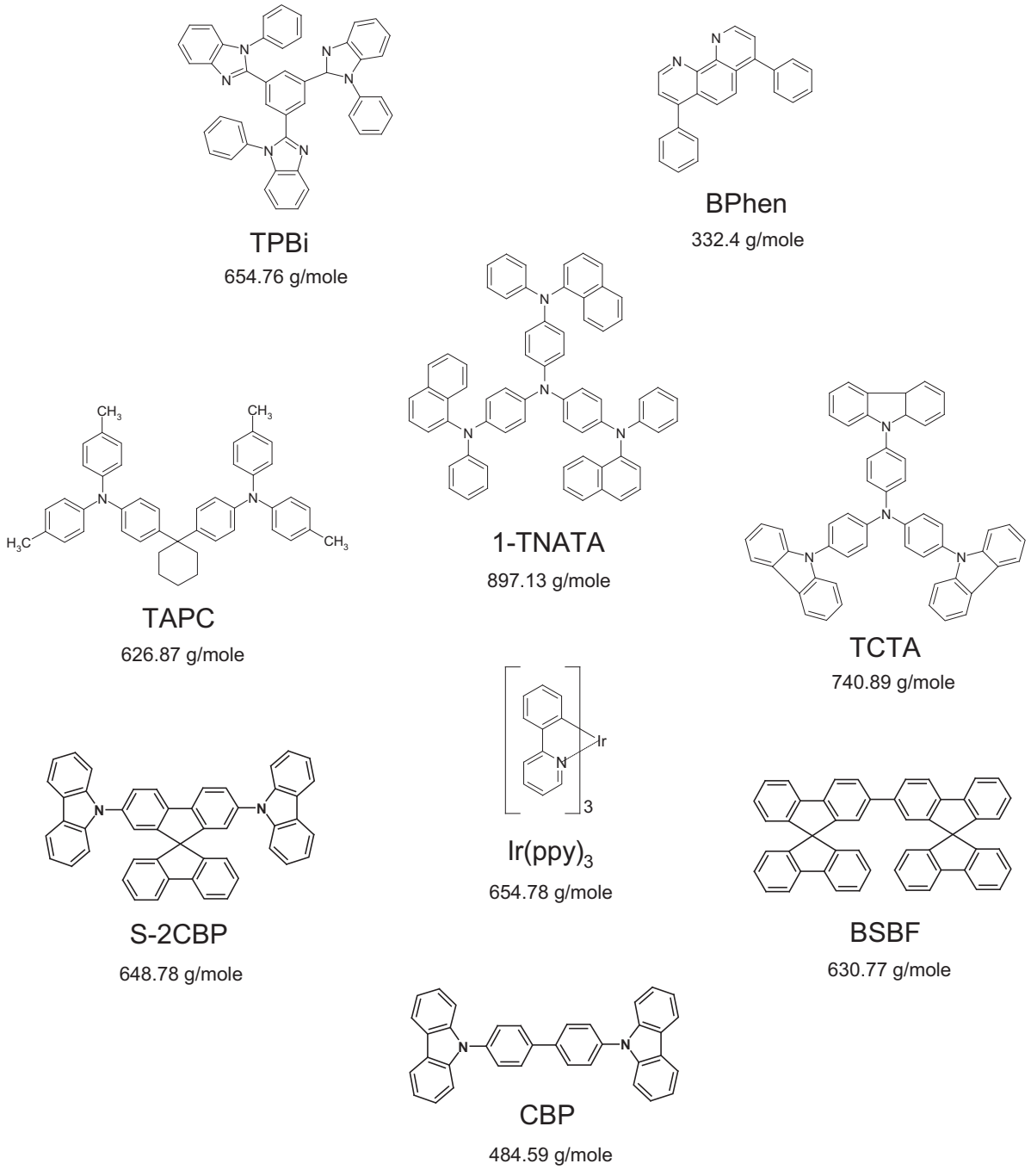

Figure A.1: Molecular structures and the molecular weight of the organic materials used in this work.

List of Publications

1. T. Rabe, S. Hamwi, J. Meyer, P. Görrn, T. Riedl, H.-H. Johannes, W. Kowalsky: *Suitability of lithium doped electron injection layers for organic semiconductor lasers.* Appl. Phys. Lett. **90**, (2007), 151103.

2. M. Kröger, S. Hamwi, J. Meyer, T. Dobbertin, T. Riedl, W. Kowalsky, H.-H. Johannes: *Temperature-independent field-induced charge separation at doped organic/organic interfaces: Experimental modeling of electrical properties.* Phys. Rev. B **75** (2007), 235321.

3. J. Meyer, T. Winkler, S. Hamwi, S. Schmale, M. Kröger, P. Görrn, H.-H. Johannes, T. Riedl, E. Lang, D. Becker, T. Dobbertin, W. Kowalsky: *Highly efficient fully transparent inverted OLEDs.* SPIE-Int. Soc. Opt. Eng. **6655** (2007), 1, 66550L.

4. A. Janssen, T. Riedl, S. Hamwi, H.-H. Johannes, W. Kowalsky: *Highly efficient organic tandem solar cells using an improved connecting architecture.* Appl. Phys. Lett. **91**, (2007), 073519.

5. J. Meyer, S. Hamwi, T. Bülow, H.-H. Johannes, T. Riedl, W. Kowalsky: *Highly efficient simplified organic light-emitting diodes.* Appl. Phys. Lett. **91** (2007), 113506.

6. J. Meyer, S. Schmale, S. Hamwi, T. Winkler, H.-H. Johannes, T. Riedl, W. Kowalsky: *Electrochemical p-type doping of organic hole transport materials with deep lying HOMO levels.* 14th International Workshop & International Conference on Science and Technology of Emissive Displays and Lighting, Rome (2008), 49.

7. J. Meyer, T. Winkler, S. Hamwi, S. Schmale, H.-H. Johannes, T. Riedl, W. Kowalsky: *Transparent inverted OLEDs with tungsten oxide buffer layer.* Adv. Mater. **20** (2008), 3839.

8. J. Meyer, P. Görrn, S. Hamwi, H.-H. Johannes, T. Riedl, W. Kowalsky: *Indium-free transparent organic light emitting diodes with Al doped ZnO electrodes grown by atomic layer and pulsed laser deposition.* Appl. Phys. Lett. **93** (2008), 073308.

9. J. Meyer, S. Hamwi, S. Schmale, T. Winkler, H.-H. Johannes, T. Riedl, W. Kowalsky: *A strategy towards p-type doping of organic materials with HOMO levels beyond 6 eV using tungsten oxide.* J. Mater. Chem. **19** (2009), 702.

10. J. Meyer, P. Görrn, F. Bertram, S. Hamwi, T. Winkler, H.-H. Johannes, T. Weimann, P. Hinze, T. Riedl, W. Kowalsky: *Al_2O_3/ZrO_2 nanolaminates as ultra-high gas diffusion barriers - A strategy towards reliable organic electronic encapsulation.* Adv. Mater. **21** (2009), 1845.

11. M. Kröger, S. Hamwi, J. Meyer, T. Riedl, W. Kowalsky, A. Kahn: *P-type doping of organic wide band gap materials by transition metal oxides: a case-study on molybdenum trioxide.* Org. Electron. **10** (2009), 932.

12. J. Meyer, D. Schneidenbach, P. Görrn, F. Bertram, T. Winkler, S. Hamwi, H.-H. Johannes, T. Riedl, W. Kowalsky, P. Hinze, T. Weimann: *Highly-efficient gas-diffusion barriers based on nanolaminates prepared by low-temperature ALD.* SID Digest 09 (2009), 1706.

13. S. Hamwi, J. Meyer, S. Schmale, T. Winkler, H.-H. Johannes, T. Riedl, W. Kowalsky: *Light emitting organic p-i-n homo diodes based on chemically doped wide band gap materials.* ICMAT 2009, Singapore, Symposium N (2009), 43.

14. D. Schneidenbach, J. Meyer, P. Görrn, S. Hamwi, T. Winkler, H.-H. Johannes, T. Riedl, W. Kowalsky: *Transparent OLED displays: technology development (invited).* EURODISPLAY 2009, Rome, (2009), 154.

15. J. Meyer, D. Schneidenbach, T. Winkler, S. Hamwi, T. Weimann, P. Hinze, S. Ammermann, H.-H. Johannes, T. Riedl, W. Kowalsky: *Reliable thin film encapsulation for organic light emitting diodes grown by low-temperature atomic layer deposition.* Appl. Phys. Lett. **94** (2009), 233305.

16. S. Hamwi, J. Meyer, T. Winkler, T. Riedl, W. Kowalsky: *P-type doping efficiency of MoO_3 in organic hole transport materials.* Appl. Phys. Lett. **94** (2009), 253307.

17. M. Kröger, S. Hamwi, J. Meyer, T. Riedl, W. Kowalsky, A. Kahn: *Role of the deep-lying electronic states of MoO_3 in the enhancement of hole-injection in organic thin films.* Appl. Phys. Lett. **95** (2009), 123301.

18. M. Lehnhardt, S. Hamwi, M. Hoping, J. Reinker, T. Riedl, W. Kowalsky: *Charge carrier densities in chemically doped organic semiconductors verified by two independent techniques.* Appl. Phys. Lett. **96** (2010), 193301.

19. J. Meyer, M. Kröger, S. Hamwi, F. Gnam, T. Riedl, W. Kowalsky, A. Kahn: *Charge generation layers comprising transition metal-oxide/organic interfaces: electronic structure and charge generation mechanism.* Appl. Phys. Lett. **96** (2010), 193302.

20. S. Hamwi, J. Meyer, M. Kröger, T. Winkler, M. Witte, T. Riedl, A. Kahn, W. Kowalsky: *The role of transition metal oxides in charge-generation layers for stacked organic light-emitting diodes.* Adv. Funct. Mater. **20** (2010), 1762.

Bibliography

[1] M. Pope, H. P. Kallmann, , P. Magnante: *Electroluminescence in organic crystals.* J. Chem. Phys. **38** (1963) 8, 2042–2043.

[2] C. W. Tang, S. A. VanSlyke: *Organic electroluminescent diodes.* Appl. Phys. Lett. **51** (1987) 12, 913–915.

[3] M. A. Baldo, D. F. O'Brien, Y. You, A. Shoustikov, S. Sibley, M. E. Thompson, S. R. Forrest: *Highly efficient phosphorescent emission from organic electroluminescent devices.* Nature (London) **395** (1998), 151.

[4] D. Tanaka, H. Sasabe, Y.-J. Li, S.-J. Su, T. Takeda, J. Kido: *Ultra high efficiency green organic light-emitting devices.* Jpn. J. Appl. Phys. **46** (2007) 1, L10–L12.

[5] G. Gu, G. Parthasarathy, S. R. Forrest: *A metal-free, full-color stacked organic light-emitting device.* Appl. Phys. Lett. **74** (1999) 2, 305–307.

[6] J. Kido, T. Matsumoto, T. Nakada, J. Endo, K. Mori, N. Kawamura, A. Yokoi: *27.1: Invited paper: High efficiency organic EL devices having charge generation layers.* In: SID 03 Digest, 2003, 964–965.

[7] C. N. R. Rao, B. Raveau: Transition metal oxides. New York: Wiley & Sons, Inc. 1998.

[8] S. Maekawa, T. Tohyama, S. E. Barnes, S. Ishihara, W. Koshibae, G. Khaliullin: Physics of transition metal oxides. Berlin, Heidelberg: Springer 2004.

[9] R. J. Colton, A. M. Guzman, J. W. Rabalais: *Photochromism and electrochromism in amorphous transition metal oxide films.* Acc. Chem. Res. **11** (1978), 170–176.

[10] S. K. Deb: *Reminiscences on the discovery of electrochromic phenomena in transition metal oxides.* Sol. Energy Mater. Sol. Cells **39** (1995), 191–201.

[11] J. Meyer, T. Winkler, S. Hamwi, S. Schmale, H.-H. Johannes, T. Weimann, P. Hinze, W. Kowalsky, T. Riedl: *Transparent inverted organic light-emitting diodes with a tungsten oxide buffer layer.* Adv. Mater. **20** (2008), 3839–3843.

[12] H. Schmidt, G. Flügge, T. Winkler, T. Bülow, T. Riedl, W. Kowalsky: *Efficient semitransparent inverted organic solar cells with indium tin oxide top electrode.* Appl. Phys. Lett. **94** (2009), 243302.

[13] S. Y. Ryu, J. H. Noh, B. H. Hwang, C. S. Kim, S. J. Jo, J. T. Kim, H. S. Hwang, H. K. Baik, H. S. Jeong, C. H. Lee, S. Y. Song, S. H. Choi, S. Y. Park: *Transparent organic light-emitting diodes consisting of a metal oxide multilayer cathode.* Appl. Phys. Lett. **92** (2008), 023306.

[14] K. S. Yook, S. O. Jeon, C. W. Joo, J. Y. Lee: *Transparent organic light emitting diodes using a multilayer oxide as a low resistance transparent cathode.* Appl. Phys. Lett. **93** (2008), 013301.

[15] J. Li, M. Yahiro, K. Ishida, H. Yamada, K. Matsushige: *Enhanced performance of organic light emitting device by insertion of conducting/insulating WO_3 anodic buffer layer.* Synth. Metals **151** (2005), 141–146.

[16] H. You, Y. Dai, Z. Zhang, D. Ma: *Improved performances of organic light-emitting diodes with metal oxide as anode buffer.* J. Appl. Phys. **101** (2007), 026105.

[17] C.-C. Chang, M.-T. Hsieh, J.-F.Chen, S.-W. Hwang, J.-W. Ma, C. H. Chen: *17.4: Highly power efficient organic light-emitting diodes with a novel p-doping layer.* In: SID 06 Digest, 2006, 1106–1109.

[18] D.-S. Leem, H.-D. Park, J.-W. Kang, J.-H. L. J. W. Kim, J.-J. Kim: *Low driving voltage and high stability organic light-emitting diodes with rhenium oxide-doped hole transporting layer.* Appl. Phys. Lett. **91** (2007), 011113.

[19] C.-C. Chang, J.-F. Chen, S.-W. Hwang, C. H. Chen: *Highly efficient white organic electroluminescent devices based on tandem architecture.* Appl. Phys. Lett. **87** (2005) 253501, 1–3.

[20] H. Kanno, R. J. Holmes, Y. Sun, S. Kena-Cohen, S. R. Forrest: *White stacked electrophosphorescent organic light-emitting devices employing MoO_3 as a charge-generation layer.* Adv. Mater. **18** (2006), 339–342.

[21] T. U. Kampen: *Electronic structure of organic interfaces – a case study on perylene derivatives.* Appl. Phys. A **82** (2006), 457–470.

[22] H. Bässler: *Charge transport in disordered organic photoconductors.* Phys. Stat. Sol. (b) **175** (1993), 15–56.

[23] P. N. Murgatroyd: *Theory of space-charge-limited current enganced by frenkel effect.* J. Phys. D: Appl. Phys. **3** (1969), 151–156.

[24] P. E. Burrow, Z. Shen, V. Bulovic, D. M. McCarty, S. R. Forrest, J. A. Cronin, M. E. Thompson: *Relationship between electroluminescence and current transport in organic heterojunction light-emitting devices.* J. Appl. Phys. **79** (1996) 10, 7991–8006.

[25] M. Kiy, P. Losio, I. Biaggio, M. Koehler, A. Tapponnier, P. Günter: *Observation of the Mott-Gurney law in tris(8-hydroxyquinoline) aluminium films.* Appl. Phys. Lett. **80** (2002) 7, 1198–1200.

[26] N. Hayashi, H. Ishii, Y. Ouchi, K. Seki: *Examination of band bending at buckminsterfullerene C_{60}/metal interfaces by the kelvin probe method.* J. Appl. Phys. **92** (2002) 7, 3784–3793.

[27] J. C. Scott: *Metal–organic interface and charge injection in organic electronic devices.* J. Vac. Sci. Technol. A **21** (2003) 3, 521–531.

[28] H. Ishii, K. Sugiyama, E. Ito, K. Seki: *Energy level alignment and interfacial electronic structures at organic/metal and organic/organic interfaces.* Adv. Mater. **11** (1999) 8, 605–625.

[29] J. Hwang, A. Wan, A. Kahn: *Energetics of metal-organic interfaces: new experiments and assessment of the field.* Mater. Sci. Eng. R **64** (2009), 1–31.

[30] G. Witte, S. Lukas, P. S. Bagus, C. Wöll: *Vacuum level alignment at organic/metal junctions: "cushion" effect and the interface dipole.* Appl. Phys. Lett. **87** (2005) 263502, 1–3.

[31] L. Yan, N. J. Watkins, S. Zorba, Y. Gao, C. W. Tang: *Thermodynamic equilibrium and metal-organic interface dipole.* Appl. Phys. Lett. **81** (2002) 15, 2752–2754.

[32] M. Knupfer, G. Paasch: *Origin of the interface dipole at interfaces between undoped organic semiconductors and metals.* J. Vac. Sci. Technol. A **23** (2005) 4, 1072–1077.

[33] H. Vázquez, W. Gao, F. Flores, A. Kahn: *Energy level alignment at organic heterojunctions: Role of the charge neutrality level.* Phys. Rew. B **71** (2005) 041306(R), 1–4.

[34] S. M. Sze: Physics of semiconductor devices. New York, London, Sydney, Toronto: Wiley & Sons, Inc. 1969.

[35] S. Barth, U. Wolf, H. Bässler, P. Müller, H. Riel, H. Vestweber, P. F. Seidler, W. Rieß: *Current injection from a metal to a disordered hopping system. iii. Comparison between experiment and Monte Carlo simulation.* Phys. Rev. B **60** (1999) 12, 8791–8797.

[36] C. K. Chiang, C. R. Fincher, Jr., Y. W. Park, A. J. Heeger, H. Shirakawa, E. J. Louis, S. C. Gau, A. G. MacDiarmid: *Electrical conductivity in doped polyacetylene.* Phys. Rev. Lett. **39** (1977) 17, 1098–1101.

[37] X. Zhou, J. Blochwitz, M. Pfeiffer, A. Nollau, T. Fritz, K. Leo: *Enhanced hole injection*

into amorphous hole-transport layers of organic light-emitting diodes using controlled p-type doping. Adv. Funct. Mater. **11** (2001) 4, 310–314.

[38] W. Gao, A. Kahn: *Controlled p-doping of zinc phthalocyanine by coevaporation with tetrafluorotetracyanoquinodimethane: a direct and inverse photoemission study.* Appl. Phys. Lett. **79** (2001) 24, 4040–4042.

[39] V. I. Arkhipov, P. Heremans, E. V. Emelianova, H. Bässler: *Effect of doping on the density-of-states distribution and carrier hopping in disordered organic semiconductors.* Phys. Rew. B. **71** (2005) 045214, 1–7.

[40] Y. Yamamoto, K. Yoshino, Y. Inuishi: *Electrical properties of phthalocyanine-halogen complexes.* J. Phys. Soc. Jpn. **47** (1979) 6, 1887–1891.

[41] F. Huang, A. G. MacDiarmid, B. R. Hsieh: *An iodine-doped polymer light-emitting diode.* Appl. Phys. Lett. **71** (1997) 17, 2415–2417.

[42] D. B. Romero, M. Schaer, L. Zuppiroli, B. Cesar, B. Francois: *Effects of doping in polymer light-emitting diodes.* Appl. Phys. Lett. **67** (1995) 12, 1659–1661.

[43] J. Endo, T. Matsumoto, J. Kido: *Organic electroluminescent devices with vacuum-deposited lewis-acid-doped hole-injecting layer.* Jpn. J. Appl. Phys. **41** (2002), 358–360.

[44] K. Walzer, B. Maennig, M. Pfeiffer, K. Leo: *Highly efficient organic devices based on electrically doped transport layers.* Chem. Rev. **107** (2007), 1233–1271.

[45] M. Maitrot, G. Guillaud, B. Boudjema, J. J. André, J. Simon: *Molecular material based junctions: formation of a Schottky contact with metallophthalocyanine thin films doped by the cosublimation methode.* J. Appl. Phys. **60** (1986) 7, 2396–2400.

[46] E. J. Lous, P. W. M. Blom, L. W. Molenkamp, D. M. de Leeuw: *Schottky contacts on a highly doped organic semiconductor.* Phys. Rev. B **51** (1995) 23, 17251–17254.

[47] J. Blochwitz, M. Pfeiffer, T. Fritz, K. Leo: *Low voltage organic light emitting diodes featuring doped phthalocyanine as hole transport material.* Appl. Phys. Lett. **73** (1998) 6, 729–731.

[48] P. Strohriegl, J. V. Grazulevicius: *Charge-transporting molecular glasses.* Adv. Mater. **14** (2002) 20, 1439–1452.

[49] C. K. Chan, A. Kahn, Q. Zhang, S. Barlow, S. R. Marder: *Incorporation of cobaltocene as an n-dopant in organic molecular films.* J. Appl. Phys. **102** (2007), 014906.

[50] C. K. Chan, A. Kahn: *N-doping of pentacene by decamethylcobaltocene.* Appl. Phys. A **95** (2009), 7–13.

[51] C. J. Bloom, C. M. Elliott, P. G. Schroeder, C. B. France, B. A. Parkinson: *Low work function reduced metal complexes as cathodes in organic electroluminescent devices.* J. Phys. Chem. B **107** (2003), 2933–2938.

[52] K. Harada, A. G. Werner, M. Pfeiffer, C. J. Bloom, C. M. Elliott, K. Leo: *Organic homojunction diodes with a high built-in potential: Interpretation of the current-voltage characteristics by a generalized Einstein Relation.* Phys. Rew. Lett. **94** (2005), 036601.

[53] J. Kido, T. Matsumoto: *Bright organic electroluminescent devices having a metal-doped electron-injecting layer.* Appl. Phys. Lett. **73** (1998) 20, 2866–2868.

[54] J. Meyer, M. Kröger, S. Hamwi, T. Riedl, W. Kowalsky, A. Kahn: *Charge generation layers comprising transition metal-oxide/organic interfaces: electronic structure and charge generation mechanism.* Appl. Phys. Lett. **96** (2010), 193302.

[55] J. Huang, M. Pfeiffer, A. Werner, J. Blochwitz, K. Leo, S. Liu: *Low-voltage organic electroluminescent devices using pin structures.* Appl. Phys. Lett. **80** (2002) 1, 139–141.

[56] G. Parthasarathy, C. Shen, A. Kahn, S. R. Forrest: *Lithium doping of semiconducting organic charge transport materials.* J. Appl. Phys. **89** (2001) 9, 4986–4992.

[57] B. W. D'Andrade, S. R. Forrest, A. B. Chwang: *Operational stability of electrophosphorescent devices containing p and n doped transport layers.* Appl. Phys. Lett. **83** (2003) 19, 3858–3860.

[58] Y. Gao, L. Yan: *Cs doping and energy level shift in CuPc.* Chem. Phys. Lett. **380** (2003), 451–455.

[59] H. Ding, Y. Gao: *Electronic structure of Cs-doped tris(8-hydroxyquinoline) aluminium.* Appl. Phys. Lett. **86** (2005), 213508.

[60] G. He, O. Schneider, D. Qin, X. Zhou, M. Pfeiffer, K. Leo: *Very high-efficiency and low voltage phosphorescent organic light-emitting diodes based on a p-i-n junction.* J. Appl. Phys. **95** (2004) 10, 5773–5777.

[61] S. Y. Kim, W. S. Jeon, T. J. Park, R. Pode, J. Jang, J. H. Kwon: *Low voltage efficient simple p-i-n type electrophosphorescent green organic light-emitting devices.* Appl. Phys. Lett. **94** (2009), 133303.

[62] J. Ma, X. Y. Jiang, Z. Liang, J. Cao, X. Zhang, Z. L. Zhang: *Highly power efficient organic light-emitting diodes based on Cs_2CO_3 n-doped and MoO_3 p-doped carrier transport layers.* Semicond. Sci. Technol. **24** (2009), 035009.

[63] I. G. Hill, A. Kahn, Z. G. Soos, R. A. Pascal, Jr.: *Charge-separation energy in films of π-conjugated organic molecules.* Chem. Phys. Lett. **327** (2000), 181–188.

[64] J. Franck: *Elementary processes of photochemical reactions.* Trans. Faraday Soc. **21** (1926), 536–542.

[65] E. Condon: *A theory of intensity distribution in band systems.* Phys. Rev. **28** (1926), 1182–1201.

[66] C. Adachi, M. A. Baldo, M. E. Thompson, S. R. Forrest: *Nearly 100% internal phosphorescence efficiency in an organic light emitting device.* J. Appl. Phys. **90** (2001) 10, 5048–5051.

[67] M. A. Baldo, C. Adachi, S. R. Forrest: *Transient analysis of organic electrophosphorescence. ii. Transient analysis of triplet-triplet annihilation.* Phys. Rev. B **62** (2000) 16, 10967–10977.

[68] G. He, M. Pfeiffer, K. Leo, M. Hofmann, J. Birnstock, R. Pudzich, J. Salbeck: *High-efficiency and low-voltage p-i-n electrophosphorescent organic light-emitting diodes with double-emission layers.* Appl. Phys. Lett. **85** (2004) 17, 3911–3913.

[69] B. W. D'Andrade, R. J. Holmes, S. R. Forrest: *Efficient organic electrophosphorent white-light-emitting device with a triple doped emissive layer.* Adv. Mater. **16** (2004) 7, 624–628.

[70] A. Köhler, J. S. Wilson, R. H. Friend: *Fluorescence and phosphorescence in organic materials.* Adv. Mater. **14** (2002) 10, 701–707.

[71] H. Riel, S. Karg, T. Beierlein, W. Rieß, K. Neyts: *Tuning the emission characteristics of top-emitting organic light-emitting devices by means of a dielectric capping layer: an experimental and theoretical study.* J. Appl. Phys. **94** (2003) 8, 5290–5296.

[72] V. Bulović, V. B. Khalfin, G. Gu, P. E. Burrows, D. Z. Garbuzov, S. R. Forrest: *Weak microcavity effects in organic light-emitting devices.* Phys. Rew. B **58** (1998) 7, 3730–3740.

[73] M.-H. Lu, J. C. Sturm: *External coupling efficiency in planar organic light-emitting devices.* Appl. Phys. Lett. **78** (2001) 13, 1927–1929.

[74] C. Adachi, M. A. Baldo, M. E. Thompson, S. R. Forrest: *Surface plasmons mediated emision from organic light-emitting diodes.* Adv. Mater. **14** (2002) 19, 1393–1396.

[75] K. Neyts: *Microcavity effects and the outcoupling of light in displays and lighting applications based on thin emitting films.* Appl. Surf. Science **244** (2005), 517–523.

[76] S. Möller, S. R. Forrest: *Improved light out-coupling in organic light emitting diodes employing ordered microlens arrays.* J. Appl. Phys. **91** (2002) 5, 3324–3327.

[77] T.-Y. Cho, C.-L. Lin, C.-C. Wu: *Microcavity two-unit tandem organic light-emitting devices having a high efficiency.* Appl. Phys. Lett. **88** (2006) 111106, 1–3.

[78] A. Böhler: Organische Elektrolumineszenz-Displays. Dissertation, Gemeinsame Fakultät für Maschinenbau und Elektrotechnik, Technische Universität Braunschweig, 1998.

[79] J. Meyer, P. Görrn, F. Betram, S. Hamwi, T. Winkler, H.-H. Johannes, T. Weimann, P. Hinze, T. Riedl, W. Kowalsky: *Al_2O_3/ZrO_2 nanolaminates as ultrahigh gas-diffusion barriers - a strategy for a reliable encapsulation of organic electronics.* Adv. Mater. **21** (2009), 1846–1849.

[80] J. Meyer, D. Schneidenbach, T. Winkler, S. Hamwi, T. Weimann, P. Hinze, S. Ammermann, H.-H. Johannes, T. Riedl, W. Kowalsky: *Reliable thin film encapsulation for organic light-emitting diodes grown by low-temperature atomic layer deposition.* Appl. Phys. Lett. **94** (2009), 233305.

[81] M. D. Groner, F. H. Fabreguette, J. W. Elam, S. M. George: *Low-temperature Al_2O_3 atomic layer deposition.* Chem. Mater. **16** (2004), 639–645.

[82] C. K. Chan: Materials, properties, and applications of n-doped organic semiconductors. Dissertation, Department of Electrical Engineering, Princeton University, 2008.

[83] S. Hüfner: Photoelectron spectroscopy. Berlin, Heidelberg: Springer 1996.

[84] J. Schöbel: UV-Photoelektronenspektroskopie zur Untersuchung von Schichtgrenzen und Kontakten in organischen Leuchtdioden. Dissertation, Gemeinsame Fakultät für Maschinenbau und Elektrotechnik, Technische Universität Braunschweig, 2001.

[85] J. Blochwitz: Organic light-emitting diodes with doped charge transport layers. Dissertation, Fakultät Mathematik und Naturwissenschaften, Technische Universität Dresden, 2001.

[86] F. J. Himpsel: *Inverse photoemission: fundamentals and applications to semiconductors.* Phys. Scr. **31** (1990), 171–178.

[87] McAllister Technical Services. KP6500 digital Kelvin probe: user's manual, 07 2005.

[88] G. Schröder, H. Treiber: Technische Optik. Würzburg: Vogel 2002.

[89] B. Ruhstaller, T. Flatz, M. Moos, G. Sartoris, M. Kiy, T. Beierlein, R. Kern, C. Winnewisser, R. Pretot, N. Chebotareva, P. van der Schaaf: *59.1: Optoelectronic OLED modeling for device optimization and analysis.* In: SID 07 Digest, 2007, 1686–1690.

[90] K. J. Reynolds, J. A. Barker, N. C. Greenham, R. H. Friend, G. L. Frey: *Inorganic solution-processed hole-injecting and electron-blocking layers in polymer light-emitting diodes.* J. Appl. Phys. **92** (2002), 7556–7563.

[91] P. A. Cox: Transition metal oxides. Oxford: Clarendon Press 1992.

[92] T. Matsushima, Y. Kinoshita, H. Murata: *Formation of ohmic hole injection by inserting an ultrathin layer of molybdenum trioxide between indium tin oxide and and organic hole-transporting layers.* Appl. Phys. Lett. **91** (2007), 253504.

[93] T. Matsushima, G.-H. Jin, H. Murata: *Marked improvement in electroluminescence characteristics of organic light-emitting diodes using an ultrathin hole-injection layer of molybdenum oxide.* J. Appl. Phys. **104** (2008), 054501.

[94] I. D. Baikie, U. Petermann, B. Lägel, K. Dirscherl: *Study of high- and low-work-function surfaces for hyperthermal surface ionization using an absolute Kelvin probe.* J. Vac. Sci. Technol. A **19** (2001) 4, 1460–1466.

[95] S. M. Tadayyon, K. Griffiths, P. R. Norton, C. Tripp, Z. Popovic: *Work function modification of indium–tin–oxide used in organic light emitting devices.* J. Vac. Sci. Technol. A **17** (1999) 4, 1773–1778.

[96] A. Wan, J. Hwang, F. Amy, A. Kahn: *Impact of electrode contamination on the α-NPD/Au hole injection barrier.* Org. Electronics **6** (2005), 47–54.

[97] F. Xie, P. von Blanckenhagen, J. Wu, J.-W. Liu, Q.-Z. Zhang, Y.-C. Chen, E.-G. Wang: *Contamination of si surfaces in ultrahigh vacuum and formation of sic islands.* Appl. Surf. Sci. **181** (2001), 139–144.

[98] R. Azimirad, N. Naseri, O. Akhavan, A. Z. Moshfegh: *Hydrophilicity variation of WO_3 thin films with annealing temperature.* J. Phys. D: Appl. Phys. **40** (2007), 1134–1137.

[99] K. Y. Song, M. K. Park, Y. T. Kwon, H. W. Lee, W. J. Chung, W. I. Lee: *Preparation of transparent particulate MoO_3/TiO_2 and WO_3/TiO_2 films and their photocatalytic properties.* Chem. Mater. **13** (2001), 2349–2355.

[100] A. Galtayries, S. Wisniewski, J. Grimblot: *Formation of thin oxide and sulphide films on polycrystalline molybdenum foils: characterization by xps and surface potential variations.* J. Elec. Spec. Rel. Phen. **87** (1997), 31–44.

[101] M. Kröger, S. Hamwi, J. Meyer, T. Riedl, W. Kowalsky, A. Kahn: *P-type doping of organic wide band gap materials by transition metal oxides: a case study on molybdenum trioxide.* Org. Electr. **10** (2009), 932–938.

[102] T. S. Sian, G. B. Reddy: *Optical, structural and photoelectron spectroscopic studies on amorphous and crystalline molybdenum oxide thin films.* Sol. Energy Mater. Sol. Cells **82** (2004), 375–386.

[103] K. S. Rao, K. V. Madhuri, S. Uthanna, O. M. Hussain, C. Julien: *Photochromic properties of double layer cds/MoO_3 nano-structured films.* Mat. Sci. Eng. B **100** (2003), 79–86.

[104] C.-W. Chu, S.-H. Li, C.-W. Chen, V. Shrotriya, Y. Yang: *High-performance organic thin-film transistors with metal oxide/metal bilayer electrode.* Appl. Phys. Lett. **87** (2005), 193508.

[105] M. G. Hutchins, O. Abu-Alkhair, M. M. El-Nahass, K. Abdel-Hady: *Electrical conduction mechanisms in thermally evaporated tungsten trioxide (WO_3) thin films.* J. Phys.: Condens. Matter **18** (2006), 9987–9997.

[106] M. Merz, J. Eisenmenger, B. Heinz, P. Ziemann: *Tailoring optical properties of WO_3 films in the visible to infrared range by ion bombardement and its description by an oscillator model.* Phys. Rev. B **66** (2002), 184102.

[107] A. Abdellaoui, L. Martin, A. Donnadieu: *Structure and optical properties of MoO_3 thin films prepared by chemical vapor deposition.* Phys. Stat. Sol. (a) **109** (1988), 455–462.

[108] S. K. Deb: *Opportunities and challanges in science and technology of WO_3 for electrochromic and related applications.* Sol. Energy Mater. Sol. Cells **92** (2008), 245–258.

[109] Y. Yi, P. E. Jeon, H. Lee, K. Han, H. S. Kim, K. Jeong, S. W. Cho: *The interface state assisted charge transport at the MoO_3/metal interface.* J. Chem. Phys. **130** (2009), 094704.

[110] K. Kanai, K. Koizumi, S. Ouchi, Y. Tsukamoto, K. Sakanoue, Y. Ouchi, K. Seki: *Electronic structure of anode interface with molybdenum oxide buffer layer.* Org. Electr. **11** (2010), 188–194.

[111] S. Y. Kim, J. M. Baik, H. K. Yu, J.-L. Lee: *Highly efficient organic light-emitting diodes with hole injection layer of transition metal oxides.* J. Appl. Phys. **98** (2005) 093707, 1–7.

[112] J. Meyer, S. Hamwi, T. Bülow, H.-H. Johannes, T. Riedl, W. Kowalsky: *Highly efficient simplified organic light emitting diodes.* Appl. Phys. Lett. **91** (2007), 113506.

[113] M. Hoping, C. Schildknecht, H. Gargouri, T. Riedl, M. Tilgner, H.-H. Johannes, W. Kowalsky: *Transition metal oxides as charge injecting layer for admittance spectroscopy.* Appl. Phys. Lett. **92** (2008), 213306.

[114] S. T. Zhang, X. M. Ding, J. M. Zhao, H. Z. Shi, J. He, Z. H. Xiong, H. J. Ding, E. G. Obbard, Y. Q. Zhan, W. Huang, X. Y. Hou: *Buffer-layer-induced barrier reduction: Role of tunneling in organic light-emitting devices.* Appl. Phys. Lett. **84** (2004) 425-427, 1–3.

[115] G. G. Malliares, J. R. Salem, P. J. Brock, J. C. Scott: *Photovoltaic measurement of the built-in potential in organic light emitting diodes and photodiodes.* J. Appl. Phys. **84** (1998), 1583–1587.

[116] M. Kröger, S. Hamwi, J. Meyer, T. Riedl, W. Kowalsky, A. Kahn: *Role of the deep-lying electronic states of MoO_3 in the enhancement of hole-injection in organic thin films.* Appl. Phys. Lett. **95** (2009), 123301.

[117] E. Ito, Y. Washizu, N. Hayashi, H. Ishii, N. Matsuie, K. Tsuboi, Y. Ouchi, Y. Harima, K. Yamashita, K. Seki: *Spontaneous buildup of giant surface potential by vacuum deposition of Alq_3 and its removal by visible light irradiation.* J. Appl. Phys. **92** (2002) 12, 7306–7310.

[118] M. Kröger, S. Hamwi, J. Meyer, T. Dobbertin, T. Riedl, W. Kowalsky, H.-H. Johannes: *Temperature-independent field-induced charge separation at doped organic/organic interfaces: experimental modeling of electrical properties.* Phys. Rev. B **75** (2007), 235321.

[119] Z. B. Wang, M. G. Helander, M. T. Greiner, J. Qiu, Z. H. Lu: *Analysis of charge-injection characteristics at electrode-organic interfaces: case study of transition-metal-oxides.* Phys. Rev. B **80** (2009), 235325.

[120] V. Shrotriya, G. Li, Y. Yao, C.-W. Chu, Y. Yang: *Transition metal oxides as the buffer layer for polymer photovoltaic cells.* Appl. Phys. Lett. **88** (2006), 073508.

[121] C. Tao, S. Ruan, X. Zhang, G. Xie, L. Shen, X. Kong, W. Dong, C. Liu, W. Chen: *Performance improvement of inverted polymer solar cells with different top electrodes by introducing a MoO_3 buffer layer.* Appl. Phys. Lett. **93** (2008), 193307.

[122] Y. Zhu, A. P. Kulkarni, S. A. Jenekhe: *Phenoxazine-based emissive donor-acceptor materials for efficient organic light-emitting diodes.* Chem. Mater. **17** (2005) 21, 5225–5227.

[123] Y. Shirota, H. Kageyama: *Charge carrier transporting molecular materials and their applications in devices.* Chem. Rev. **107** (2007), 953–1010.

[124] R. S. Crandall, B. W. Faughnan: *Electronic transport in amorphous $H_x WO_3$.* Phys. Rev. Lett. **39** (1977) 4, 232–235.

[125] H. Kamal, A. A. Akl, K. Abdel-Hady: *Influence of proton insertion on the conductivity, structural and optical properties of amorphous and crystalline electrochromic WO_3 films.* Physica B **349** (2004), 192–205.

[126] S. Hayashi, K. Kaneto, K. Yoshino: *Quenching of photoluminescence in poly(thiophene) films by electrochemical doping.* Solid State Comm. **61** (1987) 4, 249–251.

[127] D. D. C. Bradley, R. H. Friend: *Light-induced luminescence quenching in precursor-route poly(p-phenylene vinylene).* J. Phys.: Condens. Matter **1** (1989), 3671–3678.

[128] E. J. W. List, C.-H. Kim, A. K. Naik, U. Scherf, G. Leising, W. Graupner, J. Shinar: *Interaction of singlet excitons with polarons in wide band-gap organic semiconductors: a quantitative study.* Phys. Rev. B **64** (2001), 155204.

[129] C. Gärtner, C. Karnutsch, U. Lemmer, C. Pflumm: *The influence of annihilation processes on the threshold current density of organic laser diodes.* J. Appl. Phys. **101** (2007), 023107.

[130] T. Haskins, A. Chowdhury, R. H. Young, J. R. Lenhard, A. P. Marchetti, L. J. Rothberg: *Charge-induced luminescence quenching in organic light-emitting diodes.* Chem. Mater. **16** (2004), 4675–4680.

[131] S. Reineke, K. Walzer, K. Leo: *Triplet-exciton quenching in organic phosphorescent light-emitting diodes with ir-based emitters.* Phys. Rev. B **75** (2007), 125328.

[132] M. Ikai, S. Tokito, Y. Sakamoto, T. Suzuki, Y. Taga: *Highly efficient phosphorescence from organic light-emitting devices with an exciton-block layer.* Appl. Phys. Lett. **79** (2001) 2, 156–158.

[133] Y. Sun, N. C. Giebink, H. Kanno, B. Ma, M. E. Thompson, S. R. Forrest: *Management of singlet and triplet excitons for efficient white organic light-emitting devices.* Nature **440** (2006), 908–912.

[134] H. Wang, K. P. Klubek, C. W. Tang: *Current efficiency in organic light-emitting diodes with a hole-injection layer.* Appl. Phys. Lett. **93** (2008), 093306.

[135] J. Meyer, S. Hamwi, S. Schmale, T. Winkler, H.-H. Johannes, T. Riedl, W. Kowalsky: *A strategy towards p-type doping of organic materials with homo levels beyond 6 ev using tungsten oxide.* J. Mater. Chem. **19** (2009), 702–705.

[136] G. Xie, Y. Meng, F. Wu, C. Tao, D. Zhang, M. Liu, Q. Xue, W. Chen, Y. Zhao: *Very low turn-on voltage and high brightness tris-(8-hydroxyquinoline) aluminum-based organic light-emitting diodes with MoO_x p-doping layer.* Appl. Phys. Lett. **82** (2008), 093305.

[137] W.-J. Shin, J.-Y. Lee, J. C. Kim, T.-H. Yoon, T.-S. Kim, O.-K. Song: *Bulk and interface properties of molybdenum trioxide-doped hole transporting layer in organic light-emitting diodes*. Org. Electr. **9** (2008), 333–338.

[138] J.-H. Lee, D.-S. Leem, H.-J. Kim, J.-J. Kim: *Effectiveness of p-dopants in an organic hole transporting material*. Appl. Phys. Lett. **94** (2009), 123306.

[139] J. Li, D. Liu, Y. Li, C.-S. Lee, H.-L. Kwong, S. Lee: *A high Tg carbazole-based hole-transporting material for organic light-emitting devices*. Chem. Mater. **17** (2005), 1208–1212.

[140] J.-W. Kang, S.-H. Lee, H.-D. Park, W.-I. Jeong, K.-M. Yoo, Y.-S. Park, J.-J. Kim: *Low roll-off of efficiency at high current density in phosphorescent organic light emitting diodes*. Appl. Phys. Lett. **90** (2007), 223508.

[141] M. Pfeiffer, K. Leo, N. Karl: *Fermi level determination in organic thin films by the Kelvin probe method*. J. Appl. Phys. **80** (1996) 12, 6880–6883.

[142] H. Ishii, N. Hayashi, E. Ito, Y. Washizu, K. Sugi, Y. Kimura, M. Niwano, Y. Ouchi, K. Seki: *Kelvin probe study of band bending at organic semiconductor/metal interfaces: examination of Fermi level alignment*. Phys. Stat. Sol. (a) **201** (2004) 6, 1075–1094.

[143] Q. Sun, B. K. Rao, P. Jena, D. Stolcic, Y. D. Kim, G. Gantefor, A. W. Castleman: *Appearance of bulk properties in small tungsten oxide clusters*. J. Chem. Phys. **121** (2004) 19, 9417–9422.

[144] X. Huang, H.-J. Zhai, B. Kiran, L.-S. Wang: *Observation of d-orbital aromaticity*. Angew. Chem. Int. Ed. **44** (2005), 7251–7254.

[145] J. Berkowitz, M. G. Inghram, W. A. Chupka: *Polymeric gaseous species in the sublimation of molybdenum trioxide*. J. Chem. Phys. **26** (1957) 4, 842–846.

[146] B. A. Gregg, S.-G. Chen, H. M. Branz: *On the superlinear increase in conductivity with dopant concentration in excitonic semiconductors*. Appl. Phys. Lett. **84** (2004) 10, 1707–1709.

[147] B. Maennig, M. Pfeiffer, A. Nollau, X. Zhou, K. Leo, P. Simon: *Controlled p-type doping of polycrystalline and amorphous organic layers: Self-consistent description of conductivity and field-effect mobility by a microscopic percolation model*. Phys. Rew. B **64** (2001) 195208, 1–9.

[148] Y. Zhang, B. de Boer, P. W. M. Blom: *Controllable molecular doping and charge transport in solution-processed polymer semiconducting layers*. Adv. Funct. Mater. **19** (2009), 1901–1905.

[149] H. Shimotani, G. Diguet, Y. Iwasa: *Direct comparison of field-effect and electrochemical doping in regioregular poly(3-hexylthiophene).* Appl. Phys. Lett. **86** (2005), 022104.

[150] T. Rabe, P. Görrn, M. Lehnhardt, M. Tilgner, T. Riedl, W. Kowalsky: *Highly sensitive determination of the polaron-induced optical absorption of organic charge-transport materials.* Phys. Rev. Lett. **102** (2009), 137401.

[151] M. Lehnhardt, S. Hamwi, M. Hoping, J. Reinker, T. Riedl, W. Kowalsky: *Charge carrier densities in chemically doped organic semiconductors verified by two independent techniques.* Appl. Phys. Lett. **96** (2010), 193301.

[152] M.-H. Ho, M.-T. Hsieh, J.-F. Chen, K.-H. Lin, C. H. Chen: *35.4: Stable and efficient organic light emitting diodes based on a single host of p-doped and n-doped layers.* In: SID 09 Digest, 2009, 503–506.

[153] Merck KGaA. Material safety data sheet: Cs_2CO_3, 09 2004.

[154] I. G. Hill, D. Milliron, J. Schwartz, A. Kahn: *Organic semiconductor interfaces: electronic structure and transport properties.* Appl. Surf. Sci. **166** (2000), 354–362.

[155] Y. Li, D.-Q. Zhang, L. Duan, R. Zhang, L.-D. Wang, Y. Qui: *Elucidation of the electron injection mechanism of evaporated cesium carbonate cathode interlayer for organic light-emitting diodes.* Appl. Phys. Lett. **90** (2007), 012119.

[156] J. Huang, Z. Xu, Y. Yang: *Low-work-function surface formed by solution-processed and thermally deposited nanoscale layers of cesium carbonate.* Adv. Funct. Mater. **17** (2007), 1966–1973.

[157] A. H. Sommer: *Hypothetical mechanism of operation of the Ag-O-Cs (S-1) photocathode involving the peroxide* Cs_2O_2. J. Appl. Phys. **51** (1979) 2, 1254–1255.

[158] B. Woratschek, W. Sesselmann, J. Küppers, G. Ertl, H. Haberland: *The interaction of cesium with oxygen.* J. Chem. Phys. **86** (1987) 4, 2411–2422.

[159] C.-I. Wu, C.-T. Lin, Y.-H. Chen, M.-H. Chen, Y.-J. Lu, C.-C. Wu: *Electronic structures and electron-injection mechanisms of cesium-carbonate-incorporated cathode structures for organic light-emitting devices.* Appl. Phys. Lett. **88** (2006), 152104.

[160] M. Nivsarkar, M. P. Kaushik: *N-alkylation reaction of highly strained bicyclic β-lactam using silica supported cesium carbonate.* Catal. Comm. **6** (2005), 367–370.

[161] R. Fernández, J. Estelle, Y. Cesteros, P. Salagre, F. Medina, J.-E. Sueiras, J.-L. G. Fierro: *Structural characterization of NiO doped with several caesium loadings.* J. Mol. Catal. A: Chem. **119** (1997), 77–85.

[162] W. F. Pasveer, J. Cottaar, C. Tanase, R. Coehoorn, P. A. Bobbert, P. W. M. Blom, D. M. de Leeuw, M. A. J. Michels: *Unified description of charge-carrier mobilities in disordered semiconducting polymers.* Phys. Rev. Lett. **94** (2005), 206601.

[163] I. N. Hulea, H. B. Brom, A. J. Houtepen, D. Vanmaekelbergh, J. J. Kelly, E. A. Meulenkamp: *Wide energy-window view on the sensity of states and hole mobility in poly(p-phenylene vinylene).* Phys. Rev. Lett. **93** (2004) 16, 166601.

[164] K. H. Lee, H. W. Jang, K.-B. Kim, Y.-H. Tak, J.-L. Lee: *Mechanism for the increase of indium-tin-oxide work function by O_2 inductively coupled plasma treatment.* J. Appl. Phys. **95** (2004) 2, 586–590.

[165] K. Seki, T. Nishi, S. Tanaka, K. Komatsu, T. Ikame, H. Ishii, K. Kanai: *Effects of various types of doping on the electronic structure of organic interfaces.* In: IPAP Conf. Series 6, 178–183.

[166] O. M. Ottinger, C. Melzer, H. von Seggern: *Pitfalls in Kelvin probe measurements.* J. Appl. Phys. **106** (2009), 023704.

[167] C.-C. Wu, T.-L. Liu, Y.-T. Lin, W.-Y. Hung, T.-H. Ke, K.-T. Wong, T.-C. Chao: *Influences of oligomer length on carrier-transport properties of oligofluorenes.* Appl. Phys. Lett. **85** (2004) 7, 1172–1174.

[168] T.-C. Chao, Y.-T. Lin, C.-Y. Yang, T. S. Hung, H.-C. Chou, C.-C. Wu, K.-T. Wong: *Highly efficient UV organic light-emitting devices based on bi(9,9-diarylfluorene)s.* Adv. Mater. **17** (2004) 8, 992–996.

[169] S. Grecu, M. Bronner, A. Opitz, W. Brütting: *Characterization of polymeric metal-insulator-semiconductor diodes.* Synth. Metals **146** (2004), 359–363.

[170] X. D. Feng, C. J. Huang, V. Lui, R. S. Khangura, Z. H. Lu: *Ohmic cathode for low-voltage organic light-emitting diodes.* Appl. Phys. Lett. **86** (2005) 143511, 1–3.

[171] T. Rabe, S. Hamwi, J. Meyer, P. Görrn, T. Riedl, H.-H. Johannes, W. Kowalsky: *Suitability of lithium doped electron injection layers for organic semiconductor lasers.* Appl. Phys. Lett. **90** (2007), 151103.

[172] T. P. I. Saragi, T. Spehr, A. Siebert, T. Fuhrmann-Lieker, J. Salbeck: *Spiro compounds for organic optoelectronics.* Chem. Rev. **107** (2007), 1011–1065.

[173] T. Mayer, C. Hein, J. Härter, E. Mankel, W. Jaegermann: *A doping mechanism for organic semiconductors derived from sxps measurements on co-evaporated films of cupc and tcnq and on a TCNQ/CuPc interface.* In: Proc. of SPIE, 2008, 705204.

[174] Y. Zhang, B. de Boer, P. W. M. Blom: *Trap-free electron transport in poly(p-phenylene vinylene) by deactivation of traps with n-type doping.* Phys. Rev. B **81** (2010), 085201.

[175] J. Xue, S. R. Forrest: *Bipolar doping between a molecular organic donor-acceptor couple.* Phys. Rev. B **69** (2004), 245322.

[176] S. Olthof, W. Tress, R. Meerheim, B. Lüssem, K. Leo: *Photoelectron spectroscopy study of systematically varied doping concentrations in an organic semiconductor layer using a molecular p-dopant.* J. Appl. Phys. **106** (2009), 103711.

[177] S. D. Ha, A. Kahn: *Isolated molecular dopants in pentacene observed by scanning tunneling microscopy.* Phys. Rev. B **80** (2009), 195410.

[178] Dipl.-Chem. D. Schneidenbach: personal communication 2009.

[179] F. Wang, T. Xiong, X. Qiao, D. Ma: *Origin of improvement in device performance via the modification role of cesium hydroxide doped tris(8-hydroxyquinoline) aluminum interfacial layer on ito cathode in inverted bottom-emission organic light-emitting diodes.* Org. Electr. **10** (2009), 266–274.

[180] J. X. Sun, X. L. Zhu, H. J. Peng, M. Wong, H. S. Kwok: *Effective intermediate layers for highly efficient stacked organic light-emitting devices.* Appl. Phys. Lett. **87** (2005) 093504, 1–3.

[181] L. S. Liao, K. P. Klubek, C. W. Tang: *High-efficiency tandem organic light-emitting diodes.* Appl. Phys. Lett. **84** (2004) 2, 167–169.

[182] X. D. Gao, J. Zhou, Z. T. Xie, B. F. Ding, Y. C. Qian, X. M. Ding, X. Y. Hou: *Mechanism of charge generation in p-type doped layer in the connection unit of tandem-type organic light-emitting devices.* Appl. Phys. Lett. **93** (2008), 083304.

[183] F. Guo, D. Ma: *White organic light-emitting diodes based on tandem structures.* Appl. Phys. Lett. **87** (2005) 173510, 1–3.

[184] C.-W. Chen, Y.-J. Lu, C.-C. Wu, E. H.-E. Wu, C.-W. Chu, Y. Yang: *Effective connecting architecture for tandem organic light-emitting devices.* Appl. Phys. Lett. **87** (2005) 241121, 1–3.

[185] D.-S. Leem, J.-H. Lee, J.-J. Kim, J.-W. Kang: *Highly efficient tandem p-i-n organic light-emitting diodes adopting a low temperature evaporated rhenium oxide interconnecting layer.* Appl. Phys. Lett. **93** (2008), 103304.

[186] M. Terai, K. Fujita, T. Tsutsui: *Capacitance measurement in organic thin-film device with internal charge separation zone.* Jpn. J. Appl. Phys. **44** (2005) 33, 1059–1062.

[187] X. Qi, N. Li, S. R. Forrest: *Analysis of metal-oxide-based charge generation layers used in stacked organic light-emitting diodes.* J. Appl. Phys. **107** (2010), 014514.

[188] S. Hamwi, J. Meyer, M. Kröger, T. Winkler, M. Witte, T. Riedl, A. Kahn, W. Kowalsky: *The role of transition metal oxides in charge-generation layers for stacked organic light-emitting diodes.* Adv. Funct. Mater. **20** (2010), 1762–1766.

[189] L. S. Liao, K. P. Klubek: *Power efficiency improvement in a tandem organic light-emitting diode.* Appl. Phys. Lett. **92** (2008), 223311.

[190] Y.-K. Kim, J. W. Kim, Y. Park: *Energy level alignment at a charge generation interface between 4,4'-bis(N-phenyl-1-naphthylamino)biphenyl and 1,4,5,8,9,11-hexaazatriphenylene-hexacarbonitrile.* Appl. Phys. Lett. **94** (2009), 063305.

[191] W. S. Jeon, T. J. Park, J. J. Park, S. Y. Kim, J. Jang, J. H. Kwon, R. Pode: *Highly efficient bilayer green phosphorescent organic light emitting devices.* Appl. Phys. Lett. **92** (2008), 113311.

[192] Z. W. Liu, M. G. Helander, Z. B. Wang, Z. H. Lu: *Efficient bilayer phosphorescent organic light-emitting diodes: direct hole injection into triplet dopants.* Appl. Phys. Lett. **94** (2009), 113305.

[193] K. Harada, M. Riede, K. Leo, O. R. Hild, C. M. Elliott: *Pentacene homojunctions: electron and hole transport properties and related photovoltaic responses.* Phys. Rev. B **77** (2008), 195212.

[194] H. Tsuji, C. Mitsui, Y. Sato, E. Nakamura: *Bis(carbazolyl)benzodifuran: a high-mobility ambipolar material for homojunction organic light-emitting diode devices.* Adv. Mater. **21** (2009), 3776–3779.

[195] Y. Greenwald, G. Cohen, J. Poplawski, E. Ehrenfreund, S. Speiser, D. Davidov: *Photoconductivity and photoexcitation spectra of acceptor substituted poly(3-butyl)thiophene.* Mat. Sci. For. **191** (1995), 187–194.

[196] A. Gambetta, T. Virgili, G. Lanzani: *Ultrafast excitation cross-correlation photoconductivity in polyfluorene photodiodes.* Appl. Phys. Lett. **86** (2005), 253509.

[197] R. R. Lunt, N. C. Giebink, A. A. Belak, J. B. Benziger, S. R. Forrest: *Exciton diffusion lengths of organic semiconductor thin films measured by spectrally resolved photoluminescence quenching.* J. Appl. Phys. **105** (2009), 053711.

[198] C. H. Lee, G. Yu, D. Moses: *Transient and steady-state photoconductivity of a solid C_{60} film.* Phys. Rev. B **48** (1993) 11, 8506–8509.

[199] M. C. Gather, M. Flämmich, N. Danz, D. Michaelis, K. Meerholz: *Measuring the profile of the emission zone in polymeric organic light-emitting diodes.* Appl. Phys. Lett. **94** (2009), 263301.